VOLUME 75 JANUARY 21, 1971 NUMBER 2

JPCHAx

THE JOURNAL OF PHYSICAL CHEMISTRY

PUBLISHED BIWEEKLY BY THE AMERICAN CHEMICAL SOCIETY

Designed for the potential scientist in your family...

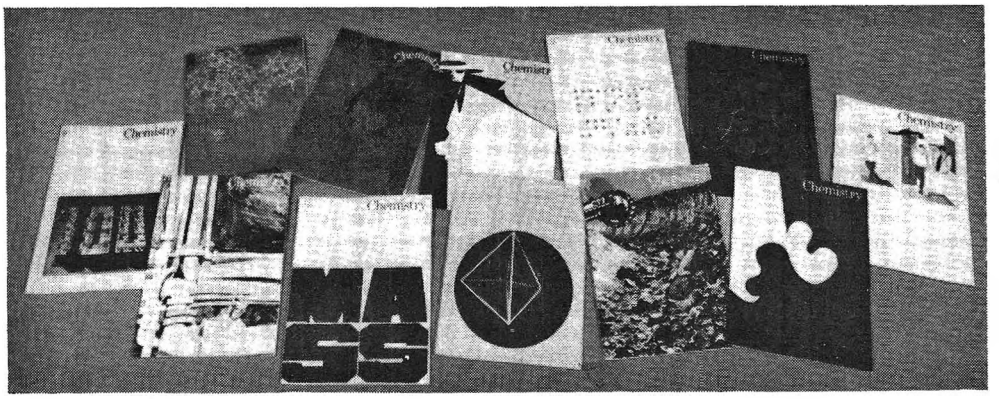

Chemistry **magazine—for the high school or college student whose curiosity of chemistry extends *beyond* required course work.**

Eleven issues a year, including a special Summer issue, bring the reader

- ☐ experimental projects and investigations
- ☐ news items on recent research developments
- ☐ feature articles on theoretical and applied science
- ☐ book reviews
- ☐ chemical puzzles
- ☐ reader's column.

All adding up to an exciting opportunity to see chemistry in *action—out of the textbook and in the real laboratory!*

Each issue of Chemistry is as broad as the science itself. It delves into the past . . . reports the present . . . relates to the future.

Below is a sample of the interesting and timely articles offered in Chemistry . . .

"Why Should Anyone Study Chemistry" . . . "The DDT Story" . . . "Conformational Analysis or How Some Molecules Wiggle" . . . "Chemistry in Language and Literature" . . . "The George Washington Carver Story" . . . "Schizophrenia —the Body's Chemical Mistake"

Each issue of Chemistry is unusual in its attractiveness and diversity of subject matter. The student can enter through many doors with a choice of reading from the rather general to the relatively technical, all informative . . . entertaining . . . useful in academic work.

Order Chemistry now and start an exciting adventure for a young member in your family!

American Chemical Society Publications
1155 Sixteenth Street, N.W.
Washington, D.C. 20036

Yes—start a subscription to **Chemistry** at the low yearly rate of $6.
☐ Canada, PUAS $7.00* ☐ Foreign $7.50*

* Payment must be made in U.S. currency, by international money order, UNESCO coupons, or U.S. bank draft, or order through your book dealer.

Send **Chemistry** to:

Name _____ ☐ Check enclosed (payable to American Chemical Society)

Address _____ ☐ Send bill to

City _____ State _____ Zip _____ _____

Recipient is a ☐ student ☐ teacher. Address _____

☐ other _____ State _____ City _____ Zip _____

E2A

THE JOURNAL OF

PHYSICAL CHEMISTRY

AMERICAN CHEMICAL SOCIETY, PUBLICATIONS DIVISION,
1155 Sixteenth St., N.W., Washington, D. C. 20036
RICHARD L. KENYON, *Director*
JOSEPH H. KUNEY, *Director of Business Operations and Director of Publications Research*
DAVID E. GUSHEE, *Publication Manager, Journals*

 Published biweekly by the American Chemical Society at 20th and Northampton Sts., Easton, Pa. 18042. Second-class postage paid at Easton, Pa.

All manuscripts should be sent to *The Journal of Physical Chemistry*, Department of Chemistry, University of Minnesota, Minneapolis, Minn. 55455.

Additions and Corrections are published once yearly in the final issue. See Volume 74, Number 26 for the proper form.

Extensive or unusual alterations in an article after it has been set in type are made at the author's expense, and it is understood that by requesting such alterations the author agrees to defray the cost thereof.

The American Chemical Society and the Editor of *The Journal of Physical Chemistry* assume no responsibility for the statements and opinions advanced by contributors.

Correspondence regarding accepted copy, proofs, and reprints should be directed to Editorial Production Office, American Chemical Society, 20th and Northampton Sts., Easton, Pa. 18042. Manager: CHARLES R. BERTSCH. Assistant Editor: EDWARD A. BORGER. Editorial Assistant: EVELYN J. UHLER.

Advertising Office: Century Communications Corporation, 142 East Avenue, Norwalk, Conn. 06851.

Business and Subscription Information

Remittances and orders for subscriptions and for single copies, notices of changes of address and new professional connections, and claims for missing numbers should be sent to the Subscription Service Department, American Chemical Society, 1155 Sixteenth St., N.W., Washington, D. C. 20036. Allow 4 weeks for changes of address. Please include an old address label with the notification.

Claims for missing numbers will not be allowed (1) if received more than sixty days from date of issue, (2) if loss was due to failure of notice of change of address to be received before the date specified in the preceding paragraph, or (3) if the reason for the claim is "missing from files."

Subscription rates (1971): members of the American Chemical Society, $20.00 for 1 year; to nonmembers, $40.00 for 1 year. Those interested in becoming members should write to the Admissions Department, American Chemical Society, 1155 Sixteenth St., N.W., Washington, D. C. 20036. Postage to Canada and countries in the Pan-American Union, $4.00; all other countries, $5.00. Single copies for current year: $2.00. Rates for back issues from Volume 56 to date are available from the Special Issues Sales Department, 1155 Sixteenth St., N.W., Washington, D. C. 20036.

This publication and the other ACS periodical publications are now available on microfilm. For information write to: MICROFILM, Special Issues Sales Department, 1155 Sixteenth St., N.W., Washington, D. C. 20036.

Notice to Authors last printed in the issue of December 24, 1970

The ADVANCES IN CHEMISTRY Series...

Excellent Reviews in Book Form of Specialized Chemical Topics

For comprehensive reviews of all the important aspects of a chemical subject... read the books in the ADVANCES IN CHEMISTRY Series.

Ranging up to 750 pages in length, ADVANCES volumes include...

- Authoritative, thought-provoking articles by as many as several dozen scientists per volume.
- Carefully compiled collections of data.
- Groups of related papers presented at important national and international symposia.
- Invited reviews of current work written by researchers eminent in the field discussed.

With the ADVANCES you learn about brand-new chemical subjects... and bring yourself up to date on familiar chemical topics. The numerous scientists contributing to each volume provide you with stimulating reading enriched by a variety of viewpoints. And the ADVANCES bring material together under one cover which would otherwise be scattered among many journals... or *not available at all.*

... Put chemical topics of interest to you in proper perspective. Read the ADVANCES IN CHEMISTRY Series.

The order form lists the 20 most recent titles in the ADVANCES IN CHEMISTRY Series. Use it to order your ADVANCES *now.*

No.	Title	Price	Number of copies ordered	Cost
96	Engineering Plastics and Their Commercial Development 128 pp (1969)	$7.50	___	_____
95	Cellulases and Their Applications 460 pp (1969)	$14.50	___	_____
93	Radionuclides in the Environment 522 pp (1970)	$15.00	___	_____
92	Epoxy Resins 224 pp (1970)	$10.50	___	_____
91	Addition and Condensation Polymerization Processes 767 pp (1969)	$19.50	___	_____
90	Fuel Cell Systems—II 446 pp (1969)	$17.50	___	_____
89	Isotopes Effects in Chemical Processes 278 pp (1969)	$13.00	___	_____
88	Propellants Manufacture, Hazards, and Testing 395 pp (1969)	$12.00	___	_____
87	Interaction of Liquids at Solid Substrates 212 pp (1968)	$9.50	___	_____
86	Pesticidal Formulations Research. Physical and Colloidal Chemical Aspects 212 pp (1969)	$9.50	___	_____
85	Stabilization of Polymers and Stabilizer Processes 332 pp (1968)	$12.00	___	_____
84	Molecular Association in Biological and Related Systems 308 pp (1968)	$10.50	___	_____
83	Chemical Marketing: The Challenges of the Seventies 199 pp (1968)	$9.50	___	_____
82	Radiation Chemistry—II 558 pp (1968)	$16.00	___	_____
81	Radiation Chemistry—I 616 pp (1968)	$16.00	___	_____
81	and 82 ordered together	$30.00	___	_____
80	Chemical Reactions in Electrical Discharges 514 pp (1969)	$15.00	___	_____
79	Adsorption from Aqueous Solution 212 pp (1968)	$10.00	___	_____

TOTAL COST _____

Postpaid U.S. and Canada; all others please add $0.20 for each volume ordered.

Payment must be in U.S. funds, by international money order, UNESCO coupon, or U.S. bank draft; or order through your book dealer.

Please ship my ADVANCES to:

Name _____

Address _____

City _____ State/Country _____ Zip _____

☐ Bill me. ☐ Payment enclosed.

Return this order form to AMERICAN CHEMICAL SOCIETY, Special Issues Sales, Dept. LG-68, 1155 16th Street, N.W., Washington, D.C. 20036.

... There are over 50 other volumes in the ADVANCES Series. To receive your pricelist for all the ADVANCES, just send us your request... or note it on your order. You'll receive the list by return mail.

THE JOURNAL OF

PHYSICAL CHEMISTRY

Volume 75, Number 2 January 21, 1971

NOTES

COMMUNICATIONS TO THE EDITOR

AUTHOR INDEX

THE JOURNAL OF
PHYSICAL CHEMISTRY

VOLUME 75, NUMBER 2 JANUARY 21, 1971

A Complementary Shock Tube Technique Study of the Exchange of Hydrogen Chloride and Deuterium[1]

by R. D. Kern, Jr.,* and G. G. Nika[2]

Department of Chemistry, Louisiana State University in New Orleans, New Orleans, Louisiana 70122
(Received August 10, 1970)

Publication costs assisted by the National Science Foundation

Kinetic data for the homogeneous exchange of equimolar mixtures of hydrogen chloride and deuterium in the presence of an inert gas diluent were obtained by the analysis of infrared emission profiles of HCl and DCl and time-resolved mass spectra of m/e 36 and 37. The reaction was studied behind reflected shock waves over a temperature range of 1700–2800°K, a total density variation of 1.7–4.0 $\times 10^{-6}$ mol/cm^3, and observation times of 500–750 μsec. Equilibrium amounts of HCl and DCl were observed in several of the experiments performed at higher temperatures. Both argon and neon were used separately as diluents. The results from the infrared emission shock tube and the time-of-flight mass spectrometer shock tube were in agreement within one standard deviation of the Arrhenius plots. The rate of product formation was found to be nonlinear with respect to time. The formation of the mole fraction of DCl ($f_{DCl} = [DCl]_t/[HCl]_0$) using both sources of data is represented by the equation $\{1 - f_{DCl}[1 + (f_{HCl}/f_{DCl})_{eq}]\} = \exp(-k[M]t^2)$, where $k = 10^{16.12\pm0.30} \exp(-34{,}340 \pm 3130/RT)$, cm^3 mol^{-1} sec^{-2}. When the rate is expressed on a concentration basis, the combined order dependence of the reactants was shown to be consistent with a value of one. The difficulties in explaining the rate law in terms of an atomic or molecular mechanism are discussed.

Introduction

Isotopic exchange reactions have been examined by the shock tube technique for several years, and the interpretation of the experimental rate laws has generated considerable theoretical interest. Bauer and his group at Cornell University have studied many systems involving deuterium and other simple molecules with the single pulse shock tube as have Burcat and Lifshitz. The exchange of D_2 with H_2,[3a,b] H_2S,[3c] NH_3,[3d,e] and CH_4[3f] are characterized by activation energies that are lower than predicted by an atomic or molecular mechanism. The rate of product formation was dependent upon the inert gas concentration. These experimental results along with vibrational relaxation data of Kieffer and Lutz for H_2[4a] and D_2[4b] led to the postulation of a vibrational excitation mechanism for the exchange process.[3a] Other exchange reactions studied by the single pulse technique include $^{30}N_2 + {}^{28}N_2$,[3g] $^{12}C^{18}O + {}^{13}C^{16}O$,[3h] $^{32}O_2 + {}^{36}O_2$,[3i] and $CH_4 + CD_4$.[3j]

(1) Support of this work by the National Science Foundation under grant GP-23137 and also funds for equipment from NSF Departmental Science Development Program GU-2632 are gratefully acknowledged. Funds for the construction of the infrared emission shock tube from PRF Grant No. 1028-G2 were most appreciated.

(2) NDEA Fellow.

(3) (a) S. H. Bauer and E. Ossa, *J. Chem. Phys.*, **45**, 434 (1966); (b) A. Burcat and A. Lifshitz, *ibid.*, **47**, 3079 (1967); (c) A. Burcat, A. Lifshitz, D. Lewis, and S. H. Bauer, *ibid.*, **49**, 1449 (1968); (d) A. Lifshitz, C. Lifshitz, and S. H. Bauer, *J. Amer. Chem. Soc.*, **87**, 143 (1965); (e) A. Burcat and A. Lifshitz, *J. Chem. Phys.*, **52**, 337 (1970); (f) W. Watt, P. Borrell, D. Lewis, and S. H. Bauer, *ibid.*, **45**, 444 (1966); (g) A. Bar-Nun and A. Lifshitz, *ibid.*, **47**, 2878 (1967); (h) A. Burcat and A. Lifshitz, *ibid.*, **51**, 1826 (1967); (i) H. F. Carroll and S. H. Bauer, *J. Amer. Chem. Soc.*, **91**, 7727 (1969); (j) A. Burcat and A. Lifshitz, *J. Chem. Phys.*, **52**, 3613 (1970).

(4) (a) J. H. Kiefer and R. W. Lutz, *ibid.*, **44**, 668 (1966); (b) J. H. Kiefer and R. W. Lutz, *ibid.*, **44**, 658 (1966).

Exchange reactions involving $^{18}O_2$ and $^{16}O_2$, CO,[5a] SO_2, and CO_2[5b] have been reported by Kistiakowsky and his coworkers. The Harvard group used a time-of-flight mass spectrometer (TOF) coupled to the shock tube and observed a nonlinear time dependence for product formation with and without added amounts of N_2O. An important finding was that even though the experimental activation energies were low with respect to an atomic mechanism, there was other considerably persuasive evidence that the exchange was dominated by three-center reactions. For example, addition of O atoms to the $^{18}O_2$ + CO exchange[5a] *via* N_2O led to rate constants which were consistent with rate constants obtained in the absence of N_2O, assuming an atomic mechanism. A quadratic time dependence for product formation was determined.

The exchange reaction that has received the most attention from theoretical considerations is $H_2 + D_2$. In two recent papers,[6] the calculation of the potential energy barrier to a four-center transition complex has been accomplished for this exchange and in all of the geometric configurations that led to products, the potential energy barrier was higher than that demonstrated by the three-center transition complex mechanism. Hence, according to these calculations, the energetics of a homogeneous atomic mechanism (110 kcal/mol) are more favorable than that of a molecular mechanism ($\geq$148 kcal/mol).

When comparison is made with the experimental value of 42 kcal/mol for the H_2–D_2 reaction,[3a] the need for proposing a mechanism other than atomic or molecular is apparent. The nature of the single pulse shock tube technique is such that the time dependence of product formation cannot be easily determined. It was assumed to be linear.[3]

The purpose of this work is to study an exchange reaction similar in many respects to $H_2 + D_2$. The bond energy of HCl (102.3 kcal/mol) is very close to that of H_2 (103.1 kcal/mol) although shock tube work on the dissociation of these two molecules yields quite different values for the activation energy of the dissociation process: 70,[7a,b] 81[7c] kcal/mol for HCl, and 97 kcal/mol[8] for H_2. The time dependence of DCl formation is of particular interest. Two independent and dynamic techniques may be used to monitor the HCl–D_2 system: infrared emission and time-of-flight mass spectrometry. The application of these techniques to the same reaction system in the past (*e.g.*, pyrolysis and oxidation of ethylene)[9] has supplied important corroborating kinetic data. The comparison of data obtained from infrared emission profiles and the time-resolved mass spectra is particularly useful as a prelude to an investigation of the $H_2 + D_2$ exchange since the TOF-shock tube combination is the only practical dynamic sampling technique currently available for this reaction.

Special attention has been[10] and must continue to be paid to impurities. The presence of oxygen can initiate chain-branching reactions which can alter drastically the form of the rate law. An example of the effect of oxygen on the HCl + D_2 exchange will be presented in this paper.

Experimental Section

A complementary shock tube facility consisting of two shock tubes has been constructed in order that dynamic sampling of reacting gases recorded by two independent methods may be compared critically. One shock tube is equipped for simultaneous observation of infrared emission from two different species through selected filters or radiation from one species filtered at two different wavelengths. The sampling may be from either the incident zone or at various distances from the end wall in the reflected shock region. In this study, a position 3.2 mm from the end wall was chosen in order that the sampling be from a portion of gas similar to that analyzed in the other shock tube. The second tube is coupled to a time-of-flight mass spectrometer which has been modified to operate in the range 30–50 kHz. Gas from the reflected shock zone flows through a nozzle which protrudes approximately 1 mm into the shock tube from the end wall. The gas passes from the nozzle to the ion source and is ionized at 20-μsec intervals for a typical reaction time of 500 μsec. A more detailed description of each tube follows.

Infrared Emission Shock Tube. The main features of the tube are: (1) a driver section 11.75 in. long fabricated out of 0.25-in. brass sheet rolled to an 11.70 in. o.d. and fitted with a spring driven knife that produces a quadrant petalling pattern in the aluminum foil used for diaphragms;[11] (2) a flanged interface 1.50 in. i.d. on either side to hold the diaphragm; (3) a 2-in. (nominal) ball valve located 12.25 in. downstream from the interface; (4) connection at a right angle to the tube 4 in. upstream from the 2-in. valve and leading to the gas handling system through 0.5-in. i.d. brass pipe, a 0.5-in. ball valve, stainless steel bellows, and finally Pyrex glass tubing; (5) a transition section of aluminum rod 6 in. long flanged to the downstream side of the 2-in. ball valve. The internal dimensions vary in a smooth fashion from a circular cross section of 1.50 in. i.d. at the

(5) (a) S. H. Garnett, G. B. Kistiakowsky, and B. V. O'Grady, *J. Chem. Phys.*, **51**, 84 (1969); (b) T. C. Clark, S. H. Garnett, and G. B. Kistiakowsky, *ibid.*, **52**, 4692 (1970).

(6) (a) C. W. Wilson, Jr., and W. A. Goddard, III, *ibid.*, **51**, 716 (1969); (b) M. Rubinstein and I. Shavitt, *ibid.*, **51**, 2014 (1969).

(7) (a) E. S. Fishburne, *ibid.*, **45**, 4053 (1966); (b) T. A. Jacobs, N. Cohen, and R. R. Giedt, *ibid.*, **46**, 1958 (1967); (c) D. J. Seery and C. T. Bowman, *ibid.*, **50**, 5374 (1969).

(8) R. L. Belford and R. A. Strehlow, *Ann. Rev. Phys. Chem.*, **20**, 260 (1969).

(9) (a) I. D. Gay, R. D. Kern, G. B. Kistiakowsky, and H. Niki, *J. Chem. Phys.*, **45**, 2371 (1966); (b) I. D. Gay, G. P. Glass, R. D. Kern, and G. B. Kistiakowsky, *ibid.*, **47**, 313 (1967); (c) J. B. Homer and G. B. Kistiakowsky, *ibid.*, **47**, 5290 (1967).

(10) See ref 3 for example.

(11) J. E. Dove and D. McL. Moulton, *Proc. Roy. Soc. Ser. A*, **283**, 216 (1965).

upstream end to a rectangular cross section 1.25 in. × 1.75 in. at the downstream end. The shock wave travels through a uniform 1.50-in. i.d. path until it reaches the transition section. (6) The remainder of the shock tube is constructed from two sections of rectangular aluminum tubing 1.25 in. × 1.75 in. internal dimensions. One piece 9.63 ft long is flanged directly to the transition section. The final section contains the velocity gauges and observation windows. Two final sections are available for selection—one piece designed for incident waves and the other suitable for reflected wave experiments. In the work described here, all of the observations were made behind reflected waves. The length of the final section is 4.9 ft, and the total length of the driven section is 16 ft.

The primary advantages in operating the tube are the ultimate vacuum attainable and low outgassing rates, typically 1×10^{-6} Torr and 0.5 μ/min, respectively. This condition is achieved by closing the 2-in. ball valve after each run and replacing the diaphragm while some 15 ft of the driven section is under vacuum. Household aluminum foil of various thicknesses is used. The petalling pattern accompanying diaphragm rupture minimizes the number of fragments blown into the test section, thus reducing substantially the frequency of cleaning the tube. The observation portion consists of flat surfaces, facilitating the mounting of velocity gauges and calcium fluoride windows flush with the internal surfaces.

Two calcium fluoride windows are centered opposite each other at a point 2.125 in. from the end of the aluminum tubing. The windows are mounted in the short dimension walls. A solid brass plug 2.375 in. × 1.25 in. × 1.75 in. flanged at one end is inserted into the end of the tube and serves as the reflecting surface for the shock wave. This flat surface can be located at various positions ranging from the center of the infrared windows to a distance 50.8 mm downstream from the windows. A distance of 3.2 mm was used for practically all of the experiments.

Four thin film velocity gauges are placed at 20-cm intervals upstream from the windows, the nearest gauge mounted 5 cm away. The signals from the gauges are amplified, displayed on a raster pattern, and recorded on Polaroid 107 film. A Tektronix 535 A oscilloscope was modified for raster presentation.[12] The cathode beam is blanked at 5-μsec intervals by a crystal controlled oscillator. The oscilloscope is triggered externally by a signal from the first velocity gauge.

Outside the shock tube, the infrared emission from the shocked gas first passes through slits set at 0.8 mm width which are positioned 6 mm from the window, then through a selected narrow bandpass interference filter and onto a front surface concave mirror. The 22-mm focal length mirror focuses the emission on the sensitive element of a Texas Instruments indium antimonide infrared detector responsive to the spectral region 2–5.5 μ. The entire optical system is contained in a stainless steel housing which rests on a massive steel slab. The signal from the liquid nitrogen cooled detector is increased by a solid state amplifier (Control and Computing Devices, Model LAB-25) and then fed into a Tektronix 531 A oscilloscope with a 1A1 plug-in unit operating in the chopped mode. The oscilloscope is triggered externally by a signal from the velocity gauge 5 cm from the observation station. The two optical system housings are nearly identical, and the signals from their respective detectors are displayed simultaneously and photographed on Polaroid 3000 speed film. The risetime of the signal is on the order of 10 μsec. The sweep speed is usually set at 50 or 100 μsec/cm. The vertical signal out on occasion is displayed on a second or third 531 A oscilloscope set at a faster (10 μsec/cm) or slower (200 μsec/cm) sweep speed in order to observe early times of the reaction and contact surface arrival events, respectively.

All of the pictures were taken from cameras constructed from polyvinyl tubing, Edmund Scientific Co. lenses, and Polaroid camera backs. The material cost for each camera was about $100.

The gas handling system consists of eight 5-l. storage bulbs, some fitted with cold fingers, two Wallace–Tiernan differential pressure gauges (0–10 and 0–400 in. water, respectively), a three-stage mercury diffusion pump, and several pressure gauges (thermocouple, McLeod and Dubrovin). The inlet system for gases into the manifold consists entirely of glass and metal connections.

TOF Shock Tube. The coupling of a shock tube to a time-of-flight mass spectrometer was first reported in the literature by Bradley and Kistiakowsky in 1961.[13] The original apparatus has been completely reconstructed[11] and continually improved by the efforts of several people working since then in Professor Kistiakowsky's laboratory.[14] Workers in different laboratories have performed successful experiments of this type on a variety of gas kinetic systems.[15]

At L.S.U.N.O., the test section consists of two pieces of 1-in. i.d. Type 316 stainless steel seamless pipe flanged together for a total length of 10.8 ft. The driver was constructed from a 13 in. length of 10-in. i.d. aluminum pipe and is connected to a Welch Model 1397 mechanical pump. The design is similar to the previously men-

(12) Design for the raster modification was kindly furnished by Mr. John Dedham, Tektronix sales engineer.

(13) J. N. Bradley and G. B. Kistiakowsky, *J. Chem. Phys.*, **35**, 256 (1961).

(14) References contained in the most recent publication, ref 5b, describe the changes.

(15) (a) R. W. Diesen and W. J. Felmlee, *J. Chem. Phys.*, **39**, 2115 (1963), independently developed an apparatus similar to ref 5b; (b) A. P. Modica, *J. Phys. Chem.*, **69**, 2111 (1965); (c) P. R. Ryason, *Rev. Sci. Instrum.*, **38**, 607 (1967); (d) S. C. Barton and J. E. Dove, *Can. J. Chem.*, **47**, 521 (1969).

tioned driver for the ir emission shock tube. The diaphragm interface is 1 in. i.d. on either side. A 1.5-in. (nominal) ball valve is located 6.5 in. downstream from the interface and sleeved with 1-in. i.d. pipe to provide a uniform cross section throughout the test section. A connection at a right angle to the pipe was placed 4 in. upstream from the valve and led to the gas handling system through a 0.5-in. ball valve, stainless steel bellows, and finally Pyrex glass tubing.

Four thin film velocity gauges are spaced at 20-cm intervals. The distance from the gauge which is closest to the end wall to the reflecting surface is 17.3 cm. The signals from the velocity gauges are recorded on the raster scope previously described. The signal from the last gauge is also fed into the time delay circuitry of a Tektronix 535 A oscilloscope, delayed for a selected time, and then used to trigger a multiple scan system[16] whose function is to space a given number of successive mass spectra on the screens of four Tektronix 531 A oscilloscopes equipped with Type G plug-in units. Photographs of the spectra are taken with Polaroid 10,000 speed film.

The mass spectrometer is a Bendix Model 14-107, modified to operate in the range 30–50 kHz, and operated with a 100-cm drift tube for shock tube experiments. The mass spectra signals are increased by a Keithley Model 109 pulse amplifier. Bendix analog units are used to analyze the test gas in its preshock state. The various peak heights are monitored by a Clevite Mark 220 dual channel recorder.

The shocked gas is introduced into the ion source of the TOF through a reentrant nozzle,[17] the shape of which was pressed into a thin copper disk. The diameter of the hole is 3.7 mils and was drilled with a jeweler's bit and press.

Ballast volumes of approximately 5-l. capacity each are attached above and below the TOF ion source cross. A cold cathode gauge is mounted in the upper ballast volume. The lower ballast volume is connected to a 3-in. i.d. stainless steel bellows which leads to a CVC modular pumping system Type PAS-41C backed by a Cenco mechanical pump Model Hyvac 14. The 4-in. oil diffusion pump is charged with Convalex-10 fluid which does not contribute an observable amount to the background mass spectra.

Typical ultimate vacuums are: 1×10^{-6} Torr in the shock tube (NRC ionization gauge Type 563-SP, NRC control 720), 5×10^{-7} Torr in the ion source ballast volume (NRC cold cathode gauge 524-2, NRC control 852), and 2×10^{-7} Torr in the TOF liquid nitrogen trap chamber (Veeco ionization gauge RG 75K, Bendix TOF vacuum gauge control). Addition of 5 Torr of a typical gas mixture (neon diluent) to the shock tube raises the latter two pressures to 4×10^{-5} and 1×10^{-6} Torr, respectively. Outgassing rates in the TOF shock tube are less than 0.01 μ/min.

The gas handling system is similar to the one described for the ir shock tube. An ionization gauge is used rather than a McLeod gauge and a Toepler pump has been added.

Signal-Concentration Ratio. A series of nonreacting mixtures was prepared to test the linearity of signal (TOF and ir) *vs.* reactant concentration.

Matheson hydrogen chloride (99.0%) was purified by two liquid nitrogen bulb-to-bulb distillations, the middle fraction was accepted at each stage. Liquid Carbonic argon (99.998%) was used as received as the diluent in the infrared experiments and was present at a 1% level in the TOF runs. Matheson research grade neon (99.995%) without additional purification was the diluent for the latter experiments. Reacting mixtures were prepared by addition of appropriate amounts of Matheson CP deuterium (99.5%). Mass spectrometric analysis of each gas indicated an impurity level for oxygen and chlorine indistinguishable from background.

Mixtures were allowed to stand 24 hr prior to use. Mass analysis of each mixture was performed with particular attention to oxygen content. Reference mixtures of various O_2 compositions were prepared to establish the impurity levels of the test mixtures. In all mixtures, the O_2 content was found to be less than 25 ppm. This level was attributed to the TOF–shock tube system.

Individual experiments performed on the TOF facility were first analyzed for O_2 content followed by analysis of the test gas. No experiment was performed at an O_2 level greater than 25 ppm. An exception to this statement was a series of runs performed on a reacting mixture that contained a small amount of oxygen.

The runs on the infrared facility were accomplished under the condition of an outgassing rate ≤ 0.5 μ/min. Diaphragm rupture was initiated in all experiments in a time interval of less than 1 min after introduction of the mixture into the test section.

The selection of appropriate infrared interference filters to monitor the fundamental vibrational–rotational envelopes of HCl and DCl was facilitated by a computer calculation of the envelopes as a function of temperature. The anharmonic oscillator, nonrigid rotator approximation was used.[18] The intensities of the rotational levels for the first five vibrational energy levels were calculated as a function of temperature.[19] Two Infrared Industries interference filters were selected with the following center wavelengths: 3.25 μ (HCl) and 5.05 μ (DCl). Both filters exhibited a half-band width of 0.1 μ.

(16) D. McL. Moulton and J. V. Michael, *Rev. Sci. Instrum.*, **36**, 226 (1965).

(17) G. P. Glass, G. B. Kistiakowsky, J. V. Michael, and H. Niki, *Symp. (Int.) Combust. 10th*, 513 (1965).

(18) G. Herzberg, "Molecular Spectra and Molecular Structure. I. Spectra of Diatomic Molecules," D. Van Nostrand, Princeton, N. J., 1965.

(19) S. S. Penner, "Quantitative Molecular Spectroscopy and Gas Emissivities," Addison-Wesley, Reading, Mass., 1959.

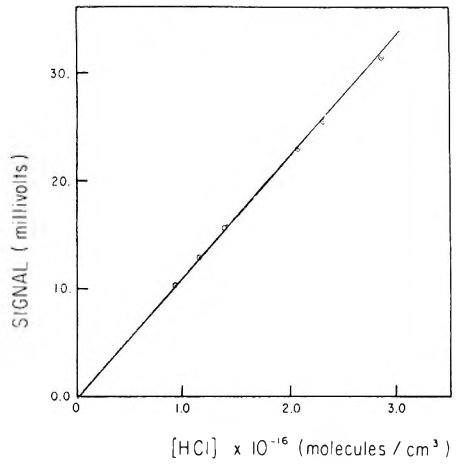

Figure 1. Calibration plot of ir detector signal (mV) of emission at 3.25 μ *vs.* HCl concentration at a temperature of approximately 2400°K.

The results of calculations at 2500°K indicated a partial overlap between the P branch of HCl and the R branch of DCl, particularly with the first two HCl vibrational levels. A series of experiments in which mixtures of HCl (1%, 2%) in Ar were shocked revealed the HCl contribution to the 5.05-μ signal. This contribution was recorded as a function of HCl concentration and temperature and was used to correct the emission profile observed at 5.05 μ for reaction mixtures in a manner to be described in the data reduction section.

Figure 1 displays the linearity of the emission signal at 3.25 μ as a function of HCl concentration. Similar plots were constructed for the HCl contribution to the 5.05-μ filter. The calibration runs established the rise-time for the infrared detector–amplifier system to be 7.5 μsec which is in agreement with the manufacturer's specifications.

Similar calibration experiments were conducted with the TOF apparatus. A diluent of Ne–1% Ar was employed along with an electron beam energy of 30 eV. A linear relationship was observed between the ratio of the peak heights of m/e 36:40 and the concentration of HCl.

Temperature Determination. Shock velocities decelerated in both shock tubes. The time that it took the shock wave to pass each gauge showed an increase with increasing distance, a typical increase being on the order of 1 μsec/20 cm. The increase was extrapolated from the last velocity gauge to the respective observation station; the center of the slits for their shock tube, the end wall for the TOF facility.

The physical properties for the reflected zone using ideal shock approximations were calculated on a PDP-10 computer. Thermodynamic data were taken from the JANAF Thermochemical Tables.[20] Corrections for nonideal behavior due to the endo- or exothermicity of a reaction[8] were not necessary for this thermoneutral system. Hydrogen was used as the driver gas.

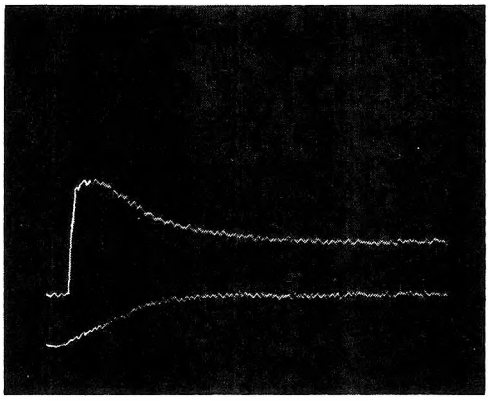

Figure 2. Experimental record of HCl at 3.25 μ (upper trace) and DCl at 5.05 μ (lower trace). Equimolar mixture in argon at 2435°K. The sweep speed is 100 μsec/cm.

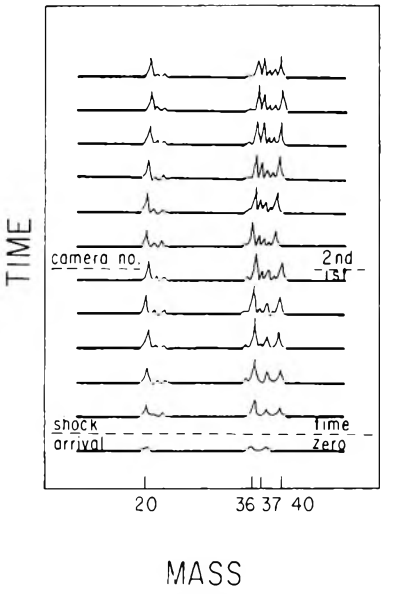

Figure 3. Tracing of TOF experimental record from first two of four cameras. Equimolar mixture in neon reacting at 2480°K. Mass spectra repeated at 20-μsec intervals.

Runs at the higher temperatures achieved an equilibrium condition within the available observation times. Calculation of the equilibrium constant for the HCl–D_2 exchange as a function of temperature was accomplished with statistical thermodynamic formulas, and the results were used to compare the computed ratio of DCl:HCl at equilibrium to the observed ratio.

Results

Experimental records from the infrared emission and TOF shock tubes are displayed in Figures 2 and 3, respectively. A total of four pictures was taken for each TOF run. Figure 3 is composed of the first two pictures only.

(20) "JANAF Thermochemical Tables," The Dow Chemical Company, Midland, Mich., 1965.

Data Reduction. The data from both sources were reduced according to the equation

$$\{1 - f_{DCl}[1 + (f_{HCl}/f_{DCl})_{eq}]\} = \exp[-k'(t - t_{ind})^z] \quad (1)$$

where f_{DCl} is the mole fraction of DCl ($[DCl]/[HCl]_0$), t_{ind} is the induction time for product formation, and z is the power dependence of the reaction time. There is no evidence for an induction period over the temperature range of the experiments, 1700–2800°K. Support for this statement is given after the treatment of the emission profiles is described.

Nonreacting mixtures of HCl (1%, 2%) in Ar were shocked in conjunction with reaction experiments. The emission signals from the 3.25- and 5.05-μ filters were plotted as a function of temperature. From these plots the average signal from HCl at each filter was obtained at the temperature of a reaction experiment.

Presence of the HCl contribution at 5.05 μ prompted calculation of the DCl mole fraction on three bases. The "HCl basis" and "DCl basis" correspond to individual treatments of the 3.25- and 5.05-μ signals respectively, while the third basis is a point by point average of the first two. Each experiment was accompanied by a calibration run at approximately the same temperature. The signal heights were measured relative to a baseline generated by the quiescent detectors. The measurements were made at 9-μsec intervals with the aid of a StereoZoom microscope and a graduated reticle. The precision of the readings was ±0.05 mV. A computer program was written to manipulate the 360 points generated from each experiment and to adjust the points for the effect of parallax.

The points for the DCl basis had to be corrected for the HCl contribution at 5.05 μ. The points at early times for the HCl basis were extrapolated to a time zero condition with the help of the calibration plots. At the higher temperature runs, an equilibrium condition was observed and by using the calculated ratio of $(DCl/HCl)_{eq}$, a value of HCl at time zero was derived. Calibration runs with DCl were not performed and hence $[HCl]_0$ on a DCl basis could only be calculated.

Early times of the reaction (0–100 μsec) were observed by recording the vertical signal out from the first oscilloscope on a second oscilloscope set a faster sweep speed, 10 or 20 μsec/cm. Treatment of the signal from the 5.05-μ filter on the DCl basis described above revealed the absence of a measurable induction period.

Points up to 100 μsec were analyzed with an expanded form of eq 1

$$f_{DCl} = \frac{k't^2}{[1 + (f_{HCl}/f_{DCl})_{eq}]} \quad (2)$$

A preliminary value of z was obtained by plotting log f_{DCl} *vs.* log t and determining the slope. An initial guess for k_{obsd} ($= k'/[1 + (f_{HCl}/f_{DCl})_{eq}]$) was obtained by plotting f_{DCl} *vs.* t raised to various powers: 1, $^3/_2$, and 2. Reproduction of an emission profile is depicted in Figure 4 for selected powers of z. Finally, a value for z was derived from plots of the log of the left-hand side of eq 1 *vs.* log t. The best fit value of z from these sources was about 1.7. The profiles were reproduced satisfactorily with an exponent of 2. A quadratic time dependence can be related to an atomic mechanism as will be shown in the Discussion section. A nonintegral time dependence does not have a direct relationship to any simple mechanism.

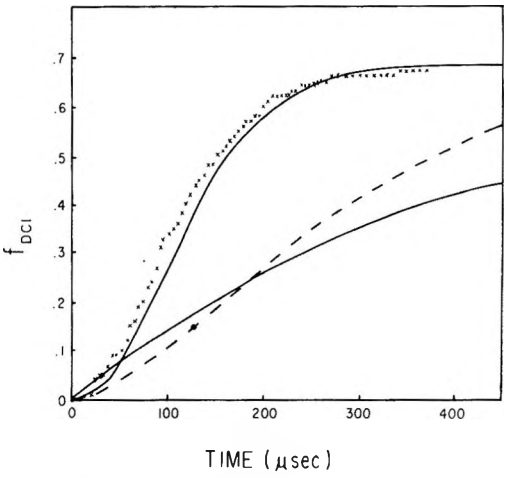

Figure 4. Infrared profiles calculated using different time dependencies for a run at 2535°K: ×, experimental points; — (uppermost), t^2 plot; - - -, $t^{1.5}$; — (lower), t^1.

A series of calculated profiles was constructed for various values of k' and matched with experimental profiles to derive an initial guess for k'. The computer then searched for the value of k' that reproduced the profile with the lowest standard deviation. Rate constants were calculated for each of the three bases. The differences were not significant, and rate constants are reported here using the average basis.

Doubling the total initial reactant concentration did not affect k'; doubling the total density doubled the value of the rate constant. Hence, k' equals $k[M]$ where [M] is the total concentration of the shocked gas in mol cm^{-3}. The total order of the reaction is two; the individual orders are first order with respect to the total density and a combined order dependence of one for the reactants HCl and D_2 when the rate is expressed on a concentration rather than mole fraction basis. An Arrhenius plot of the 2% HCl–2% D_2 mixture in argon is presented in Figure 5.

The TOF data were reduced by measuring the peak heights of m/e 36, 37, and 40 at 20-μsec reaction time intervals. The sum (Σ) of the ratios of 36:40 was fit to the equation

$$\Sigma = mt + b \quad (3)$$

where t is the reaction time in microseconds. The slope

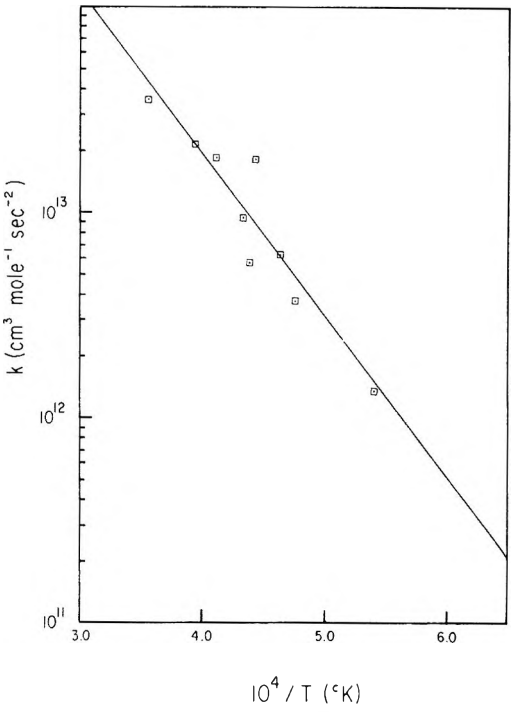

Figure 5. Arrhenius plot of 2% HCl–2% D_2 mixture in argon; P_1 = 5 Torr; infrared emission experiments: log A = 16.45 ± 0.47; E^* = 36.31 ± 4.90 kcal mol^{-1}.

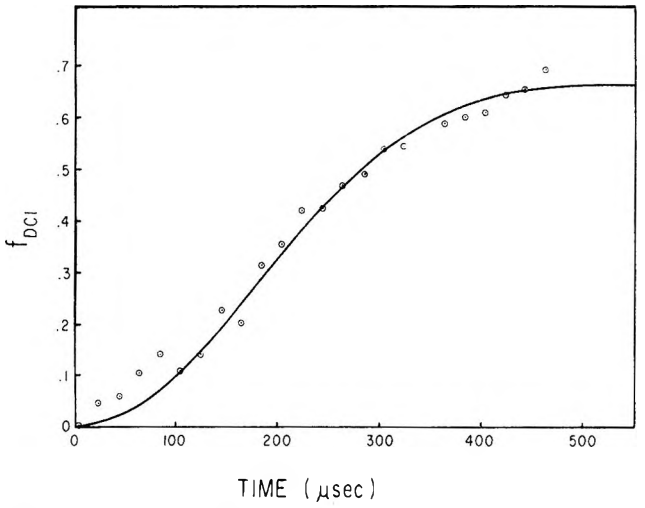

Figure 6. Fit of quadratic time dependence profile to TOF data taken at 2525°K: ○, experimental points; —, calculated.

m had a negligible value, and the intercept b was equal essentially to $[36:40]_0$, thus providing important checks on the apparatus and experimental technique. The mole fraction of DCl was determined at each point by dividing 37:40 by the sum. Calculation of k' was similar to the method described previously, and a fit of the experimental points to the profile is shown in Figure 6. Initial reactant concentrations were varied twofold with no apparent change in k'. The total density was not varied since operational difficulties were experienced when an initial pressure of 10 Torr was shocked.

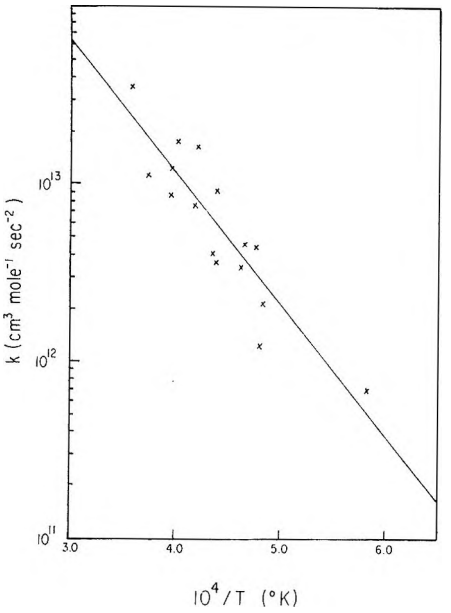

Figure 7. Arrhenius plot of 2% HCl–2% D_2 mixture in neon, P_1 = 5 Torr, TOF experiments: log A = 16.03 ± 0.42; E^* = 33.95 ± 4.40 kcal mol^{-1}.

Nozzles with slightly smaller holes are being constructed to overcome this trouble.

The points were fit with a quadratic time dependence profile. A first-order dependence on [M] was assumed, and an Arrhenius plot of a 2% HCl–2% D_2 mixture in Ne–1% Ar diluent is depicted in Figure 7.

Runs performed in the region 2480–2715°K indicated that the reaction had reached an equilibrium state. The ratio of m/e 37:36 achieved a constant value of 2.2 which is greater than the square root of the calculated equilibrium constant (K = 1.86). The observed ratio is understandable when account is taken of the self-exchange of HD

$$\begin{array}{ccc} D_2 + HCl & \rightleftharpoons & DCl + HD \\ & & \downarrow\uparrow \\ & & {}^1/_2H_2 + {}^1/_2D_2 \end{array}$$

Writing the equilibrium expression for the D_2–HCl system in the form

$$K = \left(\frac{DCl}{HCl}\right)_{eq}\left(\frac{HD}{D_2}\right)_{eq}$$

and using the calculated value of K, the ratio $(HD/D_2)_{eq}$ has a value of 0.85. By employing the equilibrium constant for the self-exchange reaction, K = 4, the ratio of $(HD/H_2)_{eq}$ is calculated to be 4.71.

Agreement with the observed ratio was obtained by writing gram atom balance equations for equimolar amounts of D_2 and HCl, making use of equilibrium constants, and solving for $(DCl/HCl)_{eq}$. Further support was gathered by the simultaneous recording of

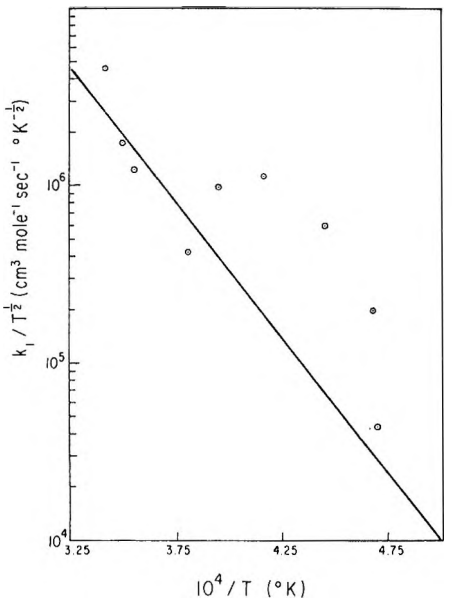

Figure 8. Comparison of dissociation rate constant data from TOF (⊙) to extrapolated Arrhenius line from ref 7a.

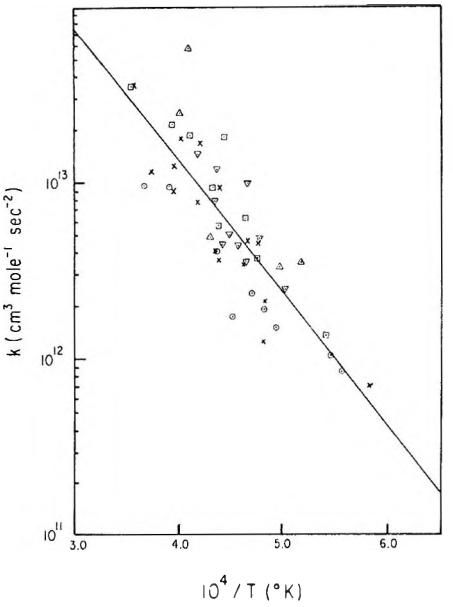

Figure 9. Arrhenius plot of data in Table I: □, mixture A; △, B; ▽, C; ×, D; ⊙, E.

m/e 2, 3, 4, 36, 37, and 40. The growth of m/e 2 was observed during the reaction process.

A van't Hoff plot of $(DCl/HCl)_{eq}$ was constructed over the temperature range covered by these experiments. Appropriate values were substituted into eq 1 for all of the TOF and ir emission runs.

A series of experiments with nonreacting mixtures of HCl and Ne–1% Ar revealed a small decrease in the ratio 36:40 which may be attributed to the dissociation process. For a given run, values of the ratio R were fit to the equation

$$R = R_0 + mt \tag{4}$$

by the method of least squares. The slopes in all but two runs[21] had small negative slopes. These slopes can be related to the dissociation process by expanding the rate law

$$HCl/HCl_0 = e^{-k_1[M]t} = 1 - k_1[M]t \tag{5}$$

and identifying m with $-HCl_0k_1[M]$. The results of several runs are plotted in Figure 8 and may be compared with an extrapolated Arrhenius plot.[7a] The scatter of the points is too great for them to be considered as kinetic data, but the experiments demonstrate results that are not inconsistent with previous work.

A series of experiments were performed with the TOF on a 2% HCl–2% D_2 mixture into which had leaked a small quantity of oxygen. Mass analysis placed the level of impurity at approximately 150 ppm. Several observations were at variance with eq 1. The higher temperature runs yielded values for the ratio $(DCl/HCl)_{eq} \geq 3$. The mixture was diluted twofold, and the order with respect to reactant concentration was found to be zero. An activation energy of 18 kcal mol^{-1} was calculated.

The results of the exchange experiments ($[O_2] < 25$ ppm) are listed in Table I. An Arrhenius plot of the rate constants in the table is shown in Figure 9. Least-squares treatment of the data yielded values of log $A = 16.12 \pm 0.30$ and $E^* = 34{,}340 \pm 3130$ cal mol^{-1}.

Discussion

The results for the D_2–HCl system are compatible with previous work on exchange reactions in which "low" activation energies have been determined[3,5] and also with the reporting of quadratic time dependence for product formation when the experiments were conducted with a dynamic sampling technique.[5,22]

An atomic mechanism provides an explanation for the quadratic time dependence but requires an activation energy on the order of 77–110 kcal mol^{-1}.

$$D_2 + M \xrightarrow{k_{d_1}} 2D + M \tag{a}$$

$$HCl + M \xrightarrow{k_{d_2}} H + Cl + M \tag{b}$$

$$H + D_2 \underset{k_{ex_{-1}}}{\overset{k_{ex_1}}{\rightleftharpoons}} HD + D \tag{c}$$

$$D + HCl \underset{k_{ex_{-2}}}{\overset{k_{ex_2}}{\rightleftharpoons}} DCl + H \tag{d}$$

Neglecting the back reactions

$$\frac{d[DCl]}{dt} = k_{ex_2}[D][HCl] \tag{6}$$

(21) These runs had small positive slopes.

(22) I. D. Gay, G. B. Kistiakowsky, J. V. Michael, and H. Niki, *J. Chem. Phys.*, **43**, 1720 (1965).

Table I

Mixture	T_5, °K	$\rho_5 \times 10^6$, mol cm^{-3}	$k \times 10^{-11}$, cm^3 mol^{-1} sec^{-2}
	Infrared		
Argon diluent	1849	1.76	13.7
	2099	1.86	37.4
	2157	1.88	62.8
A. 2% HCl–2% D_2	2251	1.91	181
P_1 = 5 Torr	2277	1.92	57.3
	2312	1.93	94.7
	2436	1.97	184
	2535	2.00	218
	2806	2.07	355
B. 1% HCl–1% D_2	1932	1.76	36.0
P_1 = 5 Torr	2014	1.79	33.5
	2322	1.89	49.1
	2437	1.93	571
	2485	1.94	247
	1994	3.64	25.0
	2099	3.72	48.1
	2149	3.76	97.2
C. 2% HCl–2% D_2	2149	3.76	35.4
P_1 = 10 Torr	2181	3.78	43.7
	2230	3.81	50.4
	2260	3.83	44.9
	2290	3.85	120
	2298	3.86	78.6
	TOF		
Ne–1% Ar diluent	2384	3.91	144
	1714	1.70	7.08
	2066	1.92	21.2
	2082	1.93	12.5
	2098	1.93	44.6
	2141	1.88	46.6
	2159	1.92	34.2
D. 2% HCl–2% D_2	2273	1.99	36.5
P_1 = 5 Torr	2273	1.96	92.4
	2294	1.93	41.2
	2369	1.91	164
	2388	1.96	77.1
	2481	2.07	176
	2516	2.00	125
	2523	1.92	88.2
	2670	2.08	115
	2780	2.07	353
	1797	1.70	13.7
	1831	1.71	37.4
E. 1% HCl–1% D_2	2028	1.79	62.8
P_1 = 5 Torr	2073	1.85	181
	2121	1.90	57.3
	2208	1.89	94.7
	2291	1.88	184
	2548	1.96	218
	2713	2.08	355

Approximating $[D_2]_t \simeq [D_2]_0$, and substituting into the following equation and integrating

$$\tfrac{1}{2}\frac{d[D]}{dt} = k_{d_1}[D_2][M] \quad (7)$$

$$[D]_t = 2k_{d_1}[D_2]_0[M]t \quad (8)$$

Using published values of k_{d_1},[8] it can be shown that the time required to attain an equilibrium amount of deuterium atoms *via* reaction a is much longer than the observed time for the exchange reaction to reach equilibrium. Substituting for [D] in eq 6 with eq 8 and integrating

$$[DCl]_t = k_{d_1}k_{ex_2}[D_2]_0[HCl][M]t^2 \quad (9)$$

The first-order dependence on [M] appears as does the quadratic time dependence. The activation energy is the sum of the activation energies for reactions a and d which is on the order of 100 kcal mol^{-1}. If the atoms are generated *via* (b) and (c), the predicted activation energy would be 77 kcal mol^{-1}. This prediction uses the experimental value of 70 kcal mol^{-1} attributed to the dissociation of HCl.[7]

A chain reaction involving vibrational energy transfer (the superscript v denotes one or more quanta of energy) may involve the following steps

$$D_2 + M \xrightarrow{k_{vib_1}} D_2^v + M \quad (e)$$

$$HCl + M \longrightarrow HCl^v + M \quad (f)$$

$$D_2^v + HCl \underset{}{\overset{k_{ex_1}}{\rightleftharpoons}} DCl + HD^v \quad (g)$$

$$HD^v + D_2 \rightleftharpoons HD + D_2^v \quad (h)$$

Other combinations are possible and the partitioning of the vibrational energy may be varied. A quadratic time dependence may be derived if the following approximations are valid

$$\frac{d[DCl]}{dt} = k_{ex_1}[D_2^v][HCl] \quad (10)$$

$$\frac{d[D_2^v]}{dt} = k_{vib_1}[D_2][M] \quad (11)$$

$$[D_2^v]_t = k_{vib_1}[D_2]_0[M]t \quad (12)$$

$$[DCl]_t = \tfrac{1}{2}k_{vib_1}k_{ex_1}[D_2]_0[HCl][M]t^2 \quad (13)$$

Reaction e may be taken to be a sequence of reactions in which the quanta are exchanged in a ladder climbing process. The vibrational relaxation times for reactions e[4] and f[23] have been measured for the transition 0 → 1 and are very much shorter than the observation times here. Hence, the assumption involved in the integration of eq 11 and its subsequent substitution to yield an equation with a quadratic time dependence is not valid. The absence of an induction period may also be explained by the short relaxation times.

A direct four-center molecular exchange complex mechanism is rejected because of the requirements of zero-order dependence on [M], an activation energy in

(23) (a) W. D. Breshears and P. F. Bird, *J. Chem. Phys.*, **50**, 333 (1969); (b) C. T. Bowman and D. J. Seery, *ibid.*, **50**, 1904 (1969); (c) P. Borrell and R. Gutteridge, *ibid.*, **50**, 2273 (1969).

the range of 60[24] kcal mol^{-1} or perhaps higher,[6] and a linear time dependence, all at variance with the results. Other mechanisms which invoke steady-state approximations are not acceptable because of the observed nonlinear time dependence.

The appearance of H_2 in the TOF experiments supports either an atomic or molecular mechanism. Hydrogen may be formed *via* atom-exchange reactions or the self-exchange of HD. The latter has been studied by the single pulse shock tube technique,[25] and the activation energy was determined to be 35.9 ± 2 kcal mol^{-1}. It is noted that the activation energies associated with all of the exchange reactions in the HCl–D_2 system are similar.

The order for the HCl–D_2 exchange is the least accurately determined quantity in this study. The data are consistent with the whole numbers reported here. A combined order of two for the reactant gases was tried and produced lesser agreement between the mixtures having a twofold difference in reactant concentrations than a combined order of one. The inert gas dependence was determined only with the ir emission technique because of previously mentioned difficulties with the TOF at starting pressures of 10 Torr. No attempt was made to establish individual orders for HCl and D_2. The overall order is taken to be two, a value consistent with previous work on other exchange systems.

The agreement of the kinetic results derived from both techniques is within one standard deviation. The values for log A and E^* are 15.83 ± 0.31 and 16.56 ± 0.47 and 32.58 ± 3.21 and 37.50 ± 4.78 kcal mol^{-1} for the TOF and ir, respectively. The experiments with Ne indicate a lower rate than those with Ar diluent, although this difference is not definitely established because of the magnitudes of the standard deviations. The sampling process is quite different, however, and the agreement attained is encouraging. It may be argued that both the TOF and ir techniques are analyzing gas that is too closely associated with the end wall. Other workers have successfully employed vacuum–ultraviolet light absorption to measure rates of dissociation at a distance 3.0 mm from the end wall[26] which is comparable to the distance used herein.

An atomic mechanism can be written to accommodate a nonlinear time dependence for product formation, but the activation energy is much too low. The energetics involved with the dissociation reactions,[8] particularly the hydrogen halides,[7,27] and the exchange reactions are indeed puzzling.

Acknowledgments. The assistance of Mr. Darryl Olivier and Mr. Joseph McPherson in the construction of the apparatus is greatly appreciated. The authors wish to thank the L.S.U.N.O. Computer Research Center (NSF Grant No. GP-2964 and GJ-131) for financial assistance.

(24) S. W. Benson and G. R. Haugen, *J. Amer. Chem. Soc.*, **87**, 4036 (1965).

(25) D. Lewis and S. H. Bauer, *ibid.*, **90**, 5390 (1968).

(26) (a) J. P. Appleton, M. Steinberg, and D. J. Liquornik, *J. Chem. Phys.*, **48**, 599 (1968); (b) *ibid.*, **52**, 2205 (1970).

(27) R. R. Giedt, N. Cohen, and T. A. Jacobs, *ibid.*, **50**, 5374 (1968).

Photoreduction of Benzophenone in Benzene. I. Mechanism of Secondary Reactions

by Jonas Dedinas

Research Laboratories, Eastman Kodak Company, Rochester, New York 14650 *(Received August 20, 1970)*

Publication costs assisted by Eastman Kodak Company

Benzopinacol, biphenyl, and 4-biphenyldiphenylcarbinol are formed in the photolysis of benzophenone in zone-refined benzene of 99.997% purity using degassed solutions and either 313- or 366-nm radiation. The initial quantum yield of benzophenone disappearance was 5.1 $(+0.8, -1.5) \times 10^{-3}$. Benzopinacol, biphenyl, and 4-biphenyldiphenylcarbinol had $\Phi_{initial}$ of 2.5 $(+0.4, -0.9) \times 10^{-3}$, 1.5 $(\pm 0.5) \times 10^{-3}$, and 1.0 $(\pm 0.5) \times 10^{-4}$, respectively. Benzopinacol is apparently formed by the combination of two ketyl radicals. Phenyl radicals, because of low concentration, underwent benzene arylation rather than radical combination reactions. Phenylcyclohexadienyl radical is an intermediate in the formation of biphenyl. It appears also to be an intermediate in the formation of 4-biphenyldiphenylcarbinol. The presence of some unidentified products that are stable in oxygen atmosphere is indicated by the uv absorption in the 300–420-nm region.

Introduction

The primary process in the photoreduction of benzophenone in hydrogen-donating solvents involves hydrogen abstraction by excited benzophenone in the lowest $^3(n, \pi^*)$ state. As a result two intermediates are formed, a ketyl radical and a substrate radical.[1,2] The secondary processes depend on the nature of the substrate radical,[3] partial pressure of oxygen,[4] acidity,[5] concentration,[6,7] and solvent.[3,8,9]

The photoreduction of benzophenone in benzene, a non-hydrogen-donating solvent, has been investigated using flash photolysis by Porter and Wilkinson,[1] by Bell and Linschitz,[10] and by Porter and Topp.[9] Bell and Linschitz[10] reported a quantum yield of 0.1 for the formation of the primary ketyl radical. However, the results obtained by Beckett and Porter,[2] using continuous irradiation, indicated a quantum yield for benzophenone disappearance as 0 ± 0.05. Thus, there appears to be a large difference between the primary yield of the ketyl radical and the quantum yield of benzophenone disappearance. To investigate further the mechanism of the photoreduction of benzophenone in benzene, a "double-barreled" approach, that of flash photolysis and continuous photolysis, was employed using zone-refined benzene (99.997%) and benzophenone (99.9%). The flash photolysis results will be reported later;[11] the present paper reports the product yields and mechanism of the secondary reactions as determined by means of the continuous irradiation.

Experimental Section

1. Reagents. In a study of a low-quantum yield photochemical problem, it is essential that the reagents be of high purity. In this investigation using benzophenone of 99.9% purity and zone-refined benzene of 99.997% purity (both chemicals were supplied by James Hinton, 358 Chicago Avenue, Valparaiso, Fla.), reproducible results were obtained and appeared to be free of any impurity effects in the range of benzophenone concentration (0.002 to 0.05 M) investigated. The zone-refined perdeuteriobenzene (James Hinton) was dried prior to use over magnesium perchlorate. The isotopic purity as determined by mass spectrometry was 96.5%. The major impurity was perdeuteriocyclohexane, which was present at a concentration of 0.11%. This reagent, when used in a mixture with pure benzene, was suitable for investigation of the mechanism of biphenyl formation and for an approximate determination of the deuterium isotope effect for hydrogen abstraction. However, the reagent was not acceptable for kinetic studies of the primary processes by flash photolysis. The zone-refined biphenyl (supplied by James Hinton) had a specified purity of 99.9%. Benzopinacol (K & K Laboratories, Inc.) and 4-biphenyldiphenylcarbinol (Alfred Bader Chemicals, a Division of Aldrich Chemical Co.) were used as received

(1) G. Porter and F. Wilkinson, *Trans. Faraday Soc.*, **57**, 1686 (1961).

(2) A. Beckett and G. Porter, *ibid.*, **59**, 2038 (1963).

(3) C. Walling and M. J. Gibian, *J. Amer. Chem. Soc.*, **87**, 3361 (1965).

(4) J. N. Pitts, Jr., R. L. Letsinger, R. P. Taylor, J. M. Patterson, G. Reckenwald, and R. B. Martin, *ibid.*, **81**, 1068 (1959).

(5) S. G. Cohen and W. V. Sherman, *ibid.*, **85**, 1642 (1963).

(6) H. L. J. Bäckström, K. L. Appelgren, and R. J. V. Niklasson, *Acta Chem. Scand.*, **19**, 1555 (1965).

(7) G. S. Hammond, W. P. Baker, and W. M. Moore, *J. Amer. Chem. Soc.*, **83**, 2795 (1961).

(8) S. G. Cohen and R. J. Baumgarten, *ibid.*, **87**, 2996 (1965).

(9) G. Porter and M. R. Topp, *Proc. Roy. Soc., Ser. A*, **315**, 163 (1970).

(10) J. A. Bell and H. Linschitz, *J. Amer. Chem. Soc.*, **85**, 528 (1963).

(11) A. V. Buettner and J. Dedinas, *J. Phys. Chem.*, **75**, 187 (1971).

for product identification. Lead tetraacetate (Matheson Coleman and Bell) was purified by crystallization from glacial acetic acid.[12]

2. Light Source and Preparation of Samples. The light source used was a high-pressure 200-W mercury arc lamp or a high-pressure 1000-W xenon–mercury arc lamp. The collimated light beam was passed through 5 cm of water and through a suitable filter system. A Corning CS-7-37 filter 5 mm thick was used to isolate 366-nm monochromatic radiation. A combination of chemical filters[13] containing aqueous solutions of inorganic salts $Co(SO_4)_2 \cdot 7H_2O$, $Ni(SO_4)_2 \cdot 6H_2O$, and $KCr(SO_4)_2 \cdot 12H_2O$ was used to obtain 313-nm radiation. The maximum transmission using the liquid filter system was at 315 nm and the bandwidth at half-height was 40 nm. The reaction vessels were Pyrex cylindrical spectrophotometer cells of 2.0-cm diameter, ranging from 1 to 10 cm in length. A side-tube for degassing and a Pyrex cell of 1-cm path length were attached to each reaction vessel. This arrangement allowed periodic measurement of uv absorption during irradiation. The solutions were held at 25° during irradiation unless indicated otherwise. The light intensity was measured with a potassium ferrioxalate actinometer.[14] The samples were degassed at −97° using four freeze–thaw cycles. The −97° temperature was obtained by means of a *n*-hexane slush bath. At this temperature the removal of gaseous impurities, such as N_2, O_2, and CO_2, is readily achieved. As a protection against fire, the vacuum line provided with a two-stage oil diffusion pump was installed in a hood and a Teflon covering was placed over the *n*-hexane slush bath while the tubes were being sealed.

3. Product Analysis. Qualitative analyses were performed by thin layer chromatography and glpc. The product mixture was separated on silica gel plate 0.2 mm thick, using for development a solvent containing 80% benzene and 20% *n*-hexane. The solvent was saturated with water and filtered prior to use. The extent of separation depended somewhat on the conditioning of the plates. The approximate R_f values found were 4-biphenyldiphenylcarbinol, 0.2; benzophenone, 0.3; benzopinacol, 0.4; and biphenyl, 0.9. These R_f values were in agreement with those of the authentic samples. The presence of benzopinacol was substantiated by mass spectrometric analysis using direct-probe sample introduction, as well as by uv and infrared analysis. 4-Biphenyldiphenylcarbinol was isolated by thin layer chromatography. The uv and mass spectra were slightly different from those of the standard sample. Subsequent gplc–mass spectrometric analysis of this fraction indicated the presence of two minor products, which apparently affected the spectra. However, the mass spectrum of the 4-biphenyldiphenylcarbinol fraction separated by glpc was identical with that of an authentic sample. Biphenyl was identified by glpc retention time and mass spectrometry.

Quantitative determination of benzopinacol was carried out by using lead tetraacetate oxidation.[15] The solvent from an irradiated sample (3–5 ml) was removed by evaporation under vacuum at room temperature. A 0.0124 *M* solution (1 ml) of $Pb(OAc)_4$ in acetic acid was added to the residue. The contents were mixed, held at 52° in a closed flask for 4 hr, and then cooled to room temperature; 0.3 ml of acidified 0.6 *M* KI solution was added and the contents were titrated with standardized 0.1 *N* $Na_2S_2O_3$ solution and starch indicator. Blank analysis of nonirradiated benzophenone solutions indicated no consumption of lead tetraacetate. Likewise, there was no oxidation of 4-biphenyldiphenylcarbinol by lead tetraacetate under the same conditions. The efficiency of benzopinacol oxidation was 90.0%. Although of the major products only benzopinacol is oxidized by lead tetraacetate, it is possible that some other products might be susceptible to lead tetraacetate oxidation. Such side reactions would indicate a falsely high yield of benzopinacol. A difference in yield using the above method and a gravimetric determination was reported by Moore, Hammond, and Foss.[12]

The yield of biphenyl and the conversion of benzophenone were determined using a glpc column and a thermal conductivity detector. The stainless steel packed columns, 1/4 in. by 6 ft, were supplied by Hewlett-Packard Co. The packing had a particle size distribution from 80 to 100 mesh and contained 10% silicone gum rubber (UC 98) supported on silanized diatomaceous earth (Diatoport S). The glpc analyses were carried out with the injection port, and the column temperature was maintained at 145°. The helium flow rate was 30 ml/min. The retention time of benzophenone was approximately 30 min. A higher column temperature was avoided because the benzopinacol present in the irradiated solutions decomposes to benzophenone at 170°.

The yield of 4-biphenyldiphenylcarbinol was determined by glpc analysis using a 1/4 in. × 10 ft glass column filled with 40–60 mesh packing containing 1% SE-30 silicone gum rubber supported on Chromosorb W(AW-DMCS) (Hewlett-Packard).

Results and Discussion

1. Products and Yields. The present results indicate that the hydrogen abstraction from benzene is very low. The initial quantum yield of benzophenone disappearance is 0.0051 (+0.0008, −0.0015) in agreement with the value of 0.00 ± 0.05 found by Beckett and Porter[2] in the sense that it likewise indicates a very

(12) W. M. Moore, G. S. Hammond, and R. P. Foss, *J. Amer. Chem. Soc.*, **83**, 2789 (1961).

(13) M. Kasha, *J. Opt. Soc. Amer.*, **38**, 929 (1948).

(14) C. G. Hatchard and C. A. Parker, *Proc. Roy. Soc., Ser. A*, **235**, 518 (1956).

(15) R. Criegee, *Ber.*, **64B**, 264 (1931).

Table I: Initial Quantum Yields of Benzophenone Photoreduction in Zone-Refined Benzene

Compd	Wavelength		
	313 nm	366 nm	Average
Benzophenone (disappearance)	0.0049	0.0053	0.0051 (+0.0008 or −0.0015)
Benzopinacol	0.0026	0.0023	0.0025 (+0.0004 or −0.0009)
Biphenyl	0.0016	0.0013	0.0015 ± 0.0005
4-Biphenyldiphenylcarbinol	0.0001	0.0001	0.0001 ± 0.00005

Table II: Photolysis of Benzophenone in Zone-Refined Benzene

Concentration, *M*	Wavelength, nm	Light intensity, quanta/min × 10^{-18}	Time of irradiation, min	Conversion, %	−Φ(ketone)	Φ(benzopinacol)	Φ(biphenyl)	Φ(4-biphenyldiphenylcarbinol)
0.01	313	2.06	302			0.0029	0.0014	
0.01	313	2.04	1240	10.2	0.0037	0.0020	0.0014	0.00012
0.01	313	1.85	1560			0.0019	0.0013	
0.01	313	1.90	1020	6.26	0.0029	0.0021	0.0013	0.00012
0.01	313	1.77	640			0.0026	0.0014	
0.02	313	1.70	666	6.22	0.0049	0.0021	0.0012	
0.02	313	1.67	3818	15.7	0.0024	0.0013	0.00076	0.00010
0.05	313	1.50	242			0.0029	0.0011	
0.05	313	1.20	1062	7.36	0.0052	0.0020	0.0010	
0.005	313	1.50	790			0.0021	0.0012	
0.005	313	1.45	1425	21.5	0.0047	0.0020	0.0011	
0.002	313	1.43	312	5.32	0.0042	0.0027	0.0022	0.00031
0.002	313	1.43	1080	18.0	0.0042	0.0025	0.0016	0.00010
0.01	366	16.3	200	12.6	0.0035	0.0024	0.0013	0.00010
0.01	366	16.2	350	18.4	0.0029	0.0021	0.00093	
0.01	366	11.1	180	10.8	0.0049		0.0012	0.00013
0.01	366	10.6	306	18.5	0.0051	0.0024	0.00082	0.00011
0.01	366	10.3	155	7.3	0.0041	0.0021	0.0013	

low reactivity of benzophenone in benzene. In some reviews[16,17] the quantum yield is given as 0.05. This is a misprint of the original value reported by Beckett and Porter. The reaction products are benzopinacol, biphenyl, and 4-biphenyldiphenylcarbinol. The presence of biphenyl in the photolyzed solution of benzophenone in benzene has been observed also by Bell and Linschitz,[10] while the other two compounds are reported here for the first time.

The results summarized in Table I show that there is no significant wavelength dependence on the initial quantum yields at the two wavelengths, 313 and 366 nm, used in this investigation. The initial yields were determined by graphical presentation of the quantum yields as a function of absorbed radiation (Figures 1 and 2) and by linear extrapolation to zero. This method was applicable since the decrease of quantum yields as a function of absorbed radiation was linear within the limits of experimental accuracy.

There appears to be no significant concentration effect on Φ(benzophenone) and Φ(benzopinacol) in the range from 0.002 to 0.05 *M* investigated. A small increase in Φ(biphenyl) is observed at 0.002 *M* concentration compared with the yields obtained at higher concentrations (Table II). In spite of this small concentration dependence, all the results obtained at the 313-nm radiation were used to correlate Φ *vs.* $I_a t$, where I_a is intensity of absorbed uv light and t is time of irradiation. The effect of $I_a t$ was determined also at 366 nm using 0.01 *M* concentration and an absorbed intensity of approximately 1.3 × 10^{19} quanta/min. This intensity is an order of magnitude higher than that used at 313 nm. In spite of the intensity difference,

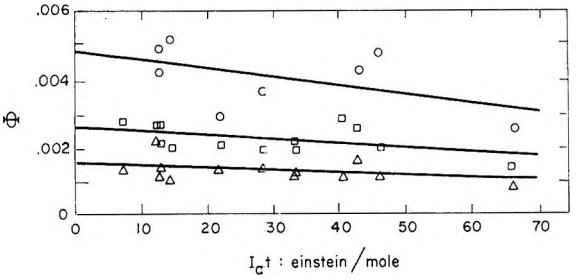

Figure 1. Φ *vs.* absorbed radiation. Excitation wavelength 313 nm: O, benzophenone (disappearance); □, benzopinacol; and △, biphenyl.

(16) J. G. Calvert and J. N. Pitts, Jr., "Photochemistry," Wiley, New York, N. Y., 1966, p 533.

(17) N. J. Turro, "Molecular Photochemistry," W. A. Benjamin, New York, N. Y., 1967, p 143.

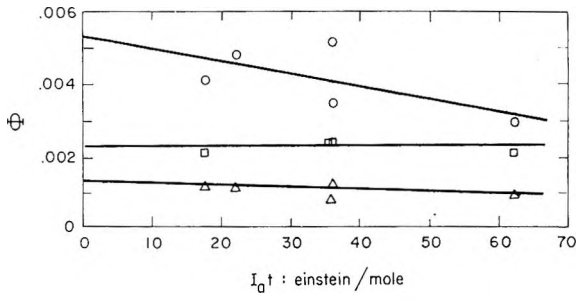

Figure 2. Φ *vs.* absorbed radiation. Excitation wavelength 366 nm: ○, benzophenone (disappearance); □, benzopinacol; and △, biphenyl.

the results at the two wavelengths are essentially the same. The decrease in benzophenone conversion with increasing $I_a t$ is probably caused by an energy transfer from the benzophenone triplet to biphenyl product. The triplet energy of the latter is 4 kcal/mol lower than that of benzophenone. The triplet energy of 4-biphenyldiphenylcarbinol should also be lower than that of benzophenone. This, too, could act as an internal quencher of benzophenone triplets. In addition, there are some unidentified products formed that have appreciable absorption at 313 nm (Figures 3 and 4). These products could affect the quantum yield of benzophenone conversion by partial absorption of light when using the 313-nm wavelength for excitation. However, it appears that this internal light filtering did not affect Φ, since the results obtained at 313 and 366 nm (Figures 1 and 2) are quite similar.

The quantum yields summarized in Table I indicate that two material-balance equations can be derived to account for the disappearance of benzophenone.

$$\Phi((C_6H_5)_2CO) = 2\Phi(\text{benzopinacol}) + \Phi(\text{4-biphenyldiphenylcarbinol}) \quad (1)$$

$$\Phi((C_6H_5)_2CO) = 2\Phi(\text{biphenyl}) + 3\Phi(\text{4-biphenyldiphenylcarbinol}) \quad (2)$$

The material balance is 100% based on initial Φ using (1) and 65% using (2). This discrepancy indicates a shortage of biphenyl. A plausible explanation of this discrepancy would be to assume that there were hydrogen-donating impurities in the zone-refined benzene. This possibility appears unlikely since cyclohexane, the major impurity, was present at a concentration of only 0.002%. The product resulting from cyclohexane dissolved in benzene is phenylcyclohexane. The concentration of this product was estimated to be two orders of magnitude lower than that of biphenyl. The lack of material balance is thus believed to be caused by unidentified products. It should be mentioned that the material balance using (1) is over 100% at high values of $I_a t$. This also suggests that the method of benzopinacol determination might have been affected by unidentified products.

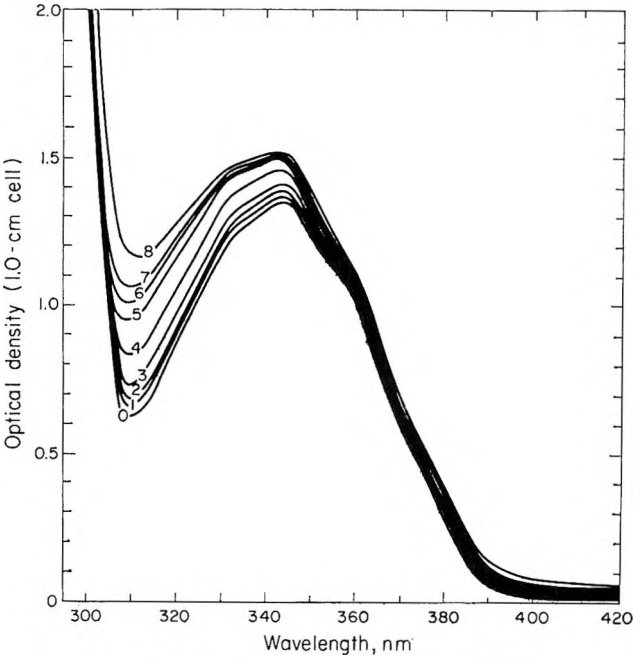

Figure 3. Effect of irradiation on uv absorption. Conditions: 0.01 *M* benzophenone concentration, 10°, 313-nm excitation wavelength, 1.35 × 10^{18} quanta/min. Time interval between measurements: 0, nonirradiated degassed solution; 1, 7 min; 2, 10 min; 3, 16 min; 4, 50 min; 5, 185 min; 6, 245 min; 7, 175 min; and 8, 891 min.

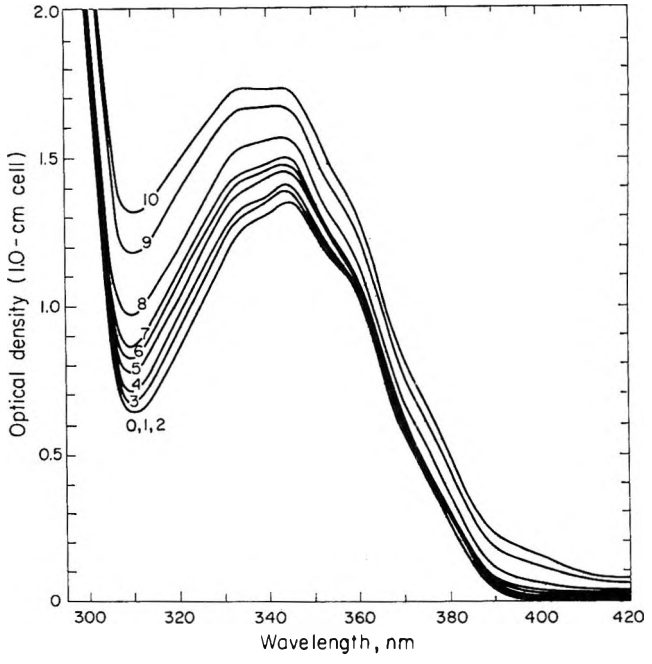

Figure 4. Effect of irradiation on uv absorption. Conditions: 0.01 *M* benzophenone concentration, 53°, 313-nm excitation wavelength, 1.37 × 10^{18} quanta/min. Time interval between measurements: 0, nonirradiated degassed solution; 1, 1 min; 2, 1 min; 3, 5 min; 4, 6 min; 5, 10 min; 6, 10 min; 7, 10 min; 8, 50 min; 9, 170 min; and 10, 210 min.

The presence of unidentified products is also indicated by the uv absorption of the irradiated solutions in the 300–420-nm region (Figures 3 and 4). It should

Table III: Relative Isotopic Distribution of Biphenyl Obtained Using 1:1 Benzene/Benzene-d_6 Solvent

Experiment	$(C_6H_5)_2CO$ concentration, M	Wavelength, nm	Light intensity, quanta/min $\times 10^{-18}$	Time of irradiation, min	Biphenyl-d_0, %	Biphenyl-d_5, %	Biphenyl-d_{10}, %	$\frac{k_H}{k_D}$[a]
1	0.01	366	9.4	890	42.1	47.0	10.9	4
2	0.025	366	11.0	1410	45.2	49.6	5.35	10
3	0.05	313	1.6	5360	47.7	48.5	3.92	12

[a] Isotope effect for hydrogen abstraction, reaction 3. It is assumed that isotope effect for reaction 7 is one.

be mentioned that in this region none of the major products has appreciable absorption. The irradiated samples, however, have a much stronger absorption than do the solutions before irradiation. As shown in Figures 3 and 4, the increase in absorption is much greater at 53° than at 10° and suggests the presence of several compounds. These uv-absorbing compounds are stable to oxygen, since no change in absorption spectrum was noticed upon opening of the reaction vessels. This was also the case after the samples were stored for several days under atmospheric conditions. Combined glpc–mass spectrometric analysis of the irradiated solutions indicated the presence of several compounds at very low concentration. However, these compounds were not isolated, and thus it is not known whether any of them have appreciable absorption in the 300–420-nm region.

2. Mechanism. The two principal products, benzopinacol and biphenyl, formed in the photochemical reduction of benzophenone in benzene are anticipated on the basis of the photochemical reaction mechanism[1] of benzophenone in hydrocarbons containing labile hydrogen. According to this mechanism, benzophenone in the lowest excited $^3(n, \pi^*)$ state abstracts hydrogen from benzene, thereby producing two primary intermediates, a ketyl and a phenyl radical.

$$^3[(C_6H_5)_2CO] + C_6H_6 \longrightarrow (C_6H_5)_2\dot{C}OH + C_6H_5\cdot \quad (3)$$

It must be mentioned that the validity of this mechanism has been substantiated in a concurrent study employing flash photolysis.[11]

The ketyl and the phenyl radical represent two extremes of free-radical reactivity. The phenyl radical is very reactive and has the same reactivity as methyl radicals[18] for the alkylation reaction of benzene. On the other hand, the ketyl radical has a resonance stabilization similar to that of a benzyl radical, and thus it is very inert with respect to hydrogen abstraction from hydrocarbons and with respect to benzene alkylation. However, the ketyl radical should undergo free-radical combination as well as disproportionation reactions. On this basis, therefore, it is reasonable to assume that benzopinacol is formed by the combination of two ketyl radicals, *i.e.*

$$(C_6H_5)_2\dot{C}OH + (C_6H_5)_2\dot{C}OH \longrightarrow (C_6H_5)_2COHCOH(C_6H_5)_2 \quad (4)$$

The ketyl radicals may disproportionate with each other or with the phenyl radical. Thus the following reactions can be postulated.

$$(C_6H_5)_2\dot{C}OH + (C_6H_5)_2\dot{C}OH \longrightarrow (C_6H_5)_2CO + (C_6H_5)_2HCOH \quad (5)$$

$$(C_6H_5)_2\dot{C}OH + C_6H_5\cdot \longrightarrow (C_6H_5)_2CO + C_6H_6 \quad (6)$$

Reaction 5 is of little importance since only a trace of benzhydrol was detected. At the level of concentration at which benzhydrol was present in the irradiated solutions, it is not probable that the primary yield of benzhydrol was reduced by a consecutive, hydrogen-abstraction reaction. Reaction 6 is a back reaction leading to the formation of the reactants and thus cannot be readily distinguished from the overall efficiency of the photochemical reaction.

Irradiation of benzophenone in 1:1 benzene/benzene-d_6 solvent indicated that arylation of benzene by phenyl radicals is the principal mechanism of biphenyl formation, as can be seen from the results presented in Table III. For example, the biphenyl distribution obtained in experiment 2 (Table III) is in a perfect agreement with this mechanism; the biphenyl-d_0 concentration being 45.2%, biphenyl-d_5 49.6%, and biphenyl-d_{10} 5.35%. From these data the deuterium isotope effect for the formation of phenyl radical can be determined assuming that the isotope effect of the arylation reaction 7 is one. The results of Table III show the values of k_H/k_D to be in the range from 4 to 12, and thus they are consistent with the hydrogen abstraction mechanism, reaction 3, proposed for the formation of phenyl radicals.

Phenyl radical addition to benzene has been studied by Hey[18] and DeTar.[19,20] The intermediate of the arylation reaction has been shown by DeTar[19,20] to be a phenylcyclohexadienyl radical. Biphenyl from this

(18) D. H. Hey and G. H. Williams, *J. Chem. Phys.*, **23**, 757 (1955).
(19) D. F. DeTar, R. A. J. Long, J. Rendleman, J. Bradley, and P. Duncan, *J. Amer. Chem. Soc.*, **89**, 4051 (1967).
(20) D. F. DeTar, *ibid.*, **89**, 4058 (1967).

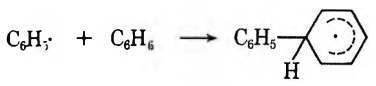

(7)

intermediate is formed by elimination of hydrogen.

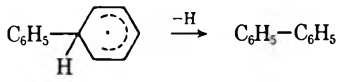

(8)

It is very likely that in this system biphenyl formation may actually involve a bimolecular reaction with benzophenone in the triplet state. Reaction 9 is suggested

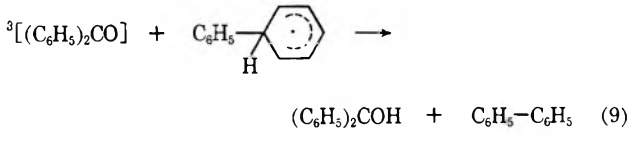

(9)

because of absence of tetrahydroquaterphenyl and quaterphenyl in the irradiated solutions. These products are formed by benzoyl peroxide decomposition in benzene[19,20] *via* combination of phenylcyclohexadienyl radicals. It is rationalized that these compounds are not formed in the photolysis of benzophenone in benzene because the phenylcyclohexadienyl radical is rapidly converted into biphenyl and thus the concentration of this radical is too low to form an appreciable amount of the dimer products.

It is very likely that phenylcyclohexadienyl radical is also an intermediate in the formation of the 4-biphenyldiphenylcarbinol. By combination with the ketyl radical a dihydro product shown by reaction 10 can be

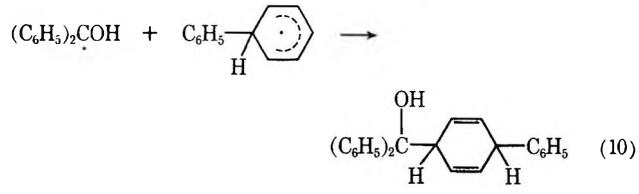

(10)

formed. Substituted cyclohexadienes can aromatize easily by hydrogen elimination. Alternatively, the

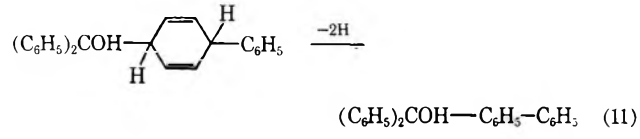

(11)

substituted cyclohexadiene (reaction 10) can be aromatized by an analogous mechanism indicated by reaction 9.

4-Biphenyldiphenylcarbinol can be formed also by the combination of ketyl and biphenyl radicals.

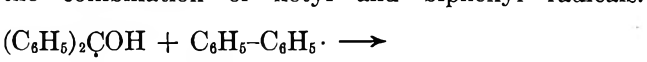

(12)

Biphenyl radicals may be formed in the system by a consecutive hydrogen abstraction from the biphenyl product, *i.e.*

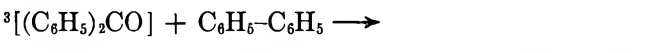

(13)

The importance of reactions 12 and 13 was tested using 0.01 *M* benzophenone solution containing 0.005 and 0.01 *M* concentrations of biphenyl. It was found that the quantum yields of 4-biphenyldiphenylcarbinol were lower than in the experiments without biphenyl addition. The decrease is attributed to the overall lower reactivity resulting from quenching of the benzophenone triplet by biphenyl. Thus the contribution of reactions 12 and 13 to the yield of 4-biphenyldiphenylcarbinol appears to be negligible.

3. Reactions of Cyclohexane-d_{12} Impurity in Benzene-d_6. The zone-refined benzene-d_6 contained cyclohexane-d_{12} impurity at a concentration of 0.11%. Hence, the effect of the deuterium isotope on the hydrogen abstraction reaction could not be determined accurately. However, the results obtained using the benzene-d_6 solvent are interesting because cyclohexane-d_{12} was converted into cyclohexyl-d_{11} radical. This radical underwent essentially the same alkylation reaction as the phenyl radical. The product resulting from the cyclohexane-d_{12} impurity was phenylcyclohexane-d_{16}. There was no bicyclohexyl-d_{22} formed on the basis of glpc–mass spectrometric analysis. In the runs using 1:1 ratio of benzene and benzene-d_6 as a solvent, the cyclohexyl-d_{11} radicals were found to alkylate benzene and benzene-d_6 at equal rates. The products were phenylcyclohexane-d_{11} and phenylcyclohexane-d_{16}. The very selective addition reaction of cyclohexyl and phenyl radicals to benzene occurs apparently only at low radical concentration. At higher concentration of radicals, as reported by Walling and Gibian,[3] bicyclohexyl and cyclohexylbenzene were obtained when benzophenone was irradiated in a mixed solvent containing cyclohexane and benzene.

Thus a general conclusion can be drawn that reactive radicals such as phenyl and cyclohexyl, when present at low concentration in benzene, primarily undergo an addition reaction with benzene rather than free-radical combination reactions.

Photoreduction of Benzophenone in Benzene. II. Flash Photolysis Study of Primary Photochemical Reactions

by A. V. Buettner and J. Dedinas*

Research Laboratories, Eastman Kodak Company, Rochester, New York 14650 *(Received September 1, 1970)*

Publication costs assisted by Eastman Kodak Company

The quantum yield of formation of ketyl radical from irradiation of benzophenone in benzene was found to be 0.022 ± 0.006 by comparative flash photolysis studies in benzene and cyclohexane. Because of the low concentration of ketyl radical in benzene, a relatively precise rate of the benzophenone triplet decay, $k_1 = 8 \times 10^4 \pm 1 \times 10^4$ sec^{-1}, could be measured in benzene at room temperature, and a third transient with a lifetime of ~50 μsec was detected. The results show that benzophenone triplet abstracts hydrogen from benzene at a rate of $k_2 = 1.6 \times 10^2 M^{-1}$ sec^{-1} and gives further confirmation that the short lifetime of the benzophenone triplet is caused by a quenching by benzene that does not involve hydrogen abstraction. The third transient may be produced in the quenching of the benzophenone triplet but probably is not an intermediate in the photoreduction of benzophenone in benzene.

Introduction

Benzophenone was first studied by flash photolysis by McClure and Hanst,[1] who measured the absorption spectrum and the mean life of the triplet state in EPA glass at 77°K. The lifetime was comparable to that of the phosphorescence,[2] 8 msec, and thus was good evidence of triplet absorption. Porter and Windsor[3] found a transient at room temperature which had an absorption spectrum similar to that found by McClure and Hanst and they believed it to be the triplet. However, Porter and Wilkinson[4] found that the lifetime of this transient at room temperature in ethylene glycol was such that its absorption was appreciable 80 msec after flashing, and yet no phosphorescence was observed. They therefore reexamined the transient and showed that it is the ketyl radical which is formed from the benzophenone triplet state by hydrogen abstraction from the solvent.

Bell and Linschitz,[5] also using flash photolysis, confirmed the absorption spectrum of the ketyl radical and detected the benzophenone triplet state at room temperature. They observed the triplet as a rapidly decaying transient absorption, $k_1 = 1 \times 10^5$ sec^{-1} ± 50%, superimposed on the ketyl radical absorption, and estimated the quantum yield of the ketyl radical in benzene to be about 0.1. It is difficult to reconcile a ketyl radical yield of 0.1 with the very low quantum yield of disappearance of benzophenone, 0.0051 (+0.0008, −0.0015) obtained by continuous irradiation, as reported in part I of this study.[6] This flash photolysis investigation was therefore undertaken to complement the continuous irradiation results.

The absorption spectrum and lifetime of benzophenone triplet has been measured in polymethylmethacrylate[7] (τ = 1.7 msec) and in trichlorotrifluoroethane[8] (τ = 20 μsec) using flash photolysis, and in benzene[9] (τ = 3.0 μsec) using pulse radiolysis. Porter and Topp,[10] using a nanosecond flash photolysis apparatus with Q-spoiled laser excitation, recently measured a 3.5-μsec lifetime for triplet benzophenone in benzene and suggested that the large yield of a longer-lived species which they observed was not ketyl radical but an addition product of benzophenone in benzene. A similar intermediate, an adduct diradical, has been proposed by Shuster and Brizzolara,[11] and it has been implied[10,11] that ketyl radical may not be formed in the photolysis of benzophenone in benzene.

We have found that benzophenone triplet does abstract hydrogen from benzene but at such a slow rate that the quantum yield of ketyl radical is 0.022 ± 0.006. Because of the low quantum yield of ketyl radical, we are able to detect a third transient with a lifetime of approximately 50 μsec. We found the lifetime of the triplet in benzene free of triplet–triplet decay, to be 12 ± 2 μsec.

(1) D. S. McClure and P. L. Hanst, *J. Chem. Phys.*, **23**, 1772 (1955).

(2) E. H. Gilmore, G. E. Gibson, and D. S. McClure, *ibid.*, **20**, 829 (1952); **23**, 399 (1955).

(3) G. Porter and M. W. Windsor, *Proc. Roy. Soc., Ser. A*, **245**, 238 (1958).

(4) G. Porter and F. Wilkinson, *Trans. Faraday Soc.*, **57**, 1686 (1961).

(5) J. A. Bell and H. Linschitz, *J. Amer. Chem. Soc.*, **85**, 528 (1963).

(6) J. Dedinas, part I of this series, *J. Phys. Chem.*, **75**, 181 (1971).

(7) W. H. Melhuish, *Trans. Faraday Soc.*, **62**, 3384 (1966).

(8) H. Tsubomura, N. Yamamoto, and S. Tanaka, *Chem. Phys. Lett.*, **1**, 309 (1967).

(9) F. S. Dainton, J. Kemp, G. A. Salmon, and J. P. Keene, *Nature*, **203**, 1050 (1964).

(10) G. Porter and R. Topp, *Proc. Roy. Soc., Ser. A*, **315**, 163 (1970).

(11) D. I. Schuster and D. F. Brizzolara, *J. Amer. Chem. Soc.*, **92**, 4357 (1970).

Experimental Section

The method for purifying the reagents and the method for deoxygenating the solutions have been described.[6] However, it should be emphasized that the benzophenone and benzene were both zone-refined, and it was determined that the purity of benzophenone was 99.9% and of benzene 99.997%. The flash photolysis apparatus has also been described.[12,13] The energy of the excitation flash was 23 J, 0.4 μF, 7.1 kV. The EG and G FX-1 flashlamp fired under these conditions has a flash half-width of 4 μsec and a one-tenth width of 10 μsec. The Pyrex cells were 5.0 cm long. The spectral monitoring system is able to measure small absorbance changes to ± 0.0005. This is possible because long-term stability, *i.e.*, more than 10 msec, is unimportant and because the signals were averaged by superimposing as many as nine oscilloscope traces of a transient on one photograph with the aperture of the oscilloscope camera stopped down to the point where each trace barely registered on the film.

Results and Discussion

Quantum Yield of Ketyl Radical in Benzene. The quantum yield of ketyl radical in benzene was determined by comparison of the yield of the ketyl radical in benzene with its yield in cyclohexane and by comparison of the yield of ketyl radical in benzene with the yield of benzophenone triplet in the same solvent. Flash excitation of a 0.01 *M* solution of benzophenone in cyclohexane produced a relatively large yield of a transient. Figure 1 shows the decay of this transient as measured by its absorbance at 525 nm. The curve in Figure 1 was not measured at the absorption maximum of the transient but at what will be shown to be the absorption maximum of the triplet state of benzophenone so that the presence of any triplet would be accentuated. A family of curves such as that in Figure 1 shows there to be a single species decaying by a purely second-order process. The absorption spectrum of the transient was constructed from a series of decay curves measured at different wavelengths. The transient spectrum agreed within experimental error with that of ketyl radical produced by flashing benzophenone in benzene with benzhydrol added.[5] The absorption spectrum of the ketyl radical in cyclohexane is shown in Figure 2.

Flashing benzophenone in benzene produced a large yield of a very short-lived transient, a much smaller yield of a much longer-lived transient, plus a third transient with an intermediate lifetime. The large differences in rates of decay and yields between the short- and long-lived transients made it possible to separate the short- and long-lived transients and so see the evidence of a transient with an intermediate lifetime.

Figure 3 shows the decay of the transients produced by flash excitation of 0.01 *M* benzophenone in benzene with the absorption measured at 525 nm. It is one of a

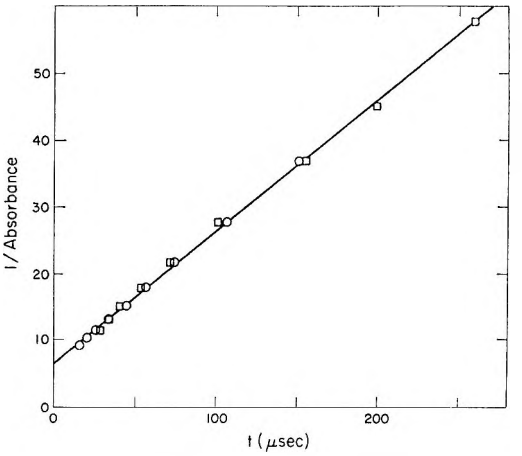

Figure 1. Decay of the ketyl radical produced by flash excitation of 0.01 *M* benzophenone in cyclohexane at room temperature: wavelength, 525 nm; cell length, 5.0 cm; flash energy, 23 J; ○ and □ are combinations of two traces each recorded at 20 and 100 μsec/cm.

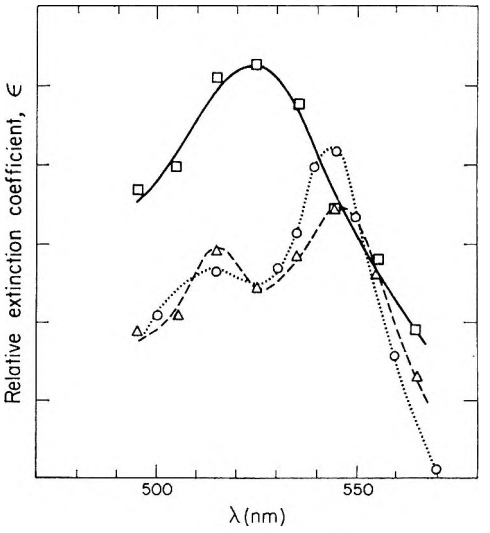

Figure 2. Absorption spectra of transients produced by flash excitation of solutions of benzophenone at room temperature: □ is triplet state of benzophenone in benzene; △ is ketyl radical in benzene; and ○ is ketyl radical in cyclohexane.

series of curves measured at different wavelengths. The short-lived transient is identified as the triplet state of benzophenone by comparison with the kinetics of Bell and Linschitz.[5]

The long-lived transient decays by a second-order mechanism. The extrapolation of the decay of this transient to time zero is shown by the dashed line in Figure 3. From a series of such curves at various wavelengths, the absorption spectrum of the long-lived transient was constructed. The spectrum, with a peak at 545 nm, is shown in Figure 2; it agrees within experimental error with the absorption spectrum of ketyl

(12) A. V. Buettner, *J. Phys. Chem.*, **68**, 3253 (1964).
(13) A. V. Buettner, *J. Chem. Phys.*, **46**, 1398 (1967).

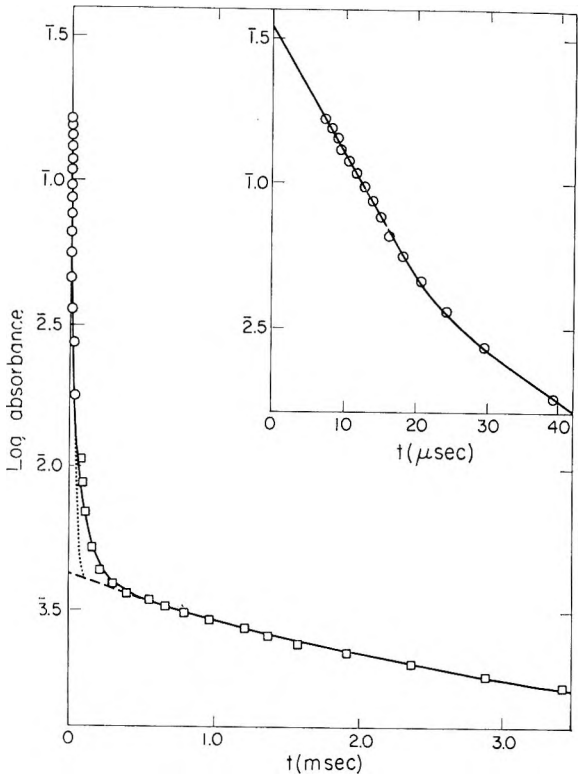

Figure 3. Decay of the transients produced by flash excitation of 0.01 M benzophenone in benzene at room temperature. The insert shows the triplet decay on an expanded time scale. O is a combination of three traces recorded at 10 μsec/cm, and □ is a combination of 12 traces recorded at 500 μsec/cm: wavelength, 525 nm; cell length, 5.0 cm; and flash energy, 23 J.

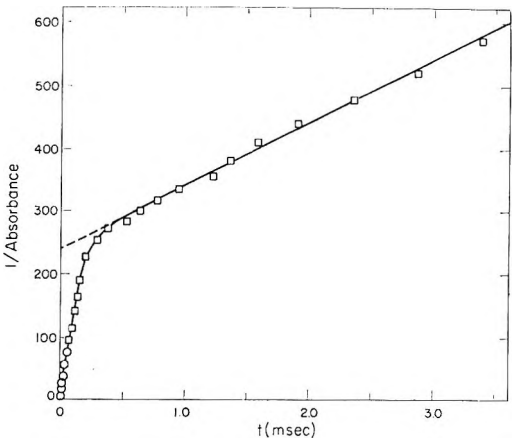

Figure 4. Decay of the transients produced by flash excitation of 0.01 M benzophenone in benzene at room temperature. O is a combination of traces recorded at 10 μsec/cm and □ is a combination of 12 traces recorded at 500 μsec/cm: wavelength, 525 nm; cell length, 5.0 cm; and flash energy, 23 J.

radical produced by flashing benzophenone in benzene with benzhydrol added.[5] (In order to compare the absorption spectra of the ketyl radical in benzene and cyclohexane, the spectra were normalized to have the same average extinction coefficient in the wavelength range shown in Figure 2.) The second-order decay of the ketyl radical is better shown in Figure 4 both because it is a reciprocal of absorbance *vs.* time plot and because the log absorbance scale of Figure 3 was compressed to show the benzophenone triplet and the ketyl radical on the same graph. Figure 4 also shows absorbance at 525 nm to maximize the effect of triplet absorbance. The curve in Figure 4 is, however, only one of a series of such curves measured at various wavelengths. The intercepts and slopes drawn through the straight-line segment of these curves are inversely proportional to the extinction coefficient of the ketyl radical showing that in the straight-line segment of the curves it is the only observable species, and giving further proof of its second-order decay. The rate of this second-order reaction is known only in terms of the extinction coefficient of the ketyl radical at a given wavelength, *i.e.*, in terms of $\epsilon_{k,\lambda}$. The measured rate is $k_2 = 2.8 \times 10^5 \times \epsilon_{k,545nm}\ M^{-1}\ sec^{-1}$, which is in agreement with the previously measured rate of decay of ketyl radical in benzene.[5]

The relative quantum yield of ketyl radical in cyclohexane and in benzene was compared by extrapolating the second-order decay to time zero for the ketyl radical in the two solvents at 545 and 525 nm. The absorbance averages 45 times greater in cyclohexane than in benzene (0.300 *vs.* 0.006 at 545 nm and 0.160 *vs.* 0.004 at 525 nm). Since the quantum yield of ketyl radical in cyclohexane has been found to be one,[10] the quantum yield of ketyl radical in benzene is 1/45 of this, or 0.022.

As a further check of this low value for quantum yield of ketyl radical, the absorbances in benzene at time zero of triplet benzophenone and ketyl radical, 0.36 *vs.* 0.0045 at 525 nm, were directly compared with results reported by previous workers[5] by using their rough extinction coefficients for the triplet and radical of 6000 and 7000. We found a ratio of ketyl to triplet of 0.011, one-tenth of the previous value.

Triplet State of Benzophenone. The mean life of the triplet state of benzophenone, 10 μsec, was measured from the straight-line portion of the curve in the insert of Figure 3. With such a fast decay and with interference from a longer-lived transient, one cannot determine from a single trace whether there is any second-order triplet–triplet annihilation decay included in the apparent first-order decay. However, a lower energy flash (5 J) produced a triplet with a 25% longer apparent first-order mean life. It was therefore concluded that triplet–triplet quenching is involved and that the longest possible first-order mean life of the triplet is 14 μsec.

Because of the low yield of ketyl radical in benzene, it was possible to measure the triplet decay at several wavelengths and thereby to determine the spectrum of

benzophenone triplet at room temperature. Although there was a large signal, a condition which should lead to precision in the absorption measurements, the triplet decay is so fast that an error of 1 μsec in the time of decay relative to the time of decay at another wavelength leads to a 10% error in extinction coefficient relative to that at another wavelength. The absorption spectrum of the triplet is shown in Figure 2. There is, indeed, much overlap of the benzophenone triplet and ketyl radical spectra, yet they are clearly different. The relative extinction coefficients of the benzophenone triplet and the ketyl radical were determined by comparing the quantum yield of triplet in benzene (unity) and the quantum yield of ketyl radical in cyclohexane (also unity) with the absorbance at time zero of benzophenone triplet in benzene and ketyl radical in cyclohexane. Comparing the extinction coefficient of triplet with the average estimates of that of ketyl radical[14,15] gives a maximum extinction coefficient for the triplet of 7000, which is in reasonable agreement with previous work.[15]

A theoretical curve was constructed by the addition of the absorbance of the triplet, which decays with a maximum mean life of 14 μsec, plus the absorbance of the radical, which is produced from the triplet during the triplet decay and simultaneously decays by the measured second-order rate. This curve is the dotted curve in Figure 3. The actual decay is significantly different from this curve and indicates the presence of a third transient with an intermediate lifetime on the order of 50 μsec. This transient may be the adduct diradical or other benzophenone–benzene addition products which have been proposed.[10,11]

Since the triplet decay was apparently first order for one lifetime (Figure 3) and the straight-line portion of the logarithmic decay curve shows the same slope at each wavelength of the triplet, the effect of the intermediate-lived transient on the apparent rate of triplet decay should not be too large. To check this effect, the absorbance of a transient, which built up with a rate of 1×10^5 sec^{-1} ($\tau = 10$ μsec), decayed with a rate of 2×10^4 sec^{-1} ($\tau = 50$ μsec) and was responsible for all the absorbance at $\tau = 40$ μsec was calculated. This maximum absorbance of such a transient was then subtracted from the experimental decay curve. The resulting curve, which was a straight line for approximately one and one-half orders of magnitude of absorbance, represents the lower limit for the mean life of the triplet. The lower limits were 8 μsec for a 25-J flash, 10 μsec for a 5-J flash, and 11 μsec for the lower limit excluding triplet–triplet decay. The true lifetime is therefore 12 ± 2 μsec ($k_1 = 8 \times 10^4 \pm 1 \times 10^4$ sec^{-1}). This is in agreement with the first approximate lifetime in benzene at room temperature ($\tau = 10^{-5}$ sec ± 50%) measured by flash photolysis[5] and that calculated from continuous irradiation studies,[16] but it is somewhat longer than the 6.5-μsec phosphorescence lifetime[17] and the 3.5-μsec lifetime recently measured by flash photolysis using laser excitation.[10] It is possible that in the last case the focusing of the excitation laser within the sample led to high local concentration of triplets resulting in triplet–triplet quenching, which gave an apparent shorter lifetime.

A note should be made about "time zero." The flash is not instantaneous. With a triplet lifetime of 10 μsec and a flash half-width of 4 μsec, a significant fraction of the triplet decays during the flash. The profile of the flash was recorded, and "time zero" was that time at which one-half of total light had been emitted. Measurements of absorption could be made 7 μsec after "time zero." This method of determining "time zero" was checked by numerically integrating the total transient formed and also the transient remaining at time t if the decay of the triplet were first-order with $\tau = 10$ μsec. It showed that even with this quick decay the total transient produced was equal to the concentration extrapolated back to within 1 μsec of "time zero."

Conclusions

Benzophenone triplet abstracts hydrogen from benzene but at such a slow rate that the quantum yield of ketyl radical is only 0.022 ± 0.006. Thus, the benzophenone triplet and the ketyl radical are the principal intermediates in the photoreduction of benzophenone in benzene. The ketyl radical which we observed is not formed from impurities since the benzene is extremely pure and since in the continuous irradiation studies of part I of this investigation,[6] for which the same solvents and deoxygenation techniques were used, the quantum yields of disappearance of benzophenone and appearance of benzopinacol and biphenyl are consistent with reaction only with benzene. The isotope effect ranging from 4 to 12, reported in part I, for the formation of biphenyl from perdeuteriobenzene indicates that the phenyl radical and therefore the ketyl radical is formed by abstraction of hydrogen from benzene.

The quantum yield of ketyl radical in benzene, 0.022, is in reasonable agreement with the quantum yield of benzophenone disappearance from the continuous irradiation studies,[6] 0.0051 (+0.0008, −0.0015). The difference between the yields may be due to back reactions of phenyl and ketyl radicals or to two-quantum processes under flash excitation, *i.e.*, the triplet absorbs light from the flash forming a highly reactive, though short-lived, excited triplet. With a triplet lifetime of 12 μsec, such a two-quantum process is virtually impossible under continuous irradiation.

(14) A. Beckett and G. Porter, *Trans. Faraday Soc.*, 59, 2038 (1963).
(15) E. J. Land, *Proc. Roy. Soc., Ser. A*, 305, 57 (1963).
(16) G. S. Hammond, W. P. Baker, and W. M. Moore, *J. Amer. Chem. Soc.*, 83, 2795 (1961).
(17) W. D. K. Clark, A. D. Litt, and C. Steel, *ibid.*, 91, 5413 (1969).

The short lifetime of the benzophenone triplet in benzene, compared with the room-temperature phosphorescence lifetime of 0.71 msec in perfluoromethylcyclohexane[18] along with the low yield of ketyl radical in benzene gives further confirmation that the benzophenone triplet is quenched by benzene by a process other than hydrogen abstraction from the benzene.[5,11,16,17]

In addition to the benzophenone triplet and ketyl radical, there is a third transient with a life of roughly 50 μsec. This transient could be a complex formed by the quenching of benzophenone triplet by benzene.[10,11] This transient is not an intermediate in the photoreduction of benzophenone since it has been shown that this reaction proceeds *via* hydrogen abstraction and the ketyl radical.

The rate of abstraction of a hydrogen atom from benzene by benzophenone triplet can be calculated. Since 0.022 of the total triplet formed reacts to give ketyl radical, and the rate constant for decay of the triplet is 9×10^4 sec^{-1}, 0.022 of this rate constant, or 16×10^3 sec^{-1}, is the pseudo-first-order rate constant due to hydrogen abstraction. Since the concentration of benzene is 11.3 M, the true second-order rate constant for hydrogen abstraction from benzene is only $1.6 \times 10^2 M^{-1}$ sec^{-1}.

(18) C. A. Parker and T. A. Joyce, *Chem. Commun.*, **13**, 749 (1968).

Effects of Radiation on the Thermal Decomposition Induction Period in Ammonium Perchlorate and Other Pseudostable Materials[1,2]

by P. W. Levy

Brookhaven National Laboratory, Upton, New York 11973

and P. J. Herley*[3]

Picatinny Arsenal, Dover, New Jersey 07801 *(Received August 17, 1970)*

Publication costs assisted by Brookhaven National Laboratory and Picatinny Arsenal

The induction period of ammonium perchlorate, and other pseudostable inorganic solids, is shortened by exposure to radiation prior to isothermal decomposition. Specifically, the induction period, I, is related to the prior dose Φ, by the equation $I = C_1 - C_2 \log \Phi$, where C_1 and C_2 are constants. This relation applies to many materials over dose ranges between two and four orders of magnitude and, most likely, is not fortuitous. To relate it to both the thermal decomposition kinetics and the radiation-induced processes, induction period *vs.* total dose equations have been derived for a variety of different conditions. The equations can be derived without specifying the exact nature of the thermal or radiation-induced mechanisms. It is assumed that these mechanisms are functions of a parameter which increases from a small initial value to a considerably larger limiting value. This unspecified parameter could refer to numerous physical quantities, *e.g.*, average size or concentration of decomposition nuclei, crack length, bubble volume, etc., or to any of a large number of other more abstract variables. These considerations lead to 11 different induction period *vs.* total dose equations. Only one of these, the equation for exponential growth during heating and linear growth during irradiation, corresponds to the experimentally observed relation. The fact that 11, out of a possible 12, different equations are obtained forms the basis for a new method of determining both the thermal and radiation-induced induction period kinetics.

Introduction

Many recent studies on the isothermal decomposition of inorganic solids have included measurements on samples that were exposed to radiation prior to heating. Almost every type of radiation has been used, but a large fraction of the published work describes effects produced by uv light, X-ray, γ-ray, and reactor irradiations. Most often, studies on irradiated material were performed for one or both of the following two reasons. First, the material may have been irradiated to investi-

(1) Research was performed primarily at Brookhaven National Laboratory and was supported by Picatinny Arsenal and the U. S. Atomic Energy Commission.

(2) Presented in part at the 1969 Spring Meeting of the Western States Section/The Combustion Institute, China Lake, Calif.

(3) Guest Scientist at Brookhaven National Laboratory.

gate one or more features of the decomposition process. For example, uv light or X-ray irradiation may produce effects which would indicate whether a particular decomposition involves one or more electronic processes. Second, it may have been included in a "radiation damage" study to determine if irradiation can modify one or more properties of the material in any important way. For example, irradiation may introduce lattice defects or trapped charges which modify any subsequently measured process such as thermal stability or burning rate.

A large fraction of materials decomposed at a constant temperature exhibit a well defined induction period preceding the main reaction. In most of these the induction period may be reduced or eliminated by exposure to radiation. The analysis described below was undertaken to relate the radiation effect to the thermal decomposition processes.

Nature of the Thermal Decomposition Process

Detailed descriptions of isothermal chemical decomposition kinetics are given by Jacobs and Tompkins[4] and Young.[5] Most often the irreversible isothermal decomposition of solids is described by the equation A(solid) → B(solid) + C(gas) and is represented as a curve of $\alpha(t)$ *vs.* t where $\alpha(t)$ is a measure of the amount of product formed and t is the time. Usually $\alpha(t)$ is the fraction of product present at time t and approaches unity when the time is very large and the reaction is effectively complete. For example, if the reaction is carried out in a closed system, where $p(t)$ is the evolved gas pressure at a given time and p_0 is the final pressure obtained when the reaction is completed, then $\alpha(t)$ is $p(t)/p_0$.

In the most general case $\alpha(t)$ *vs.* t curves contain five distinct regions. Initially, immediately after the sample is inserted into the (hot) decomposition chamber, occasionally a small burst of gas may be observed which is often referred to as "the (initial) puff." In the second region, the induction period, the reaction proceeds very slowly (or possibly not at all); *e.g.*, the product gas pressure may increase very slightly or a negligible amount during this period. The third region, the acceleratory period, is characterized by a rapidly increasing rate of product formation. In this paper, the onset of the acceleratory period will be defined as that point where the more or less constant slope characteristic of the induction period undergoes a transition to the rapidly increasing slope characteristic of the acceleratory period. During the acceleratory period the slope of the $\alpha(t)$ *vs.* t curve increases monotonically from a comparatively low value to a large maximum value called the inflexion point. Usually the end of the acceleratory period and the beginning of the next or fourth region, the decay period, is taken as the point where the slope is a maximum. Throughout the decay period the slope decreases monotonically until it is zero or very nearly so. For most substances, at the end of the decay period all of the original material has decomposed. However, if some of the original material remains *in an unreacted form* the thermal decomposition process includes a fifth region usually called the retention. As is well known, the ammonium perchlorate retention is unusually high below 240°, namely, between 60 and 70%.

Inasmuch as this paper will describe results relating to the induction period, comments relating to the other periods will be reduced to the absolute minimum. Almost all of the available information about them is contained in the references given above. However, it is necessary to make one comment about the initial gas release or "puff." In most instances, and this includes ammonium perchlorate, the puff would appear to be an artifact that is not directly related to the thermal decomposition process. Most likely it is caused by the physical desorption of gases, water vapor, etc., from the crystallite surfaces or the accessible interior.

The processes that have been, at least up to now, assumed to occur during the induction period are also described by Jacobs and Tompkins[4] and Young.[5] The most important of these are in one of four categories usually characterized by the names of the equations describing the applicable induction period kinetics, namely, exponential, linear, power law, and instantaneous. The name instantaneous is used when the induction period is not observed, either because it is absent or the reaction proceeds so rapidly it cannot be detected. For example, in silver oxide the nucleation evidently occurs too rapidly to be detected.[6] The instantaneous induction period case will not be considered in this paper. Each of the three other processes can be related to familiar types of chemical reactions.

It is surprising that the saturating exponential induction period behavior, *i.e.*, nuclei formation described by expressions of the form $N = N_m(1 - \exp - ht)$, is not encountered more often in thermal decomposition studies. Perhaps this can be attributed to the fact that this equation describes a process requiring an infinite time for completion even if it is unlikely that it will remain applicable at large t. This type of behavior is regularly observed in a large variety of kinetic processes and especially those induced by radiation. Consequently, it is included among the processes to be considered in detail. Several other processes, including those occurring in branching network treatments, have been analyzed in the manner described below. Unfortunately most of the resulting equations are too complex

(4) P. W. M. Jacobs and F. C. Tompkins, "Chemistry of the Solid State," W. E. Garner, Ed., Butterworths, London, 1955, Chapter VII.

(5) D. A. Young, "Decomposition of Solids," Pergamon Press, London, 1966.

(6) P. J. Herley and E. G. Prout, *J. Amer. Chem. Soc.*, 82, 1540 (1960).

Table I: Equations Describing Nucleus Growth during Heating

Differential equation	Name	Growth equation
$\frac{dn}{dt} = l$	Linear (L)	$n = n_0 + lt$
$\frac{dn}{dt} = gn$	Exponential (E)	$n = n_0 e^{gt}$
$\frac{dn}{dt} = \alpha t^{p-1}$ $(p \neq 0)$	Power (P)	$n = n_0 + \beta tp$, $\beta = \alpha/p$
$\frac{dn}{dt} = h(n_m - n)$	Saturating exponential (S)	$n = n_m[1 - (1 - n_0/n_m)e^{-ht}]$ $n = n_m(1 - e^{-ht})$ if $n_0 \ll n_m$

to be immediately associated with simple physical processes and these cases will not be described.

The differential equations describing all of the processes which will be discussed in detail are contained in Table I. However, it is essential to recall that these equations *do not* describe anything other than the macroscopic results of processes occurring during the reaction. Clearly, they provide useful information about the induction period processes, but they do not contain sufficient information to identify the nature of the mechanisms they describe. This point is especially important to the development below and is illustrated in the following paragraph.

Most often it is assumed that the physical process occurring during the induction period is the formation of new decomposition nuclei; *i.e.*, at the beginning of the period a negligible number of nuclei are present and toward the end a large number exist. Alternatively, the physical process occurring during this period could be the growth of a fixed number of nuclei from a relatively small initial size to a considerably larger size; *i.e.*, the number of nuclei does not change, but each one enlarges or develops. Thus, another related and often repeated point must be emphasized; namely, both of these processes, as well as others, can be described by exactly the same kinetic equations. Furthermore, in these two examples the words "number" and "size" have been used to describe the variable parameter that changes during the induction period, and the same equations may, in reality, describe still other physical quantities. Included in this category are, *e.g.*, dislocations, point defects, strain, stress, crack length, bubble size, trapped charge concentration, surface coverage, fraction of consumed impurity, fraction of surface "cleansed" of impurity, impurity product, and a large number of more abstract variables such as branching node concentration, onset of chain overlap, etc. In the remainder of this paper, the word size, or occasionally extent, will be used to refer to the "*induction period variable.*" It will always be used in the most general sense, and until it is experimentally related to a specific physical process should not be associated with any particular physical quantity.

A large amount of evidence indicates that the induction period processes start at specific crystal lattice imperfections such as the intersection of an edge or screw dislocation with the crystal surface, at a grain or mosaic block boundary, or at any number of smaller defects such as vacancies or impurities, etc.[4,5] Once the nuclei formation process has been completed, *i.e.*, after the nuclei have grown from their initial to a critical size, and both of these are, at the moment, ill defined, the reaction is assumed to enter the acceleratory period. Also, it is reasonably well established that the acceleratory period reaction proceeds almost entirely in a manner dictated by the geometry of the decomposition site, *i.e.*, by the crystal structure of the reacting material and the nature of the reaction.

The induction period properties described above can be modified by subjecting the material to various forms of treatment prior to decomposition. A considerable number of measurements have been interpreted in a way that indicates that additional decomposition sites may be formed by irradiating with ultraviolet light,[7] by electrons,[8] by γ rays,[9] by X-rays,[10,11] and by reactor irradiation.[12] Almost all of the processes involved in nuclei formation during irradiation have been summarized by Young.[5] This includes some of the electronic processes discussed recently by Levy and Herley.[13,14] It would be appropriate to summarize the most probable radiation-induced processes in this paper but, simply to be brief, this will not be done. However, it is necessary to describe below the experimental evidence for one

(7) W. E. Garner and J. Maggs, *Proc. Roy. Soc., Ser. A*, **172**, 299 (1939).

(8) J. M. Groocock and F. C. Tompkins, *ibid.*, **223**, 267 (1954).

(9) E. G. Prout and P. J. Herley, *J. Phys. Chem.*, **66**, 961 (1962).

(10) P. J. Herley and P. W. Levy, *J. Chem. Phys.*, **49**, 1493 (1968).

(11) P. J. Herley and P. W. Levy, *ibid.*, **49**, 1500 (1968).

(12) E. G. Prout, *J. Inorg. Nucl. Chem.*, **7**, 368 (1958).

(13) P. W. Levy and P. J. Herley, "Kinetics of Reactions in Ionic Systems," T. J. Gray and V. D. Frechette, Ed., Plenum Publishing Co., New York, N. Y., 1969, Chapter 8.

(14) P. W. Levy and P. J. Herley, "Reactivity of Solids," Sixth International Symposium, J. W. Mitchell, R. C. DeVries, R. W. Roberts, and P. Cannon, Ed., Wiley, New York, N. Y., 1969, pp 75–81.

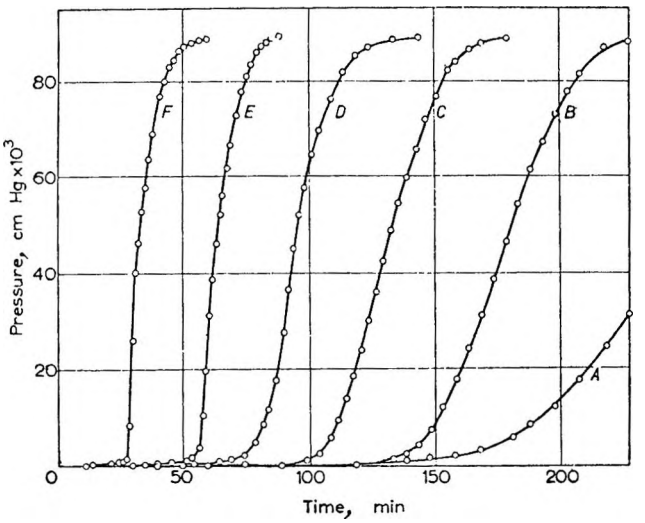

Figure 1. The original observation by Prout[12] showing that the $KMnO_4$ induction period is shortened by exposure to γ-ray irradiation prior to thermal decomposition: A, 0 min; B, 10 min; C, 2 hr; D, 16.5 hr; E, 72 hr; F, 168 hr of ^{60}Co γ-ray irradiation at a dose rate of 1.6×10^6 rep/hr.

empirical equation relating the prior radiation exposure to the duration of the induction period.

Empirical Relation between Induction Period and Prior Irradiation Dose

Some years ago Prout,[12] in a study of the thermal decomposition of potassium permanganate which had been irradiated with either thermal neutrons, γ rays, electrons, or protons prior to decomposition, reported that the irradiation shortened the induction period. A typical example of the observed effect is shown in Figure 1. More specifically, he reported that the shortened induction period was related to the prior dose by the equation

$$\text{(induction period)} = \text{(constant)}_1 - \text{(constant)}_2 \log \text{(irradiation dose)} \quad (1)$$

Subsequently, it was found that this empirical relation applied to several other substances.[9-11, 16-17] In particular, it was found to apply to ammonium perchlorate that had been exposed to γ rays before decomposition.[10,11,17] Most importantly, the relation accurately describes the induction period for ammonium perchlorate samples which had been irradiated with γ-ray doses of from 10^2 to 10^7 rads, *i.e.*, five orders of magnitude. The data for ammonium perchlorate and five other substances are shown in Figure 2. This appears to constitute strong evidence indicating that the relation is not fortuitous. Consequently, the analysis to be described below was undertaken to determine if the behavior expressed by this relation could be used to obtain information about the induction period processes and if and how these processes are affected by radiation.

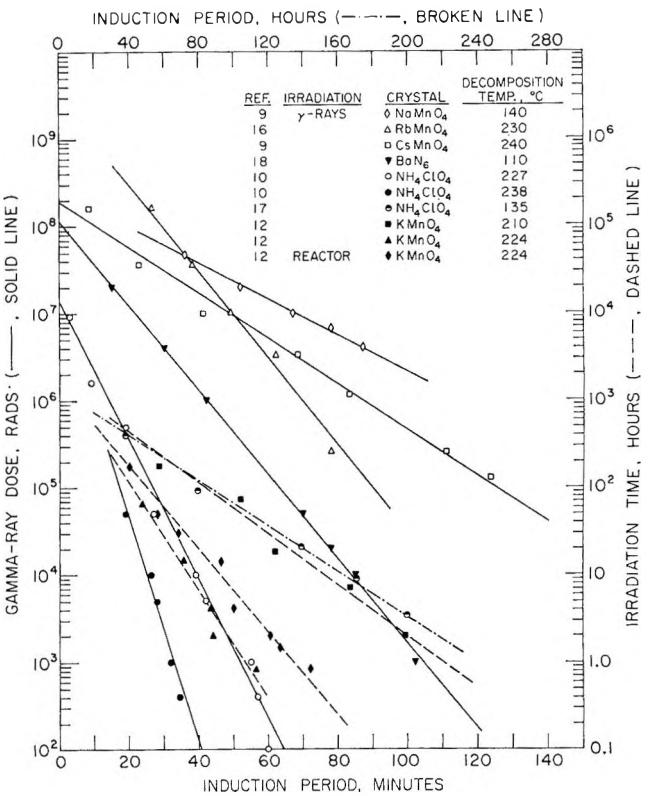

Figure 2. Induction period *vs.* total dose curves for a variety of pseudostable materials. All of them can be described by the relation (induction period) = $(\text{constant})_1 - (\text{constant})_2$ log (dose). Additional information about each curve is contained in Table IV.

Induction Period Processes

Additional experimental information regarding the induction period processes, other than that contained in eq 1, can be obtained from some of the previous work.[10,11] Figure 3 shows the induction period region of $\alpha(t)$ *vs.* t curves for ammonium perchlorate samples that had been subjected to various doses of γ rays prior to decomposition. The curve for unirradiated material indicates that the transition from the induction period to the acceleratory period is gradual and the rate of change during the initial part of this region is small. In contrast, as the γ-ray dose is increased curvature in the acceleratory region increases. Furthermore, the transition from the induction period to the acceleratory period becomes more abrupt as the dose increases. However, it is important to note that both slope and height of the $\alpha(t)$ *vs.* t curves for irradiated ammonium perchlorate do not increase during the induction period. These observations suggest the following. During the thermal induction period, the average "size" or extent of the decomposition nuclei is increased by one or more

(15) E. G. Prout and M. J. Sole, *J. Inorg. Nucl. Chem.*, **9**, 232 (1959).

(16) P. J. Herley and E. G. Prout, *ibid.*, **16**, 16 (1960).

(17) S. Fogler and D. Lawson, *J. Phys. Chem.*, **74**, 1637 (1970).

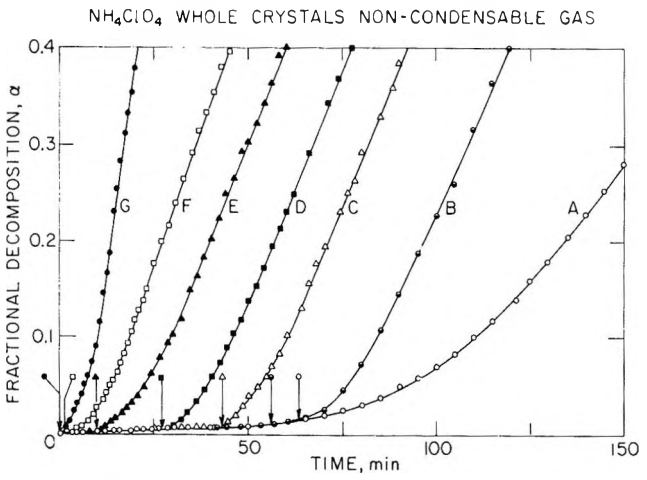

Figure 3. Effect of prior γ-ray irradiation on the decomposition induction period at 227°: A, O, unirradiated; B, ◒, 0.001 × 10^6 rads; C, △, 0.001 × 10^6 rads; D, ■, 0.05 × 10^6 rads; E, ▲, 1.6 × 10^6 rads; F, □, 14.4 × 10^6 rads; G, ●, 24.8 × 10^6 rads. The shortening of the induction period of ammonium perchlorate whole crystals exposed to radiation prior to thermal decomposition. The samples were irradiated with ^{60}Co γ rays at room temperature and decomposed at 227°. The arrows indicate the end of the induction period. Note that the decomposition rate during the induction period is independent of the amount of prior irradiation, and in addition, that the demarkation between the induction and acceleratory periods becomes more abrupt as the irradiation increases.

physical processes. Furthermore, during the time that the material is exposed to radiation, the average nuclei size also increases. Since the induction period is negligible for samples exposed to approximately 10^7 rads it would appear that this dose causes the nuclei to reach the critical size. If the critical size is not attained during irradiation any subsequent heating causes the nuclei to grow by thermal processes until the critical size is attained. Once the nuclei reach a critical size, or extent, the induction period processes become unimportant and are superceded by one of the acceleratory period processes. In fact, the available information suggests that, once the reaction has entered the acceleratory region, the substance has "forgotten" whether the induction period growth was induced by heat or irradiation. Yet, it cannot be assumed that the thermal and radiation-induced growth are described by the same equations.

The concepts described above can be stated as a series of assumptions which can be regarded as the starting point for the derivations that follow.

1. The progress of the reaction occurring in the induction period, either during heating or exposure to radiation, is described by an "induction period variable," n, which increases from an initial value, n_0, to a final value n_c. The nature of n is not specified. It could refer to a physical quantity, *e.g.*, size or concentration of nuclei, or any one of a large number of more abstract quantities.

2. The dependence of n on heating time may be different from the dependence on total dose but it is assumed to follow simple "growth" equations.

3. The onset of the acceleratory period reactions occurs when $n = n_c$, the average critical size of the nuclei at the end of the induction period. The acceleratory period processes are assumed to be independent of the heating time and dose, applied during the induction period, and the sequence in which they occurred.

The assumptions given above have been stated in terms of a single variable n. However, they apply, without any alteration, to distributions of this or a similar variable.

Nucleus Growth during Irradiation

Although, in the previous section, nucleus growth during irradiation has been described in general terms, it is necessary to describe this growth in more precise mathematical terms. This will be done for the three cases chosen primarily because they describe typical radiation-induced processes that are specified by simple equations. The following definitions are used. t is the time; note that t may refer to either the time that material is exposed to irradiation at ambient temperature or isothermal heating time at a higher temperature. n is the induction period variable, usually referred to as the size or extent of the decomposition nuclei. It may be a function of t and/or Φ. n_0 is the initial average size of the nuclei; *i.e.*, $n(t) = n_0$ when $t = 0$. n_c is the average critical size of the nuclei at the end of the induction period, *i.e.*, the size of the nuclei at the onset of the acceleratory period. n_m is the average maximum size of the nuclei which can be obtained by irradiation; n_m may be less than, equal to, or greater than n_c; however, it is most likely that n_m is approximately equal to n_c. ϕ is the irradiation dose rate in, for example, R or rads per unit time. Φ is the total dose, *i.e.*, $\Phi = \phi t$. j is the factor relating dn/dt to the dose rate and/or irradiation time for nuclei growth during irradiation, *i.e.*, $n(t)$ will be a function of $j\phi t = j\Phi$. In more general cases j could be a function of one or more variables, but it will be seen that j = constant is adequate for this treatment.

The following definitions apply to the equations, describing the various types of thermally induced growth occurring during the induction period, summarized in Table I. g is the rate of growth of the decomposition nuclei according to the "exponential law." h is the rate of growth of the decomposition nuclei according to the "saturating exponential law." l is the rate of growth of the decomposition nuclei according to the "linear law." p is the exponent in the "power law" equation. α is the rate of growth of the decomposition nuclei according to the "power law" (different from and should not be confused with $\alpha(t)$). β = constant in the "power law" equation = α/p.

The following definitions apply to material that has

Table II: Equations Describing Radiation-Induced Nucleus Growth

Differential equation	Name	Growth equation
$\frac{dn}{dt} = j\phi$	Linear (L)	$n = n + j\phi t = n_0 + j\Phi$
$\frac{dn}{dt} = j\phi n$	Exponential (E)	$n = n_0 e^{j\phi t} = n_0 e^{j\Phi}$
$\frac{dn}{dt} = j\phi(n_m - n)$	Saturating exponential (S)	$n = n_m[1 - (1 - n_0/n_m)e^{-j\phi t}]$ $= n_m(1 - e^{-j\Phi})$ if $n_0 \ll n_m$

Table III: (Induction Period) *vs.* (Total Dose) Equations for Four Induction Period Kinetic Equations and Three Equations Describing Nuclei Growth during Irradiation. (The Abbreviations L, P, S, and E Are Defined in Tables I and II.)

Thermal equation	Irradiation equation	(Induction period) *vs.* (dose) equation, small terms *not* neglected	Approximations and conditions	(Induction period) *vs.* (dose) equation, small terms neglected
E	L	$I = \frac{1}{g}\ln\left(\frac{n_c}{n_0} - \frac{j}{n_c}\Phi\right)$	$n_0 \ll n_c$	$I = C_1 - C_2 \ln \Phi$
E	S	$I = \frac{1}{g}\left(\ln\frac{n_c}{n_m} - \ln[1 - e^{-j\Phi}]\right)$	$n_0 \ll n_m$	$I = C_1 - C_2 \ln[1 - e^{-C_3\Phi}]$
E	E	$I = \frac{1}{g}\left(\ln\frac{n_c}{n_0} - j\Phi\right)$	None	$I = C_1 - C_2\Phi$
L	L	$I = \frac{1}{l}(n_c - n_0 - j\Phi)$	None	$I = C_1 - C_2\Phi$
L	S	$I = \frac{1}{l}(n_c - n_m + n_m e^{-j\Phi})$	$n_0 \ll n_m$	$I = C_1 + C_2 e^{-C_3\Phi}$
L	E	$I = \frac{1}{l}(n_c - n_0 e^{-j\Phi})$	None	$I = C_1 - C_2 e^{C_3\Phi}$
S	L	$I = \frac{1}{h}\left[\ln\left(\frac{n_m}{n_m - n_c} - \frac{j}{n_m - n_c}\Phi\right)\right]$	$n_0 \ll n_m$ $n_m > n_c$	$I = C_1 \ln(C_2 - C_3\Phi)$
S	S	$I = \frac{1}{h}\left[\ln\frac{n_m - n_c}{n_m} + j\Phi\right]$	$n_0 \ll n_m$ $n_m > n_c$	$I = C_1 + C_2\Phi$
S	E	$I = \frac{1}{h}\left[\ln\frac{n_m - n_c}{n_m} - \ln\left(1 - \frac{n_0}{n_m}e^{j\Phi}\right)\right]$	None	$I = C_1 - C_2 \ln(1 - C_3 e^{C_4\Phi})$
P	L	$I = \left[\frac{1}{\beta}(n_c - n_0 - j\Phi)\right]^{1/p}$	None	$I = (C_1 - C_2\Phi)^{1/C_3}$
P	S	$I = \left[\frac{1}{\beta}(n_c - n_m + n_m e^{-j\Phi})\right]^{1/p}$	$n_0 \ll n_m$	$I = (C_1 + C_2 e^{-C_3\Phi})^{1/C_4}$
P	E	$I = \left[\frac{1}{\beta}(n_c - n_0 e^{j\Phi})\right]^{1/p}$	None	$I = (C_1 - C_2 e^{C_3\Phi})^{1/C_4}$

been irradiated and then subjected to subsequent thermal decomposition at a fixed temperature. I is the induction period, *i.e.*, it is the value of t corresponding to the end of the induction period, or the onset of the acceleratory period, for samples that had previously been subjected to a total dose Φ. I_0 is the induction period observed with unirradiated material. C_i refers to the constants in the various I *vs.* Φ equations contained in Table III after they have been reduced to their most simple form; usually the C_i represent various combinations of the constants given above.

Linear Radiation-Induced Nuclei Growth during Irradiation. Clearly, this is the simplest type of radiation-induced nuclei growth. In terms of the definitions given above, the differential equation for linear growth will be $dn/dt = j\phi$ and the average size of the decomposition nuclei at time t after the radiation has commenced will be given by the expression

$$n = n_0 + j\phi t \qquad (2)$$

If the total irradiation time is t, the average size of the nuclei will be given by

$$n = n_0 + j\Phi \tag{3}$$

Saturating Exponential Nuclei Growth during Irradiation. As implied above, it is conceivable that there is a maximum average size of the nuclei which could be formed during irradiation. The rate of formation of the nuclei which would lead to this could follow any of a large number of possible kinetic equations. However, one of the most likely is the "saturating exponential" equation. In this case, the differential equation describing the nucleus growth is

$$\frac{dn}{dt} = j\phi(n_m - n) \tag{4}$$

The solution of this is

$$n = n_m\left[1 - \left(1 - \frac{n_0}{n_m}\right)e^{-j\Phi}\right] \tag{5}$$

Since the constant n_m is expected to be very much larger than n_0, the quantity $n_0/n_m \ll 1$, and this equation reduces to

$$n = n_m[1 - e^{-j\Phi}] \tag{6}$$

In *every* instance (6) is the saturating exponential radiation-induced nuclei growth equation that will be used below.

Exponential Nuclei Growth during Irradiation. It would appear that nuclei formation during heating follows the "exponential law" in an appreciable fraction of the materials that have been studied to date. Consequently, it may be also reasonable to assume that the nuclei may grow exponentially during radiation. This case is included here even though it is difficult to cite examples of other radiation-induced processes that follow this dependence. The differential equation for this is

$$\frac{dn}{dt} = j\phi n \tag{7}$$

and its solution is

$$n = n_0 e^{j\phi t} = n_0 e^{j\Phi} \tag{8}$$

The various equations for nuclei growth during irradiation described in this section are summarized in Table II. The behavior of the equations for nuclei growth during heating, Table I, and those in Table II are both illustrated in Figure 4. The parameters used to compute these curves were chosen arbitrarily and do not have any particular significance.

Very few radiation processes describable by a power law can be found in the literature. Consequently, these cases are not included.

Induction Period *vs.* Total Dose Equations

Having described, in previous sections, the most commonly observed induction period kinetics and, hopefully, the more probable types of radiation-induced nuclei growth processes, all of the necessary information is available to derive (induction period) *vs.* (total dose) equations for materials that have been subjected to irradiation prior to thermal decomposition. Actually, the four induction period "laws" and three types of radiation-induced nuclei growth equations which are considered produce a maximum of 12 induction period equations. Simply to save space one derivation will be given in detail. The obvious choice for this is the combination of induction period and radiation-induced growth equations that leads to the experimentally observed eq 1, namely

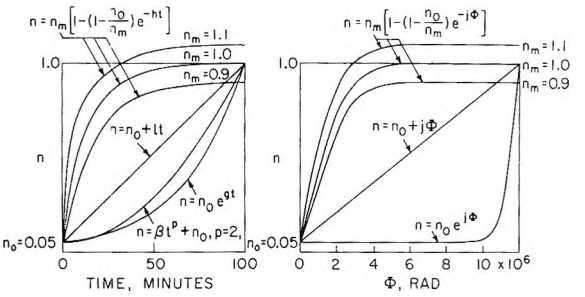

Figure 4. Graphical representations of: (a) thermal induction period growth equations and (b) radiation-induced growth equations, summarized in Tables I and II.

$$I = C_1 - C_2 \log \Phi$$

To begin, the differential equation leading to the "exponential law" nuclei growth during heating is

$$\frac{dn}{dt} = gn \tag{9}$$

The solution of this is

$$\ln n = gt + \text{constant} \tag{10}$$

The constant in this equation is to be evaluated in two specific cases: first, when this equation is applied to unirradiated material and second, when the material had been subjected to prior irradiation. In the first case, the constant is obtained by putting $n = n_0$ at $t = 0$. Thus the solution is

$$n = n_0 e^{gt} \tag{11}$$

This equation describes the nucleus growth of unirradiated material during heating. (The situation when $n = 0$ at $t = 0$ is interesting from both a thermal decomposition and radiation effects viewpoint but will not be discussed here.) If the material has been subjected to radiation prior to heating, the average nucleus size will have increased beyond its original size, n_0, when heating is commenced.

The second solution of eq 10 occurs when the material has been irradiated prior to heating. In the case when the radiation-induced nucleus growth is linear, the equation

$$n = n_0 + j\Phi \tag{12}$$

specifies the size of the nucleus as heating is commenced. Thus using (12) to evaluate the constant in (10), one obtains

$$n = (n_0 + j\Phi)e^{gt} \tag{13}$$

Next, let $t = I$ be the length of the induction period observed, after irradiation. In other words, after irradiation the average nucleus size will increase from $n_0 + j\Phi$ to n_c while the sample is heated for a time $t = I$. This sequence of events is illustrated in Figure 5. Thus, when $n = n_c$, eq 13 becomes

$$n_c = (n_0 + j\Phi)e^{gI} \tag{14}$$

This equation can be written

$$\ln n_c = \ln (n_0 + j\Phi) + gI \tag{15}$$

or

$$gI = -\ln\left(\frac{n_0}{n_c} + \frac{j}{n_c}\Phi\right) \tag{16}$$

since $n_c \gg n_0$ (this is the approximation used throughout the paper and is justified below) and $j\Phi/n_c = j\phi t/n_c$ approaches unity for a sufficiently large dose

$$\frac{n_0}{n_c} + \frac{j}{n_c}\Phi \approx \frac{j}{n_c}\Phi \tag{17}$$

and

$$I = \frac{1}{g}\left(\ln \frac{n_c}{j} - \ln \Phi\right) \tag{18}$$

Then, putting $C_1 = (1/g) \ln (n_c/j)$ and $C_2 = 1/g$ (note that C_1 and C_2 are both constants)

$$I = C_1 - C_2 \ln \Phi \tag{19}$$

This is the experimentally observed expression which describes all of the data contained in Figure 2 and incidentally additional data which have not been mentioned. Some of the properties of this equation will be described in a later section.

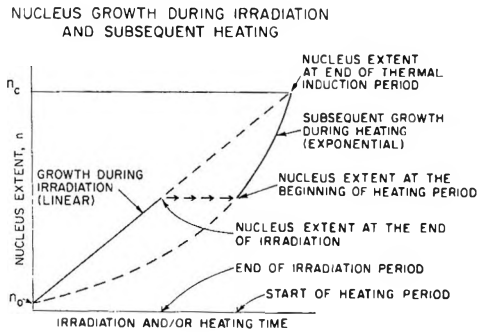

Figure 5. This figure illustrates the particular combination of linear nuclei growth during irradiation and exponential growth during thermal decomposition that leads to the $I = C_1 - C_2 \log \Phi$ relation demonstrated by Figure 2. Also, it shows the nucleus size, or extent, at various stages in the calculation.

In an analogous fashion, (induction period) *vs.* (total dose) equations were obtained for the 11 remaining cases. The equations obtained for all 12 combinations are listed in Table III. Clearly, only one of these equations has the form observed experimentally. It is essential to point out that it can be obtained as a special case of some of the other equations that contain exponential terms. This occurs, as it should, when the exponential is approximated by a series expansion and only the linear term is retained. Consequently, these special cases are equivalent to those obtained by assuming a linear radiation-induced growth.

Two useful results are contained in Table III. First, as mentioned above, the experimentally observed relation $I = C_1 - C_2 \ln \Phi$ is obtained, from the set of equations that were considered, only when linear nucleus growth during irradiation is subsequently combined with exponential growth during heating. In order to ensure that this point is not overstated, its logical limitations must be described in detail. Obviously, additional thermal and irradiation growth laws could be considered and combinations of these, or alternatively, combinations of the additional laws with those already considered could lead to the observed relations. Thus, it is proper to conclude that *one* combination of thermal and irradiation-induced behavior has been found which leads to the observed relation. The possibility that additional combinations exist has not been excluded, nor has it been demonstrated that they exist. In addition, it *has* been demonstrated that the 11 other combinations of commonly occurring kinetic equations do *not* lead to the observed relations. Nevertheless, it is entirely proper to proceed on the assumption that whenever the $I = C_1 - C_2 \ln \Phi$ relation is observed, it results from the exponential thermal and linear irradiation law combination and to determine if any additional conclusions are forthcoming. One such conclusion is discussed in the next section.

A second useful result is exemplified in Table III. Namely, it provides a means for determining the induction period behavior. In practice one would measure the induction period as a function of dose and ascertain which data can be fitted to any of the equations. If an unambiguous fit is obtained, then one can conclude that the data are consistent with a particular combination of thermal and irradiation period laws. However, the limitations discussed above also apply in this case. Incidentally, note that the 12 combinations lead to only 11 different induction period dose equations, and if the $I = C_1 - C_2 \Phi$ relation is observed, the analysis is not unique. Incidentally, induction period measurements on irradiated samples that were describable by equations other than $I = C_1 - C_2 \log \Phi$ could not be found.

Ratio of Initial to Final Value of the "Size" or "Extent"

Additional useful information can be obtained from

the exponential induction period equations and the data in Figure 2. Consider the case where the induction period is measured for a sample that has not been irradiated. This corresponds to putting $t = I_0$ when $n = n_c$ in eq 11, which becomes

$$n_c = n_0 e^{gI_0} \text{ or } \ln \frac{n_c}{n_0} = gI_0 \tag{20}$$

Also, eq 18 may be written

$$\ln \Phi = \ln \frac{n_c}{j} - gI_0 \tag{21}$$

which shows that g can be determined from the experimental curves; *e.g.*, it is the slope of the curves in Figure 2. Thus, these relations can be used to estimate the ratio of the final to the initial nucleus size, n_c/n_0. It should be noted that this derivation makes use of assumption 3 in the section on Induction Period Processes above; namely, it is assumed that the thermal rate parameter, g, is the same for both irradiated and unirradiated material. The extension of this treatment to include the possible modification of g by irradiation is straightforward. However, the available data are consistent with the assumption that g is not significantly modified by irradiation.

Using the ammonium perchlorate data in Figure 2, one obtains

$$\log \frac{n_c}{n_0} \approx 4 \text{ or } \frac{n_c}{n_0} \approx 10^4 \tag{22}$$

Approximate values of n_c/n_0 for all of the substances included in Figure 2 are given in Table IV. This provides justification for the approximation $n_0 \ll n_c$ and $n_0 \ll n_m$ used above. The values of n_c/n_0 for the same substances appear to vary considerably, but when the errors in these values are taken into consideration, one realizes that the agreement is really quite good.

Equations 14, 15, and 16 are simply different expressions for the relation between the induction period and the prior dose, for the exponential thermal and linear radiation-induced growth combination, before the $n_c \gg n_0$ approximation is made. All of the constants or ratios of the constants in these equations also can be determined from the data in Figure 2 and Table IV. The data for the ammonium perchlorate decomposition at 227 and 238° have been replotted in Figure 6 which also shows curves computed from eq 16 using the appropriate constants. This figure demonstrates that, in this material, the $j\Phi/n_0 \gg n_0/n_c$ approximation is valid only for doses in excess of 10^3 rads. It also shows that, at different decomposition temperatures, the same dose would be required to reduce the induction period effectively to zero. This last conclusion can be stated in a different but useful way, namely, at different decomposition temperatures the same value of the ratio n_c/n_0 should be obtained. Incidentally, it should be

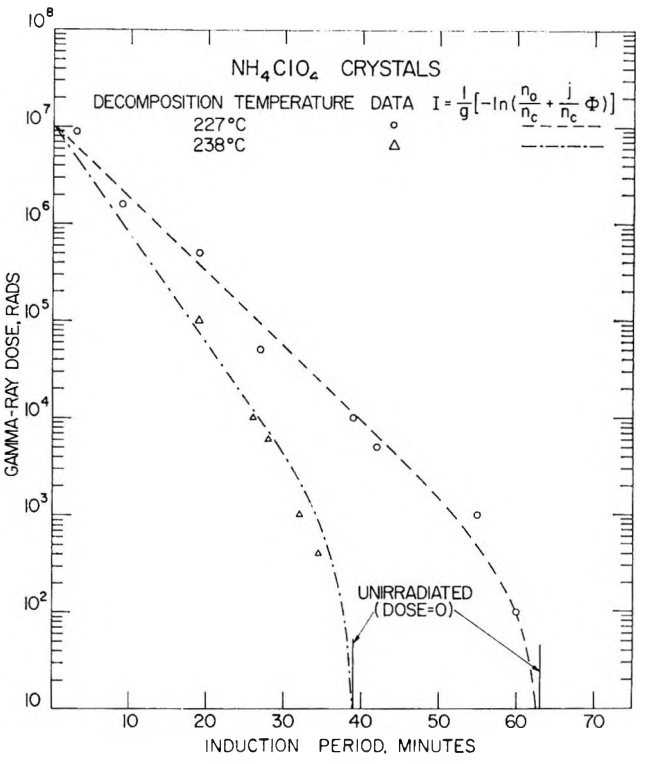

Figure 6. Induction period *vs.* total dose data for ammonium perchlorate crystals thermally decomposed at two different temperatures. The dashed lines were computed from the exact induction period *vs.* total dose equation (18) in the text, using the linear high dose data and the induction period data from unirradiated material.

quite difficult to obtain data conclusively demonstrating the curvature at low doses of the theoretical curves in Figure 6. At these doses it is difficult to separate the end of the induction period from the onset of the acceleratory period and thus the induction period determinations will contain large errors.

Successive Cycles of Heating and Irradiation

The considerations described above have been confined to the simple case of a single irradiation followed by a single irradiation induction period measurement. The extension of this treatment to more complicated situations is straightforward. A number of specific cases including (1) a single period of thermal decomposition followed by irradiation, (2) a cycle consisting of an initial thermal decomposition, an irradiation, and a final thermal decomposition, or (3) numerous cycles of alternating heating and irradiation, etc., have been worked out. There does not appear to be any reason to exhibit these solutions here, especially since some of them are not readily written in a compact form and do not provide additional physical insight.

Simultaneous Heating and Irradiation

A situation which has practical applications arises when ammonium perchlorate is irradiated at a temperature high enough to produce thermal decomposition,

Table IV: The Ratio n_c/n_0, *i.e.*, the Ratio of the Critical to the Initial Size, or Extent, of the Decomposition Nuclei Determined from the Radiation-Induced Decrease in the Induction Period

Material	Ref	Decomposition temperature, °C	Induction period unirradiated material, min	Type of radiation	Ratio
$KMnO_4$	12	210	47	^{60}Co γ rays	2.0×10^4
		224	65	Reactor	7.4×10^3
		224	65	^{60}Co γ rays	1.2×10^3
$NaMnO_4$	9	140	101		1.15×10^2
$RbMnO_4$	16	230	103		3.2×10^5
$CsMnO_4$	9	240	167		1.3×10^4
BaN_6	18	110	180		4.9×10^8
NH_4ClO_4	11	227	63		6.75×10^4
	11	238	39		1.4×10^4
	17	135	1.94×10^4		1.22×10^4

even at a very low rate. The concepts described above can be immediately applied to this case if it is assumed that the irradiation effects do not modify the heating effects and *vice versa*. In other words, it must be assumed that the combined effects are additive or that they are *not* synergistic. The validity of this assumption can be determined only by experiments which, to the best of our knowledge, have not been carried out. Consider just one example, the case which arises when the irradiation effect is given by a linear law and the thermal decomposition by an exponential law. Then if the material is subjected to a constant dose rate at a fixed temperature, the differential equation for the nucleus growth is

$$\frac{dn}{dt} = gn + j\phi \tag{23}$$

The solution of this is

$$n = n_0 e^{gt} + \frac{j\phi}{g}(e^{gt} - 1) \tag{24}$$

The relation between this solution and the nonsimultaneous case can be obtained by writing the second e^{gt} term as a series then

$$n = n_0 e^{gt} + j\phi t + j\phi t \sum_{k=2}^{\infty} \frac{(gt)^{k-1}}{k!} \tag{25}$$

This equation shows that the nucleus growth can be expressed as the addition of terms representing the individual thermal and irradiation contributions and a term, *i.e.*, the one containing the sum, describing the effects of their operating simultaneously. Incidentally, the last equation is *not* an approximation and it does *not* demonstrate a failure of the additivity assumption described above.

The induction period obtained from eq 24 before any approximations are made is

$$I = \frac{1}{g}\left[\ln\left(\frac{g}{j}\frac{n_c}{\phi} + 1\right) - \ln\left(\frac{g}{j}\frac{n_0}{\phi} + 1\right)\right] \tag{26}$$

When the approximation $n_c \gg n_0$ is used this becomes

$$I = C_1 \ln (1 + C_2/\phi) \tag{27}$$

Note that (27) is a function of the dose rate ϕ, not the total dose Φ. The physical meaning of (26) and (27) is quite apparent.

In a similar way, equations can be obtained for any combination of thermal and irradiation growth laws. Also, it is possible to write equations for the induction period I for the value of t corresponding to $n = n_c$. Again, there does not appear to be any reason to exhibit these equations.

Conclusions

The results described above, particularly those summarized in Table III, lead to the following conclusions. First, it is noteworthy that it has been possible to derive the experimentally observed equation from relatively simple and straightforward assumptions. Second, when only large terms are retained, 10 separate equations are obtained for 10 of the 12 cases considered in detail, and an eleventh equation was obtained for the remaining two cases. This appears to provide a basis for differentiating between the four types of induction period kinetics and the three radiation-induced growth processes considered. In other words, systematic determinations of induction period *vs.* total dose curves could become a useful tool for ascertaining induction period kinetics. Third, subject to the limitation stated below, the fact that only one theoretical equation matches the empirical equation would appear to require the conclusion that all materials which obey the empirical equation, *e.g.*, ammonium perchlorate, follow exponential law induction period kinetics. Fourth, for the reason stated immediately above, it would appear that it must also be concluded that these materials undergo linear radiation-induced nucleus growth. The last two conclusions are subject to the following restrictions. Namely, only a finite number of thermal and radiation growth laws have been considered and thus the possi-

bility that the experimentally observed equation could be derived from other kinetics, which were not investigated, has not been eliminated. However, all of the commonly observed kinetics were considered.

It must be emphasized that a large part of the discussion given above is best described as phenomenological; that is, the equations for various physical processes have been written down without recourse to any specific mechanism. Actually, these equations are so general, *i.e.*, they describe such a large number of different physical processes, it is possible to cite a large number of mechanisms which lead to the same equations. Consequently, the problem is not to find a mechanism which leads to these equations but to ascertain which of a large number of possible mechanisms is actually occurring. It is hoped that experiments now underway, or other experiments to be started in the near future, employing both physical and chemical measurements will make it possible to ascertain the nature of the specific induction period processes operating in ammonium perchlorate and similar materials.

Acknowledgment. We wish to thank Professor E. G. Prout[18] for allowing us to include his barium azide data prior to publication.

(18) E. G. Prout, University of Cape Town, South Africa, personal communication, 1969.

An Electron Spin Resonance Study of Trapped Radicals Produced by the Radiolysis of Hydrogenous Materials on Porous Glass[1]

by P. K. Wong

Chemistry Department, Brookhaven National Laboratory, Upton, New York 11973 *(Received July 25, 1970)*

Publication costs assisted by the U. S. Atomic Energy Commission

The γ radiolysis of water or hydrocarbons adsorbed on silica at 77°K produces trapped hydrogen atoms examinable by electron spin resonance spectroscopy. The radiolytic yields of the stabilized H atoms from water, cyclohexane, and 3-methylhexane depend on surface coverage, while that from ethane is independent of coverage from about 0.1 to 1.5 monolayer. The G(H) values (number of H atoms per 100 eV absorbed in the glass) from the hydrocarbons seem to decrease as the molecular weight increases. Charge scavengers such as biphenyl, triphenylamine, and tetracyanoethylene (TCNE) added to the surface prior to the irradiation reduce G(H) values to about 10% of their original yield without the scavengers; argon has a parallel effect. This observation is attributed to direct competition for excitonic energy from the irradiated Vycor between the hydrogenous adsorbate and the scavenger. The stability of hydrogen atoms at 77°K depends on the nature of the surface. Some characteristics of the trapping sites are revealed by the line widths of the esr signals and their lack of satellites. Other radicals produced in the radiolysis have also been observed and their identity has been speculated upon.

Introduction

It has been shown that the radiation chemistry of organic compounds in their adsorbed state is quite different from that of the same materials in their pure state. Caffrey and Allen[2] investigated the γ radiolysis of pentane adsorbed on mineral solids and found that the ionizing radiation energy dissipated in the mineral is efficiently utilized to decompose the adsorbed pentane. The extent of this energy transfer from the solid phase to the sorbed phase depends on the nature of the mineral.[3] Using the electron spin resonance technique, Kinell[4] and coworkers showed that most of the products obtained from the radiolysis of hexane on silica gel are formed from the recombination of carbon radicals. More recent work suggests that the precursors of the radicals might be due to electrons ejected from the solid by the ionizing radiation. For instance, the molecular hydrogen yield from γ-irradiated cyclohexane on silica gel[5] is depressed by the addition of nitrous oxide, which

(1) Research performed under the auspices of the U. S. Atomic Energy Commission.

(2) J. M. Caffrey, Jr., and A. O. Allen, *J. Phys. Chem.*, **62**, 33 (1958).

(3) J. W. Sutherland and A. O. Allen, *J. Amer. Chem. Soc.*, **83**, 1040 (1961).

(4) P.-O. Kinell, *Acta Chem. Scand.*, **19**, 2113 (1965).

(5) N. H. Sagert and P. J. Dyne, *Can. J. Chem.*, **45**, 615 (1967).

is known to be an electron scavenger. This observation is attributed to the effect of direct competition for electrons between cyclohexane and N_2O. The radiolysis of water on a wide variety of oxide surfaces has also been studied.[6] The high yield of H_2, compared to that from irradiating ice, is thought to be the outcome of energetic electrons reacting with the water molecules.

Since ionizing radiation produces electrons and positive ions in the material being irradiated, it is to be expected that the electrons are a reactive species. Evidence of this has been obtained in many laboratories. Wong and Willard[7] found that electrons react extensively with scavengers on silica gel surface. This observation has essentially been substantiated by the work on nitrous oxide[8] and methyl iodide[9] on silica gel. Apparently electrons excited into the conduction band are capable of interacting with adsorbates, which probably behave as surface defects. More recently, rather convincing evidence of reactions involving electrons as well as holes on porous glass surface has been obtained by Wong and Allen.[10] The yield of cation radicals following positive charge capture is comparable to that of anion radicals formed by electron attachment. This demonstrates that holes are just as reactive as electrons on high surface area materials.

The organic substrates on the surface are either decomposed *via* a highly excited state of the neutral molecules or *via* a dissociative capture of energetic electrons. If excitation energy transfer is the only operative process, any additional foreign material capable of competing for this energy should affect the product yield whereas if charge transfer is the only predominant mechanism, the presence of charge scavengers is expected to alter the yield accordingly.

We report in this communication on work initiated to investigate the relative importance of pure excitation energy transfer to charge transfer. For this purpose we have compared the yield of hydrogen atoms trapped on porous glass surface at 77°K from the radiolysis of water and ethane with and without an additive. The yield of stabilized hydrogen atoms has also been examined as a function of surface coverage to gain some insight into the process of self-quenching.

Experimental Section

Materials. The experimental detail has been given in a previous communication.[10] Molecular sieves such as NaX and CaY were from Linde Co. Gases (pure grade) were from Matheson Co.; liquids (research grade) were from Phillips Co. Porous Vycor glass in 1-mm plates was obtained from Corning Glass. Strips of about 5-cm length were made from the plates to fit into 4-mm o.d. esr quartz tubes. The glass strips were then pretreated in air at 650° for an extended period before being degassed at the same temperature. When the residual pressure reached 5×10^{-6} Torr, the glass samples were cooled to room temperature and adsorbates were introduced.

Irradiation. Samples were irradiated at 77°K in a Dewar containing liquid nitrogen with a cobalt-60 source operating at a dose rate of 0.679 Mrad/hr.

Spectra. The stabilized radicals on the glass surface were examined by a Varian 4500 epr spectrometer, the field dial of which was calibrated by Fremy's salt (Na_2SO_3NO), using A_N = 13 G.[11] Spin concentrations of hydrogen atoms were obtained by comparing areas of their esr signals with a known quantity of Fremy's salt adsorbed on Vycor.

Results

γ-Irradiated porous Vycor glass containing water at 77°K produces stable radicals, whose esr signals are displayed in Figure 1a. There is a pair of sharp lines separated by approximately 500 G; this doublet flanks a broad asymmetric signal shown in better detail in Figure 1b. The doublet can be easily recognized as that of the trapped hydrogen atoms, while the broad signal (Figure 1b) is identifiable as the hydroperoxyl radical ($HO_2\cdot$). Several hydrogenous materials have been used as a source for hydrogen atoms, which are trapped and observable on silica surfaces. On the other hand, we could not observe trapped H atoms on magnesium oxide or on CaY molecular sieve, and on NaX, the signal was just barely discernible after the sample was given 2 Mrads of irradiation. The results are summarized in Table I. Trapped deuterium atoms,

Table I: Doublet Splitting of Hydrogen Atoms Trapped on Surfaces at 77°K

Surface	Sorbate	Splitting, G	Line width, G
Porous Vycor	H_2O	502.0	1.50
	D_2O	76.9	1.70
	CH_4	498.8	
	CD_4	76.9	
	C_2H_6	498.8	
	HCl	503.0	
Cab-O-Sil	H_2O	505.1	1.45
Molecular sieve			
NaX	H_2O	505.1	
CaY	H_2O	No trapped H atoms observed	
	HCl	No trapped H atoms observed	
	C_2H_6	No trapped H atoms observed	
Magnesium oxide	H_2O	No trapped H atoms observed	

(6) Chemical Technology Division Annual Progress Report, May 31, 1965, ORNL-3830, p 233.

(7) P. K. Wong and J. E. Willard, *J. Phys. Chem.*, **72**, 2623 (1968).

(8) N. H. Sagert and R. W. Robinson, *Can. J. Chem.*, **46**, 2075 (1968).

(9) N. H. Sagert, J. A. Reid, and R. W. Robinson, *ibid.*, **48**, 17 (1970).

(10) P. K. Wong and A. O. Allen, *J. Phys. Chem.*, **74**, 774 (1970).

(11) M. D. Sevilla, *ibid.*, **74**, 669 (1970).

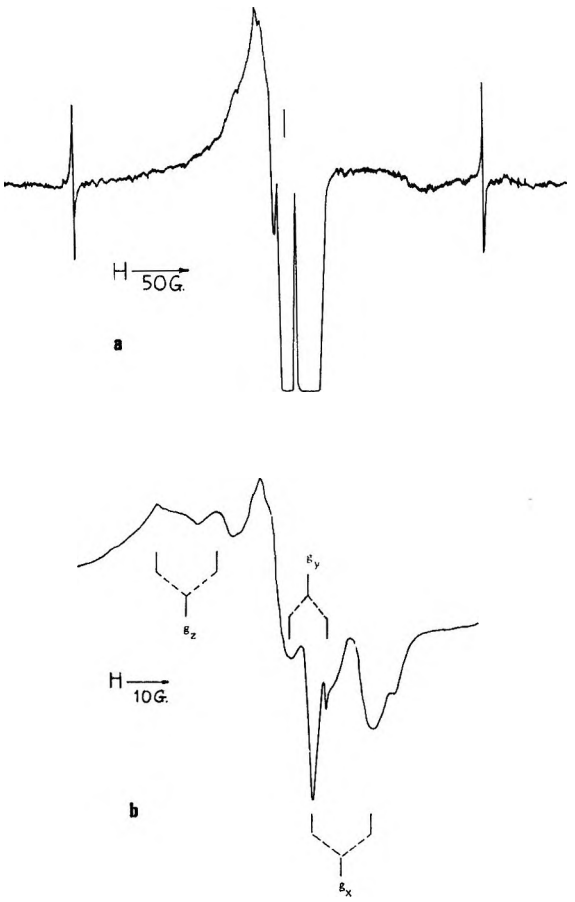

Figure 1. (a) Esr spectrum of γ-irradiated H_2O on porous Vycor glass at 77°K: dose, 0.3 Mrad. The vertical line marks $g = 2.0023$. (b) Central spectrum of (a) displayed in greater detail.

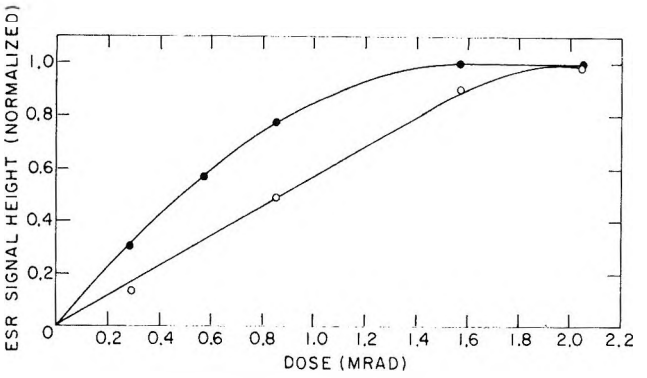

Figure 2. Growth of H and HO_2 radicals with γ dose; coverage of H_2O, 0.65.

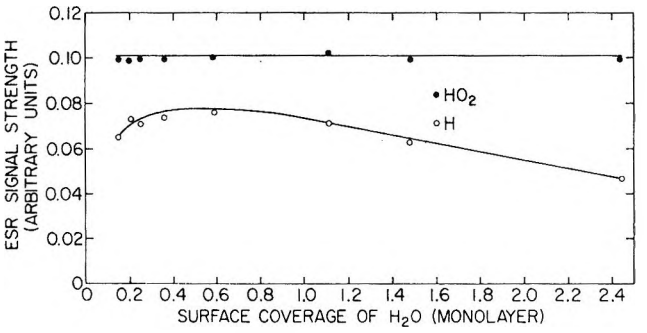

Figure 3. Relative concentration of H and HO_2 as a function of H_2O coverage: surface area of H_2O = 12 Å²; dose, 0.3 Mrad; ●, HO_2; ○, H.

produced by the radiolysis of perdeuterated methane and water, have also been observed. The line width (average of the high- and low-field lines) is approximately 1.5 G and does not seem to vary with the nature of the substrate. In Figure 2, the growth of the H atoms and HO_2 radicals produced by irradiating moisture-containing Vycor glass is plotted against total accumulated dose absorbed by the glass. Similar curves were obtained for the same species from samples containing different amounts of adsorbed water.

Since the esr line widths of the trapped H atoms and HO_2 radicals do not vary with the surface coverage of water, their signal heights can be used as a measure of their change in concentration as the water content of the Vycor is changed. Such a plot is given in Figure 3, where the ordinates are presented in arbitrary units. The water content of the Vycor is expressed in monolayers, the surface area of a water molecule being 12 Å². The HO_2 concentration is invariant up to two monolayers, whereas the H-atom concentration has a broad maximum at 0.4–0.7 monolayer and thence gradually decreases with coverage. The radiolytic yield is given in G units, or the number of radicals produced per 100 eV of radiation energy absorbed by the porous glass. The maximum yield of H atoms at a total dose of 0.3 Mrad is 0.70 G unit; at one monolayer, the G value is 0.67. Similar plots are shown in Figure 4 for ethane, cyclohexane, and 3-methylhexane (the surface areas are, respectively, 21, 46, and 54 Å²).[12] The G(H) value for ethane is 0.54, being independent of coverage from 0.1 to 1.5 monolayer. The behavior of the concentration *vs.* surface coverage curve is, however, different for different hydrocarbons. For cyclohexane, the G value of trapped H atoms drops precipitously with coverage from 0.1 to 1 monolayer, and then decreases very slowly after that. The yield of trapped H atoms from 3-methylhexane is even lower ($G \simeq 0.003$ at one monolayer). On the other hand, the rate of decrease is not as rapid as in the case of cyclohexane.

The yield of stabilized hydrogen atoms is very sensitive to the presence of charge scavengers on the surface. When a small quantity of these is added to the water, the hydrogen atom signal decreases significantly. In Figure 5, we have plotted the trapped H-atom esr signal [H_t], obtained from the radiolysis of water, as a function of charge scavenger concentration expressed as mole percentage relative to that of H_2O, which is

(12) A. L. McClellan and H. F. Harnsberger, *J. Colloid Interface Sci.*, **23**, 577 (1967).

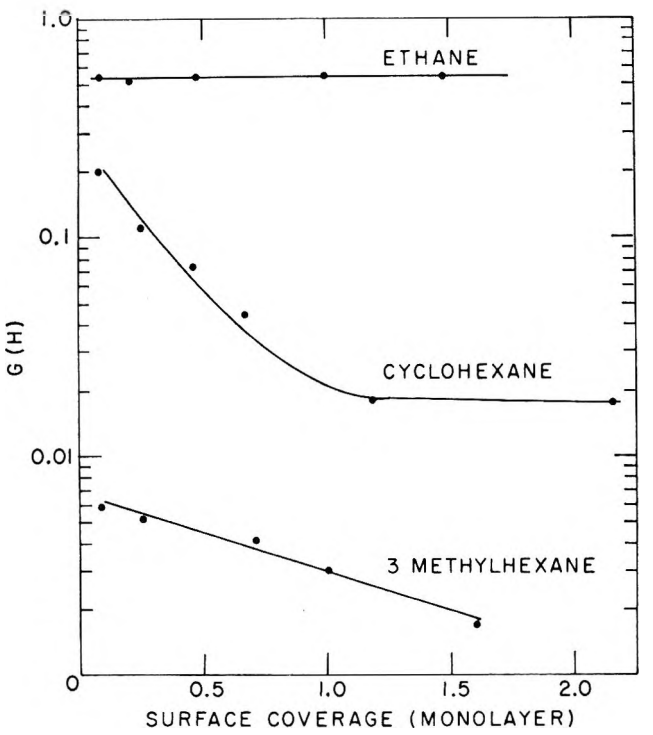

Figure 4. G(H) values from radiolysis of adsorbed ethane, cyclohexane, and 3-methylcyclohexane as a function of coverage.

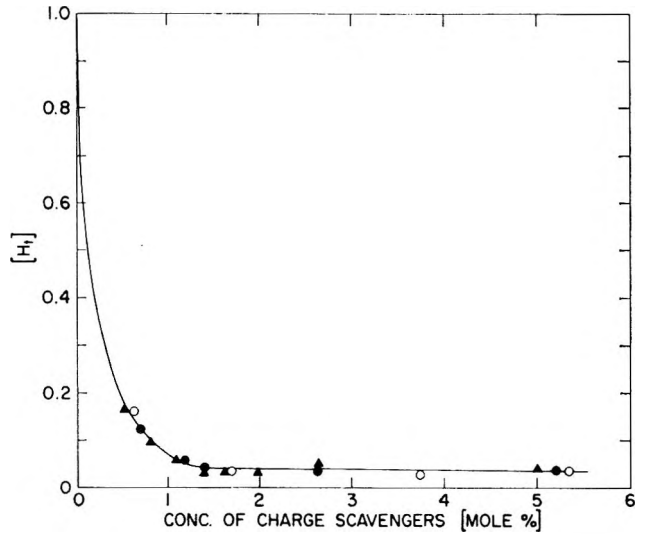

Figure 5. Relative concentration of H atoms as a function of concentration of added charge scavengers in mole % relative to water. Coverage of water fixed at 0.65: dose, 0.3 Mrad; ●, $(C_6H_5)_3N$ added; ○, TCNE added; ▲, $(C_6H_5)_2$ added.

kept constant at 0.65 monolayer. Three compounds have been used, and they are adsorbed on the porous glass prior to exposing the latter to water vapor. As shown in Figure 5, G(H) from ethane is comparable to that from H_2O, and it would be interesting to test whether charge scavengers exert a similar quantitative effect on the hydrocarbons as they do on water. Figure 6 shows the effect of added tetracyanoethylene (TCNE)

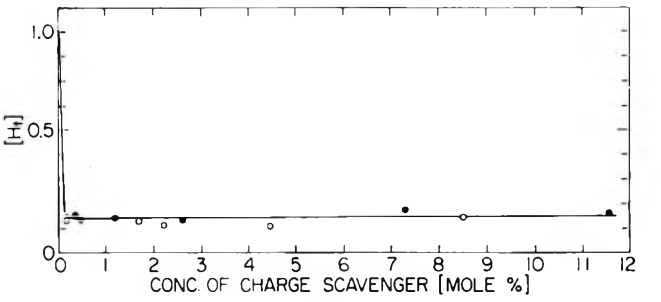

Figure 6. Relative concentration of H atoms as a function of concentration of added charge scavengers in mole % relative to ethane: coverage of ethane fixed at 0.59; dose, 0.3 Mrad; ●, TCNE added; ○, biphenyl added.

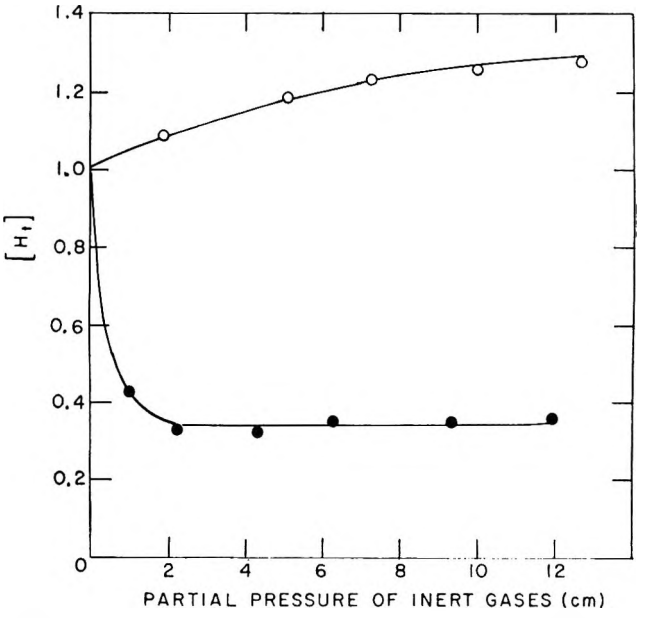

Figure 7. Relative concentration of H atoms as a function of partial pressure of inert gases: coverage of H_2O fixed at 0.65; dose, 0.5 Mrad; ○, helium; ●, argon.

and biphenyl on atomic hydrogen yield, using ethane as the source for hydrogen (coverage of C_2H_6 = 0.6 monolayer). Comparison between Figures 5 and 6 suggests that the charge scavengers used are just as effective in depressing H-atom production from water as it is from ethane.

Weakly adsorbed gases also have a discernible effect on atomic hydrogen yield. The consequence of having atomic gases co-adsorbed with water on trapped H atoms is shown in Figure 7. After water was added to the outgassed Vycor glass, it was exposed to a known pressure of either argon or helium for about 10 min, after which the sample was sealed off and irradiated. The concentration of trapped H atoms is examined as a function of partial pressures. The effect of argon is to depress the yield, while that of helium is to increase it.

As mentioned previously, the irradiation of water on Vycor produces H atoms as well as HO_2 radicals, plus other products not directly observable with the esr

technique. Hydrocarbons such as methane and ethane produce hydrogen atoms (as shown in Table I); they also produce carbon radicals whose esr signal at $g \simeq 2$ cannot be identified. They are essentially broad asymmetric lines with some structure and their yields are approximately six times larger than that of trapped H atoms.

Discussion

Identity and Location of H and D Atoms. The doublet esr signal in Figure 1a is attributable to trapped hydrogen atoms. The nuclear spin couplings for H and D (502.0 and 76.9 G, respectively) are very close to those observed in liquid matrices.[13] Moreover, the ratios (a_D/a_H) in the two cases are identical. Since the irradiated glass which contains no water or hydrocarbons does not produce any H atoms, we can safely assume that the observation is due to the radiolysis of the adsorbates. This assumption is substantiated by the fact that CD_4 and D_2O yield trapped D atoms. There is the question, however, as to whether the atomic hydrogen is stabilized in the sorbate phase or on the silica surface. To resolve this point, we consider the following observations.

(a) Hydrogen atom is observed at well below one monolayer of water or hydrocarbons, which at this coverage are unlikely to provide a suitable matrix for H atoms. Moreover, it is known that H atoms are unstable at 77°K in pure ice[14] and hydrocarbons.[15]

(b) The stability of H atoms depends on the surface. CaY molecular sieve and magnesium oxide, both of which are crystalline, cannot stabilize H atoms, although molecular hydrogen in appreciable yield has been observed on the former.[16] NaX zeolite is not nearly as good as Cab-O-Sil in this respect.

Line Widths Measurements and Satellite Lines. It is also worthwhile to compare the environments of hydrogen atoms trapped on a surface with those trapped in other matrices by making use of the information on esr line widths. In oxyacid ices, the line width (ΔH) of trapped H atoms is about 3–5 G,[14] while that produced by irradiating crystalline quartz is only 0.1 G.[17] ΔH for surface trapped hydrogen atoms is 1.5 G, suggesting that the surface provides a matrix somewhat in between a glassy and crystalline solid.

Another interesting observation is the lack of satellite lines in the esr signal of surface-trapped atoms. As a result of magnetic interaction with protons of the surrounding molecules, the H-atom doublet in γ-irradiated acidic ice exhibits satellite lines in the esr spectrum.[18a] The average distance between the H atom and the closest proton of the water molecules is estimated to be roughly 1.8 Å.[18b] Using this figure as a guide, we conclude that the H atoms are stabilized in traps on the silica surface at least 1.8 Å from the adsorbate.

Yield of Trapped H Atoms As a Function of Coverage. The yield of H atoms from water peaks at 0.4–0.6 monolayer with a maximum G value of 0.7. The molecular hydrogen yield from the radiolysis of water on porous Vycor has been studied.[6] The $G(H_2)$ value at 0.6 monolayer is about 0.4 and reaches a maximum value of 0.8 at 3.6 monolayers, after which the yield gradually decreases in a manner similar to Figure 3 in this paper. However, the $G(H)$ peaks at a surface coverage where the $G(H_2)$ is still on the rise. Since H_2 is at least partially derived from the recombination of H atoms, the decrease of $G(H)$ after 0.7 monolayer is possibly due to the increased formation of H_2 at the expense of H atoms.

The behavior of the trapped H atoms yield is not only a function of coverage alone, it also depends on the nature of the substrate. $G(H)$ is independent of ethane from about 0.1 to 1.5 monolayers, and its value of 0.54 is very much larger than that from cyclohexane and 3-methylhexane (Figure 4). However, the $G(H)$ value is strongly concentration dependent if cyclohexane and 3-methylhexane are used as substrates. When the coverage of cyclohexane increases from 0.1 to 1 monolayer, a tenfold decrease in $G(H)$ is observed, while only a twofold decrease is observed for 3-methylhexane. It would appear that we need to explain two observations here: (a) the different absolute $G(H)$ values from different hydrocarbons at the same coverage; (b) the different behavior of relative $G(H)$ with respect to coverage among different hydrocarbons. Since the C–H bond energies of the three hydrocarbons are not very different and their excitation energies are presumably similar, we will assume that the phenomena are not due to differences in energetic states, but rather to the essentially different nature of the molecules with respect to hydrogen production. The products of irradiated cyclohexane on silica gel have been studied; the main products are molecular hydrogen, cyclohexane, and bicyclohexyl, probably from the following reactions.

$$C_6H_{12}^* \longrightarrow C_6H_{11} + H \quad (1)$$

$$2C_6H_{11} \longrightarrow (C_6H_{11})_2 \quad (2)$$

$$C_6H_{12} + H \longrightarrow C_6H_{11} + H_2 \quad (3)$$

$$H + H \longrightarrow H_2 \quad (4)$$

$$C_6H_{12}^* \longrightarrow C_6H_{10} + H_2 \quad (5)$$

Thus the H-atom yield does not necessarily correlate with the H_2 yield. As a matter of fact, $G(H_2)$ is ex-

(13) R. W. Fessenden and R. H. Schuler, *J. Chem. Phys.*, **39**, 2147 (1963).

(14) (a) J. Zimbrick and L. Kevan, *ibid.*, **47**, 5000 (1967); (b) B. G. Ershov and A. K. Pikaev, *Radiat. Res. Rev.*, **2**(1), 32 (1969).

(15) D. Timm and J. E. Willard, *J. Phys. Chem.*, **73**, 2403 (1969).

(16) Chemical Technology Division Annual Progress Report, May 31, 1967, ORNL-4145, p 262.

(17) R. A. Weeks and M. Abraham, *J. Chem. Phys.*, **42**, 68 (1965).

(18) (a) D. E. Holmes, N. E. Nazhat, and J. J. Weiss, *J. Phys. Chem.*, **74**, 1622 (1970); (b) W. Kohnlein and J. H. Venable, Jr., *Nature*, **215**, 618 (1967).

pected to be much larger than $2G(H)$. Since we only followed the trapped H atoms in this work, our $G(H)$ values are accordingly lower than the $G(H_2)$ values. Examining the figures in Figure 4, the extent of the H_2 elimination (reaction 5) will have to be in the order of 3-methylhexane > cyclohexane > ethane. As the substrate molecules crowd together (*i.e.*, as the surface coverage increases), cross linking (reaction 3) becomes important, thus further decreasing the $G(H)$ value. Notwithstanding the hypothesis of the relative importance between cross linking and molecular elimination, the experimental data do point to the fact that hydrogen atom yield decreases as the molecular weight increases. For this point, the observation of Timm and Willard[15] on γ-irradiated hydrocarbons at 4°K is noteworthy. Solid methane yields trapped H atoms, while solid ethane, *n*-hexane, 3-methylpentane, and methylcyclohexane do not produce the expected hydrogen doublet in their esr spectra. This absence of trapped hydrogen atoms in irradiated organic solids is presumably due to molecular structure. When sorbed on the surface, ethane produces H atoms with a yield almost as large as that of water. On the other hand, as the coverage of 3-methylhexane increases, the molecules tend to behave in a manner similar to that in the pure solid.

Effect of Charge Scavengers. Whereas the yield of H atoms is only mildly dependent on water content of the porous glass and is independent of ethane, the addition of foreign substances greatly affects the yield. In Figure 5, we note that the effect of triphenylamine, TCNE, and biphenyl are quantitatively similar, despite the divergent nature of these compounds. At slightly more than 1 mol % of additives (with respect to water), 97% of the total H atoms are removed. When ethane is used as a source for hydrogen, the effect of the scavengers is similar (Figure 6). This effect is not due to the removal of H atoms by the added compounds, since their reactivities are different and should not scavenge hydrogen atoms to the same extent. Triphenylamine is a positive charge (hole) scavenger; TCNE is an electron trap and, as verified by us, biphenyl acts in both capacities in cyclohexane[19] as well as on Vycor glass. Therefore these compounds will scavenge either the positive charges or electrons produced by the radiation in the glass. It thus appears that to produce hydrogen atoms it is necessary to have both the positive charge (hole) and electron available to the substrate as a complementary pair. One entity that has this property is the exciton, which comprises of the hole and electron as a bound pair and is capable of long-range migration in a crystalline solid. On reaching the surface, the exciton is annihilated and the excitonic energy is transferred to the substrate which is then thrown into an excited state and subsequently decomposes. When a charge scavenger is present, the excitons are intercepted; their charge (the sign of which depends on the scavenger) is removed, and energy is no longer available to excite the hydrogenous material. This picture is based on the assumption that the charge scavengers react preferentially with the excitons. There is a conceptual difficulty in using exciton as the precursor of hydrogen atoms since they are known to exist only in crystals and their existence in glassy materials such as porous Vycor remains to be demonstrated. However, the average thickness of this material is only about 30 Å, and if there are regions of short-range order in the glass, it is not impossible for this species to be created by the action of ionizing radiation. Excitons have recently been thought to exist in γ-irradiated polymers.[20]

The Effect of Inert Gases. The first excited state of argon is 11.6 eV. If the excitonic energy is of this order of magnitude, there should be direct competition between adsorbed argon and water. This expectation is qualitatively borne out in Figure 7, in which the concentration of trapped H atoms is plotted against the partial pressure of argon. The result suggests that argon is effective in competing for 65% of the total available energy. This is a good indication that energy transfer is the operative process in producing hydrogen atoms, since argon has no known chemical affinity for this species. The effect of added helium is, however, to increase the yield by some 20%. This is unexpected since He has its first resonance excited state at 21.22 eV, which is presumably not available from the irradiated solid. This observation should be regarded as anomalous.

Other Radicals. The asymmetric nature of the esr signals displayed in Figure 1b makes unambiguous identification rather difficult. The features of the spectrum, however, run parallel to those obtained by irradiating $SrCl_2 \cdot 6H_2O$, which Catton and Symons[21] identified as due to HO_2. Their hyperfine parameters A_x, A_y, and A_z are 12.7, 6, and 17.2 G, respectively, compared to our values of 13, 10, and 14 G. The hyperfine splittings and tensorial g values vary, however, according to different methods of preparation[21] and therefore can only be used as a rough guide. One would expect that the radical from the irradiated water on Vycor surface should be HO, rather than HO_2. But the esr signal of the HO is a doublet, separated by 40 G.[22] If this radical is present on the irradiated glass, its concentration must be lower than that of HO_2 such that the signal of the former is completely masked by the latter. Kryola and Dolin[23] have examined the radicals produced from irradiated silica gel containing water. They observed an H-atom esr doublet plus a signal attributable

(19) J. K. Thomas, K. Johnson, J. Klippert, and R. Lowers, *J. Chem. Phys.*, **48**, 1608 (1968).

(20) R. H. Partridge, *ibid.*, **52**, 2491 (1970).

(21) R. C. Catton and M. C. R. Symons, *J. Chem. Soc., A*, 1393 (1969).

(22) J. Kroh, B. C. Green, and J. W. T. Spinks, *Can. J. Chem.*, **40**, 413 (1962).

(23) Z. L. Kryola and P. I. Dolin, *High Energy Chem.*, **3**, 133 (1969).

to OH radicals. The concentration of H atoms, however, decreased with increasing amount of adsorbed water. When a sample of silica gel was heated at 700° under oxygen, followed by evacuation at 500°, and then irradiated at 77°K to a total dose of 25×10^{19} eV/ml, $G(H)$ was found to be 0.005 (using 2 for the density of the gel). When 0.5 monolayer of water was present, $G(H)$ was below 0.002. These authors attributed the production of hydrogen atoms to O–H bond scission of surface hydroxyls

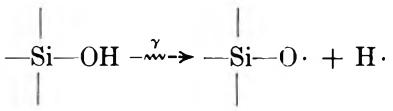

When water was added prior to the irradiation, the $\geqslant$Si–O· signal was replaced by a hydroxyl radical (OH) signal, and the H· signal was diminished as a result of their interaction with adsorbed water. The features of the OH signal vary, depending on the pretreatment of the gel. We have undertaken similar work on pure fused silica (Cab-O-Sil) but could not find the evidence of any OH radicals being produced, nor could we find the $\geqslant$Si–O· signal from irradiated Vycor that had been dehydrated. In terms of these results, it seems that hydrogen atoms are produced on silica gel samples prepared by Kryola and Dolin *via* a mechanism different from that on porous Vycor. It is noteworthy that the maximum $G(H)$ on silica gel (0.002) is smaller than that on Vycor glass by three orders of magnitude. The condensate from electron irradiated water vapor has also been examined.[24] An asymmetric signal was found to react with $C(NO_2)_4$, forming NO_2 observable by esr spectroscopy. The growth of H and HO_2 with respect to γ dose is shown in Figure 2. The different growth rate suggests that the two radicals may be produced by different processes. Moreover, the HO_2 radical yield is much larger than that of H atoms, although the difference in thermal stability may be a contributing factor. In Figure 3, we also note that the yield of HO_2 is quite independent of water content. When dehydrated over 400°, the surface of the silica contains isolated silanol groups ($\geqslant$Si–OH) and siloxyl groups ($\geqslant$Si–O–Si$\leqslant$). Added water molecules are physisorbed rather than rehydroxylating the surface.[25] When γ-irradiated, the Si–O–Si could react with the water molecules in the following manner.

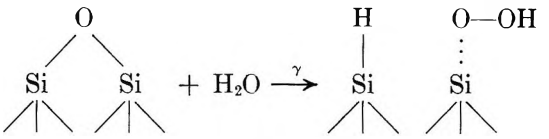

The existence of a reactive silica surface generated by γ rays has been suggested in two previous publications. γ-Irradiated silica–alumina when contacted with CO and SO_2 yields, respectively, CO_2^- and SO_3^-, apparently the consequence of O^- attachment to the additives.[26] When preirradiated silica gel is exposed to CO_2,[27] O_2^- is detected.

We have mentioned that although irradiated methane and ethane on porous Vycor produces hydrogen atoms, no alkyl radicals have been observed. There is no question as to the stability of alkyl radicals on Vycor surface, since CH_3 and C_2H_5 have been produced by the photolysis of CH_3Br[28] and the radiolysis of C_2H_5I.[29] The carbon radicals produced by the radiolysis of CH_4 and C_2H_6 cannot be positively identified by their featureless esr spectra. Their general profile is quite similar to the methoxy and ethoxy radicals,[30] which could be generated by a process analogous to one that produces HO_2

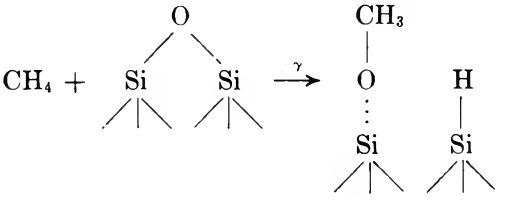

Acknowledgment. The author wishes to thank Dr. A. O. Allen for his encouragement throughout this work and his constructive criticism of the manuscript.

(24) P. Wardman and W. A. Seddon, *Can. J. Chem.*, **47**, 2149 (1969).

(25) M. L. Hair and A. M. Filbert, *Res./Develop.*, **20**, 34 (1969).

(26) R. R. Hentz and D. K. Wickenden, *J. Phys. Chem.*, **73**, 817 (1969).

(27) P. K. Wong and J. E. Willard, *ibid.*, **73**, 2226 (1969).

(28) (a) J. Turkevich and Y. Fujita, *Science*, **152**, 1619 (1966); (b) H. D. Gesser, B. Garbutt, and A. Cohen, *ibid.*, **154**, 381 (1966).

(29) Unpublished work by the author.

(30) (a) P. J. Sullivan and W. S. Koski, *J. Amer. Chem. Soc.*, **85**, 384 (1963); (b) P. J. Sullivan and W. S. Koski, *ibid.*, **86**, 159 (1964).

Study of the Low-Temperature Hydrogenation of Ethylene on Zinc Oxide by Temperature-Programmed Desorption[1]

by A. Baranski[2a] and R. J. Cvetanović*[2b]

Division of Chemistry, National Research Council of Canada, Ottawa, Canada *(Received May 5, 1970)*

Publication costs assisted by the National Research Council of Canada

The temperature-programmed desorption technique has been used to study the chemisorption of ethylene and hydrogen and the catalytic hydrogenation of ethylene on zinc oxide at low temperatures (0° and lower). At these low temperatures ethylene is normally chemisorbed almost exclusively as a weakly bound form (probably π complexed), with a heat of adsorption of about 4 to 6 kcal/mol. Another form of adsorbed ethylene is also observed, but it is formed in much smaller amounts and, unlike the first, is not hydrogenated at 0° and lower temperatures. Rates of hydrogenation of presorbed ethylene have been determined and an activation energy of 10 kcal/mol has been obtained. Five forms of chemisorbed hydrogen on ZnO have been observed at adsorption temperatures between about −70 and +300°. Only the form which is desorbed first, presumably the least strongly chemisorbed hydrogen, reacts readily with ethylene at low temperatures.

Introduction

Catalytic hydrogenation of ethylene on zinc oxide has been recently thoroughly investigated by two research groups. Teichner and coworkers[3,4] have studied the reaction in the temperature range between about 100 and 400° and found considerable complexities, such as variations in the reaction order and activation energies and poisoning by ethylene residue on the catalyst. Kokes and his collaborators,[5-9] on the other hand, have found that catalytic hydrogenation of ethylene on zinc oxide at room temperature is remarkably simple, agreeing in this respect with the previous similar observations of Burwell, *et al.*,[10,11] with chromia.

Hydrogenation of ethylene on zinc oxide is a classical catalytic reaction of considerable fundamental importance. It was therefore thought of interest to apply the temperature-programmed desorption (TPD) technique, recently developed in this laboratory,[12] to the $ZnO–H_2–C_2H_4$ systems in the hope that additional information may be obtained. The results are reported in the present paper. The main emphasis has been on the processes which occur at close to room temperature, although some experiments have dealt also with the effects of the higher and lower adsorption temperatures.

Experimental Section

The apparatus used for the temperature-programmed desorption (TPD) experiments has been described in previous papers from this laboratory.[12] Gas adsorbed on the zinc oxide sample was desorbed by linearly raising the temperature into the stream of the carrier gas, where it was monitored by means of a thermistor detector and recorded as a "TPD chromatogram." The rate of temperature increase, β, was generally between 10 and 20°/min and was kept constant in each experiment. Uniformity of β was important since abrupt departures from a uniform temperature increase could cause distortion of chromatograms and even an appearance of false desorption peaks. A small correction (6° at a β of 12°/min) for the temperature lag in the catalyst sample was determined in a separate experiment and was applied to all TPD data. Helium was used as the carrier gas in the TPD experiments involving desorption of ethylene while nitrogen was used in experiments involving desorption of hydrogen. The flow rate of the carrier gas was about 1 l./min at a pressure of about 30 Torr. Assuming the catalyst bed volume to be approximately 1 cc, the residence time was about 0.06 sec.

Kadox 25 zinc oxide of the New Jersey Co. was used as the catalyst in view of the detailed kinetic study with the same catalyst by Kokes and coworkers.[5-9] It was formed into pellets about 6 mm in diameter, 3 to 5 mm

(1) Issued as NRCC No. 11750.

(2) (a) Department of Inorganic Chemistry, Jagellonian University, Cracow, Poland; NRCC Postdoctorate Fellow; (b) to whom correspondence should be addressed.

(3) (a) J. Aigueperse and S. J. Teichner, *Ann. Chim.* (Paris), **7**, 13 (1962); (b) J. Aigueperse and S. J. Teichner, *J. Catal.*, **2**, 359 (1963).

(4) (a) F. Bozon-Verduraz, B. Arghiropoulos, and S. J. Teichner, *Bull. Soc. Chim. Fr.*, 2854 (1967); (b) F. Bozon-Verduraz and S. J. Teichner, *J. Catal.*, **11**, 7 (1968).

(5) W. C. Conner, R. A. Innes, and R. J. Kokes, *J. Amer. Chem. Soc.*, **90**, 6858 (1968).

(6) W. C. Conner and R. J. Kokes, *J. Phys. Chem.*, **73**, 2436 (1969).

(7) A. L. Dent and R. J. Kokes, *ibid.*, **73**, 3772 (1969).

(8) A. L. Dent and R. J. Kokes, *ibid.*, **73**, 3781 (1969).

(9) A. L. Dent and R. J. Kokes, *J. Amer. Chem. Soc.*, **91**, 7207 (1969).

(10) R. L. Burwell, Jr., A. B. Littlewood, M. Cardew, G. Pass, and C. T. H. Stoddard, *ibid.*, **82**, 6272 (1960).

(11) A. B. Littlewood and R. L. Burwell, Jr., *ibid.*, **82**, 6287 (1960).

(12) R. J. Cvetanović and Y. Amenomiya, *Advan. Catal.*, **17**, 103 (1967).

high, and of average weight of about 0.3 g per pellet. Samples of three to six pellets, *i.e.*, 1.1 to 1.7 g, were used.

Fresh catalyst samples were treated with 150 to 200 Torr of oxygen or in dry air at 1 atm for 1 hr at 400° to oxidize any organic contamination. The samples were then outgassed at a selected temperature for 1 hr, if not otherwise stated, using a diffusion pump to remove the desorbed gas. When the outgassing was carried out at 350° and higher temperatures, a deposit of zinc was observed on the walls of the reactor. This deposit was subsequently moved away from the reactor by careful heating with a torch. Two experiments, in one of which this deposit was intentionally made to distil toward the ZnO sample and in the other away from it, showed no significant differences in adsorption and TPD experiments.

Two general outgassing procedures of the ZnO samples were used. In the standard procedure, the sample was outgassed while it was heated to a selected temperature, t_{outg}, and then for a further hour at this temperature. In the second procedure, used for some series of experiments in the hydrogenation of preadsorbed ethylene, the outgassing for the first experiment was carried out in the standard manner at a selected t_{outg} but before each of the subsequent experiments the outgassing was done at 200° for 1 hr. This procedure was adopted to minimize variations in catalyst activity and will be later referred to as the "second outgassing procedure."

Surface area of the ZnO catalyst was determined by the BET technique with nitrogen at −196°. Areas of 8.3 and 8.6 m^2/g were obtained for two samples exposed to highest temperatures of 400 and 380°, respectively. The former was determined after three and the latter after a series of eight experiments. These values are to be compared with 8.2 m^2/g obtained by Amberg and Seanor[13] for a sample exposed to 400°, and with 9.6 m^2/g obtained by Dent and Kokes[7] for a Kadox 25 ZnO sample exposed to 450° and 5–6 m^2/g for the same catalyst after prolonged treatment with oxygen at 500°. For fresh catalyst a value of 10 m^2/g is quoted commercially. When ZnO samples are exposed to higher temperatures, they tend to sinter. A sample of ZnO outgassed at 600° for 1 hr was visibly sintered and showed decreased capacity for ethylene adsorption.

Chromatographic analysis of ethylene and the products of its hydrogenation were made on a Porapak Q column and quantitative determinations of C_2H_4 and C_2H_6 were based on daily calibrations. In some cases the analysis for C_2H_4 and C_2H_6 was done on a 2% squalane modified alumina column. CO_2 and H_2O were observed qualitatively on the Porapak Q column.

In the determination of the material balance of ethylene, use was made of a solid nitrogen trap for its recovery. Corrections were made where necessary for the finite vapor pressures of ethylene (2×10^{-3} Torr) and ethane (3×10^{-4} Torr) at −196°.

Phillips 66 research grade ethylene was degassed at −196° and distilled twice from an acetone–Dry Ice bath. Matheson ultrahigh-purity hydrogen was used for the chemisorption and the ethylene hydrogenation experiments. Oxygen was obtained by thermal decomposition of $KMnO_4$.

Matheson ultrahigh-purity helium was used as the carrier gas after passage through a molecular sieve and a liquid nitrogen trap before the reactor. In the TPD experiments with chemisorbed hydrogen Matheson prepurified nitrogen was used as the carrier gas, again after passing through a molecular sieve and a liquid nitrogen trap.

Results

Blank Experiments with Zinc Oxide. Zinc oxide outgassed at a temperature (t_{outg}) of 400 or 450° for up to 6 hr gave a very broad TPD peak, extending from approximately t_{outg} + 30° to 750–800°. The desorption products collected in a trap behind the detector were CO_2 and H_2O. With a liquid nitrogen trap between the reactor and the detector, no TPD peaks were observed, showing absence of noncondensable products. These results are consistent with a ZnO surface strongly saturated with water vapor, in agreement with the data in the literature.[14]

Adsorption of Ethylene on Zinc Oxide. In an attempt to establish whether only one or more than one surface species is formed when ethylene is adsorbed at room temperature on outgassed ZnO, a number of TPD experiments were carried out.

After the outgassing of the ZnO sample at a higher temperature (t_{outg} = 350 to 500°) and cooling to room temperature, a known amount of ethylene was admitted at room temperature, usually for a period of 15 min, at a pressure between 0.05 and 1 Torr. Excess ethylene vapor, including ethylene which is desorbed from the surface at room temperature under these conditions, was frozen over for 30 min into a liquid nitrogen trap and measured. Ethylene retained on the catalyst was calculated by difference. However, when only a small amount of ethylene was admitted to the outgassed sample and its pressure decreased below the saturation pressure at −196° (2×10^{-3} Torr), no attempt was made to remove any ethylene vapor and the total amount admitted was regarded as adsorbed.

With larger amounts of ethylene adsorbed, only a single TPD peak was observed. With small amounts adsorbed, TPD commenced at room temperature or, in a few cases, at 0°, gave more complex chromatograms which were of two general types, as shown in Figure 1. Their characteristic features were a main peak A with a

(13) C. H. Amberg and D. A. Seanor, Proceedings of the Third International Congress on Catalysis, Amsterdam, July 20–25, 1964, p 450.

(14) M. M. Egorov, N. N. Dobrovol'skii, V. F. Kiselev, G. F. Furman, and S. V. Khrustaleva, *Zh. Fiz. Khim.*, **39**, 3070 (1965); *Russ. J. Phys. Chem.*, **39**, 1639 (1965).

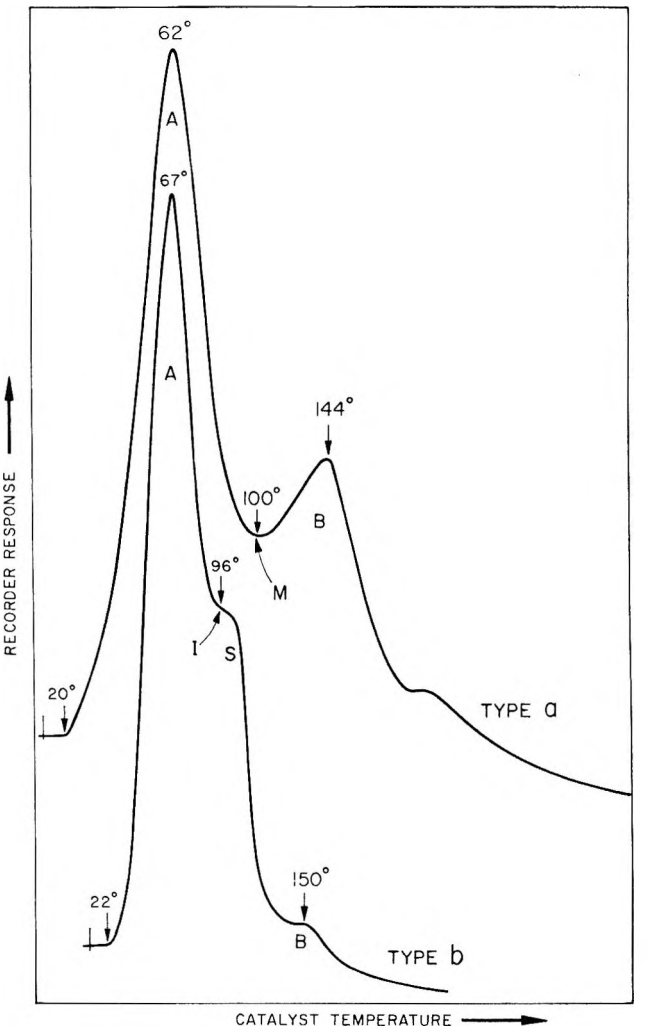

Figure 1. Examples of typical TPD chromatograms of ethylene presorbed on ZnO at 23°, type a (upper) and type b (lower) chromatograms.

smaller peak B and a minimum (M) separating the two (type a), or a shoulder (S) on peak A, marked by an inflexion point (I) (type b). The rate of temperature increase, β, was between 10 and 14°/min in the 27 TPD experiments carried out. The peak temperatures were approximately constant, and their mean values were: A (65 ± 3°) and 52°, for TPD commenced at 25 and 0°, respectively, B (141 ± 5°), I (97 ± 5°), and M (110 ± 8°). The indicated deviations are the probable deviations for a single experiment for all chromatograms which show the particular characteristic feature. It is possible that S and I are masked when B is well developed. Similarly, when A is very large, it is the only peak observed. Development of various features appears to depend on the outgassing of ZnO. With samples outgassed at and above 450° type a chromatograms (Figure 1) are considerably more frequent while with ZnO samples outgassed below 450° type b is more frequent. The temperature and duration of the outgassing of ZnO affect also to some extent the total amount of C_2H_4 retained on the ZnO surface, as shown in Table I. In blank TPD experiments in which no ethylene was adsorbed on ZnO samples outgassed for example at 450° for 5 to 6 hr no TPD peaks appeared up to a temperature approaching 500°. In general, no TPD peaks appeared in blank experiments up to a temperature close to t_{outg}.

Table I: Effect of Temperature and Duration of the Outgassing of ZnO on the Amount of C_2H_4 Retained on the Surface after Adsorption at 23 to 24° for 15 min and Removal of the Vapor at the Same Temperature by Freezing over for 30 min into a Trap at −196°

	ZnO —outgassing—		Adsorbed ethylene	
	Temp,	Time,	—(10^4 × cc (NTP)/g ZnO)—	
Experiment	°C	hr	Individual expt	Mean
9_1, 9_2, 12_1, 12_2, 12_3	350	1	90, 91, 63, 86, 86	83
7, 8_1, 8_3, 8_4, 8_5[a]	400	1	100, 91, 100, 96, 83[a]	
5[b]	400	1	94	96
6[b]	400	8	93	
2	450	5	162	162

[a] Adsorption in darkness. [b] After outgassing at 400° for the indicated time, the temperature was linearly increased to 600° in the course of about 10 min.

After temperature-programmed desorption of ethylene, only ethylene was found in the trap behind the detector, with only very rarely some water and CO_2 as well. The shapes of the TPD peaks were not affected when a Dry Ice–acetone trap was interposed between the reactor containing the ZnO sample and the detector. However, no peaks appeared when a liquid nitrogen trap was used instead.

The material balance of ethylene was determined with ZnO samples outgassed at 350 and 450° and with the adsorbed amounts of ethylene as high as 0.7 and as low as 0.0019 cc (NTP). For eight such experiments the mean material balance of ethylene was 99.7 ± 1.0%, with the probable error in a single experiment of somewhat less than 3%. In four of these experiments (with ZnO outgassed at 450°) B peak was well developed and the B/A ratio was between 0.4 and 1.2. The good material balance of ethylene and the fact that only ethylene was recovered by TPD show that both peaks A and B are desorbed as ethylene.

From these results it may be concluded that ethylene adsorbed on ZnO at room temperature forms at least two kinds of "complexes" (surface species). They will be referred to as A and B adsorbed ethylene or, for brevity, simply as ethylene A and B. Since ethylene B and the shoulder peak S were generally much smaller than ethylene A, they were distinctly observable only at small total adsorptions. Under these conditions maximum detector sensitivity was used and the quality of the TPD chromatograms was much poorer since the

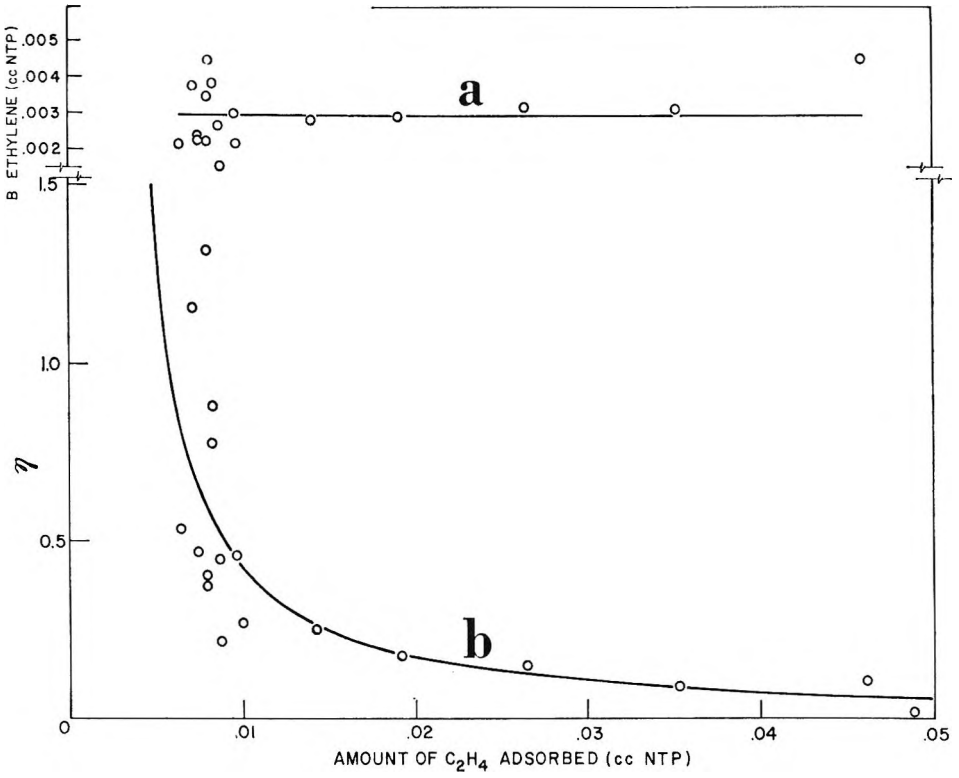

Figure 2. (a) The total amounts of (B + S) ethylene and (b) the ratios η of (B + S) to A ethylene as a function of the amount of ethylene adsorbed.

effects of base line drifts and occasional detector instability became appreciable. Furthermore, the extensive overlapping of the peaks made quantitative evaluation difficult. To obtain an approximate idea of the potential importance of B and S, we have grouped them together and evaluated the ratio η of B (including S) to A ethylene from the respective TPD peak areas by drawing vertical lines through the inflexion point (I), when present, or through the minimum (M) between A and B. It is clear that this method of evaluation is only very approximate, and it is indeed possible that B and S may be appreciably smaller than thus assessed. Moreover, there was some loss of A in the stream of the carrier gas during the period of base line stabilization before TPD. Nevertheless, the procedure used gave an upper limit of η and from it and the total amount of C_2H_4 adsorbed an upper limit of the amount of B ethylene formed in a number of experiments was calculated.

Different amounts of C_2H_4 (not smaller than 0.006 cc (NTP)) were adsorbed at 0° or at room temperature on a ZnO sample outgassed at 450°. The values of B (*i.e.*, B + S) and of η are plotted in Figures 2a and b, respectively. The amount of B ethylene is seen to be approximately constant and quite small, averaging 0.0026 ± 0.0005 cc (NTP) C_2H_4/g of ZnO. However, it should be remembered that the values of η and B in Figure 2 represent only upper limits, as already pointed out. In these experiments, with the standard outgassing of ZnO at 450°, no effect of the biography of the sample on the amount of B ethylene is evident. On the other hand, in a series of experiments with the "second outgassing procedure" (described in the Experimental Section) the amounts of B ethylene were consecutively 0.0020, 0.0017, 0.0017, 0.0012, 0.0009, and 0.0009 while A ethylene declined only from about 0.0050 to 0.0040 cc (NTP)/g of ZnO; *i.e.*, there was a considerably greater percentage decline in the amount of B ethylene. In each experiment in this series, after the catalyst evacuation, 0.5 Torr of C_2H_4 was introduced into the reactor at room temperature about 3 hr prior to TPD.

The amount of ethylene retained on the ZnO surface was much larger when adsorption was carried out at temperatures substantially below 0°. In four such experiments C_2H_4 was adsorbed at 6 Torr, and its excess was removed by freezing over for 30 min into a liquid nitrogen trap. At −68°, for example, 0.52 cc (NTP) C_2H_4/g of ZnO was retained on the surface and subsequent TPD, commenced at −60°, gave a single very broad peak at −12°. A 250 times lower detector sensitivity had to be used to record the peak and B ethylene was not observable. For a surface area of the ZnO sample of 8 m^2/g and taking the cross section of ethylene molecule as 23 $Å^2$, the surface coverage for A ethylene would be 0.40. Assuming a level of B comparable to that shown in Figure 2, the corresponding coverage of B ethylene would be only about 0.002.

Hydrogenation of Preadsorbed Ethylene. Rates of

hydrogenation at 0° of ethylene presorbed on ZnO were measured by determining the amount of ethane formed at a given hydrogen pressure (p_{H_2}) and reaction time (t). The expected rate expression is

$$-dE/dt = k \cdot E \cdot f(p_{H_2}) \quad (1)$$

or, at constant p_{H_2}

$$\frac{1}{t} \log \frac{E_i}{E_i - (C_2H_6)} = \frac{k}{2.3} f(p_{H_2}) \quad (2)$$

where E_i and E are, respectively, the amounts of ethylene adsorbed initially and remaining on the surface at time t and $f(p_{H_2})$ is the functional dependence of the rate on p_{H_2}.

The same sample of ZnO catalyst was used in all experiments, and its amount was 1.35 g and the BET surface area 8.6 m^2/g. Before each experiment it was outgassed for 1 hr at 350° *in vacuo*, cooled down to 0°, a known amount of ethylene (between 0.04 and 0.08 cc (NTP)) was adsorbed as described earlier, and the required amount of hydrogen (between 1 and 53 Torr) was admitted. The reaction time was 10 min with the exception of two experiments in which it was about 30 min. After the reaction, hydrogen was removed (at 0°) gradually through a solid nitrogen trap in about 30–60 sec, half of which time was added to the reaction time. Outgassing through the solid nitrogen trap was continued for 30 min, and the condensed ethylene and ethane were measured manometrically and analyzed by gc. Additional ethane was found when the ZnO sample was subsequently subjected to TPD up to 250 to 350° and the products were collected and analyzed. However, this amount of ethane was not added to that collected before TPD because, as expected,[15] special experiments showed that ethane adsorption on ZnO was negligible at the partial pressures of interest and the additional ethane was therefore formed during TPD, presumably by reaction of ethylene with hydrogen on the surface which was not removed by outgassing for 30 min at 0°.

The best straight line plot of eq 2 with zero intercept, shown in Figure 3, was obtained for $f(p_{H_2}) = p_{H_2}^{1/2}$. The least-squares value of the slope gives $k = 1.2 \times 10^{-4}$ sec^{-1} $Torr^{-1/2}$ (g ZnO)$^{-1}$ or $k = 1.3 \times 10^{-5}$ sec^{-1} $Torr^{-1/2}$ m^{-2}, with the probable error[16] of about 4%. Individual rate constants, calculated from eq 2, showed random scatter independent of the experimental sequence, showing absence of an ethylene poisoning effect.

Hydrogenation at lower temperatures was investigated between −20 and −78°, at conversions of ethylene between 2 and 14%. The "second outgassing procedure" of ZnO, described in the Experimental Section, was used. The general procedure for the reaction and analysis was the same as outlined above with the exception that the reaction times were longer (20 min at −20°, 35 min at −40°, 40–50 min at −78°) and after the removal of the gas phase at the reaction temperature, the catalyst was warmed up to 0° and outgassed through the solid nitrogen trap for 30 min.

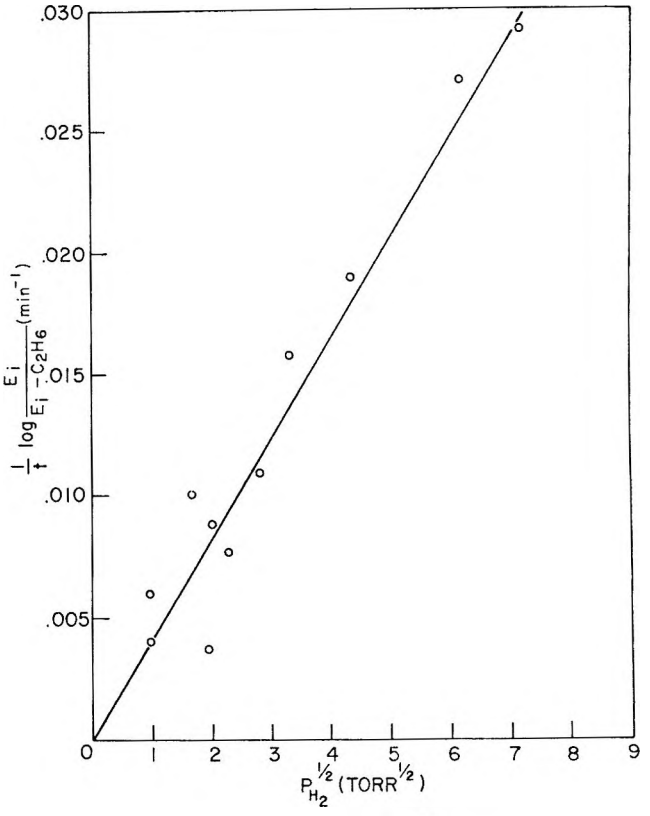

Figure 3. Plot of eq 2, with $f(p_{H_2}) = p_{H_2}^{1/2}$, for hydrogenation at 0° of ethylene presorbed on ZnO.

From the series of eight experiments at 0° and the data at −20 and −41° the Arrhenius plot in Figure 4 was obtained and the least-squares value of the slope gave an activation energy of 10.4 ± 0.2 kcal/mol.

The rate constants at −73 and −78° were found to be an order of magnitude greater than expected from the linear Arrhenius plot in Figure 4. Addition of helium (filled points) to ensure adequate cooling of the catalyst to the bath temperature and its subsequent removal before admitting hydrogen had only a slight effect on the results. The reason for these larger rates therefore remains unknown, although the reactions are slow at these low temperatures and the experimental error is larger.

After extensive hydrogenation of presorbed ethylene, the TPD chromatograms obtained (at β from 11 to 15°/min) starting from 0° consisted of small single peaks at about 57° with pronounced tailing extending on the average to about 150°. This shows that A ethylene is readily hydrogenated but, since it would appear that the tailing represents largely B and S eth-

(15) W. E. Garner and J. F. Veal, *J. Chem. Soc.*, 1487 (1935).

(16) H. Margenau and G. M. Murphy, "The Mathematics of Physics and Chemistry," Van Nostrand, Princeton, N. J., 1951, pp 493–502.

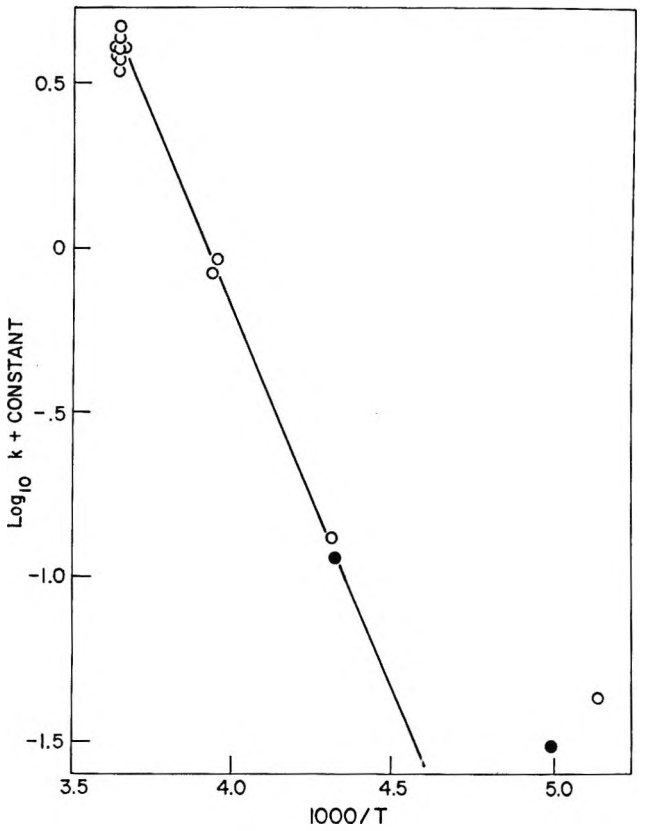

Figure 4. The Arrhenius plot of the rates of hydrogenation of ethylene presorbed on ZnO. Filled circles indicate experiments with helium added (and subsequently removed before the admission of hydrogen) to ensure faster cooling of the catalyst to the bath temperature prior to the reaction.

ylene, the question arises whether these forms of adsorbed ethylene are also hydrogenable at room and lower temperatures. Special experiments carried out indicate that they are not. Thus, in a series of three experiments, hydrogenation was done (for 125 min at 23°, 14.5 Torr of H_2 and 0.0090 cc (NTP) of preadsorbed C_2H_4) in the middle experiment only and subsequent TPD (from 0°) showed the ratio η = (B + S)/A to be about 14 in contrast to the usual values of 0.1 to 1 under comparable conditions. Moreover, the calculated amount of (B + S) ethylene was 0.0018 cc while in the first and the third experiment it was 0.0027 and 0.0015 cc, respectively. Since in these experiments the "second outgassing procedure" of ZnO was used, the amount of ethylene (B + S) in the middle experiment, if it is not hydrogenated, would be expected to have an intermediate value, as observed. The material balance in the middle experiment showed that of the 0.0090 cc of the initially presorbed ethylene 0.0054 cc C_2H_6 and 0.0013 cc C_2H_4 were collected before TPD and TPD gave 0.0018 cc (B + S) and 0.0001 cc ethylene A. Ethylene (B + S) was evidently not hydrogenated to any extent.

It should be pointed out that although ethylene (B + S) does not appear to be hydrogenated at room temperature, it does not normally interfere with the reaction at room or lower temperatures because ethylene A is formed in much larger amounts. For example, in the hydrogenation experiments described above, ZnO samples outgassed at 350° were used and (B + S) was only a small fraction of A ethylene (an estimated upper limit is 6%).

Rates of Desorption of Ethylene A. The rate constants of desorption (k_d) of ethylene adsorbed on ZnO were determined at 0 and −28° from the expression

$$k_d = \frac{2.3}{t} \log \frac{E_i}{E_i - E_{des}} \qquad (3)$$

where E_i is the initial amount of ethylene A adsorbed and E_{des} is the amount of ethylene desorbed at time t.

At −28° ethylene presorbed on ZnO surface was outgassed by means of a diffusion pump for five 30-min intervals, and the desorbed vapor was collected in a solid nitrogen trap and measured after each interval. After fifth interval the residual ethylene A on the surface was determined by TPD. In this way it was possible to evaluate E_i at the beginning of each interval and to calculate k_d from eq 3. The mean of five determinations was $k_d = 8.7 \pm 0.3 \times 10^{-5}$ sec^{-1}. Seven experiments at 0° gave $k_d = 2.1 \pm 0.3 \times 10^{-4}$ sec^{-1}. The two values give 4.2 kcal/mol for the activation energy of desorption of ethylene. This is only an approximate value in view of the small temperature interval and the fact that it is based on k_d values at two temperatures only.

Adsorption of Hydrogen on ZnO. For the TPD experiments with hydrogen, the ZnO sample was outgassed for 1 hr at 450° and brought to the desired temperature for hydrogen adsorption. The conditions used for adsorption of hydrogen and its outgassing before TPD and the rates of temperature increase in TPD (β) are summarized in Table II.

Experiments H_1 to H_{18} inclusive were done with a ZnO sample which had been used previously in about 40 other experiments (involving adsorption of ethylene, etc.) The first trial experiment in this series, H_1, is not included in Table II because the chromatograms were not suitable for quantitative evaluation. (Similarly, the blank experiment, H_{13}, is not listed in the table.) In other experiments the total amount of hydrogen released by TPD was evaluated by comparing the peak areas in the chromatograms with that of a known standard of H_2 run immediately after the TPD. The chromatograms generally consisted of more than one peak, as will be seen further below, and the amounts corresponding to the individual peaks have been evaluated approximately by drawing vertical lines through the minima between the peaks. These amounts are also listed in Table II, but it must be emphasized that in many cases they are only very approximate because of an extensive overlapping of the peaks.

The TPD chromatograms of hydrogen presorbed on ZnO at room temperature are shown in Figure 5. Be-

Table II: Summary of TPD Experiments with Adsorbed Hydrogen

Expt no.	ZnO sample	Adsorption of H_2: Temp, °C	Pressure, Torr	Time, hr	H_2 outgassing before TPD: Temp, °C	Time, min	H_2 adsorbed, cc (NTP): Ia	Ib	II	III	IV	Total	β, deg/min
H_2	14[a]	23	18.0	1	−58	15	0.026	0.064				0.090	15
H_3	14[a]	23	19.9	15.2	−58	15	0.011	0.082				0.093	14
H_4	14[a]	23	19.0	17.8	23	40			0.028			0.028	20
H_5	14[a]	23	19.2	1	23	40			0.015			0.015	14
H_6	14[a]	23	19.5	0.05	−56	15	0.021	0.031				0.054	11
H_7	14[a]	23	18.2	0.05	23	40			0.004			0.004	16
H_8	14[a]	23	199.4	15	−71	15		0.119				0.119	14
H_9	14[a]	23	206.4	16	23	80			0.053			0.053	14
H_{10}	14[a]	−51	178.8	1	−50	15		0.083				0.083	14–17
H_{11}	14[a]	200	209.5	1.42	−50	15	0.031	0.023	0.034	0.096		0.184	20
H_{12}	14[a]	−51	180.4	4	23	40			0.024			0.024	20
H_{14}	14[a]	−62	176.0	0.33	23	40			0.020			0.020	20
H_{15}	14[a]	23	19.7	1	23	300			0.014			0.014	15
H_{16}	14[a]	−69	201.7	0.33	23	40			0.012			0.012	21
H_{17}	14[a]	300	204.5	1.5	−50	15	0.061	0.030	0.029	0.040	0.098	0.258	18–24
H_{18}[b]	14[a]	23	17.1	1.1	23	40			0.020			0.020	22
H_{19}	14s[c]	300	181.7	1.33	−50	15				0.027	0.034	0.061	18
H_{20}	14s[c]	300	204.3	1.5	−50	15				0.030	0.034	0.064	10–20
H_{21}	14s[c]	23	192.7	1	−50	15			0.018			0.018	19
H_{22}	14s[c]	23	205.8	1.5	−50	15			0.017			0.017	15–16
H_{23}	14s[c]	−67	206.8	1.11	−67	15		0.003	0.005			0.008	16–19
H_{24}	14s[c]	200	193.4	1.5	−67	15			0.003	0.032		0.035	18–20
H_{25}	14s[c]	100	209.7	1.5	−67	15			0.008	0.024		0.032	20
H_{26}	15[d]	23	188.9	1	−50	15		0.150			0.028	0.178	20–22
H_{27}	15[d]	300	200.3	1	−68	15	0.059	0.029	0.021	0.058	0.041	0.208	17–22
H_{28}	15[d]	23	191.7	1.42	23	40			0.049		0.023	0.072	21

[a] 1.14 g of ZnO sample no. 14. [b] Experiment with D_2 instead of H_2. [c] The same ZnO sample as in the series H_1 to H_{18} but sintered as described in the text. [d] 1.21 g of ZnO, activated as described in the text.

fore TPD, hydrogen was evacuated either at about −60° (runs H_2, H_3, H_6, H_8) or at room temperature (runs H_4, H_5, H_7, H_9). In the former case two peaks are evident, I and II, with peak I splitting further into Ia and Ib when it is not too large. At higher hydrogen pressure (200 Torr) and longer adsorption time (15 hr), as in run H_8 (broken line in Figure 5), hydrogen I is very large and a separate existence of Ia and Ib is not distinct although it is suggested by the truncated shape of the peak. Evacuation at room temperature (H_4, H_5, H_7, H_9) removes peaks Ia and Ib and leaves only peak II. It is evident from Figure 5 and the data in Table II that the amount of hydrogen II is largely increased at longer adsorption time and higher pressure but is affected very little when the outgassing of hydrogen is extended from 40 min to 5 hr (runs H_5 and H_{15}). (It should be pointed out that in the figures showing TPD chromatograms in this paper the temperature scale is generally not uniform because of variations of β from run to run and occasionally to some extent in the same run—the characteristic temperatures of interest, especially those corresponding to the peak maxima, are indicated (in °C) on the chromatograms.)

TPD chromatograms of hydrogen adsorbed at −50 to −60° and evacuated before TPD at −50 (H_{10}) or at 23° (runs H_{12}, H_{14}, H_{16}) are shown in Figure 6. They exhibit similar features to those shown in Figure 5 although under comparable conditions of hydrogen presorption peak II tends to be smaller.

Adsorption of hydrogen at 200 and 300° results in the appearance of two additional peaks, III and IV, the latter only for the adsorption at 300°. This is shown by the top two chromatograms in Figure 7 (runs H_{17} and H_{11}). There is extensive overlapping of peaks but the corresponding approximate amounts of adsorbed hydrogen are shown in Table II.

In the series of experiments H_1 to H_{18} the ZnO sample showed distinct metal deposit on the vessel walls and perhaps also on the catalyst pellets. Before experiment H_{19} the catalyst pellets were removed and, after the reactor was washed in HNO_3, rinsed in doubly distilled water, and dried by evacuating at 600° for 20 min,

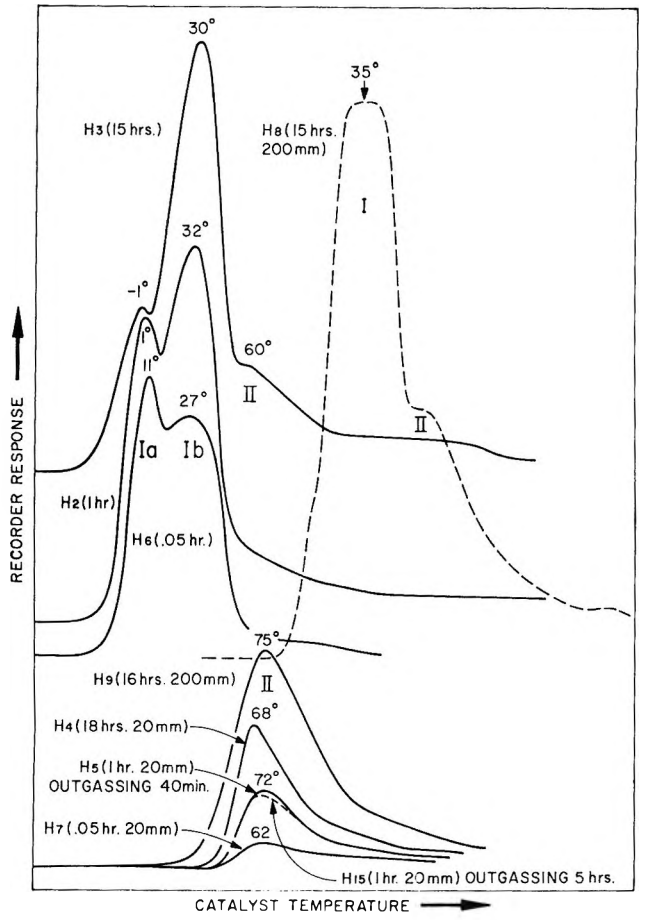

Figure 5. TPD chromatograms of hydrogen presorbed on ZnO at room temperature and outgassed before TPD at about −60° (runs H_2, H_3, H_6, H_8) and at room temperature (runs H_4, H_5, H_7, H_9). The chromatogram for run H_8 (broken line) has been displaced to avoid overlapping. (*Remarks:* The temperature scale is not uniform because of variations in β and ordinates are staggered. The figures in the brackets are the approximate times in hours and pressures in Torr during hydrogen presorption. Experimental conditions are detailed in Table II.)

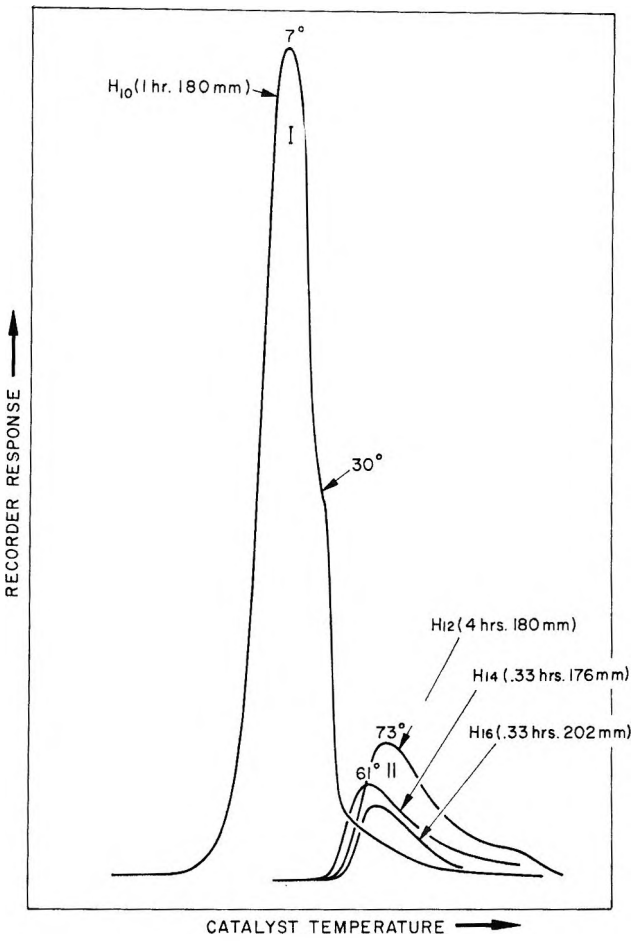

Figure 6. TPD chromatograms of hydrogen presorbed on ZnO at −50 to −60° and outgassed before TPD at −50° (run H_{10}) and at room temperature (runs H_{12}, H_{14}, H_{16}). (See "Remarks" in caption to Figure 5.)

the pellets were placed back into the reactor and treated at 400° in dry air at 1 atm for 1 hr. After this treatment the catalyst was strongly sintered and its BET surface area was reduced from about 8 to 3 m^2/g. Experiments H_{19} to H_{25} were carried out with this sintered catalyst. Experimental details are given in Table II and some of the TPD chromatograms are shown in the lower part of Figure 7 (runs H_{20}, H_{21}, H_{24}, H_{25}). The adsorbed amounts were considerably smaller on this sample as expected in view of the smaller surface area. However, a very conspicuous feature of the TPD chromatograms is an essentially complete absence of peak I under conditions under which hydrogen I was very prominent on the same ZnO sample before it was sintered. Peaks II, III, and IV, on the other hand, remained well developed at appropriate adsorption temperatures, as shown in Figure 7. Further investigation should be carried out to confirm and extend these observations. They are shown here, nevertheless, because of the striking difference in the adsorption pattern.

In view of the somewhat unusual results with the sintered ZnO sample, a fresh sample of ZnO was taken and activated in a manner similar to the procedure used by Dent and Kokes.[7] The sample was first heated in dry air 1 hr at 350° and then in 100 Torr of H_2 at 300° for 30 min. It was finally outgassed for 3 hr at 450°. The TPD chromatograms (H_{26}, H_{27}, H_{28}, Table II) obtained with this sample of ZnO were normal and similar to those obtained in the series H_1 to H_{18}. For example, the TPD chromatogram of hydrogen adsorbed at 300° and evacuated at −68° (H_{27}) is shown in Figure 8 (broken line). Peaks Ia, Ib, II, and III are well developed, and the existence of peak IV is indicated although it is not as pronounced as with the former catalyst.

Reaction of Presorbed Hydrogen with Ethylene. In an attempt to learn which forms of chemisorbed hydrogen can take part in ethylene hydrogenation on ZnO at low temperatures, the experiments summarized in Table III were carried out. Hydrogen was presorbed at room

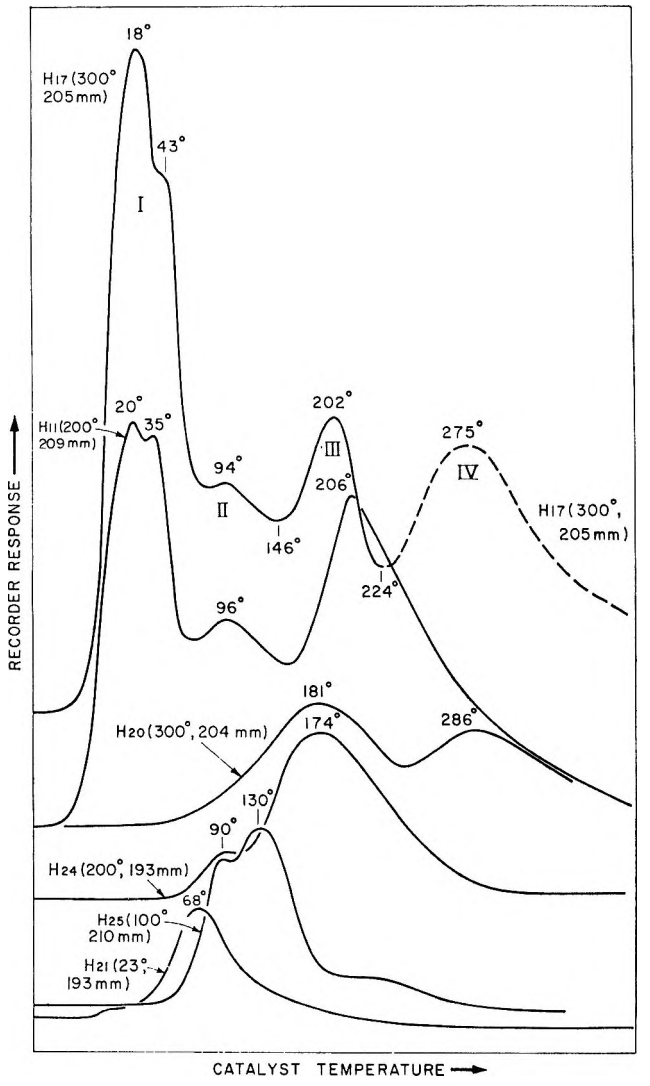

Figure 7. TPD chromatograms of hydrogen presorbed on unsintered ZnO at 300 (H_{17}) and 200° (H_{11}) and on sintered ZnO (as described in the text) at different temperatures (H_{20}, H_{21}, H_{24}, H_{25}). Toward the end of run H_{17} the temperature programmer developed some instability and peak IV (the part shown by the broken line) has been smoothed out. (See also "Remarks" in caption to Figure 5.)

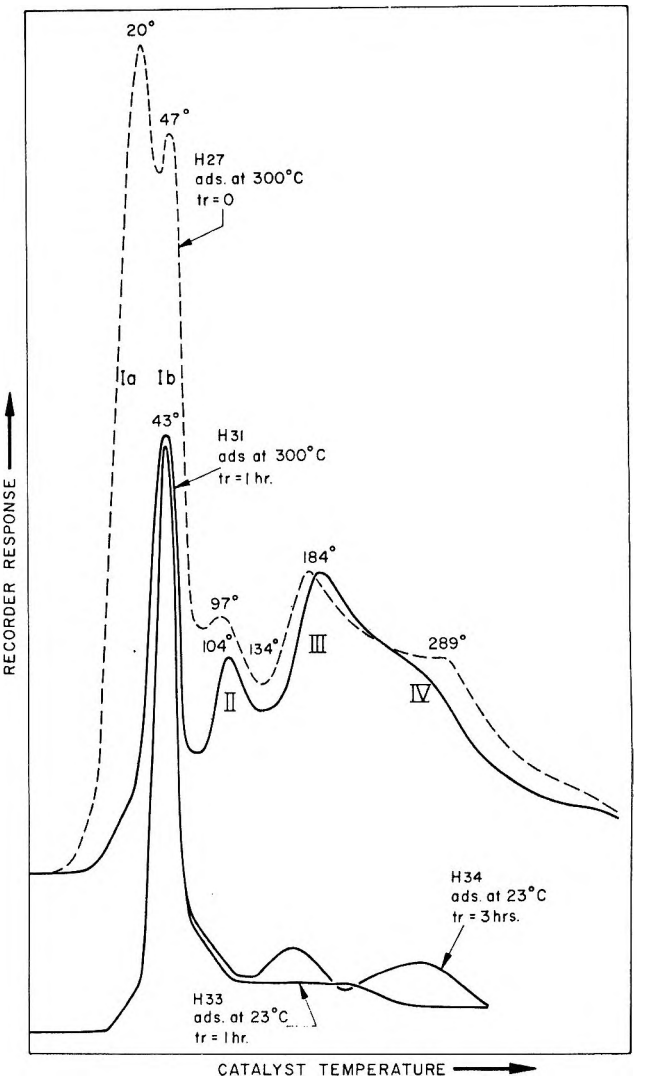

Figure 8. Reaction of presorbed hydrogen with approximately 10 Torr of ethylene. Different reaction times (*tr*) and temperatures of hydrogen adsorption have been used, as indicated. Details of run H_{27} (broken line) are given in Table II. No reaction with ethylene was carried out in this case, *i.e.*, *tr* = 0 and the chromatogram is shown for comparison. Details for the other runs (H_{31}, H_{33}, H_{34}) are given in Table III.

temperature or at 300° at close to 200 Torr for about 1 hr and evacuated for 15 min at −50 to −70° or, in one case, for 40 min at 23°. Hydrogen retained on the surface was allowed to react with about 10 Torr of ethylene under several different conditions. The hydrocarbons condensed out after the reactions were analyzed for ethane and the residual hydrogen on the surface was determined by TPD.

It can be seen from Table III (run H_{29}) that at −50° the reaction is negligibly slow. At 0 and 23° appreciable amounts of ethane are formed although even at these temperatures large amounts of adsorbed hydrogen remain unreacted. The comparison in Figure 8 of the TPD chromatograms after the reaction with ethylene at 0° (runs H_{31}, H_{33}, H_{34}) with an earlier run (H_{27}, Table II) without ethylene added is of interest. It is seen in run H_{31}, in which hydrogen was preadsorbed at 300°, that Ia hydrogen is almost entirely removed and a roughly comparable amount of ethane (~0.080 cc) is formed. The quantitative data are not accurate enough to say whether any of the other forms of adsorbed hydrogen have reacted although it is evident that if a reaction had occurred at all it must have been at best only very minor. It is significant that Ib hydrogen reacts at best only very little with ethylene at 0° even when the reaction time is extended to 3 hr (run H_{34}). A similar result is obtained (run H_{33}) when hydrogen is outgassed first at −67° for 15 min and then at 0° for 5 min. Ib peak is the same as in run H_{34}, but the amount of ethane formed is much smaller because a large part of Ia hydrogen is removed by 5-min outgas-

Table III: Reaction of Preadsorbed Hydrogen with Ethylene Vapor

	Run					
	H_{29}	H_{30}	H_{31}	H_{32}	H_{33}	H_{34}
Preadsorption of H_2						
Temp, °C	22	22	300	23	23	23
Pressure, Torr	170	190.5	205.9	183.2	192.5	208.7
Time, min	95	60	60	63	60	62
H_2 outgassing						
Temp, °C	−59	23	−66.5	−50,0	−67,0	−70
Time, min	15	40	15	15,5	15,5	15
C_2H_4 introduction						
Temp, °C	−50	23	−35	...	0	0
Pressure, Torr	13.3	12.7	10.9	...	9.9	12.2
Reaction						
Temp, °C	−50	23	0	...	0	0
Time, min	185	60	60	...	60	180
Outgassing before TPD						
Temp, °C	−50	23	−53	*a*	−59	−56
Time, min	30	30	30	*b*	30	37
Hydrocarbons recovered						
Total, cc (NTP)	0.653	0.650	0.522	...	0.299	0.363
C_2H_6, cc (NTP)	0.0004	~0.020	~0.080	...	0.017	0.062
TPD start, °C	−60	−58	−45	−47	−36	−42
TPD end, °C	400	450	460	455	445	450
β, deg/min	19	20	17–20	20	17–40	18–22
H_2 shown by TPD, cc (NTP)						
I	0.161		0.037	0.044	0.038	0.036
II		0.026	0.023	0.037	0.010	0.010
III	0.044				0.016	0.020
IV		0.025	0.137	0.021	0.021	0.020
Total	0.205	0.051	0.197	0.102	0.085	0.086

[a] See row 5 in this column (−50,0). [b] See row 6 in this column (15,5).

sing at 0°. Run H_{32} (Table III) is a zero reaction analog (no C_2H_4 admitted at all) of H_{33} with dual hydrogen evacuation (including 5 min at 0°), and it shows considerably smaller I hydrogen (0.044 cc) than in other zero reaction runs but with hydrogen outgassing only at −60 to −70°, for example H_{27} (0.088 cc) and H_{29} (0.161 cc). It should be pointed out that experiments H_{31}, H_{33}, and H_{34}, with the reaction at 0°, are open to the objection that at this temperature some of Ia hydrogen may be thermally desorbed from the surface before reacting and may then perhaps participate in ethylene hydrogenation in some other form and not as Ia. However, the fact remains that it does (eventually) react, as shown by large ethane formation in H_{31} and H_{34} and much smaller in H_{33}, and, in view of the TPD data in this temperature range, it would be difficult to conceive that any other form of adsorbed hydrogen may be involved.

In experiment H_{30} hydrogen was outgassed at 23° for 40 min and under such conditions peaks Ia and Ib are removed. The fact that some ethane is formed (~0.020 cc) would indicate that one or more of II–IV hydrogen may react with ethylene at 23° to some extent. However, a more detailed investigation is required before a definite conclusion can be drawn.

Discussion

The empirical rate expression obtained in this work for the hydrogenation of presorbed ethylene, eq 1, is the same as that of Dent and Kokes[8] for conventional hydrogenation of ethylene vapor at room temperature on zinc oxide. These authors obtained their rate expression after evaluating indirectly the amount of ethylene actually adsorbed on the catalyst from a measured adsorption isotherm. At the low temperatures used the reaction rate is within the experimental error first order in the amount of adsorbed ethylene and half order in the pressure of hydrogen. The activation energies are essentially identical (10 kcal/mol), and the calculated rate constants (reduced to 25°) are the same within a factor of 2. The processes observed in the two studies are therefore the same. The present TPD experiments show that at the temperatures employed ethylene is almost entirely adsorbed as a surface species

which gives a single TPD peak, ethylene A, which is hydrogenated when hydrogen gas is admitted. Ethylene B (including ethylene S) is also formed on the ZnO surface but normally in much smaller amounts, and it is apparently not hydrogenated, at least not at 0° and lower temperatures. No attempt was made in present work to determine ethylene adsorption at temperatures higher than room temperature although this is an obvious extension for future study.

Ethylene A is evidently bound to the surface of zinc oxide only relatively weakly. This is shown by the value of only 4.2 kcal/mol obtained for the activation energy of its desorption although, as already pointed out, this value is only approximate. The variation in the amount of ethylene left on ZnO surface after outgassing at different temperatures leads to a similar conclusion. In these experiments excess ethylene vapor was frozen over for 30 min into a liquid nitrogen trap. The average amounts of ethylene retained on the surface at 23 and −65°, respectively, corresponded to surface coverages (θ) of 0.0074 and 0.36. The residual vapor pressure of ethylene would be expected to be the same in the two cases ($\sim 2 \times 10^{-3}$ Torr) and, assuming that equilibrium between the vapor and the adsorbed ethylene was established, a value of 6.5 kcal/mol is obtained for the heat of adsorption ($-\Delta H$) from the expression (for Langmuir adsorption on a homogeneous surface)

$$-\Delta H = 2.3R\left\{\frac{T_1T_2}{T_2 - T_1} \log \frac{\theta_1(1 - \theta_2)\,[Eg]_1}{\theta_2(1 - \theta_1)\,[Eg]_2}\right\}$$

where $[Eg]$ stands for the concentration of the ethylene vapor. The value obtained is again only approximate, but it does show that ethylene A is bound to the surface relatively weakly. These results are in agreement with the observation of Dent and Kokes[8] that ethylene adsorbed on ZnO at room temperature does not show any infrared bands that could be ascribed to the opening of the double bond with formation of a saturated species and with their conclusion that ethylene chemisorption at room temperature occurs by π complexing.

The present TPD results show the great complexity of hydrogen chemisorption on ZnO at different temperatures. Five energetically different forms of chemisorbed hydrogen (Ia, Ib, II, III, and IV) are indicated. Hydrogen IV is formed very slowly at low temperatures but is present in appreciable amounts when adsorption takes place in the neighborhood of 300°. However even at 300° and at relatively long adsorption times the TPD peak corresponding to hydrogen IV is not always well developed. It is possible that its formation depends on how well ZnO is degassed although this point requires detailed study. Substantial formation of hydrogen III also occurs only at higher temperatures (approaching 200°), while hydrogen Ia and Ib are readily formed not only at room temperature but also at −50 to −60°. Formation of hydrogen II, on the other hand, is somewhat slower at these temperatures, becoming larger after longer adsorption times and at higher hydrogen pressures. An approximate calculation from the data in Table II of the rate constants of adsorption of hydrogen II shows a marked retardation as the surface coverage increases.

Some of the complexity of hydrogen chemisorption on ZnO was recognized already in the early stages of the development of the concepts of "activated adsorption."[17,18] H. S. Taylor and Sickman[18] observed one type of chemisorption (in addition to the physical adsorption at temperatures approaching −196° and with $-\Delta H$ = 1.1 kcal/mol). This was shown by an isobar maximum at about 200°. H. S. Taylor and Strother[19] found subsequently not one but two types of chemisorption, with the corresponding isobar maxima at about 80 and 220°. The two maxima have been since observed by other workers although at variable temperatures. Kesavulu and Taylor[20] observed the first maximum at temperatures from 30 to 80° and the second around 300°. Cimino, Molinari, and Cipollini[21] found the maxima at about 50 and 200°.

While the appearance of two isobar maxima indicates the presence of two types of chemisorption (or two types of chemisorption sites), it does not prove absence of additional types of chemisorption. H. S. Taylor and Liang[22] discussed the possible interaction between two types of chemisorption on a heterogeneous surface and similar views were expressed later by Kesavulu and H. A. Taylor.[20] The form of an isobar in a certain temperature region may be affected by simultaneous desorption of one chemisorbed type and adsorption of the other with the result that some significant features may become obliterated or concealed. Recognizing these limitations, Narvaez[23] used a stepwise desorption technique, desorbing presorbed hydrogen at 20 to 25° intervals for 0.5-hr periods and removing intermittently during each of these steps the larger part of the desorbed gas. This technique is probably only partly free from the above objection since it is still possible that the desorbed gas may be partitioned between different adsorption sites during the 0.5-hr heating periods. It did demonstrate, nevertheless, a considerably greater complexity of chemisorption of hydrogen on zinc oxide than indicated by the isobars, showing four desorption

(17) H. S. Taylor, *J. Amer. Chem. Soc.*, **53**, 578 (1931); *Chem. Rev.*, **9**, 1 (1931).

(18) H. S. Taylor and D. V. Sickman, *J. Amer. Chem. Soc.*, **54**, 602 (1932).

(19) H. S. Taylor and C. O. Strother, *ibid.*, **56**, 586 (1934).

(20) V. Kesavulu and H. A. Taylor, *J. Phys. Chem.*, **64**, 1124 (1960).

(21) A. Cimino, E. Molinari, and E. Cipollini, *Actes Congr. Intern. Catalyse, 2e, Paris, 1960*, p 263.

(22) H. S. Taylor and S. C. Liang, *J. Amer. Chem. Soc.*, **69**, 1306 (1947).

(23) R. Narvaez, Ph.D. Thesis, New York University, Oct 1963 (University Microfilms, Ann Arbor, Mich., 1968); *Dissertation Abstr.*, **25**(1), 132 (1964).

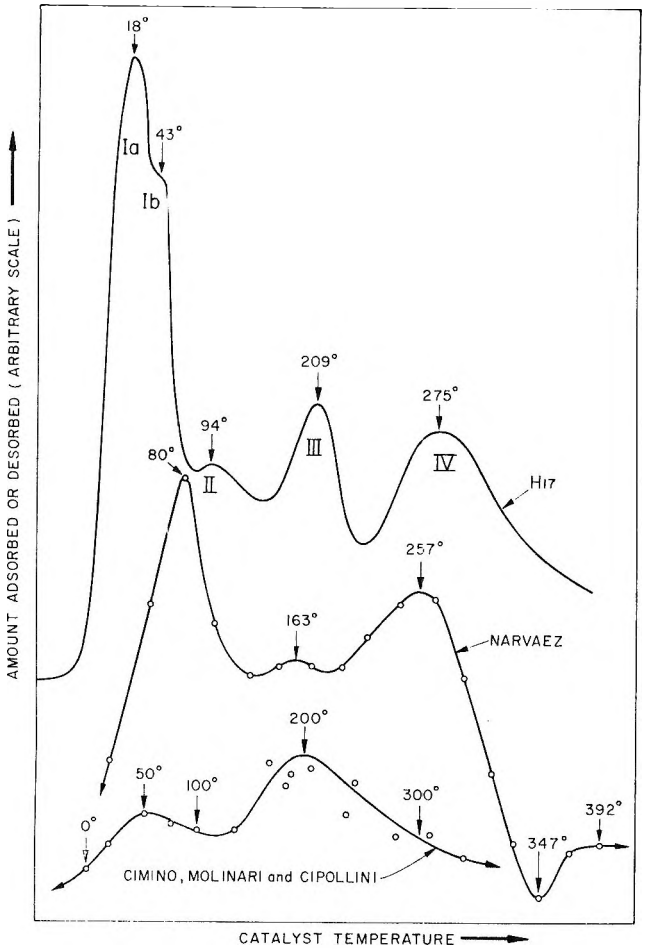

Figure 9. Qualitative comparison of the features of hydrogen chemisorption on zinc oxide as revealed by an adsorption isobar (the bottom tracing, replotted approximately from a graph of Cimino, Molinari, and Cipollini[21]), a "*d*–*T*" graph (middle tracing, based on the data of Narvaez[23]) and a TPD chromatogram (top tracing, run H_{17} of present work). (The smooth curves through the experimental points of the isobar and the "*d*–*T*" graph have been drawn, somewhat arbitrarily, by the present authors.)

maxima, at approximately 60, 150, 250, and 400°, respectively. Qualitatively, this result is somewhat similar to the TPD results obtained in present work. However, there are also some conspicuous differences between the two which should be discussed.

In Figure 9 a TPD chromatogram obtained in present work with hydrogen presorbed at 300° and outgassed at −50° (run H_{17}, Table II) is compared with a "*d*–*T*" graph based on the data of Narvaez[23] and with the top part of an isobar (approximately replotted from a graph of Cimino, Molinari, and Cipollini[21]). The increase in the detail and complexity in going from the isobar to the "*d*–*T*" graph and the TPD chromatogram is striking. The isobar shows the amounts of H_2 adsorbed at different temperatures while the other two graphs show the amounts of H_2 desorbed from the ZnO surface. (A quantitative comparison should not be made since the concentration scales are arbitrary and different in the three cases. They are also staggered to avoid overlapping.) Some "smearing" out effect of simultaneous desorptions and adsorptions on different sites is evidently operative in the isobar and is apparently responsible for the presence of only two maxima. A similar "smearing" out effect is perhaps responsible for the lack of a more detailed structure in the 100–200° interval of the "*d*–*T*" graph of Narvaez. Since in this case the presorbed hydrogen was outgassed at 0° down to a residual pressure of 1.3 mm of dibutyl phthalate, it is likely that the larger part of hydrogen Ia and Ib was removed and is thus not shown in the "*d*–*T*" graph in Figure 9. In the TPD experiment in Figure 9, on the other hand, the presorbed hydrogen was outgassed at −50° and hydrogen Ia and Ib are distinctly shown. Moreover, it is likely that readsorption of desorbed hydrogen is negligible since it is rapidly and continuously removed in the stream of carrier gas. Thus any tendency for "smearing" out would be expected to be drastically reduced or absent. (It should be mentioned also that the differences between present results and those of Narvaez may be due partly to the different origin of the ZnO samples used. This point deserves further investigation.)

The present finding that hydrogen Ia reacts with ethylene at 0° while the other adsorbed forms apparently react at best only very slowly may be compared with a similar observation by Dent and Kokes.[7] These authors found that a part of the rapidly chemisorbed hydrogen (termed "type I") was the principal source of hydrogen for the hydrogenation of ethylene at 25°, while the remaining chemisorbed hydrogen (termed "type II"), adsorbing rapidly initially but slowly in later stages, did not participate in the hydrogenation at room temperature. There does not seem to be any conflict between the two findings although TPD data provide more detailed information. "Type I" chemisorbed hydrogen of Dent and Kokes is readily removed from ZnO by outgassing at room temperature for more than 15 min. Evidently this includes both hydrogen Ia and Ib observed by TPD. Present results indicate that only a part of this hydrogen (Ia) is readily hydrogenated at 0°. It is not known whether the same is true for 25°, but even if it is, it is not in basic disagreement with the experimental results of Dent and Kokes. "Type II" chemisorption of Dent and Kokes would seem to be the present hydrogen II and perhaps some of its "slow" part might involve even hydrogen III. As already mentioned, experiment H_{30} in Table III seems to indicate that hydrogen II may react to some extent with ethylene at 23° when hydrogen Ia and Ib are absent. However, the isotopic tracer experiments of Dent and Kokes show that this reaction (at least when deuterium II is involved) cannot compete efficiently with hydrogen Ia.

The present results evidently leave room for more detailed further investigation of these processes by the

TPD technique and for extensions to other experimental conditions and catalyst preparations. Some of the desirable further work has already been mentioned in several places in the text. However, these and other extensions were not feasible at present because of time limitations. We feel that we should abstain at this time from speculations regarding the likely identity of the various surface species observed and from a discussion of the mechanistic details of ethylene hydrogenation on zinc oxide at room and lower temperatures. Various aspects of this process have been discussed extensively by Dent and Kokes,[7-9] who appear also to have obtained direct spectroscopic evidence[9] for the intermediate formation of the frequently postulated "half-hydrogenated" species (adsorbed ethyl radicals). An extensive agreement between our results and the general observations of Dent and Kokes should be emphasized.

The Structure and Properties of Acid Sites in a Mixed Oxide System. II. *tert*-Butylbenzene Cracking and Benzene Adsorption

by K. H. Bourne, F. R. Cannings,* and R. C. Pitkethly

The British Petroleum Company Ltd., BP Research Centre, Sunbury-on-Thames, Middlesex, England
(Received March 17, 1970)

Publication costs assisted by The British Petroleum Company Ltd.

Aluminum atoms in different environments in a silica matrix show distinguishable acidic properties. Such materials, previously characterized by infrared studies of adsorbed pyridine, have been tested for benzene adsorption and *tert*-butylbenzene cracking activity. Benzene adsorbs selectively on the aluminum-containing surface complexes. Thermodynamic data, derived from the isotherms, indicate that this adsorption is localized. Activation energies of cracking differentiate between aluminum on and within the silica lattice. The aluminum-in-silica catalysts display activity commensurate with pure Brønsted acidity. The measurements support the concepts of acid-site structure, proposed in a previous paper.

Introduction

In a previous paper[1] we described the preparation of two materials containing silica and alumina where the aluminum atoms were believed to be in different environments. In one, the aluminum was introduced onto the surface of a silica; in the other, small amounts were coprecipitated with the silica, the surface of which was then completely freed of aluminum by washing with acid, leaving aluminum atoms only in the silica matrix.

The intention of the work was to produce materials containing discrete forms of acid sites resembling those coexisting in commercial silica–alumina. Infrared studies with adsorbed pyridine showed differences on dehydration. The silica with the aluminum only on its surface displayed acidic properties typical of those reported for silica–alumina, in that a progressive conversion of Brønsted into Lewis acid sites occurred as the temperature of the calcination was raised. The aluminum-in-silica species behaved only as a Brønsted acid and showed no tendency to generate Lewis acid sites on dehydration. The data suggested that the Al atoms behaved as discrete entities.

This paper describes the characterization of these two types of material in terms of catalytic and adsorption properties and presents kinetic data on the cracking of *tert*-butylbenzene and thermodynamic data calculated from benzene adsorption isotherms.

Experimental Section

(*A*) *Materials.* Flowing nitrogen gas ("White Spot" grade from British Oxygen Gases) was deoxygenated over manganous oxide and dried over 5A molecular sieve.

Benzene and *tert*-butylbenzene were obtained from the BP Research Center's Hydrocarbon Bank. Both contained less than 0.03 mol % impurity. They were stored over freshly activated 4A molecular sieve, in sealed glass vessels.

Silica gel (70–100 mesh BSS, U-30 grade "Sorbosil") was supplied by Messrs. Joseph Crosfield, Warrington, Lancs. The procedures for preparing aluminum–on-silica catalysts from this gel have been described pre-

(1) K. H. Bourne, F. R. Cannings, and R. C. Pitkethly, *J. Phys. Chem.*, **74**, 2197 (1970).

Table I: Catalyst Preparation and Aluminum Content

Catalyst no.	Technique used to introduce aluminum to the gel	Al on/in silica	% wt aluminum
1	None, parent acid-washed silica	...	0.02
2	Percolation; 40 vol aluminum sulfate soln[a]/vol gel passed in 31 hr	On	1.3
3	Percolation; 5.5 vol aluminum sulfate soln[a]/vol gel passed in 24 hr	On	0.87
4	Percolation; 46 vol aluminum sulfate soln[a]/vol gel passed in 4 hr	On	0.58
5	Soaking; 5 × 2.5 vol aliquots of aluminum sulfate soln in 72 hr	On	0.38
6	Soaking; 1 × 12.5 vol aliquots of aluminum sulfate soln in 16 hr	On	0.30
7	Soaking; 1 × 10 vol aliquots of aluminum sulfate soln in 4 hr[b]	On	0.21
8	Soaking; 2 × 1.5 vol aliquots of aluminum sulfate soln in 4 hr	On	0.14
9	By cogellation. Details in ref 1	In	0.10
10		In	0.045

[a] Decimolar aluminum sulfate hexadecahydrate solution used throughout. [b] Sample prepared by placing silica gel on a cellophane membrane clamped between two horizontally held vacuum desiccator lids, and covered with aluminum sulfate solution. Water was passed across the underside of the membrane while the gel and solution above were vigorously stirred.

viously as has the preparation of aluminum-in-silica.[1] Further details are given in Table I.

Incorporation of the largest quantity of aluminum (catalyst no. 2) reduced the BET surface area of the gel from 590 to 560 m^2/g.

(*B*) *Cracking Studies with tert-Butylbenzene.* Reactions were carried out at atmospheric pressure in a flow microreactor system, closely resembling one previously described.[2] The major components are a vapor introduction device,[3] by which a hydrocarbon (in this case *tert*-butylbenzene) is fed by gaseous diffusion from a thermostated glass tube into the purified nitrogen carrier stream, a temperature-controlled furnace surrounding the microreactor, and an effluent sampling valve and glpc apparatus. Nitrogen, flowing at 15 ml/min across the end of a 5 mm bore × 60 mm long diffusion tube held at various temperatures between 62.5 and 90.0°, produced *tert*-butylbenzene partial pressures in the range 0.09 to 0.56 mm (12–75 N m^{-2}).

In each experiment 0.1 g of catalyst was packed between quartz wool plugs at the center of the stainless steel microreactor and pretreated for 16 hr at 570° in a 25 ml/min flow of nitrogen.

Pyrex spacers reduced dead volume in the reactor. After cooling the reactor and catalyst in flowing nitrogen to the required temperature, a stream of nitrogen containing *tert*-butylbenzene was passed over the catalyst at a constant partial pressure for about 1 hr until the cracking rate was constant. Conversions were then measured over 30-min periods at a series of six temperatures in the range 247.5–100° (in descending order), finally returning to the highest temperature to observe any long-term deactivation. Initial and final activities agreed to within 4% on total conversion. Steady cracking rates were obtained within 30 min at each temperature, except for the first measurement. This procedure was then repeated at a different partial pressure of *tert*-butylbenzene.

Reaction rates were calculated from conversion data obtained by chromatographic analysis of 0.3-ml samples of reactor effluent. An alumina-packed glass capillary column (30 cm long × 0.3 mm i.d.) separated the isobutene, benzene, and *tert*-butylbenzene in the effluent. The adsorption characteristics of the column were modified with water vapor, introduced by passing the hydrogen eluent gas over copper sulfate pentahydrate crystals heated to 50°. Product analysis took 6 min, with the column at 85°. Conventional hydrogen flame ionization equipment detected the reaction products. Calibration for benzene (peak height) and *tert*-butylbenzene (peak area) was carried out before and after each complete activity determination. The detector responded linearly with hydrocarbon partial pressures, in the range used.

(*C*) *Benzene Adsorption Studies.* Benzene adsorption characteristics of the various materials were investigated using nitrogen carrier gas, under flow conditions, in a microreactor apparatus similar to that described in the preceding section. Benzene was substituted for *tert*-butylbenzene in the diffusion unit, and the input partial pressure of benzene was varied between 0.5 and 5.5 mm (67–730 N m^{-2}) by changing the nitrogen flow rate and the diameter of the diffusion tube.

Weighed samples (0.25 g) of catalyst were pretreated in the same manner as for the cracking studies and cooled in flowing nitrogen to one of the adsorption temperatures, 100, 120.5, or 141°. Benzene in nitrogen was then diverted over the catalyst and the ensuing adsorption recorded. Once equilibrium was achieved, the benzene was desorbed at the same temperature using a 6 ml/min flow of nitrogen. The adsorption and desorption cycle was followed by chromatographic analysis of samples of the effluent taken every minute. A

(2) R. C. Pitkethly and A. G. Goble, American Chemical Society Symposium on Instrumental Techniques in Study of Catalysis Mechanism, Boston, Mass., Apr 1959, p C-103.

(3) D. H. Desty, C. J. Geach, and A. Goldup, Third International Symposium of Gas Chromatography, Edinburgh, June 1960, p 46.

fresh charge of catalyst was used for each cycle, and two sets of measurements were made at each temperature.

A 2 m × 0.25 mm i.d. stainless steel capillary column, internally coated with squalane, served to separate any lighter hydrocarbons from the benzene in the effluent. However, only benzene was detected in these experiments.

Isotherms were constructed from the desorption fronts using the method of Glueckauf[4] as adapted by Gregg and Stock[5] for gas–solid interactions. Polynomial isotherms were fitted with the added restriction that the regression line must pass through the origin. The reported thermodynamic data were then calculated at selected coverages of benzene.

Results and Discussion

(*A*) *Cracking Studies with tert-Butylbenzene.* (*i*) *Preliminary Studies.* The parent silica showed no activity for cracking *tert*-butylbenzene over the temperature range 140–225°. Since all the aluminum-on- and aluminum-in-silica catalysts showed considerable activity under these conditions and because the parent silica contained 0.02 wt % of aluminum, this result is rather surprising. We can only assume that the environment of the aluminum in the parent silica differs from that in the aluminum-in-silica. That retained by the former may be present as clumps of alumina buried in the silica matrix.

There was no indication of alkylation or isomerization reactions, and no recombination of the primary products from the cracking reaction, namely isobutene and benzene, occurred when a gaseous mixture of these hydrocarbons was passed over catalyst no. 10 under test conditions. The kinetics of cracking were shown to be virtually unaffected by diffusion within the solids under the experimental conditions used.

(*ii*) *Kinetic Data.* Following Horton and Maatman's development[6] of the Prater and Lago review[7] on the kinetics of cracking a feedstock molecule, F, on an active site, S, through the intermediate adsorbed state, FS, the relationship

$$\mathrm{F} + \mathrm{S} \underset{K_2}{\overset{K_1}{\rightleftharpoons}} \mathrm{FS} \xrightarrow{K_3} \text{products}$$

represents the overall reaction. In the steady state, two equations can be derived from this equation, being

$$K_1[Pf][\mathrm{S}] = (K_2 + K_3)[\mathrm{FS}]$$

where Pf is the feedstock partial pressure and the rate of formation of products

$$\left(\frac{\mathrm{d}n}{\mathrm{d}t}\right) = K_3[\mathrm{FS}]$$

If Z is the total number of active sites per unit weight of catalyst, and $G = (K_2 + K_3)/K_1$ then

$$\frac{\mathrm{d}n}{\mathrm{d}t} \text{ per unit weight of catalyst} = K_3Z - \frac{G}{Pf}\cdot\frac{\mathrm{d}n}{\mathrm{d}t} \qquad \text{(I)}$$

Since both $\mathrm{d}n/\mathrm{d}t$ and Pf may be varied, G and K_3Z can be derived graphically. Table II gives the measured values of $\mathrm{d}n/\mathrm{d}t$ and Pf for the various catalysts used in the work and Table III the values of K_3Z and G. The latter were determined by the method of least squares.

The activities of the aluminum-on- and aluminum-in-silica catalysts are shown in the data of Table IV, where the specific cracking rates are recorded. The activities of the aluminum-on-silica catalysts (no. 2–8) with no. 4 an exception form a consistent group. Although the aluminum-in-silicas (no. 9 and 10) have a wide range of activity, the later discussion of their properties will show they belong to a separate group.

Following Horton and Maatman,[6] if the Arrhenius relationship holds in this system, the equation

$$K_3Z = A_k e^{-Q_k/RT} \qquad \text{(II)}$$

will be correct. Linear Arrhenius plots were found for K_3Z and the derived values of A_k and Q_k are shown in Table V.

The magnitude of Q_k effectively sorts the catalysts into categories corresponding to their method of preparation. Thus the aluminum-on-silica catalysts, except no. 7, have Q_k values in the range 17.5 to 18.5 kcal/mol; the value for no. 7, which was prepared by a dialysis technique, is significantly lower at 15.8 kcal/mol. The aluminum-in-silica catalysts have Q_k values of 21–22 kcal/mol. The data suggest that different methods of preparation have led to the formation of sites capable of reacting in different ways toward a given feedstock, perhaps because of structural differences.

When $Pf \gg G$, eq I reduces to

$$\mathrm{d}n/\mathrm{d}t = K_3Z$$

and the reaction may be regarded as zero order.

Absolute reaction theory states[8] that the rate, $\mathrm{d}n/\mathrm{d}t$, for zero-order reactions on heterogeneous catalysts, assuming that the partition functions for the activated complex and adsorbed molecule are equal, is

$$\frac{\mathrm{d}n}{\mathrm{d}t} = \frac{ZkT}{h}e^{-Q/RT}$$

where k and h are Boltzmann's and Planck's constants, respectively. Hence, from eq II above

$$A_k = \frac{ZkT}{h}$$

and the number of active sites, Z, can be found for any temperature. Table VI gives the number of active

(4) E. Glueckauf, *J. Chem. Soc.*, 1302 (1947).

(5) S. J. Gregg and R. Stock, Second International Symposium on Gas Chromatography, Amsterdam, May 1958, p F-44.

(6) W. B. Horton and R. W. Maatman, *J. Catal.*, **3**, 113 (1964).

(7) C. D. Prater and R. M. Lago, *Advan. Catal.*, **8**, 298 (1956).

(8) S. Glasstone, K. J. Laidler, and H. Eyring, "The Theory of Rate Processes," McGraw-Hill, New York, N. Y., 1941, Chapter VII.

Table II:[a] *tert*-Butylbenzene Partial Pressures (Pf)[b] and Observed Cracking Rates (dn/dt)[c]

Temp, °C	Catalyst no. 2 —1.3 wt % Al-on-silica— Pf	$dn/dt \times 10^8$	Catalyst no. 3 —0.87 wt % Al-on-silica— Pf	$dn/dt \times 10^8$	Catalyst no. 4 —0.58 wt % Al-on-silica— Pf	$dn/dt \times 10^8$	Catalyst no. 5 —0.38 wt % Al-on-silica— Pf	$dn/dt \times 10^8$
100	0.563	4.24	0.522	3.90	...	...	...	...
120	0.563	15.60	0.522	13.69	0.556	10.67	...	...
140	0.563	40.35	0.522	36.09	0.556	30.65	0.545	6.24
160	0.563	90.50	0.522	84.21	0.556	69.01	0.545	16.37
180	0.563	181.5	0.522	163.0	0.556	144.2	0.545	33.20
200	...	...	...	...	...	...	0.545	58.32
100	0.286	3.48	0.282	2.40	...	...	...	...
120	0.286	12.31	0.282	9.31	0.299	8.79	...	...
140	0.286	31.94	0.282	25.60	0.299	23.20	0.294	4.75
160	0.286	69.22	0.282	55.28	0.299	48.62	0.294	11.34
180	0.286	122.2	0.282	105.9	0.299	89.97	0.294	22.44
200	...	...	...	...	...	...	0.294	38.51
100	0.164	2.88	0.161	2.64	...	...	...	...
120	0.164	9.83	0.161	9.15	0.156	6.82	...	...
140	0.164	26.74	0.161	24.36	0.156	18.79	0.161	4.79
160	0.164	56.04	0.161	51.55	0.156	38.73	0.161	11.04
180	0.164	90.05	0.161		0.156	65.62	0.161	21.11
200	...	...	...	...	...	...	0.161	33.63
100	0.090	2.45	0.089	2.17	...	...	...	...
120	0.090	7.68	0.089	7.07	0.086	5.32	...	...
140	0.090	18.61	0.089	17.10	0.086	12.90	0.088	3.47
160	0.990	36.25	0.089	33.33	0.086	25.51	0.088	8.06
180	0.090	51.58	0.089	48.34	0.086	37.61	0.088	14.09
200	...	...	...	...	...	...	0.088	20.37

Temp, °C	Catalyst no. 6 0.30 wt % Al-on-silica Pf	$dn/dt \times 10^8$	Catalyst no. 7 0.21 wt % Al-on-silica Pf	$dn/dt \times 10^8$	Catalyst no. 8 0.14 wt % Al-on-silica Pf	$dn/dt \times 10^8$	Catalyst no. 9 0.10 wt % Al-in-silica Pf	$dn/dt \times 10^8$	Catalyst no. 10 0.045 wt % Al-in-silica Pf	$dn/dt \times 10^8$
140	0.553	9.36	0.545	6.24	...	...	...	...	...	...
160	0.553	23.62	0.545	16.37	0.548	10.93	0.636	7.71	0.538	8.01
180	0.553	47.90	0.545	33.20	0.548	22.71	0.636	18.20	0.538	21.36
200	0.553	91.34	0.545	58.32	0.548	41.25	0.636	36.47	0.538	41.82
225	0.553	156.0	...	...	0.548	75.37	0.636	71.43	0.538	77.86
247.5	...	...	...	...	0.548	113.7	0.636	105.2	...	...
140	0.297	8.74	0.294	4.75	...	...	...	...	...	...
160	0.297	21.14	0.294	11.34	0.299	7.76	0.402	6.31	0.300	7.74
180	0.297	41.46	0.294	22.44	0.299	16.47	0.402	14.13	0.300	16.07
200	0.297	65.32	0.294	38.51	0.299	27.92	0.402	26.60	0.300	29.76
225	...	...	...	...	0.299	45.34	0.402	48.76	0.300	51.66
247.5	...	...	...	...	0.299	65.62	0.402	79.80	0.300	72.75
140	0.161	3.99	0.161	4.79	...	...	...	...	...	...
160	0.161	9.53	0.161	11.04	0.160	5.43	0.204	4.37	0.162	5.30
180	0.161	18.92	0.161	21.11	0.160	10.98	0.204	8.97	0.162	10.47
200	0.161	30.70	0.161	33.63	0.160	18.74	0.204	15.74	0.162	18.23
225	0.161	45.76	...	...	0.160	29.85	0.204	27.23	0.162	28.96
247.5	...	...	...	...	0.160	38.77	0.204	37.50	0.162	38.66
140	0.093	4.20	0.088	3.47	...	...	...	...	...	...
160	0.093	9.19	0.088	8.06	0.090	4.84	0.130	3.34	0.091	3.84
180	0.093	15.55	0.088	14.09	0.090	8.41	0.130	6.65	0.091	7.17
200	0.093	22.64	0.088	20.37	0.090	12.63	0.130	11.30	0.091	11.35
225	0.093	31.18	...	...	0.090	18.05	0.130	18.37	0.091	16.61
247.5	...	...	...	...	0.090	22.71	0.130	24.04	0.091	21.67

[a] Catalyst no. 1 (the parent silica) showed no cracking activity under these conditions. [b] In mm. [c] In mol/(g min).

sites for each catalyst at 160° and compares the percentage of active aluminum present. The results show that the catalysts fall into distinct categories, again according to their method of preparation, with the aluminum-in-silica catalysts containing the highest percentage of active aluminum and the dialyzed aluminum-on-silica the lowest.

Table VI also shows the activities of the different active site types in terms of feed molecules cracked per active site. These results also differentiate between

Table III: Values of K_3Z[a] and G[b] from Data of Table II

Temp, °C	Catalyst no. 2		Catalyst no. 3		Catalyst no. 4		Catalyst no. 5		Catalyst no. 6	
	$K_3Z \times 10^8$	$G \times 10^2$	$K_3Z \times 10^8$	$G \times 10^2$	$K_3Z \times 10^8$	$G \times 10^2$	$K_3Z \times 10^8$	$G \times 10^2$	$K_3Z \times 10^8$	$G \times 10^2$
100	4.67	8.72	3.44	3.94	...	...	...	...	...	...
120	18.63	13.46	13.73	7.46	12.68	12.38	5.88	12.76	...	...
140	50.59	15.31	39.38	10.16	38.70	17.16	21.51	25.38	10.71	14.20
160	123.3	21.01	97.82	15.03	91.97	22.34	62.88	39.28	29.24	18.54
180	326.5	45.95	...	...	261.6	50.52	149.7	57.79	69.73	30.31
200	...	...	...	...	...	...	344.0	96.42	181.6	62.96

Temp, °C	Catalyst no. 7		Catalyst no. 8		Catalyst no. 9		Catalyst no. 10	
	$K_3Z \times 10^8$	$G \times 10^2$	$K_3Z \times 10^8$	$G \times 10^2$	$K_3Z \times 10^8$	$G \times 10^2$	$K_3Z \times 10^8$	$G \times 10^2$
140	6.71	7.85	...	...	...	...	...	...
160	17.76	10.62	12.53	15.84	12.02	35.1	10.96	16.44
180	38.84	15.07	32.10	27.03	31.99	51.5	36.00	37.64
200	77.89	23.72	70.80	42.91	86.30	83.9	94.61	67.06
225	...	...	177.8	80.30	291.8	175	301.2	152.3
247.5	...	...	491.2	187.2	708.0	442	...	...

[a] In mol/(g min). [b] In mm.

Table IV: The Cracking Activities of the Catalysts at Three Temperatures (mol of *tert*-Butylbenzene Cracked/g atom of Aluminum/min × 10^5)

Feed partial pressure, P_f, mm	Catalyst no. 2	3	4	5	6	7	8	9	10
	Al-on/in-silica	On	On	On	On	On	On	In	In
	Wt % Al	1.3	0.87	0.58	0.38	0.30	0.21	0.14	0.10[a]	0.045
	Cracking temp, 140°								
0.55		83.7	111.9	142.5	105.8	84.2	80.1			
0.29		66.3	79.4	107.9	88.7	78.6	61.0			
0.16		55.5	75.5	87.4	52.2	35.9	61.5			
0.09		38.6	53.0	60.0	41.0	37.8	44.5			
	Cracking temp, 160°								
0.55		187.8	261.1	320.9	259.0	212.3	210.2	210.6	208.2	480.1
0.29		143.6	171.4	226.1	197.4	190.1	145.6	149.5	170.5	463.9
0.16		116.3	159.8	180.1	125.9	85.7	141.8	104.6	118.2	317.6
0.09		75.2	103.3	118.6	83.5	82.6	103.5	93.2	90.2	230.1
	Cracking temp, 180°								
0.55		376.4	505.4	670.3	508.5	430.6	426.4	437.5	491.5	1280.2
0.29		253.5	328.3	418.4	376.3	372.7	288.2	317.3	382.0	963.1
0.16		186.8	246.3	305.1	233.5	170.1	271.1	211.5	242.1	627.5
0.09		107.0	149.9	174.9	137.8	139.8	181.0	162.0	179.6	429.7

[a] The feedstock partial pressures used with this catalyst are those shown in Table II. They differ slightly from those used with the other catalysts.

the catalyst types with the aluminum-in-silica catalyst possessing relatively large numbers of weakly active sites and the aluminum-on-silica catalysts small numbers of more highly active sites.

The percentages of the aluminum which is active in our catalysts are three orders lower than Horton and Maatman[6] found in their studies. However, their catalysts, prepared by impregnating a commercial silica with aluminum nitrate, drying, and calcining the resulting solid, were used at much higher temperatures, *viz.*, 300–500°. From the described method of preparation, their material would have contained deposited alumina as well as "exchanged" aluminum atoms, and both these species may have been contributing to the cracking under the conditions they used.

Further, the percentage of active aluminum in our catalysts declines with increasing aluminum content, as might reasonably be expected.

(*B*) *Benzene Adsorption Studies.* (*i*) *Distinctions between the Catalyst Types.* The data of the original

Table V: Values of A_k and Q_k

Catalyst No.	Catalyst Al content	Catalyst Al in/on silica	A_k, mol/(g min)	Q_k, kcal/mol
2	1.3	On	8.80×10^3	17.5
3	0.87	On	10.75×10^2	17.9
4	0.58	On	7.59×10^2	17.6
5	0.38	On	6.17×10^2	17.9
6	0.30	On	4.30×10^2	18.2
7	0.21	On (dialysis)	0.17×10^2	15.8
8	0.14	On	2.50×10^2	18.4
9	0.10	In	4.56×10^3	21.0
10	0.045	In	11.7×10^3	21.8

Table VI: The Number and Activity of Active Sites of the Various Catalysts at 160°

Catalyst No.	Catalyst Wt % Al	Number of active sites/g of catalyst $\times 10^{-11}$	Al content atoms/g of catalyst $\times 10^{-20}$	Per cent of Al present that is active ($\times 10^2$)	Feed molecules cracked[a]/active site min at 160°
2	1.3	9.79	2.90	3.37	5.57×10^5
3	0.87	11.96	1.94	6.16	4.24×10^5
4	0.58	8.44	1.295	6.515	4.93×10^5
5	0.38	6.86	0.85	8.09	3.20×10^5
6	0.30	4.78	0.67	7.14	2.98×10^5
7	0.21	0.185	0.47	0.395	55.3×10^5
8	0.14	2.78	0.31	8.885	2.37×10^5
9	0.10	50.71	0.22	227.4	9.11×10^3
10	0.045	130.1	0.10	1301	5.29×10^2

[a] Data taken from the conversions at the highest feed partial pressure, *ca.* 0.56 mm, in Table II.

isotherms (*i.e.*, not the fitted ones) at 120° for the catalysts examined follow Langmuir plots above a coverage particular to the specimen (see Figure 1). If the "non-Langmuir" region of adsorption measures the number of heterogeneous sites on the catalysts, the figure can be used to determine how this number varies with catalyst aluminum content. The information is listed on the figure. It shows that the number does not increase linearly with the aluminum content of the catalysts but approaches a limit at about 1.5 wt % Al. In the *tert*-butylbenzene cracking studies, described in the previous section, it was found that there was no significant increase in the number of active sites between catalysts no. 3 and 2.

A possible explanation for these observations is that as more aluminum is introduced to the silica surface the chance of forming clumps of alumina increases and the discrete nature of the sites is lost. With 1.3 wt % Al on a silica whose surface area is 560 m^2/g, the average area available to each Al atom is 193 $Å^2$, *i.e.*, the average distance between adjacent Al atoms is only 14 Å.

The aluminum-in-silica catalyst no. 10, behaved differently to the aluminum-on-silica catalysts in the adsorption studies, as it had in the cracking work; the

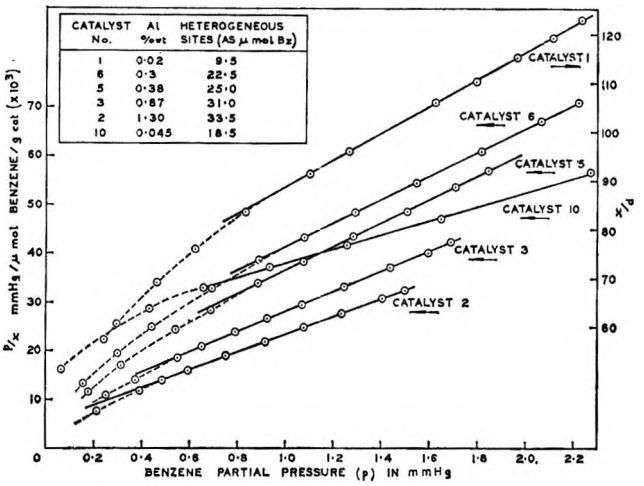

Figure 1. Langmuir plots for the catalysts shown, at 120.5°.

number of heterogeneous sites on this material was large for its very low aluminum content. This result is consistent with the earlier observations that a large proportion of its aluminum is catalytically active.

If we assume that benzene adsorption occurs preferentially on those sites which are catalytically active, then we are observing distinctive behavior between the two types of synthesized site

(*ii*) *Thermodynamic Data.* Calculations of the heat and entropy of adsorption of benzene on the catalysts were made, using results from the fitted isotherms.

The integrated form of the Clausius–Clapeyron equation provided isosteric heats of adsorption (q_{st}) data. The use of this equation seems justified, in spite of the assumptions in its derivation,[8] on account of the low coverages and partial pressures used. A benzene uptake of 25 μ mol/g, the highest quoted, corresponds to 1.1×10^{-2} theoretical monolayers on the silica, assuming an area of 40 $Å^2$ for adsorbed benzene. Calculated values of q_{st} appear in Table VII.

Table VII: Isosteric Heats of Adsorption (q_{st}) of Benzene (in kcal/mol) on the Catalysts

Benzene coverage, μmol/g of catalyst	Catalyst no. 1	2	3	5	10
	Al content, wt % 0.022	1.3	0.87	0.38	0.045
0.5	...	25.0	26.8	23.9	...
1	...	23.2	24.6	21.7	...
1.5	...	22.1	23.4	20.5	...
2	7.6	21.3	22.5	19.7	14.9
2.5	8.1	20.7	21.7	19.0	...
3	8.5	20.2	21.2	18.5	...
4	9.6	19.4	20.3	17.8	14.4
5	9.6	18.7	19.6	16.9	...
7	9.7	17.6	18.5	16.6	...
10	9.8	17.3	17.4	15.7	13.4
12	9.8	17.4	17.5	14.4	...
15	9.7	17.0	17.4	13.9	13.0
20	...	16.6	16.4	12.4	12.7
25	...	15.9	15.6	11.5	12.4

For the parent silica, they remain constant over the range 4–25 μmol/g and are about 2.5 kcal/mol above the latent heat of vaporization of benzene. Adsorption is predominantly physical. This might be reasonably expected from the work of Kiselev,[9] on a surface so extensively dehydrated.

For aluminum-on-silica catalysts, q_{st} values decrease rapidly with increasing adsorption, but even at the larger coverages, the energies involved are appreciably higher than those of the pure silica. The results indicate that benzene is interacting preferentially with introduced aluminum.

Molar entropy changes have been determined relative to a standard state of 1 atm of benzene vapor. These are listed in Table VIII, together with the entropy change associated with adsorption as an ideal two-dimensional gas. This latter value was calculated using the method of Kemball[10] and assumes an available surface area of 550 m^2/g for all catalysts. Comparison with the experimental data indicates that only benzene adsorption on pure silica shows a similar entropy loss. We conclude that this benzene is highly mobile. All aluminum-treated silicas display higher values of $\Delta\bar{S}_u$, corresponding to the loss of other than one degree of translational freedom. The trend in entropy loss suggests that the strongest adsorbent–adsorbate interaction occurs at lowest coverages. At levels of 1 or 2 μmol/g, the entropy change on adsorption onto the highest aluminum content silicas indicates that there is still some freedom of movement.

Table VIII: Differential Molar Entropy Changes, $\Delta\bar{S}_u$, on Adsorption of Benzene onto the Catalysts at 120.5°; the Values, in eu, are Negative

Coverage, μmol of benzene/g of catalyst	Catalyst no.					
	a	1	2	3	5	10[b]
1	6.6	...	28.3	31.9	26.1	...
2	...	...	26.3	29.4	23.9	...
3	...	...	25.1	27.9	22.7	...
4	...	8.2	24.2	26.9	22.0	15.8
5	9.7	8.9	23.4	26.1	20.8	...
10	11.1	11.2	22.6	23.7	21.0	...
15	11.9	12.2	23.7	25.8	18.7	...
20	12.5	...	24.3	24.8	16.7	18.0
25	13.0	...	23.8	24.1	15.7	...

[a] Calculated for adsorption as an ideal two-dimensional gas. [b] Measured at 122°.

Comparative data for aluminum-in-silica materials show that more mobile adsorbed species are present.

(*C*) *The Nature of the Sites.* The possible structure of the various acid sites has been outlined in a previous paper.[1] Results from benzene adsorption studies do little to verify these proposals. They do indicate however, that the incorporation of aluminum ions onto the silica surface provides a location for selective adsorption and that these sites are capable of chemisorbing benzene. Centers formed when aluminum is buried within the lattice are not such powerful adsorbents.

Kinetic data, derived from the cracking of *tert*-butylbenzene, are sufficiently well defined to sort the catalysts into categories corresponding to method of preparation, *i.e.*, the type of acid site present. This corroborates the concept of fundamental differences between sites formed on one hand by cogelling and acid extraction and on the other by surface ion exchange. These two types differ also in that the former exhibit a noticeable resistance to deactivation during the cracking reaction, when compared with aluminum-on-silica catalysts. This is a reasonable property of the pure Brønsted acid, which is unable to dehydrate to give a Lewis acid. Coke precursors are believed to be generated at Lewis acid sites by a mechanism originally proposed by Thomas,[11] and their formation is partly due to the strong retention of site-bound benzene. Thus

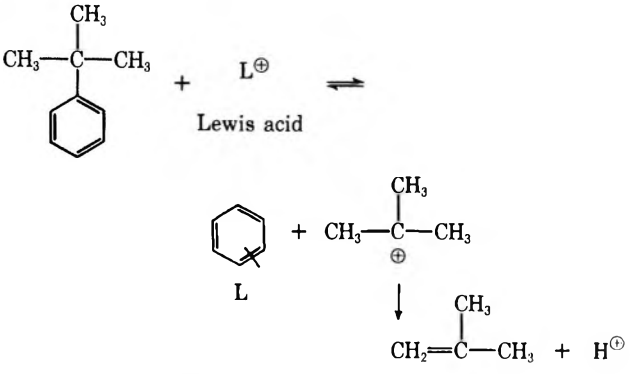

The regeneration of the Lewis acid site by release of the chemisorbed species depends on its interaction with a proton. The process is obviously more complex than the reaction on aluminum-in-silica and more liable to produce carbonaceous deposits.

Acknowledgment. Permission to publish this paper has been given by The British Petroleum Company Ltd.

(9) A. V. Kiselev, *Quart. Rev.*, **15**, 99 (1961).
(10) C. Kemball, *Proc. Roy. Soc., Ser. A*, **187**, 73 (1946).
(11) C. L. Thomas, *Ind. Eng. Chem.*, **41**, 2564 (1949).

Binding States of Hydrogen and of Nitrogen on the (100) Plane of Molybdenum[1]

by H. R. Han and L. D. Schmidt*

Chemical Engineering Department, University of Minnesota, Minneapolis, Minnesota 55455 *(Received September 8, 1970)*

Publication costs assisted by Advanced Research Projects Agency

The binding states and desorption kinetics of hydrogen and nitrogen on the (100) plane of Mo are examined by flash desorption mass spectrometry, and the results are compared with the adsorption of these gases on (100)W. Since molybdenum and tungsten are isoelectronic and have the same crystal structure and lattice constant, differences must be attributed to differences in the electronic properties of the substrates. It is found that, while there is a good correlation between the binding states of these gases and between the binding states of each gas on the substrates, there are several interesting differences. There is an extra binding state observed for hydrogen on (100)Mo which is not observed on (100)W. It is suggested that this state may also exist on (100)W but not be observed in flash desorption. It is also found that there are significant differences between the binding energies on the substrates. Hydrogen is much more strongly bound on W while nitrogen is more strongly bound on Mo. The difference in hydrogen adsorption is interpreted in terms of the greater bonding capabilities of the 5d *vs.* 4d electrons of the substrates, while the strength of the nitrogen adsorption bond on Mo is attributed to the lateral interaction in the plane of the substrates which should be stronger for Mo than for W.

Introduction

In spite of considerable experimental and theoretical effort devoted to investigations of adsorption, the complexity of the atomic and electronic structures of surfaces has thus far prevented more than qualitative explanations of chemisorption bonding. One fruitful approach in attempting to elucidate the nature of chemisorption bonds should be a precise comparison of similar adsorbates on the same substrate and a comparison of an adsorbate on similar substrates.

In this paper the adsorption of hydrogen and nitrogen on the (100) crystal plane of molybdenum will be examined. These adsorbates exist on the surface as atoms, probably in identical sites, and therefore such measurements should reveal the differences in bonding between a single 1s orbital and three 2p orbitals.

The (100) plane was chosen because of its high symmetry and because detailed measurements of hydrogen[2,3] and nitrogen[4-6] adsorption on the (100) plane of tungsten have been made. Molybdenum and tungsten are isoelectronic, and both form body-centered cubic crystals with nearly identical lattice constants (3.147 *vs.* 3.158 Å); therefore differences in bonding of an adsorbate on these surfaces must be attributed largely to the differences between the 4d and the 5d electrons of the metals.

There have been some studies of the adsorption of these gases[7-9] on polycrystalline Mo wires and ribbons. From such measurements it should be possible to qualitatively compare adsorption on Mo with that on polycrystalline W, an extensively studied substrate. However, there are difficulties in obtaining reproducible results even on polycrystalline W due to crystallographic averaging and in comparing results obtained in different laboratories using different techniques. From such measurements one can only say that nitrogen and hydrogen behave similarly on both substrates. A notable exception to this conclusion comes from the work of Moore and Unterwald,[9] who found evidence for bulk solution of both gases in Mo. We do not observe any effects which appear to indicate bulk solution in Mo and attribute the difference to the fact that Moore and Unterwald employed much higher temperatures and pressures than we do. Further measurements are in progress to examine in more detail the extent of bulk solution.

Experimental Section

The apparatus and experimental procedure have been described in detail previously.[2a,6] Adsorption and desorption of these gases on a single crystal of Mo, ex-

(1) This work partially supported by ARPA under Grant DAHC15-69-G6.

(2) (a) P. W. Tamm and L. D. Schmidt, *J. Chem. Phys.*, **51**, 5352 (1969); **52**, 1150 (1970); (b) P. J. Estrup and J. Anderson, *ibid.*, **45**, 2254 (1966).

(3) K. Yonehara and L. D. Schmidt, *Surface Sci.*, to be published.

(4) P. J. Estrup and J. Anderson, *J. Chem. Phys.*, **46**, 567 (1967).

(5) T. A. Delchar and G. Ehrlich, *ibid.*, **42**, 2686 (1965).

(6) L. R. Clavenna and L. D. Schmidt, *Surface Sci.*, **22**, 365 (1970).

(7) R. A. Pasternak and U. D. Wiesendanger, *J. Chem. Phys.*, **31**, 2062 (1961).

(8) R. A. Pasternak and N. Endow *J. Phys. Chem.*, **70**, 4044 (1966).

(9) G. E. Moore and F. C. Unterwald, *J. Chem. Phys.*, **48**, 5378, 5398 (1968).

posing only the (100) plane, are studied by flash desorption mass spectrometry. The absence of temperature nonuniformities or significant amounts of other crystal planes permits quantitative determination of the rate parameters and stoichiometry.

The crystal was cut from a single crystal of triply zone-refined molybdenum and was in the shape of a rectangular parallelepiped of dimensions 0.3 × 0.2 × 0.010 in. All faces were aligned by X-ray diffraction to within 0.5° of the (100) plane and were polished with successively finer abrasives to a mirror finish. The crystal was suspended by a 0.015-in. tungsten wire and 0.005-in. W–Re thermocouple wires and was heated by electron bombardment from a thoriated tungsten filament. The quadrupole mass spectrometer, tantalum film getter, and chemical gas sources (N_2, H_2, D_2, and O_2) have been described previously.[2a,3,6]

The system was evacuated and baked until the pressure attained $\sim 10^{-10}$ Torr. The crystal was then heated to 1300°K in O_2 at $\sim 10^{-7}$ Torr for several days to remove impurities such as carbon and sulfur. It was cleaned by flashing repeatedly to ~2300°K in O_2 and in ultrahigh vacuum. It was found that extended heating in O_2 was necessary to obtain reproducible flash desorption spectra. Following treatment in O_2 for 1 day, the desorption spectra of H_2 were initially those of the clean surface to be described, but after flashing several times, the amount in the β_1 state diminished. Continued heating in O_2 produced a surface from which reproducible flash desorption spectra could be obtained over a period of months without further oxygen treatment. That the surface after such treatment is indeed clean is attested by several measurements using Auger spectroscopy:[10,11] in some cases heating a Mo crystal to 2300°K *in vacuo* was adequate to produce a clean surface;[11,12] in all instances contaminant-free surfaces were reported after heating in oxygen.

The measurements were duplicated on two crystals, one etched after polishing and one only polished; all adsorption results were identical. In addition one crystal was removed from the system after some measurements had been completed, and ~0.001 in. of metal was removed from each face. This procedure should remove any metal impurities which could have migrated to the surface region during the initial heating. As before, all adsorption results werer eproducible. Spectrochemical analysis of one of the crystals after use indicated a purity greater than 99.99%, with iron, silicon, and chromium as the only detectable impurities.

In flash desorption[2a,6] an adsorbate is allowed to accumulate to a desired coverage n_0 on the surface maintained at a temperature T_0, and then the desorption rate parameters are determined by measuring the amount desorbed as a function of time by programming the surface temperature to vary approximately as $T = T_0 + \beta t$ where β is a constant. The desorption rate from a single state is given by the expression

$$-\frac{dn}{dt} = \nu_0^{(m)} e^{-E_d/RT} n^m \qquad (1)$$

where $\nu_0^{(m)}$ is the preexponential factor for desorption with order m, and E_d is the activation energy of desorption. For high pumping speeds one obtains a peak for each binding state, and by analysis of the position and shape of these peaks the parameters ν_0, E_d, m, and n_0 for each state can be obtained.

Results

Binding States of Hydrogen. The flash desorption spectra of hydrogen are shown in Figure 1 for different initial coverages up to saturation. The adsorption temperature was 78°K and the heating rate β was 74°/sec. There are three major peaks in the spectra, labeled β_1, β_2, and β_3. Computer generated desorption traces[2a,6,13] for each of these states, using parameters to

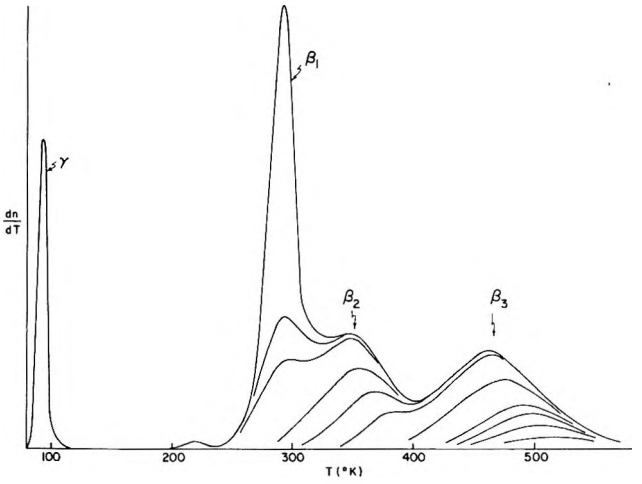

Figure 1. Flash desorption spectra of hydrogen from (100)Mo.

be discussed below, show that over 90% of the adsorbed hydrogen is in these three states.

A plot of log θT^2 *vs.* $1/T$ for the β_3 state, shown in Figure 2, yields a straight line from $\theta = 0.05$ to 0.23 of saturation. This indicates that this state obeys second-order kinetics. The slope and intercept give E_d = 27 kcal mol^{-1} and $\nu_0^{(2)} n_0 = 1.25 \times 10^{13}$ sec^{-1} at low coverage. If the saturation coverage n_0 is assumed to be 5.0×10^{14} atoms cm^{-2} as discussed later, then one obtains $\nu_0^{(2)} = 0.05$ cm^2 molecule^{-1} sec^{-1}.

The desorption spectrum of the β_2 state is symmetric and the maximum shifts to lower temperature with increasing coverage, typical of second-order kinetics.

(10) D. W. Vance, *Phys. Rev.*, **164**, 372 (1967).

(11) G. J. Dooley, III, and T. W. Haas, *J. Chem. Phys.*, **52**, 993 (1970).

(12) K. Hayek, H. E. Farnsworth, and R. L. Park, *Surface Sci.*, **10**, 429 (1968).

(13) P. W. Tamm and L. D. Schmidt, Ph.D. Thesis, University of Minnesota, 1970; also, *J. Chem. Phys.*, to be published.

Table I

System	State	m	Saturation density[a]	E_{d_0}, kcal mol^{-1}	$\nu_0(m)$ ($\theta = 0$), sec^{-1}	a, kcal monolayer^{-1}	a_c/a
H_2 on (100)Mo	β_1	1	2.0 ± 0.05	16 ± 2	$\sim 10^{13}$	0	...
	β_2	2	1.0 ± 0.05	20 ± 2	~ 0.05	...	...
	β_3	2	1	27 ± 2	0.05	2.8	0.86
N_2 on (100)Mo	γ	1	>1.75	9.7 ± 1	$\sim 10^{13}$	...	...
	β	2	1	87 ± 3	0.030	1.5	0.15
H_2 on (100)W	β_1	1	2.0	26	$\sim 10^{13}$	0	...
	β_2	2	1	32	0.042	3.5	0.89
N_2 on (100)W	γ's	1	2.0	9.2 10.5	$\sim 10^{13}$	...	...
	β_2	2	1	80	0.011	5.0	0.6

[a] Densities measured relative to state on that plane designated 1.

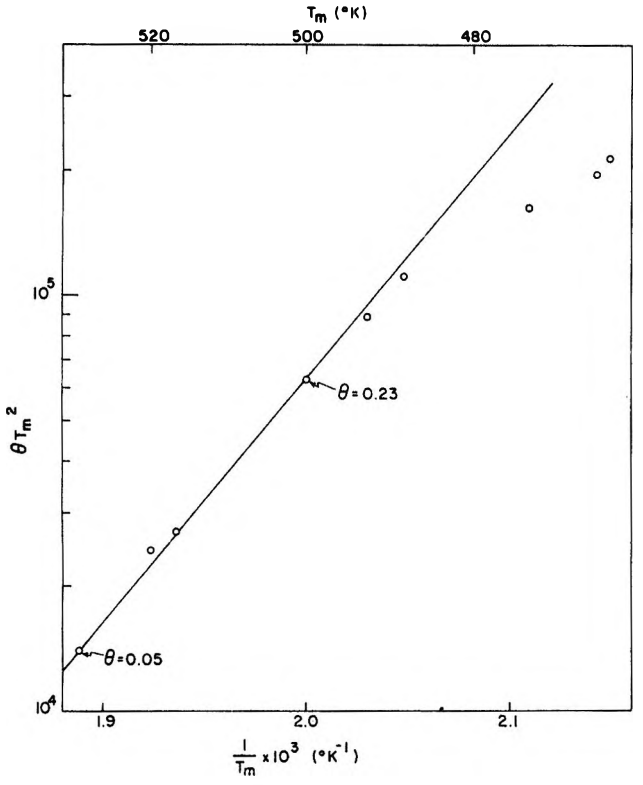

Figure 2. Second-order plot for the β_3 state of hydrogen on (100)Mo. A straight line for coverages ≤ 0.2 of saturation of this state indicates second-order desorption kinetics. The slope and intercept give $E_{d_0} = 27$ kcal mol^{-1} and $\nu_0^{(2)} = 0.05$ cm^2 molecule^{-1} sec^{-1}.

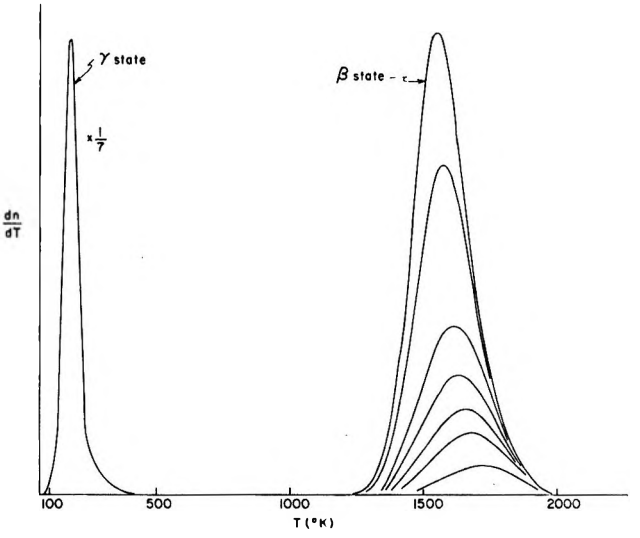

Figure 3. Flash desorption spectra of nitrogen from (100)Mo.

A second-order plot is not possible for this state because of overlap with the β_3 state. However if one assumes $\nu_0^{(2)} = 0.05$, one obtains $E_d = 20$ kcal mol^{-1}.

The β_1 state is much narrower than the β_2 or β_3 states and does not shift with increasing coverage, typical of first-order kinetics. Assuming $\nu_0^{(1)} = 10^{13}$ sec^{-1}, one obtains $E_d = 16$ kcal mol^{-1}. These parameters are summarized in Table I.

The uncertainties in the desorption activation energies listed in Table I arise primarily from assumed uncertainties in the temperature calibration. The activation energies are not very sensitive to almost order of magnitude changes in ν_0.

Binding States of Nitrogen. The flash desorption spectra of nitrogen at various initial coverages[6] are shown in Figure 3. Since the low-temperature γ state is much narrower than the β state, separate spectra at different heating rates were used to obtain quantitative measurements.

There is a single high-temperature state, labeled β, which obeys second-order desorption kinetics as shown by the second-order plot in Figure 4. The slope and intercept give $E_d = 87$ kcal mol^{-1} and $\nu_0^{(2)} n_0 = 7.5 \times 10^{12}$ sec^{-1}. Assuming $n_0 = 5 \times 10^{14}$ atoms cm^{-2}, one obtains $\nu_0^{(2)} = 0.03$ cm^2 molecule^{-1} sec^{-1}.

The β state desorbs at such high temperatures that the heating rate could not be maintained constant throughout, even at very high rates, because of radiative cooling of the crystal. The spectra of the β state shown in Figure 3 have been drawn with a linear temperature scale and an ordinate of $(dn/dt)/\beta(T)$ where $\beta(T)$ is the heating rate (degrees per second) at the corresponding temperature. This gives spectra which appear very

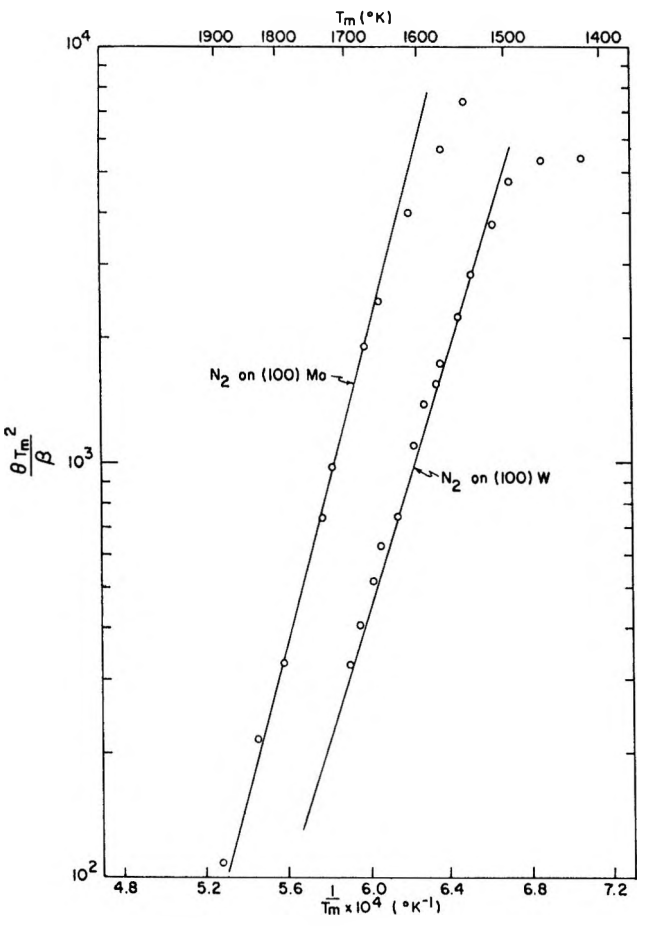

Figure 4. Second-order plots for the tightly bound states of nitrogen on (100)Mo and (100)W. The desorption parameters obtained from these plots are shown in Table I.

similar to those with a precisely constant heating rate and for which the area under a curve still corresponds to the amount adsorbed. Calculated spectra can be compared with experimental ones for any heating rate; this was done by making a polynomial fit of the actual heating curve (obtained from thermocouple–temperature measurements) and using this expression for $T(t)$ to numerically integrate[6] the desorption rate expression.

For nitrogen exposure at pressures up to 1×10^{-7} Torr and times up to 10^3 sec, no additional high-temperature states were observed. This indicates that, if there is a state on (100)Mo corresponding to the first-order nitrogen β_1 state observed on (100)W, it must have a sticking coefficient at least as low as that on tungsten.

The γ state does not shift with coverage and has a width characteristic of first-order desorption kinetics. If $\nu_0^{(1)}$ is assumed to be 10^{13} sec^{-1}, one obtains E_d = 9.7 kcal mol^{-1}. On (100)W two γ states were observed,[6] separated by ~20°. Only one γ state could be resolved in the present measurements.

High Coverage Rate Parameters. At low coverages (less than ~0.2 of saturation) all flash desorption peaks can be fit quantitatively by integrating eq 1 using constant parameters. However, as the amount in a state approaches saturation, it is observed that all second-order states exhibit considerable broadening and shifting of the peak maximum to lower temperatures.[2a,6] The first-order states (β_1 of H_2 and γ of N_2 on both W and Mo) do not broaden or shift at all.

This may arise from a variation of the rate parameters or the presence of other overlapping states. It was shown previously[6] that either a variable activation energy of desorption of the form

$$E_d = E_{d0} - \alpha\theta \tag{2}$$

or a variable preexponential factor of the form

$$\nu_0^{(2)} = \frac{a^2\nu_0}{\left(1 - \frac{a_c}{a}\theta^{1/2}\right)^2} \tag{3}$$

could quantitatively explain the shape of the flash desorption spectra. Equation 3 was derived assuming second-order desorption limited by surface diffusion-controlled recombination of atoms. In these expressions α is an empirical constant, a the diffusion jump length, ν_0 the vibrational frequency, and a_c the critical distance for recombination.

Computer fits of the flash desorption spectra of Figures 1 and 3 were used to determine the values of α and a_c/a, and these values are shown in Table I. The procedure for determining these parameters will be considered in detail elsewhere.[13]

While either equation can be made to fit the data using α and a_c/a as adjustable parameters, and while the values of α so obtained are within the range of those calculated from adsorbate repulsions, the preferred explanation appears to be that of a variable preexponential factor. The evidence for this is that (1) the form of eq 3 is predicted for second-order desorption and (2) broadening is only observed for states which obey second-order desorption kinetics. Similar behavior has also been observed for all first- and second-order states of nitrogen and hydrogen on other crystal planes of tungsten.[13]

Amounts Adsorbed. The relative amounts adsorbed in each state were determined by measuring the areas under peaks in Figures 1 and 3. These results are shown in Table I. It is seen that for hydrogen the ratio is very nearly 2:1:1 for β_1:β_2:β_3 while for nitrogen the ratio γ:β is close to 2:1. Since one expects a simple ratio of saturation amounts for adsorption on a highly symmetric surface, the measured ratios give added support to the supposition that the states being measured do actually exist on the (100) plane.

Absolute amounts are much more difficult to measure accurately because they require absolute calibration of the sensitivity of the mass spectrometer for each mass. Calibration against an ion gauge gave total saturation amounts between 10^{14} and 10^{15} molecules cm^{-2} for both gases, but no more accurate determination was at-

tempted. These amounts agreed well with an estimate from a comparison of the saturation amounts adsorbed on the (100)Mo crystal and the polycrystalline tungsten filament used for bombardment heating.

We conclude from these measurements that bulk solution of hydrogen or nitrogen does not occur under these conditions; if one or more of the peaks observed in flash desorption were from the gases dissolved in the substrates, the saturation amounts would be a function of gas pressure and crystal temperature, contrary to the results.

Isotope Exchange and Conversion between States. Exposure of the crystal at 78°K to a mixture of H_2 and D_2 produced flash desorption spectra of H_2, HD, and D_2 which were characteristic of *complete exchange* in all three states. This is predicted for the atomic states which obey second-order kinetics, and also shows that the first-order β_1 state is either dissociated on the surface or exchanges readily with other atomic species. No HD was observed from the small states below 300°K which are expected to be molecular.

Sequential dosing[2a] of H_2 and D_2 was also studied to determine the extent of conversion between states. In these measurements the β_3 or β_3 and β_2 states were saturated with one isotope, and then the rest of the states were saturated with the other isotope. In all cases complete mixing between states was observed. This shows that conversion between states is rapid compared to the desorption time (~1 sec).

Rate Parameters for Nitrogen on (100)W. One prediction of eq 3 is that at low coverage the preexponential factor for states which obey second-order kinetics should be given by $a^2\nu_0$. This quantity should be approximately 10^{-2} cm^2 molecule^{-1} sec^{-1} for all systems. For the β_2 state of nitrogen on (100)W[6] the value of $\nu_0^{(2)}$ obtained was 0.2 cm^2 molecule^{-1} sec^{-1}, an order of magnitude larger than that predicted. We have redetermined the temperature scale on another W crystal and obtain somewhat different parameters.

The second-order plot for the β_2 state of nitrogen on (100)W is shown in Figure 4 along with that on (100)-Mo. The corrected values of $\nu_0^{(2)}$, E_{d0}, α, and a_c/a are shown in Table I. It is seen that now all of the values of $\nu_0^{(2)}$ determined so far are within a factor of 2 of 0.02 cm^2 sec^{-1}; while this could be fortuitous, it does support the model[6] used in formulating eq 3.

Discussion

Comparison with States on (100)Tungsten. Figure 5 shows flash desorption spectra of hydrogen and nitrogen on (100)Mo and W.[2a,6] The ordinates have been adjusted to give approximately the same peak heights, and therefore the areas under the peaks do not directly represent comparable coverages. The heating rates for hydrogen from both surfaces were ~75°/sec and those for nitrogen were ~350°/sec.

General similarity in binding states for each adsorbate on the two substrates is evident from Figure 5. The relative amounts in the different states also agree closely on both substrates. *In all four systems there is a 2:1 ratio in saturation amounts between those states which obey first-order kinetics and those which obey second-order kinetics.*

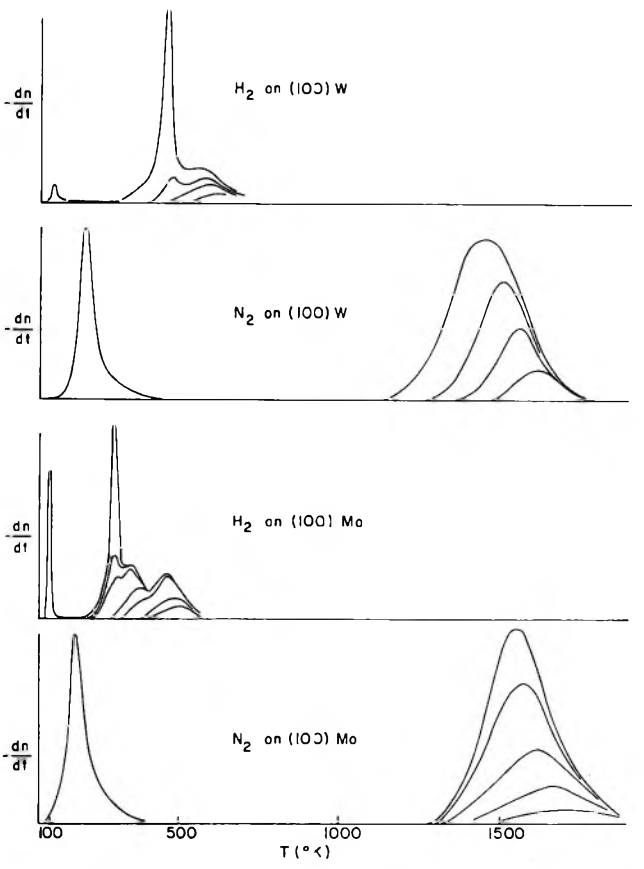

Figure 5. Comparison of flash desorption spectra of hydrogen and nitrogen on (100)W and (100)Mo. The low and high temperature peaks have been normalized to give the same peak heights. In all cases there is one (or more) high-temperature atomic state and a low-temperature state which obeys first-order desorption kinetics. The ratio of saturation densities in these states is approximately 1:2 in all cases.

Comparison of adsorption on the two substrates does reveal two distinct differences, however. First, there is observed *no state of hydrogen on (100)W comparable to the β_3 state on (100)Mo.* The fact that this state was observed on three crystals and has precisely the same saturation amount as the β_2 state argues that it is actually associated with the (100) plane. Second, it is evident from Figure 5 that *hydrogen is significantly more strongly bound on W while nitrogen is more strongly bound on Mo.* The corresponding activation energies for the most tightly bound states are shown in Table I. Inaccuracies in temperature calibrations would of course affect these results. However, we do not believe that these could alter the order of the activation energies. Measurements from room temperature show clearly that hydrogen desorbs from Mo at just over 300°K but at a

much higher temperature from W, and pyrometer measurements of the nitrogen desorption temperatures confirm the temperatures stated.

From the observation of a 2:1 saturation ratio between states for both nitrogen and hydrogen (100)W it was suggested[6] that nitrogen and hydrogen occupy similar sites in the atomic β_2 states and also in the first-order γ and β_1 states. Further evidence for similar sites comes from mixed adsorption studies[14] of these gases on tungsten: the total saturation amount of both gases in the tightly bound states is approximately the same for all compositions, showing that the presence of one adsorbate blocks the adsorption of the other.

The same argument also seems to apply to these gases on (100)Mo. However, the existence of the β_3 state of hydrogen on (100)Mo makes the correspondence less than perfect.

It should also be noted that these results show that there could be no additional binding states with desorption activation energies above $\sim$6 kcal mol^{-1} which had sticking coefficients greater than 10^{-3}. Such states would populate at 78°K and be observed in the flash desorption spectra. States with desorption activation energies less than this would be bound with essentially van der Waals forces.

LEED Structures. Low energy electron diffraction (LEED) has been used for extensive studies of many adsorbates including hydrogen[2b,3] and nitrogen[4] on (100)W; only qualitative LEED measurements have been reported for these gases on (100)Mo.[11,15]

Hydrogen adsorption on (100)W at 300°K produces a succession of LEED patterns.[2b] At low coverage the (1 × 1) structure of the clean surface changes to a c(2 × 2) structure; the extra spots in the $^1/_2,^1/_2$ positions then split and diminish in intensity. Third-order streaks and fourth-order spots are observed at even higher coverages, and finally a (1 × 1) structure is observed at saturation.

Tamm and Schmidt[2a] tentatively identified the c(2 × 2) structure with the β_2 state and postulated that the β_1 state filled in the alternate vacant sites to give the (1 × 1) pattern at saturation. However, more recent LEED measurements[3] at temperatures below 300°K indicated a more complex situation than had been assumed. When an apparently clean surface (less than 0.02 monolayer of desorbable gases) was cooled below 300°K, a sharp and intense c(2 × 2) structure was observed. The extra spots remained sharp even at 78°K where hydrogen (or any other adsorbate) should be immobile. The c(2 × 2) structure still appears to be associated with the β_2 state, but not in the simple fashion envisioned.

One explanation which appears to reconcile the flash desorption and LEED results postulates the existence of a third state of hydrogen (termed β_3 in ref 3) on the tungsten surface at low temperature which dissolves rather than desorbs upon heating. Hydrogen solution in tungsten is endothermic, and therefore its solubility increases with increasing temperature. Consequently it is possible that heating in ultrahigh vacuum even to 2500°K may not be sufficient to remove this state of hydrogen from the crystal.

Dooley and Haas[11] examined the LEED structures resulting from hydrogen adsorption on (100)Mo at room temperature. The (1 × 1) structure of the clean surface changed upon hydrogen exposure to a c(4 × 2) structure; then at "saturation" a (1 × 1) structure was again obtained, but with increased background intensity. They also reported that slight heating of the saturated surface, such as by the electron beam, was adequate to restore the c(4 × 2) structure. Coverages were not determined in these measurements. However, from our results, the states populated at saturation in the measurements of Dooley and Haas should be only the β_2 and β_3 states; at 300°K the β_1 state would have $\geq$0.1 of its saturation coverage only for pressures above 10^{-5} Torr. Further "slight heating" at 300°K should be adequate to remove the β_2 state, leaving only the β_3 state. Therefore we conclude that the β_3 state of hydrogen on (100)Mo produces a c(4 × 2) structure, while population of both the β_2 and β_3 states produces a (1 × 1) structure.

Nitrogen adsorption on (100)W at 300°K produces a c(2 × 2) structure which remains at saturation.[4] These conditions should fill only the β_2 state, and no LEED measurements have been made at lower temperatures or higher exposures where γ or β_1 states are populated. Nitrogen adsorption on (100)Mo has only been qualitatively studied using LEED.[12]

Additional State of Hydrogen on Molybdenum. Comparison of hydrogen on Mo and W shows that, while both have β_1 and β_2 states in a ratio of 2:1 and both give (1 × 1) LEED patterns at saturation, there is an extra state (β_3) observed in flash desorption from Mo.

The different configurations shown by LEED must be due to the different electronic structures of the substrates. The c(2 × 2) structure was predicted[2a] if the substrate atom has bonding electrons with only s and d character. However, if significant p character exists (wave functions of odd symmetry), the c(2 × 2) structure should be less stable. It is readily possible to devise atomic configurations which could give a c(4 × 2) structure, but the significance of these is doubtful without precise coverage determinations.

Estrup[15] has noted that the surface structure proposed by Dooley and Haas[11] for hydrogen on (100)Mo, requiring two types of sites for hydrogen, is incorrect. A simple 4 × 2 configuration with an atom in the center of the cell would produce the observed LEED pattern.

(14) T. E. Madey and J. T. Yates, Jr., *J. Vac. Sci. Tech.*, to be published.

(15) P. J. Estrup, private communication.

The coverage (fraction of the fourfold coordination sites on the surface) of this structure is $^1/_4$, precisely the fraction of the hydrogen observed to be in the β_3 state. The only obvious way for population of the β_2 state to result in a (1×1) pattern is by producing a disordered absorbate configuration.

As discussed previously, one possible explanation of the apparent absence of the β_3 state of hydrogen on (100)W is that this state actually exists on the W surface also but goes into solution upon heating rather than desorbing. While hydrogen is endothermically dissolved in both Mo and W, it is more strongly bound (less endothermic) in Mo. Therefore it is possible that the β_3 state on (100)Mo desorbs upon heating because its solubility does not increase rapidly enough with temperature for bulk solution. A satisfying feature of this picture is that now completely analogous states of hydrogen are postulated for both substrates.

Binding Energies. In this section we offer some qualitative suggestions regarding the differences in binding energies on W and Mo in terms of the electronic structures of the constituents. The results summarized in Figure 5 and Table I show that, while the crystal structures and lattice constants of the substrates are the same, hydrogen is more strongly bound on W while nitrogen is more strongly bound on Mo. From presently available evidence it is not possible to unequivocally determine adsorbate atom configurations, although the models proposed previously[2-4] are reasonable alternatives. In this discussion it will only be assumed that the *same* type of sites are involved for the most tightly bound states of both nitrogen and hydrogen on both substrates.

More detailed considerations of the electronic structure of surface and changes produced by adsorbates will be presented later. Basically we assume that the altered and asymetric potential near the surface shifts and splits the bulk energy states of the solid; adsorbed molecules further perturb these states, the difference in total energy being the binding energy of the adsorbate. The reduced symmetry at the surface produces crystal field splitting of the valence levels of the surface atoms into components perpendicular and parallel to the surface. The wave vector describing the parallel component remains real while that for the perpendicular component is complex, corresponding to the wave function being damped at the surface. Since these components have different energies and symmetries, it is convenient to consider them separately. In both directions binding results from overlap between the wave functions of the metal and the adsorbate. However, parallel to the surface there is the possibility of long-range interactions. A major factor in determining chemisorption binding energies on the transition metals should be the lowering of the surface energy of the metal by adsorption because these solids have surface energies comparable to or greater than adsorption binding energies.

The pertinent wave functions of the adsorbates should be the 1s orbital of the hydrogen atom and the three 2p orbitals of nitrogen. The wave functions of the metal which are involved in adsorption bonding are obviously more difficult to describe. The wave functions of proper energy for bonding should be primarily the 4d and 5s of Mo and the 5d and 6s of W. However, the asymmetric potential at the surface should shift states of even symmetry (s and d) upward in energy from their bulk values and those of odd symmetry (p) downward. Therefore it is possible that bonds at the surfaces of transition metals may have significant p character. (The lowest bulk p band of W is only $\sim$0.3 eV above the Fermi energy.)

1. Bonding Perpendicular to Surface. This is a major component of bonding for both adsorbates, and, since hydrogen has only one electron, it is probably involved primarily in such interactions. The three 2p orbitals of the nitrogen atom are in orbitals perpendicular to each other; from symmetry (assuming sites with fourfold coordination) one of these orbitals should be directed perpendicular to the surface and the other two directed parallel to the surface. The crystal field of the substrate also removes the degeneracy of these orbitals of nitrogen.

There are at least two effects which should result in different binding energies on Mo and W from bonds directed largely perpendicular to the surface: (1) overlap of 4d *vs.* 5d wave functions of the substrates, and (2) the different surface energies of the metals. Both of these appear to predict stronger adsorption bonding on W than on Mo. The 5d wave function has a greater radial extension than the 4d. The lattice constants are the same, and it is reasonable to assume the adsorbates to be approximately the same distance from the substrate atoms. Therefore greater overlap is possible with W than with Mo.

2. Bonding Parallel to Surface. While the preceding arguments may explain why hydrogen is more strongly bound on W than on Mo, the results for nitrogen show an opposite trend. To explain this we consider the parallel component which is more important for nitrogen because two electrons are in possible σ-bonding orbitals with this orientation.

Nitrogen and hydrogen atoms in the sites with fourfold symmetry are almost coplanar with the layer of surface metal atoms.[6] Therefore a significant contribution to bonding in this direction should be due to the strengthening of metal–metal bonds by the presence of the nonmetal atom. This is a major contribution to the stability of the transition metal nitrides, carbides, and hydrides.[16-18] The body-centered cubic metals incorporate these atoms in octahedral (interstitial) sites;

(16) R. G. Lye in "Atomic and Electronic Structure of Metals," American Society for Metals, Metals Park, Ohio, 1967, p 99.

(17) V. Ern and A. C. Switendick, *Phys. Rev.*, **137**, A1927 (1965).

(18) H. Bilz, *Z. Phys.*, **153**, 338 (1958).

this produces only a slight change in lattice constant but a large increase in cohesive energy. Calculations using the tight binding approximation indicate that the presence of a p orbital in these sites significantly increases the overlap of the d wave functions of the metal atoms.[16-18]

We suggest that nitrogen and, to a lesser extent, hydrogen adsorbed in these sites on (100)W or Mo stabilizes the surface in an analogous fashion. The geometry of adjacent adsorbate atoms on the (100) plane is similar to that of these atoms in the bulk compounds, and it is expected that the interactions should also be similar.

Summary

There are close similarities between nitrogen and hydrogen as adsorbates on (100)Mo and between (100)-Mo and (100)W as substrates for these gases; this implies that similar bonding mechanisms are operative. Yet the differences between the four systems, different LEED structures of hydrogen and different binding energies on the substrates, show definite effects of the "chemical" nature of the substrates.

Precise experimental comparison of simple adsorption systems promises to provide an important means of elucidating the nature of solid surfaces and their interactions with adsorbates. However, the evidence to date indicates that, while ideas such as those discussed here may be possibilities, chemisorption is complex enough that additional correlation between systems will be necessary to establish the character of adsorption bonds.

Infrared Studies of Adsorption and Surface Reactions of Some Secondary Alcohols, C_3 to C_5, on γ-Alumina and γ-Alumina Doped with Sodium Hydroxide

by A. V. Deo, T. T. Chuang, and I. G. Dalla Lana*

Department of Chemical and Petroleum Engineering, University of Alberta, Edmonton, Alberta, Canada
(Received May 18, 1970)

Publication costs assisted by the National Research Council of Canada

Infrared studies of the adsorption of secondary alcohols, 2-propanol, 2-butanol, and 3-pentanol, on γ-alumina and γ-alumina doped with sodium hydroxide catalysts, in the temperature range from room temperature to 300° are described. On γ-alumina four types of surface species were observed: (i) alcohol hydrogen-bonded to surface hydroxyl groups; (ii) an alkoxide-type structure chemisorbed on Lewis acid sites, Al^{3+}; (iii) a partial double bond type structure which on desorption gives an olefin; and (iv) a carboxylate species which is stable even at high temperatures. The physically adsorbed species are mainly dehydrated, forming a mixture of olefinic isomers. On sodium hydroxide doped γ-alumina, in addition to the species i, ii, and iv, a ketone-like species was detected which on desorption gave a ketone. Two types of carboxylate species may exist on sodium hydroxide doped catalyst. A mechanism for the formation of carboxylate species, identical for both of the catalysts studied, is proposed. The three alcohols follow similar mechanisms for dehydration and dehydrogenation, with 3-pentanol reacting at a lower temperature than encountered with 2-butanol and 2-propanol.

Introduction

In an earlier paper,[1] we reported an infrared study of the adsorption and surface reactions of 1-propanol on γ-alumina doped with sodium hydroxide and chromium oxide. The main reaction on γ-alumina was observed to be dehydration of the alcohol to the olefin. On sodium hydroxide doped γ-alumina, dehydrogenation was predominant, but some olefinic products with conjugation were still observed.

Previous studies of the adsorption of primary alcohols[1-4] on γ-alumina using the infrared spectroscopic

(1) A. V. Deo and I. G. Dalla Lana, *J. Phys. Chem.*, **73**, 716 (1969).
(2) R. G. Greenler, *J. Chem. Phys.*, **37**, (9), 2094 (1962).
(3) de M. V. Corso, *Compt. Rend.*, **259**, 1413 (1964).

technique indicated the presence of three types of surface complexes: physically adsorbed alcohol, an alkoxide type species, and a carboxylate type species. Our previous results[1] on sodium hydroxide doped γ-alumina showed the presence of a conjugated hydrocarbon species in addition to the above three surface species.

While studying the adsorption of isopropyl alcohol on alumina, Yakerson, *et al.*,[5] suggested that hydrogen-bonded alcohol yields propylene while alcohol bonded to a lattice aluminum atom forms acetone, with the formation of a complex with acetate character as a side reaction. Knozinger, *et al.*,[6] studied the kinetics of dehydration of primary and secondary alcohols and reported that the stable alkoxide is an intermediate in the formation of ether while the olefin is formed through a secondary elimination-type reaction intermediate. Tamaru and coworkers,[7] studying the decomposition of 2-propanol over alumina, suggested that the alkoxide is an intermediate for the function of both ether and olefin. Pines and Manassen[8] reported that the olefin formation also goes through a secondary elimination reaction intermediate. Our present paper discusses the results of adsorption of secondary alcohols from C_3 to C_5 on γ-alumina and sodium hydroxide doped γ-alumina catalyst systems from room temperature to 300°.

Experimental Details

The procedures for preparing γ-alumina (Cabot Corp., Boston, Mass.) and 2% sodium hydroxide doped γ-alumina catalyst wafers, their pretreatment, and the recording of their infrared spectra on a Perkin-Elmer Model 621 infrared spectrophotometer were similar to those reported earlier.[1]

All of the alcohols, ketones, and alkenes used in this work were of spectroscopic grade and were purified by freezing and thawing under vacuum. Differential spectra were recorded by placing an identical cell, but without the catalyst wafer, in the reference beam to eliminate any gas phase interference. To evaluate the extent of reaction, the gas phase was analyzed by infrared and gas chromatographic or mass spectral analysis.

After recording the base line spectrum, *i.e.*, the spectrum obtained for the catalyst wafer in an evacuated cell, the reactant vapor was introduced to a pressure of 10 Torr. The reactant was exposed to the wafer, and the cell was then either pumped off or heated to various temperature levels. Depending on the sequence of experiments being performed, various combinations of heating and/or degassing cycles were performed. The ir spectra were measured at room temperature during the experimental cycles. Figures 1 and 2 show selected representative spectra and the significant changes in them which were noted during this study. To improve differentiating between spectra,

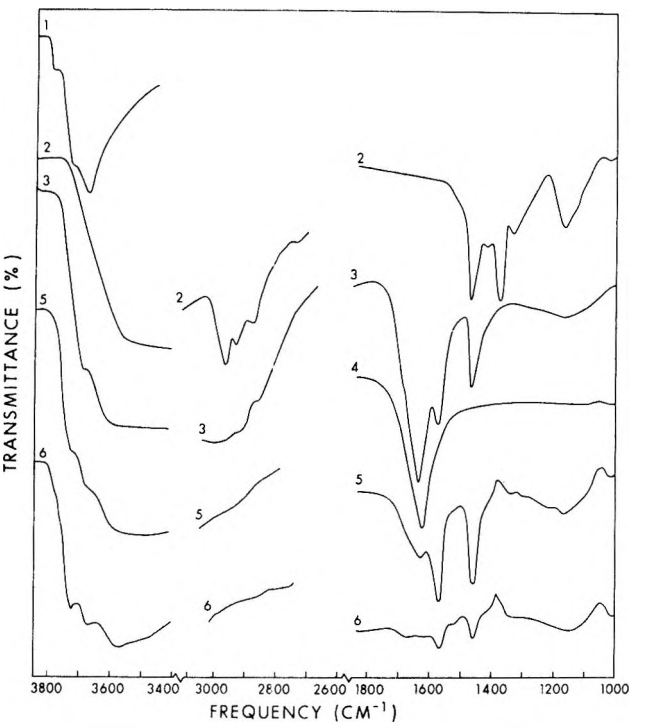

Figure 1. 2-Propanol on γ-alumina: 1, base line; 2, γ-alumina and 2-propanol at 10 Torr and room temperature; 3, γ-alumina and 2-propanol at 300° for 1 hr; 4, γ-alumina and water vapor at 5 Torr and room temperature; 5, degassing of 3 at room temperature for 1 hr; 6, degassing of 5 at 300° for 1 hr.

the successive spectral curves are shown displaced from one another on an arbitrary transmission coordinate scale. The curves drawn in the region from 1000 to 1800 cm^{-1} are shown with the base line spectrum subtracted from the recorded adsorption spectrum.

Results and Discussion

The base line spectra of γ-alumina and sodium hydroxide doped γ-alumina were discussed previously.[1] The base line of γ-alumina was interpreted using the model proposed by Peri.[9,10]

The level of sodium hydroxide doping which was used results in the disappearance of the high-frequency 3785-cm^{-1} hydroxyl bond suggesting a reaction to form =Al—O—Na. If this interpretation is correct it is inconsistent with Peri's view that the higher acidity is associated with the lower frequency hydroxyl groups.

I. 2-Propanol on Pure γ-Alumina. Figure 1 shows the spectra of 2-propanol adsorbed on pure γ-alumina

(4) R. O. Kagel, *J. Phys. Chem.*, **71**, 844 (1967).
(5) Y. Yakerson, L. Lafer, and A. Rubinshtein, *Dokl. Akad. Nauk SSSR*, **174**, (1), 111 (1967).
(6) H. Knozinger, H. Buhl, and E. Ress, *J. Catal.*, **12**, 121 (1968).
(7) Y. Soba, T. Onishi, and K. Tamaru, *Trans. Faraday Soc.*, **65**, 2215 (1969).
(8) H. Pines and J. Manassen, *Advan. Catal.*, **16**, 49 (1966).
(9) J. B. Peri and R. B. Hannan, *J. Phys. Chem.*, **64**, 1526 (1960).
(10) J. B. Peri, *ibid.*, **69**, 20 (1965).

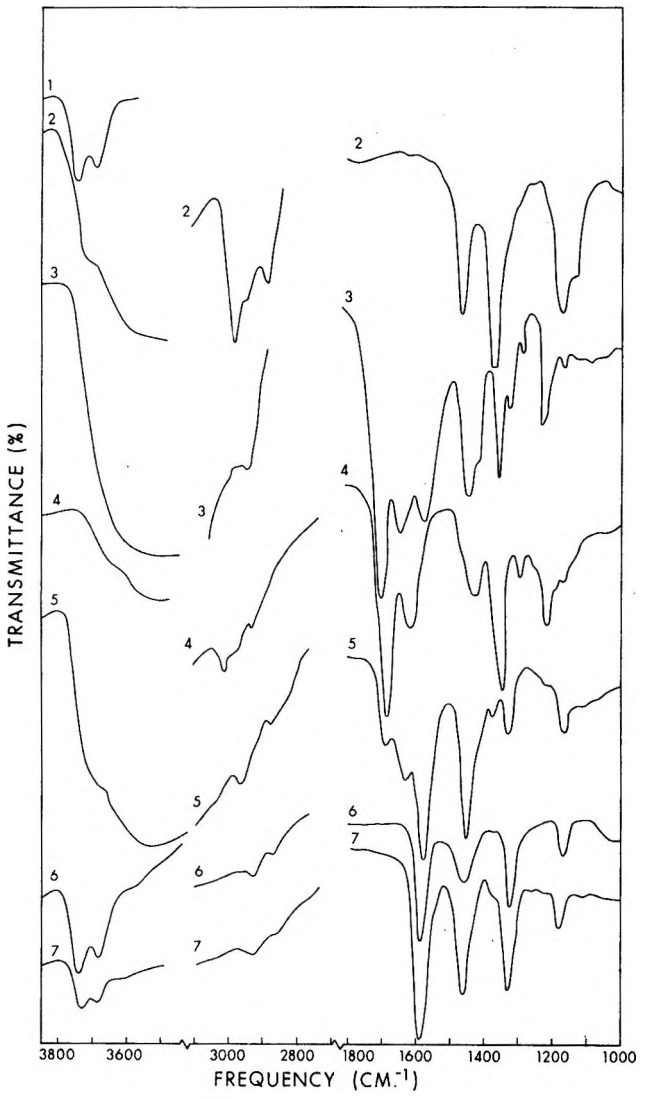

Figure 2. 2-Propanol on NaOH doped γ-alumina: 1, base line; 2, doped alumina and 2-propanol at 10 Torr and room temperature; 3, doped alumina and 2-propanol at 300° for 1 hr; 4, doped alumina and acetone at 10 Torr and room temperature; 5, degassing of 3 at room temperature for 1 hr; 6, degassing of 5 at 300° for 1 hr; 7, degassing of 4 at 300° for 1 hr.

from room temperature to 300°. Up to 80° (curve 2), the surface hydroxyl groups are displaced considerably to the lower frequency with the formation of a large broad hydrogen-bonded hydroxyl region. On adsorption, the three bands observed in the gas phase at 2981, 2972, and 2888 cm^{-1} have shifted to the lower frequencies at 2960, 2930, and 2870 cm^{-1}. The C–H bending region shows almost no change in frequencies except that the intensity of the band at 1465 cm^{-1} has increased twofold over that in the gas phase in contrast to the band at 1373 cm^{-1}. These changes are similar to those observed during the transition from gas to liquid phases.[6] The three distinct bands at 1245, 1145, and 1065 cm^{-1} in the O–H bending and C–O stretching regions, observed in the gas phase spectrum, on adsorption merge into a single broad band at 1170 cm^{-1}. These observations suggest that 2-propanol is physically adsorbed through the hydrogen bonding between the –C–OH of the alcohol and the surface hydroxyl groups (as shown in structure I).

In addition to the hydrogen-bonded species, the close similarity between the spectrum of the adsorbed species and that of aluminum isopropoxide suggests the presence of an alkoxide[2,4] type of structure, II. Pumping at room temperature and up to 80° removed most of the physically adsorbed hydrogen-bonded species, leaving the alkoxide type structure on the surface. The formation of such an alkoxide species on the electron-abstracting Lewis acid site, Al^{3+}, is in agreement with other work.[1,2,4]

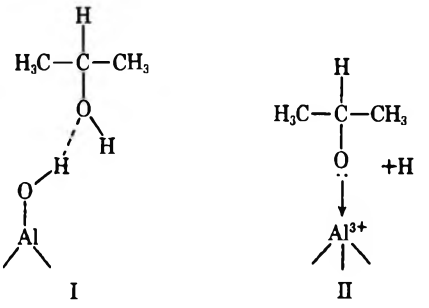

On heating above 100° and up to 300° (curve 3), all of the band structure attributable to these two species disappears, giving propylene in the gas phase and leaving adsorbed water on the alumina surface. This is indicated by the strong band at 1635 cm^{-1}, the O–H bending vibration. For comparison, curve 4 shows this band when water vapor is adsorbed on γ-alumina. This adsorbed water can be removed by pumping, even at room temperature. The dehydration reaction[8] can proceed as shown in reaction 1.

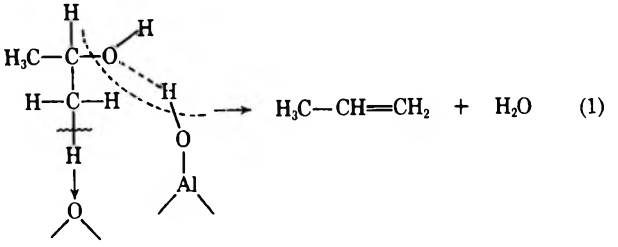

Above 130°, two new bands appear at 1575 and 1465 cm^{-1}, and they increase in intensity with increasing temperature. The observed bands could be assigned to the symmetrical and asymmetrical stretching vibrations of the COO^- groups of an acetate.[2] The formation of a carboxylate from the alkoxide species as explained by Greenler[2] and Kagel[4] has been subject to criticism by Fink;[11] *i.e.*, it seems unlikely that three hydrogen atoms will split from the alkoxide and an adjacent hydroxyl group. However, the adsorption of acetone on γ-alumina at 220° produced the same

(11) P. Fink, *Rev. Roum. Chim.*, **14**, 811 (1969).

infrared characteristics that were observed for the proposed carboxylate species IV obtained with 2-propanol. Although acetone was not detected as an intermediate product from 2-propanol, the adsorbed acetone may have been present in the form of species III preceding the formation of the carboxylate structure. Additional evidence[12] supporting this explanation arises from the studies with the sodium hydroxide doped γ-alumina. The doping eliminates or modifies active surface hydroxyl groups. Under these conditions, large amounts of the adsorbed acetone-like species III can be found by adsorbing 2-propanol at 130°. Upon further heating above 220°, large amounts of the carboxylate species were detected. Reaction 2 seems plausible for the formation of carboxylate.

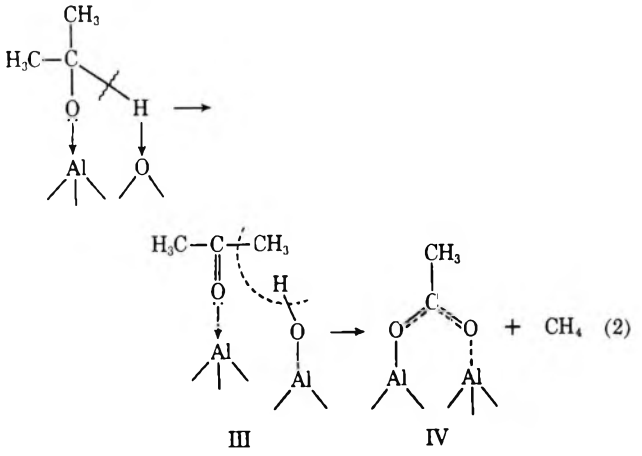

III IV (2)

The presence of methane in the gas product was confirmed by high-resolution mass spectral analysis. In addition, the acetate structure IV could be partially hydrolyzed by water above 220° to form acetic acid. These observations further support the proposed reaction steps (2).

The formation of ether observed elsewhere,[6] particularly at low temperatures, was not observed in this study. It is possible that the ether is present in undetectable amounts or that it rapidly forms the alkoxide species.[13] Moreover, the formation of ether from secondary alcohols is thermodynamically less favorable than the formation of olefins.[14]

II. 2-Butanol on γ-Alumina. The spectra obtained from the adsorption of 2-butanol on γ-alumina up to 300° suggested that the surface reactions are similar to those observed with 2-propanol. The products from dehydration were detected in the gas phase to be a mixture of 1-butene and *trans*- and *cis*-2-butene. Consistent with thermodynamics, their distribution appeared in the order *trans*-2- > *cis*-2- > 1-butene. Little of the carboxylate species was noted even at a temperature of 300°. Since the carboxylate species is formed from the alkoxide species, the reduced amount of alkoxide initially present could account for this. Two infrared bands detected at 1561 and 1479 cm^{-1} and analysis of the gas phase confirmed the presence of a propionate[1] structure. Methane accompanied the dehydration products and propionic acid was found upon hydrolysis at 220°. These observations are consistent with the explanation for the acetate structure formation shown in reaction 1. It would thus be anticipated that a secondary alcohol may form some carboxylate and an alkane fragment upon heating in the presence of γ-alumina.

III. 3-Pentanol on γ-Alumina. The spectrum of 3-pentanol adsorbed on γ-alumina at room temperature is similar to those for 2-propanol and 2-butanol, showing the presence of both hydrogen-bonded and alkoxide species. On heating at 80°, a stable new band was observed at 1685 cm^{-1} accompanied by the formation of a trace amount of mixture of *cis*- and *trans*-2-pentene. This 1685-cm^{-1} band occurs at a frequency too high to be attributable to the O–H bending band of water formed on dehydration. An alternative explanation attributes this 1685-cm^{-1} band to some partial double bond character similar to but not necessarily identical with that associated with an adsorbed olefin. This species may be represented by structure V, which could be an intermediate in the dehydration reaction.

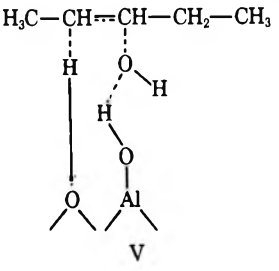

V

A similar band at 1675 cm^{-1} was observed on adsorbing either *cis*-2-pentene or *trans*-2-pentene on γ-alumina, stable even on prolonged pumping at room temperature. Because of its position near to this frequency and because it was stable and reproducibly obtained only from 3-pentanol adsorption, the 1685-cm^{-1} band was not attributed to an adsorbed olefin. However, the existence of the intermediate V does require further substantiation. Above 80°, the dehydration proceeds at a faster rate, making it more difficult to observe the 1685-cm^{-1} band. The 1640-cm^{-1} band due to O–H bending of adsorbed water increases with temperature and above 220°, 1-pentene is formed.

At 130°, the carboxylate species is formed along with the alkoxide species, shown by an increase in the intensity of the broad band at 1150 cm^{-1}. The carboxylate structure (in this case, propionate) remains stable even when pumping at 300° and would be expected to produce ethane, analogous to the methane formed in reaction 2.

IV. 2-Propanol on NaOH Doped γ-Alumina. Fig-

(12) T. Chuang and I. G. Dalla Lana, unpublished results.

(13) E. Heiba and P. Landis, *J. Catal.*, 3, 471 (1964).

(14) H. Knozinger and R. Kohne, *ibid.*, 3, 559 (1964).

ure 2 shows the spectra obtained from adsorption of 2-propanol on sodium hydroxide doped γ-alumina from room temperature to 300°. At temperatures up to 130° (curve 2), the hydrogen-bonded species I is formed to a much lesser degree than was observed on the γ-alumina. The elimination of many surface hydroxyl groups by reaction to form =Al—O—Na would account for this reduced physical adsorption. The presence of the alkoxide species II was shown by the deep band at 1165 cm^{-1}.

Above 130°, dehydrogenation occurs to form acetone along with minor dehydration indicated by a trace of propylene. The bands at 1705, 1640, 1440, 1360, 1300, and 1227 cm^{-1} (curve 3) originate with the acetone adsorbed on Al^{3+} sites. The band at 1640 cm^{-1} results from the adsorbed acetone as well as from some adsorbed water formed during dehydration. In addition to this band structure, four more bands are observed at 1572, 1456, 1330, and 1170 cm^{-1} (curve 3). The pair of bands at 1572 and 1456 cm^{-1} are attributed to the carboxylate species, similar to those found on γ-alumina. The remaining two bands at 1330 and 1170 cm^{-1}, which also always appear as a pair and occur in the carboxylate frequency range, were tentatively assigned to a second type of carboxylate structure. On pumping from room temperature (curve 5) to 300° (curve 6), the band structure due to acetone completely disappears, leaving only the four carboxylate bands.

Additional studies[12] with only the ketone and carboxylate adsorbed species present on the doped alumina indicated, upon heating, a decrease in the intensity of ketone bands along with an increase in intensity of both pairs of carboxylate bonds. Further, mass spectral analysis of the degassed phase showed only methane to be formed, in substantial agreement with the proposed mechanism shown in reaction 2. On this basis, the assignment of the additional band pair at 1330 and 1170 cm^{-1} to a second carboxylate structure seemed logical.

The presence of these two pairs of bands may be the result of differences in charge distributions and in symmetry considerations for oxygen atoms and their energy of bonding to the surface.[15] By doping γ-alumina with sodium hydroxide, it was observed that the high-frequency hydroxyl groups disappeared. This, according to Peri's model, should change the charge distribution of oxygen atoms which are responsible for the carboxylate formation.

Acetone was adsorbed on unused sodium hydroxide doped γ-alumina catalyst, and the system was then heated to 130° (curve 4) to compare adsorbed acetone and its behavior with the intermediate III which led to the formation of acetone. This spectrum is very similar to that observed on heating the catalyst in the presence of 2-propanol (curve 3). Upon degassing the catalyst exposed to pure acetone at 300°, only the carboxylate structure remained (curve 7). This confirms the formation of an adsorbed acetone-like species, III, like that obtained from 2-propanol and which on desorption gives acetone.

V. 2-Butanol on NaOH Doped γ-Alumina. The spectra of 2-butanol adsorbed on sodium hydroxide doped γ-alumina from room temperature to 300° were also studied but are not shown because of their similarity to Figure 2. At temperatures up to 80°, the alkoxide species is formed with very little hydrogen-bonded species appearing. Near 130°, the dehydrogenation reaction starts to form species II as shown by the increased band intensity at 1730 cm^{-1} attributed to the C=O stretching frequency. After heating at 300°, the carboxylate structure spectrum became dominant. Heating of adsorbed 2-butanone on a newly prepared catalyst wafer gave spectra similar to those from 2-butanol. Both 2-butanol and 2-butanone produced carboxylates with bands identical with those observed with 1-propanol[1] on the doped γ-alumina.

VI. 3-Pentanol and NaOH Doped γ-Alumina. The various spectra of 3-pentanol adsorbed on sodium hydroxide doped γ-alumina from room temperature to 300° were also compared. At room temperature, the main species is again the alkoxide type. The dehydrogenation reaction occurs at a still lower temperature, 80°, and continues up to 300° with the formation of the stable carboxylate species. Adsorption of 3-pentanone formed by heating shows spectral characteristics comparable to those expected from reaction 2.

Conclusions

I. γ-Alumina. Secondary alcohols are primarily dehydrated by hydrogen bonding to surface hydroxyl groups on γ-alumina at temperatures ranging from 80° for 3-pentanol to higher temperatures for 2-butanol and 2-propanol, respectively. At lower temperatures, an alkoxide surface species also appeared and reacted at higher temperatures to form a surface carboxylate structure, stable to 300°. Contrary to other reports,[7,13] the alkoxide did not lead to the formation of detectable amounts of ether.

With 3-pentanol, a hydrogen-bonded surface intermediate suspected of possessing a partial double bond character was postulated to form during the dehydration but before formation and desorption of the olefin occurs. A mixture of olefins was obtained with some catalytic selectivity exhibited. Up to 80°, only 2-pentenes were observed and above 80°, significant 1-pentene also appeared.

II. NaOH Doped γ-Alumina. Doping of γ-alumina with sodium hydroxide reduced the number of high-frequency surface hydroxyl groups, thus leading to a reduction in the hydrogen-bonded surface species formed from secondary alcohols. Correspondingly increased amounts of alkoxide surface species were detected for the three

(15) L. Bertsch and H. Habgood, *J. Phys. Chem.*, 67, 1621 (1963).

alcohols studied. At high temperatures, minor dehydration was accompanied by increasing dehydrogenation to ketones. An adsorbed ketone-like intermediate was observed analogous to the adsorbed secondary alcohol. With further heating to 300° the ketone-like intermediate formed a stable carboxylate surface structure accompanied by release of methane from the secondary alcohols, 2-propanol and 2-butanol.

The doping of γ-alumina with sodium hydroxide alters the catalytic activity from dehydration to dehydrogenation. Since two types of sites are involved, elimination of the more active surface hydroxyl groups by doping enables the less active aluminum ion sites to assume the primary catalytic role. It appears unlikely that a product degassed from the surface carboxylate species will appear in other than trace amounts.

Acknowledgment. Financial support for A. V. D. and T. T. C. from the National Research Council of Canada and the University of Alberta is gratefully acknowledged.

An Examination of the Zwanzig Theory of Dielectric Friction. II

by Roberto Fernández-Prini and Gordon Atkinson*

Department of Chemistry, University of Maryland, College Park, Maryland 20740 *(Received September 25, 1970)*

Publication costs assisted by Office of Saline Water, Department of the Interior

The recent revision of the Zwanzig theory for the dielectric friction effect on ion mobility has been examined for representative monovalent ions in a number of pure solvents and solvent mixtures. The theory is shown to predict quantitatively the dependence of mobility on ion radius in dipolar aprotic solvents. The correct trends are predicted in protic solvents but the absolute magnitudes of the mobilities show systematic deviations from the predictions. Some possible explanations for these deviations are advanced.

Introduction

One of the most unappealing features of the classical electrolyte theory is the primitive view taken of ion–solvent interactions. The Debye–Fuoss–Onsager solvent is a classical continuum completely characterizable by macroscopic parameters such as dielectric constant, viscosity, and density. Generally it is also assumed that the solvent parameters are those of the pure solvent unaffected by the presence of the ions. Since most research workers in the field had little faith that this was an adequate model, the search for more sophisticated views of ion–solvent interaction has gone on simultaneously with the search for a more complete treatment of ion–ion interactions.

The ionic conductance at infinite dilution, λ_i^0, has been a favorite measure of ion–solvent interaction for many years. However, the basis for the discussion was commonly taken as Stokes' law

$$\lambda_i^0 = z\mathfrak{F}^2/(6\pi N r_i \eta) \qquad (1)$$

(all symbols are defined in the Appendix) which leads to the often-used Walden rule

$$(\lambda_i^0\eta) = \frac{z\mathfrak{F}^2}{6\pi N r_i} \qquad (2)$$

Since it became clear that r_i was rarely equal to the crystallographic radius, a literature developed on the discussion of solvation in terms of the discrepancy, r_i (Stokes) $> r_i$ (crystal). The discussion was often couched in terms of solvation numbers. The discussion, of course, was somewhat muted in the cases where r_i (Stokes) $< r_i$ (crystal).

However, it is well known that most of this type of calculation is of dubious value since the frictional force acting on a moving ion depends not only on the viscosity of the medium but on its dielectric properties.[1] Boyd[2] and Zwanzig[3] calculated the dielectric frictional force assuming the relative velocity between the ion and any volume element in the medium is constant. This frictional force arises from the energy dissipated by the ion in orienting the solvent dipoles it encounters as it moves through the medium. Combining this with Stokes' law gives a Walden product expression of the form

$$(\lambda_i^0\eta)^{-1} = Ar_i + B/r_i^3 \qquad (3)$$

where A and B characterize the viscous and dielectric

(1) (a) M. Born, *Z. Physik.*, **1**, 221 (1920); (b) R. M. Fuoss, *Proc. Nat. Acad. Sci.*, **45**, 807 (1959).

(2) R. H. Boyd, *J. Chem. Phys.*, **35**, 1281 (1961); **39**, 2376 (1963).

(3) R. Zwanzig, *ibid.*, **38**, 1603 (1963).

frictional forces due to the medium. The ionic mobilities required by eq 3 when r_i was made equal to the ionic crystal radius were much smaller than those observed experimentally.[4,5] Furthermore, plots of $(\lambda_i^0\eta)^{-1}$ *vs.* B for a given ion in different solvents gave different values of r_i depending on whether the slope or the intercept of the line was taken.[4,6] Therefore, though the dielectric drag effect seemed to be real and qualitatively calculable, the quantitative features left much to be desired.

In addition, Frank[7] and Agar[8] pointed out that the dielectric friction force was overestimated by Zwanzig since in its calculation the medium was considered to move at a constant velocity relative to the ion. In actuality, due to viscous drag, the relative velocity of ion and solvent will depend on the distance between the ion and a volume element of solvent. Zwanzig (Z)[9] has recently revised his theory of dielectric friction to allow for this effect. In the calculation he examines both the velocity field for the solvent surrounding the ion which corresponds to perfect sticking (Stokes' viscous motion) and also that corresponding to perfect slipping of solvent at the surface of the ion. The resulting equation is

$$(\lambda_i^0\eta) = \frac{ze\mathcal{F}}{A_V\pi r_i + A_D\dfrac{(ze)^2}{r_i^3}\dfrac{(\epsilon_0 - \epsilon_\infty)\tau}{\epsilon_0(2\epsilon_0 + 1)\eta}} \tag{4}$$

Case	A_V	A_D
Perfect sticking	6	$^3/_8$
Perfect slipping	4	$^3/_4$

Dielectric friction is smaller for the case of sticking since the solvent dipoles in the immediate neighborhood of the ion move together with it.

We have examined the mobilities of alkali metal ions (M^+) and tetraalkylammonium ions (R_4N^+) in a variety of solvents using eq 4.

Calculations

A. Ions in Pure Solvents. In order to facilitate the visualization of the different contributions to the dielectric friction it is useful to define an *effective dynamic radius*, r_s, for the solvent such that

$$\tau = \frac{4\pi\eta r_s^3}{kT} \tag{5}$$

and a characteristic *equilibrium distance*, d, for the solvent such that

$$d = \frac{(ze)^2}{kT}\frac{\epsilon_0 - \epsilon_\infty}{\epsilon_0(2\epsilon_0 + 1)} \tag{6}$$

(The parameter d is numerically close to the Bjerrum parameter for ion association). Using eq 5 and 6 and letting

$$Q^* \equiv dr_s^3 \tag{7}$$

eq 4 becomes

$$(\lambda_i^0\eta) = \frac{ze\mathcal{F}}{A_V\pi r_i + \dfrac{4\pi A_D}{r_i^3}Q^*} \tag{8}$$

For small ions, dielectric friction dominates since the electric field near the ion is strong. For large ions, on the other hand, the viscous force is the dominant contribution to the total frictional force. Thus we find that $(\lambda_i^0\eta)$ for any given solvent has a maximum at a certain value of r_i given by

$$(r_i^{max})^4 = \frac{12A_DQ^*}{A_V} \tag{9}$$

Table I gives the needed physical properties of the solvents examined in this work and the calculated values of r_i^{max} and $(\lambda_i^0\eta)_{max}$ for both the "sticking" and "slipping" cases. Table I also summarizes the values of ionic conductances at infinite dilution examined here.

The dielectric frictional force in a solvent is determined by its Q^* value. For solvents having large Q^* (low ϵ_0 and/or large r_s), r_i^{max} will occur at larger r_i. It should be noted (Table I) that for alcohols with their large τ values, r_s is very large and the maximum mobility would be expected to occur at relatively large values of r_i.

Figures 1–4 are plots of the experimental $(\lambda_i^0\eta)$ for M^+ and R_4N^+ for representative solvents examined. The curves are the theoretical predictions for the two different boundary conditions. It is clear that the "slipping" case corresponds most closely to the experimental findings. For the three dipolar aprotic solvents (DAS) the maximum mobilities are predicted quantitatively by the theory. For protic solvents the agreement is poor except for formamide (Fo). However, the trend of r_i^{max} is correctly predicted, Fo with a small Q^* has $\lambda^0_{Cs^+} > \lambda^0_{Me_4N^+}$; MeOH and EtOH have $\lambda^0_{Et_4N^+} < \lambda^0_{Me_4N^+} > \lambda^0_{Cs^+}$; and PrOH and BuOH with very large Q^* values have $\lambda^0_{Et_4N^+} > \lambda^0_{Me_4N^+}$. To a first approximation, $\lambda^0_{R_4N^+}$ agrees with prediction in AN, AC, NB, Fo, and DMF. A somewhat closer look shows the $(\lambda_i^0\eta)$ decreases more rapidly than predicted with increasing R size.

Therefore, we have reached the following conclusions. (1) Even for DAS where R_4N^+ mobilities are satisfactorily described by the Z-continuum model, M^+ ions have higher mobilities than predicted. The dis-

(4) G. Atkinson and Y. Mori, *J. Phys. Chem.*, 71, 3523 (1967).

(5) R. L. Kay and D. F. Evans, *ibid.*, 70, 2325 (1966).

(6) R. L. Kay, G. P. Cunningham, and D. F. Evans in "Hydrogen Bonded Solvent Systems," A. K. Covington and P. Jones, Ed., Taylor and Francis, London, 1968, p 249.

(7) H. S. Frank in "Chemical Physics of Ionic Solutions," B. E. Conway and R. G. Barradas, Ed., Wiley, New York, N. Y., 1966, p 53.

(8) J. N. Agar, *Ann. Rev. Phys. Chem.*, 15, 469 (1964).

(9) R. Zwanzig, *J. Chem. Phys.*, 52, 3625 (1970).

Table I: Solvent Properties and Theoretical Predictions, 25° [n]

Solvent	ϵ_0	ϵ_∞	$\tau \times 10^{11}$, sec	$\eta \times 10^3$, P	r_s, Å	r_i^{max} (Å) Stick	r_i^{max} (Å) Slip	$(\lambda_i^0\eta)^{max}$ Stick	$(\lambda_i^0\eta)^{max}$ Slip
Water (W)	78.39[a]	5.2[b]	0.833[b]	0.8903[c]	1.45	1.65	2.18	0.376	0.423
Methanol (MeOH)	32.62[i]	5.6[b]	4.77[b]	0.5445[m]	3.06	3.49	4.61	0.170	0.200
Ethanol (EtOH)	24.33[d]	4.2[b]	12.8[b]	1.084[d]	3.38	4.06	5.34	0.151	0.173
Propanol (PrOH)	20.1[b]	3.2[b]	37.1[b]	1.952[d]	3.96	4.79	6.30	0.128	0.146
Butanol (BuOH)	17.1[b]	1.95[b]	47.7[b]	2.589[e]	3.92	5.02	6.32	0.122	0.140
Formamide (Fo)	109.5[f]	3[g]	3.9[g]	3.301[f]	1.57	1.63	2.15	0.376	0.428
Acetonitrile (AN)	36.0[i]	(2)[i]	0.39[j]	0.341[i]	1.55	2.12	2.79	0.290	0.330
Dimethylformamide (DMF)	36.7[h]	(3)[g]	1.5[g]	0.796[h]	1.60	2.14	2.82	0.288	0.327
Nitrobenzene (NB)	34.3[k]	2.42[k]	4.09[k]	1.811[m]	1.95	2.54	3.33	0.242	0.276
Acetone (AC)	20.7[m]	1.9[l]	0.31[l]	0.3040[m]	1.49	2.34	3.07	0.263	0.300

[a] G. A. Vidulich, D. F. Evans, and R. L. Kay, *J. Phys. Chem.*, **71**, 656 (1967). [b] F. Buckley and A. A. Maryott, *Nat. Bur. Std. Circ.*, 589 (1958). [c] J. F. Swindells, J. R. Coe, and T. B. Godfrey, *J. Res. Nat. Bur. Stand.*, **48**, 1 (1952). [d] D. F. Evans and P. Gardam, *J. Phys. Chem.*, **72**, 3281 (1968). [e] D. F. Evans and P. Gardam, *ibid.*, **73**, 150 (1969). [f] G. P. Johari and P. H. Tewari, *ibid.*, **69**, 2862 (1965). [g] S. J. Bass, W. I. Nathan, R. M. Meighan, and R. H. Cole, *ibid.*, **68**, 509 (1964). [h] J. E. Prue and P. J. Sherrington, *Trans. Faraday Soc.*, **57**, 1795 (1961). [i] G. P. Cunningham, G. A. Vidulich, and R. L. Kay, *J. Chem. Eng. Data*, **12**, 366 (1967). [j] R. Krishmaji and A. Marsingh, *J. Chem. Phys.*, **41**, 827 (1964). [k] R. H. Boyd, *ibid.*, **35**, 1281 (1961); G. L. Clark, *ibid.*, **25**, 125 (1956). [l] J. Calderwood and C. P. Smyth, *J. Amer. Chem. Soc.*, **78**, 1295 (1956). τ at 25° from $(\tau/\eta)_{20°}$ assumed constant. [m] R. A. Robinson and R. H. Stokes, "Electrolyte Solutions," Butterworths, London, 1959, p 458. [n] Sources of Ionic Mobility Data (25°): The values of the ionic conductances at infinite dilution used in the present paper are from the following sources: W, MeOH, and alkali metal ions in EtOH, ref 5; EtOH and PrOH (R_4N^+), see footnote *d;* PrOH (Na^+ and K^+): Λ^0 for iodides from R. L. Kay, *J. Amer. Chem. Soc.*, **82**, 2099 (1960), using λ_I^{-0} from previous reference; BuOH, see footnote *c;* Fo, J. M. Notley and M. Spiro, *J. Phys. Chem.*, **70**, 1502 (1966); AN, C. H. Springer, J. F. Coetzee, and R. L. Kay, *ibid.*, **73**, 471 (1969); DMF, see footnote *h* and P. G. Sears, E. D. Wilhoit, and L. R. Dawson, *ibid.*, **59**, 373 (1955); NB, from Λ^0 for R_4NPi and $\lambda_{Bu_4N^+}{}^0 = \lambda_{BPh_4^-}{}^0$, D. F. Evans, C. Zawoyski, and R. L. Kay, *ibid.*, **69**, 3878 (1965); R. M. Fuoss and E. Hirsch, *J. Amer. Chem. Soc.*, **82**, 1013 (1960); AC, M. B. Reynolds and C. A. Kraus, *J. Amer. Chem. Soc.*, **70**, 1709 (1948); M. J. McDowell and C. A. Kraus, *ibid.*, **73**, 3293 (1951), $\lambda_{Cs^+}{}^0$ from G. Pistoia and G. Pecci, *J. Phys. Chem.*, **74**, 1450 (1970).

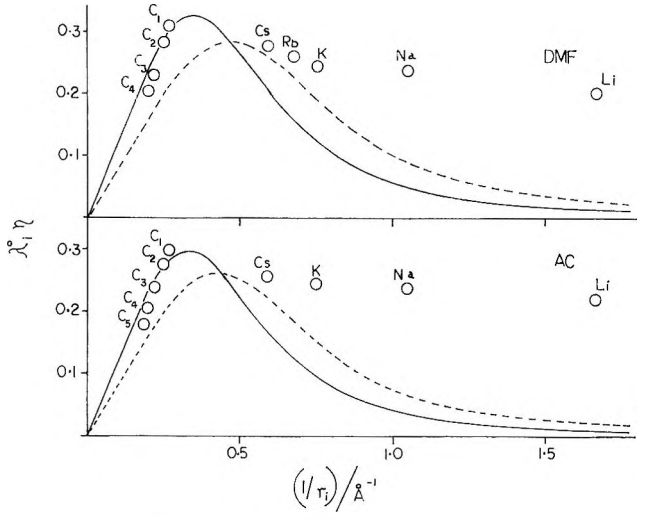

Figure 1. Ion mobilities against reciprocal crystal radius. Mobilities calculated with eq 8 represented by the full curve (slipping) and the dashed curve (sticking): ○, experimental $\lambda_i^0\eta$; C_n, denotes ion $(C_nH_{2n+1})_4N^+$.

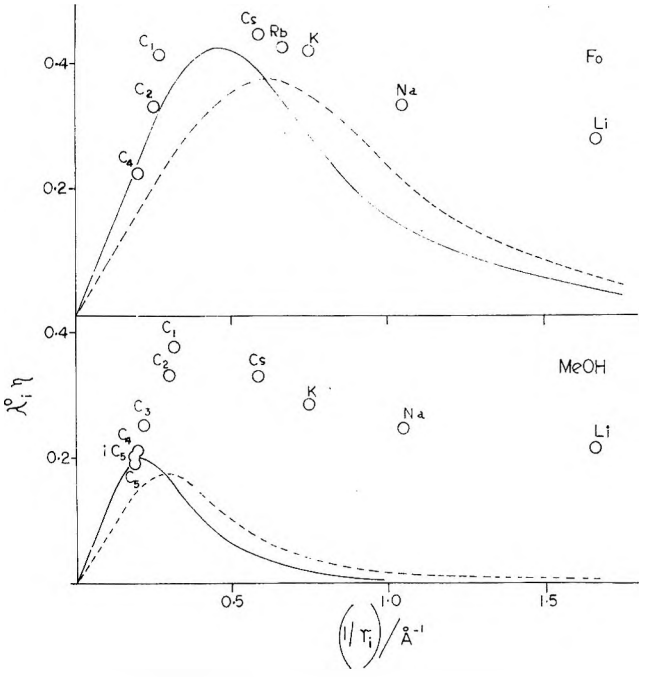

Figure 2. Ion mobilities against reciprocal crystal radius: curves and symbols as in Figure 1.

crepancy is largest for the smallest ions. (2) Water is unique in that the structure-breaking M^+ ions show a much higher mobility than predicted by the theory. However, the R_4N^+ mobilities in H_2O are described to a good first approximation. (The deviation from prediction increases to about 28% when R = Bu.) Only a closer examination reveals the deviation of these ions from normal behavior. (3) For the other protic solvents, the agreement with theory becomes poorer as the dielectric frictional force becomes larger. Since Fo has a small Q^*, the agreement is fair for this solvent, but

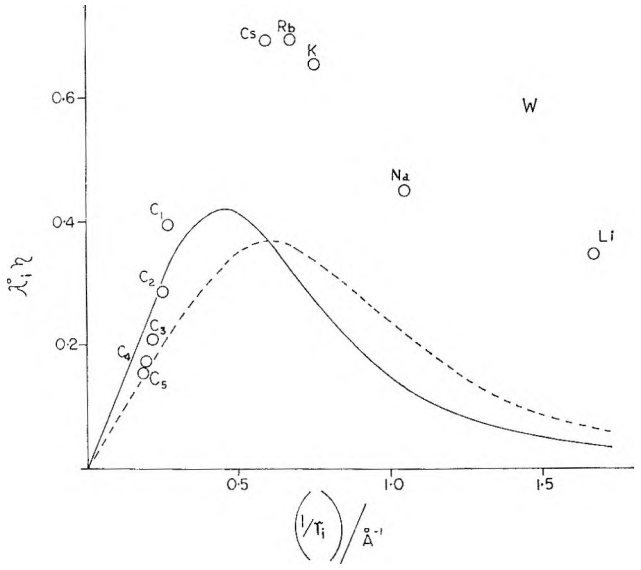

Figure 3. Ion mobilities against reciprocal crystal radius: curves and symbols as in Figure 1.

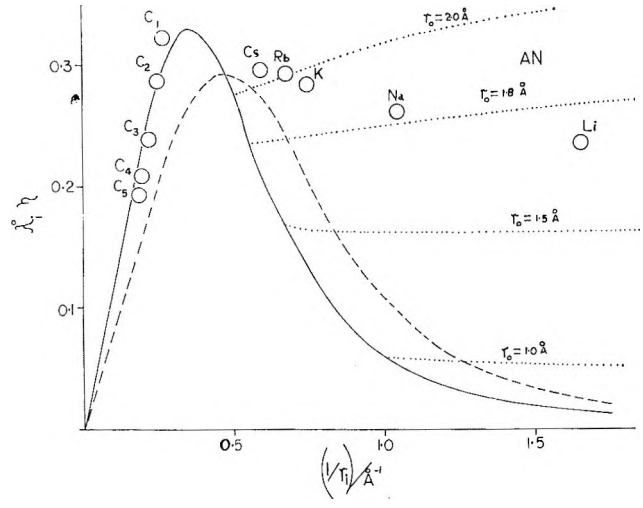

Figure 4. Ion mobilities against reciprocal crystal radius: curves and symbols as in Figure 1; dotted lines; effect of dielectric saturation for different r_0 values.

for the ROH solvents we find very poor agreement stemming largely from their very large r_s values.

B. Mixed Solvents. In the first section it was shown that the mobilities of R_4N^+ ions in DAS were correctly described by the Z-continuum model. Therefore it seems reasonable to examine such systems to test the ability of the model to predict variations of λ_i^0 with solvent properties (Q^*) in a mixed solvent. Since for the bulky R_4N^+ ions viscous forces dominate, Me_4N^+ and Et_4N^+ were examined in pure DAS and in AN–CCl_4 mixtures. For the solvent mixtures the conductance and static dielectric constant data of Berns and Fuoss[10] for R_4NBPh_4 were chosen. The ionic conductances for Me_4N^+ and Et_4N^+ were calculated by assuming that $\lambda^0_{BPh_4^-} = \lambda^0_{Bu_4N^+}$ in all solvent mixtures.

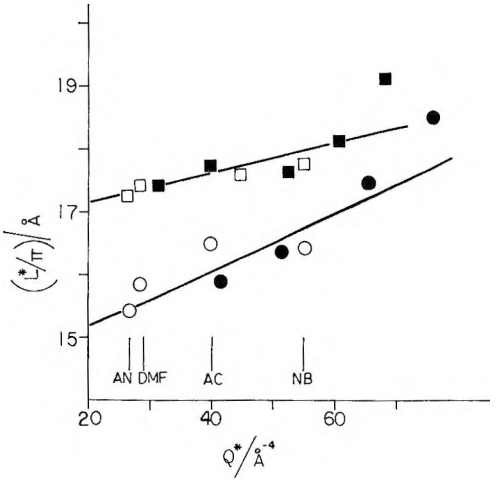

Figure 5. Ion mobilities in DAS. Open symbols: pure DAS; closed symbols; AN–CCl_4 solvent mixtures; ○, Me_4N^+, □, Et_4N^+.

Furthermore, r_s was assumed to be independent of solvent composition and equal to the value in pure AN (probably the weakest assumption). Equation 8 can be rearranged to give

$$L^*/\pi \equiv \frac{ze\mathfrak{F}}{\pi\eta\lambda_i} = A_V r_i + \frac{4A_D}{r_i^3}Q^* \qquad (10)$$

Figure 5 shows (L^*/π) plotted *vs.* Q^* for both ions in the DAS media. From the least-square straight lines, the r_i found are given in Table II. The points corresponding to more than 75% CCl_4 show the greatest deviation. For the "slip" case the values of r_i from intercept and slope are satisfactorily close to each other and to the crystal radii for both ions.

Table II: Experimental Radii, Å

	"Stick" Intercept	"Stick" Slope	"Slip" Intercept	"Slip" Slope	Crystallographic radii
Me_4N^+	2.4	3.3	3.6	3.9	3.5
Et_4N^+	2.8	3.8	4.2	4.7	4.0

In Figure 6, (L^*/π) is plotted *vs.* Q^* for R_4N^+ in protic solvents and compared with the behavior in aprotic solvents. The latter data are represented by straight lines since the points for aprotic solvents cluster in the Q^* interval 26–75. The straight lines for Me_4N^+ and Et_4N^+ are those from the previous figure. The lines which describe the behavior of Pr_4N^+ and Bu_4N^+ correspond to r_i values of 5.0 and 5.9 Å, respectively, in eq 10 for the "slip" condition. This figure illustrates the fact that the R_4N^+ ions have higher mobilities in protic solvents than in aprotic ones and that

(10) D. S. Berns and R. M. Fuoss, *J. Amer. Chem. Soc.*, 82, 5585 (1960).

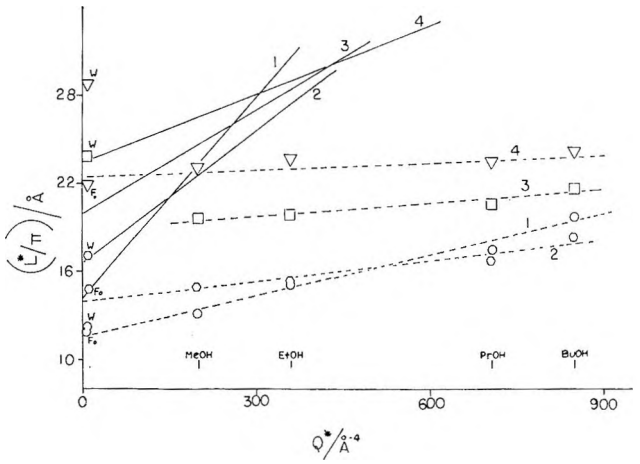

Figure 6. Ion mobilities of R_4N^+ in protic solvents compared with DAS: □, 1: R = Me; ○, 2: R = Et; □, 3: R = Pr; ▽, 4: R = Bu. Full lines, behavior predicted by eq 10 (see text). The dashed lines have no theoretical meaning.

the Z-continuum model fails to predict the dependence of mobility on solvent dielectric properties in protic solvents, particularly alcohols. Mobilities in Fo are close to the aprotic predicted value due to the small Q^* value. In this instance Fo is more similar to ROH than to H_2O. Water behaves like the other protic solvents for Me_4N^+ but the mobility of Et_4N^- is very well predicted by the aprotic line. The mobilities for R_4N^+ ions larger than Et_4N^+ are smaller than for the same ions in DAS.

Discussion

The widely held view that the radii calculated from conductance data by Stokes' law are much too small is not correct. Except for the "structure breaking" Cs^+, Rb^+, and K^+ ions in water, the Stokes radii for the M^+ ions are larger than their crystal radii for all the solvents studied in the present work. On the other hand, for R_4N^+ the values of $\lambda_i^0\eta$ are between those predicted by Stokes' law and those predicted by viscous friction with perfect slipping. Only for Me_4N^+ in protic solvents are the radii obtained from viscous friction significantly smaller than the crystal radius.

According to the Z-continuum model the translational (viscous) activation energy and the rotational (dielectric) activation energy of the solvent determine the mobility of ions independent of ion size. Activation parameters for ionic transport have been found to be little dependent on ion size.[11,12] This is particularly true of large cations (R_4N^+).[13] The discrepancy between the predicted and observed mobilities of the M^+ ions could be attributed to a firmly held solvation sheath. This would increase the effective kinetic ionic radius leading to smaller dielectric friction and enhanced mobility. However, this approach would require a new parameter (solvated radius) for each ion in each solvent since there is as yet no satisfactory theory of ion solvation. It would also imply that the deviation between experimental and predicted ($\lambda_i^0\eta$) behavior for M^+ in DAS would depend specifically on the solvent, an implication not borne out by the data.

It did not prove fruitful to attempt to translate the Z-continuum analysis results to a molecular level beyond the above discussion of solvent translation and viscosity. However, some possibilities exist for the improvement of the theory within the context of a continuum model. The discrepancy between theory and experiment for M^+ ions increased with decreasing ion radius. It might be due to the effect of the increasing electric field at the ion surface on the static dielectric constant of the solvent in the vicinity of the ion. Since the variation of dielectric constant with field intensity is a complicated function of the distance from the ion,[14] we have initially tested this idea on a simplified model where ϵ' is a step function of the distance from the center of the ion such that

$$\epsilon'(R) = \epsilon_\infty \text{ when } r_i \leq R \leq r_0$$
$$\epsilon'(R) = \epsilon_0 \text{ when } R \geq r_0 \qquad (11)$$

The parameter r_0 has been assumed to be the same for all ions in a given solvent. The ionic electrostatic potential is then given by

$$\Phi_1 = ze/R + C_1VR\cos\theta \qquad R \leq r_i \qquad (12a)$$

$$\Phi_2 = ze/\epsilon_\infty R + (C_2R + C_3R^{-2})\cos\theta \qquad r_i \leq R \leq r_0 \qquad (12b)$$

$$\Phi_3 = ze/\epsilon_0 R + \Phi'(R)\cos\theta \qquad r_0 \leq R \qquad (12c)$$

In the two inner regions the Laplace equation applies while in the third region the potential was obtained by solving the corresponding Poisson equation, $\Phi'(R)$ being the particular solution of the latter.[9] If there were no dielectric saturation ($r_0 \to r_i$), the second region would vanish and eq 12a and 12b are simply the solutions of the potential equations obtained by Zwanzig.[9] V is the velocity of the ion relative to the bulk of the solvent, θ is the angle between R and the direction of ionic motion, and the C_i are integration constants evaluated using the same boundary conditions as Zwanzig.

With this approach we obtain

$$\zeta_D = \frac{4\pi A_D}{r_i^3}\eta Q^*\left[\frac{(1+X)(1+2\epsilon_0)}{2(\epsilon_0-\epsilon_\infty)+(2\epsilon_0+\epsilon_\infty)m^3X}\right] \qquad (13)$$

where

$$X = \frac{1+2\epsilon_\infty}{\epsilon_\infty - 1}$$

$$m = (r_0/r_i)$$

(11) F. Barreira and G. J. Hills, *Trans. Faraday Soc.*, **64**, 1359 (1968).

(12) S. Brummer and G. J. Hills, *ibid.*, **57**, 1823 (1961).

(13) S. Brummer, *J. Chem. Phys.*, **42**, 1636 (1965).

(14) F. Booth, *ibid.*, **19**, 391 (1951).

We use this expression for (ζ_D) in eq 8. When $r_i \geq r_0$ $(m = 1)$ there is no dielectric saturation and the term in brackets in eq 13 is unity. For a vanishingly small ion, eq 13 becomes the dielectric friction corresponding to a sphere of radius r_0, having a point charge in its center and a dielectric constant equal to ϵ_∞.

The values of r_0 calculated from eq 8 modified by eq 13 and the experimental mobilities of the M^+ are given in Table III for the case of perfect slip. It is clear that the dielectric saturation effect is not successful in explaining the $\lambda^0_{M^+}$ deviations found in water since the necessary r_0 varies widely. On the other hand, for the DAS the values found for r_0 are fairly constant. In Figure 4 the dotted lines illustrate the values of $(\lambda_i^0\eta)$ for different r_0 values in AN. It is clear that very small variations in r_0 produce marked variations in $(\lambda_i^0\eta)$ for a given ion size.

Table III: Values of r_0 (Å) Calculated from Dielectric Saturation

Ion	AN	DMF	AC	W
Li^+	1.7	1.4	1.7	1.4
Na^+	1.8	1.8	2.1	1.7
K^+	2.0	1.9	2.1	2.6
Rb^+	2.0	1.9		3.2
Cs^+	2.1	2.0	2.3	4.5

Since ϵ' is more likely to be a smooth function of R, dielectric saturation will be operative for $r_i > r_0$, but the magnitude of the effect will be smaller than predicted here, approaching the $(\lambda_i^0\eta)$ value predicted by the step function asymptotically as $r_i \to 0$. For the ϵ' step function Figure 4 shows that when $r_i \leq r_0$ dielectric saturation makes $(\lambda_i^0\eta)$ rather insensitive to ionic radius or even makes it increase with decreasing r_i. Both effects will also appear for small r_i if the correct ϵ' function is used. Incidentally, the increase of $(\lambda_i^0\eta)$ for small r_i predicted here due to dielectric saturation would rationalize the effect seen in some solvents where the small M^+ ions show a higher mobility than some of the larger M^+ ions. This effect has been observed in sulfolane,[15] HCN,[16] dimethylacetamide,[17] and dimethylpropionamide.[17]

The failure of the Z-continuum model to account for the observed λ_i^0 in ROH seems to be due to the particular nature of the hydrogen bonding in these solvents. Any interaction where correlation in the reorientation of solvent molecules in a changing field would occur could not be dealt with satisfactorily in the Z-continuum framework.

Conclusion

In this paper we have explored the utility of the Zwanzig theory in explaining the mobility of ions in a continuum solvent. It is clear that the theory quantitatively predicts the effect of ion radius on mobility for representative ions in dipolar aprotic solvents. It is equally clear that the theory is unable to deal quantitatively with the behavior of some simple trends in protic solvents.

However, it should be emphasized that even this limited success marks a very real advance in our view of the solvent in electrolyte solutions. The Zwanzig theory introduces a dynamic character to the solvent through its utilization of the dielectric relaxation property.

Other facets of the ion–solvent interaction that could be explored further within the context of a continuum solvent are the following: (1) a more sophisticated view of dielectric saturation which we explored in a crude fashion; (2) the introduction of a dynamic viscosity, a property of liquids just as well characterized as the dynamic dielectric properties; (3) the examination of the introduction of the effect of ion field on properties such as the ϵ_∞ and τ of the solvent; (certainly an effect known from dielectric measurements on aqueous solutions).

Finally, we feel that it is no longer useful to attribute all deviations from the Walden rule to ill-defined "structural effects." The fact that Walden's rule is not sufficient is well established. It is now time to use the Zwanzig theory and any other conceptually sound and calculable effects to explore the deviations from Walden's rule in detail. The recent advances in the dynamic structural aspects of pure liquids make this both feasible and necessary.

Acknowledgments. The authors would like to thank Professor Robert Zwanzig for an advance copy of his theoretical revision. They acknowledge the generous financial support of the Office of Saline Water under Grant 14-01-0001-1656 and the Center of Materials Research of the University of Maryland.

Appendix

Symbols

λ_i^0	Ionic mobility at infinite dilution
$\mathfrak{F}$	Faraday
N	Avogadro's number
r_i	Ionic crystal radii
η	Solvent viscosity
e	Proton charge
z	Ion charge number
ϵ_0	Static dielectric constant
ϵ_∞	Optical (high-frequency) dielectric constant
ϵ'	Dielectric coefficient
τ	Relaxation time

(15) R. Fernández-Prini and J. E. Prue, *Trans. Faraday Soc.*, 62, 1257 (1966).

(16) J. E. Coates and E. G. Taylor, *J. Chem. Soc.*, 1245 (1936).

(17) G. R. Lester, C. P. Groves, and P. G. Sears, *J. Phys. Chem.*, 60, 1076 (1956).

Acid–Base Equilibria of Fluorescein and 2′,7′-Dichlorofluorescein in Their Ground and Fluorescent States

by Horst Leonhardt,[1a] Larry Gordon,[1b] and Robert Livingston*

Department of Chemistry, San Diego State College, San Diego, California 92115 *(Received August 24, 1970)*

Publication costs assisted by National Science Foundation Undergraduate Research Participation Program

The acidic forms of dichlorofluorescein are stronger acids than the corresponding forms of fluorescein. For the cationic and monoanionic acids, the difference in pK is 1.7; for the neutral acids, it is 0.9. The anionic acids of fluorescein and dichlorofluorescein are both slightly weaker in their first excited singlet than in their ground states, the difference in pK being −0.2. The fluorescence spectra of both dyes were measured in aqueous solutions, ranging from 8 m $HClO_4$ to a pH of 12. The emission spectra of the dianonic, monoanonic, and cationic forms have been estimated. The neutral acids appear to be nonfluorescent.

Introduction

As Zanker and Peter[2a] pointed out, fluorescein in aqueous solutions occurs in cationic, C, neutral, N, monoanionic, A, and dianionic, D, forms, the relative concentrations depending on the pH of the solutions. Neutral fluorescein in dry dioxane exists as a lactone, L, but in aqueous solutions the dominant neutral form is a quinoid, Q.[2b] The fundamental equilibria are as follows

$$K_1' = \frac{[Q][H^+]}{[C]}$$

$$K_2' = \frac{[A][H^+]}{[Q]}$$

$$K_3' = \frac{[D][H^+]}{[A]}$$

$$K_I = \frac{[Q]}{[L]} = \frac{[Q]}{[N] - [Q]}$$

The isomeric equilibrium in aqueous solutions cannot be determined from available spectroscopic data. Accordingly, the equilibrium constants that can be derived from absorption spectra are K_3', K_2, and K_1, where $K_1 = K_1'[1 + K_I)/K_I$ and $K_2 = K_2'K_I/(1 + K_I)$.

It is impossible to obtain aqueous solutions which contain only the monoanionic or the neutral form of fluorescein; also the absorption spectra of the several species overlap seriously. However, it is possible to evaluate K_1, K_2, and K_3' from spectroscopic data by a simple iterative process.[2b]

If, during the lifetime of fluorescence, molecules in their first-excited singlet state attain acid–base equilibrium it should be possible to evaluate their equilibrium constants from the results of quantitative measurements of fluorescence spectra, corresponding to different values of pH. However, as is discussed in a following section, this is practicable only for K_3'*. Uncertainties in regard to the fluorescence and the isomeric equilibrium of the neutral dye, difficulties due to overlap of the fluorescence spectra of the several forms, and nonnegligible corrections necessitated by fluorescence quenching and wavelength shifts observed in concentrated $HClO_4$, render estimates of K_2* and K_1* too unreliable to be of real value.

Experimental Methods and Materials

Materials. CH_3COONa, CH_3COOH, Na_2HPO_4, KH_2PO_4, and 95% C_2H_5OH were reagent grade and were used without further purification. The $HClO_4$ used in the fluorescein measurements was of reagent grade, but that used with dichlorofluorescein was Baker's Ultrex. Perylene and fluorescein were purified chromatographically.[3] Our sample of fluorescein, dissolved in 0.010 m NaOH, had an extinction coefficient at λ 490 nm of 87,600, in good agreement with 88,800 reported by Lindquist.[2b] The 2′,7′-dichlorofluorescein had an extinction coefficient of 101,000 at 503 nm in 0.010 m NaOH and was used without further purification.

Apparatus. Absorption measurements were made with a Cary Model 14 spectrophotometer. Fluorescence intensities were measured relative to a perylene standard (10^{-5} m in 95% C_2H_5OH) with a modified Farrand fluorometer, a double-beam instrument, used as a null device. The exciting light was predominantly of 365 nm, isolated from a GE-H85A3 Hg lamp by a Corning 7-60 filter. The intensities of the fluorescent and compensating light were measured with RCA 1P28PM tubes. The fluorescent light passed through a grating monochromator before striking the PM tube.

(1) (a) Deceased February 1969; (b) Department of Chemistry, University of California, Berkeley, Calif.

(2) (a) V. Zanker and W. Peter, *Chem. Ber.*, **91**, 572 (1958); (b) L. Lindquist, *Arkiv. Kemi.*, **16**, 79 (1960).

(3) (a) L. Koch, *J. Ass. Offic. Agr. Chem.*, **39**, 397 (1956); (b) R. Sangster and J. Irvine, *J. Chem. Phys.*, **24**, 697 (1956).

The fluorescence intensities of the solutions were normalized by dividing them by their absorbance (measured in a 100-mm silica cell) at 366 nm. For the concentrations of dye used, Beer's law is valid for the entire pH range. Scattering of the exciting light from a water-filled cell was not detectable under our experimental conditions. The fluorometer was stable within ±1% during the 40-min periods required to complete a run.

Preparation of Solutions. Solutions were prepared by dissolving a weighed amount of the purified dye in 0.10 *m* NaOH and then neutralizing the excess base with $HClO_4$. In preliminary experiments, fluorescein was dissolved by heating it in distilled water. However, fluorescein in hot aqueous solutions proved to be unstable, and this procedure was discontinued.

For solutions of pH <3, the hydrogen ion concentration was fixed by the addition of an appropriate amount of concentrated $HClO_4$. For pH ⩾3, either an acetate or phosphate buffer was used. The total (acid and salt) concentration was 0.10 *m* for acetate and 0.025 *m* for phosphate buffers. All solutions were air-saturated. pH values greater than 2 were measured with a Beckman pH meter; more acidic solutions were titrated with a standard NaOH solution.

Ground-State Equilibria. Figure 1 consists of plots of the molar, decadic extinction coefficient, ϵ (for 10^{-6} *m* dichlorofluorescein), against wave number, $\tilde{\nu}$, at several typical values of pH. The absorption maxima (*cf.* ref 2b, pp 42, 43) of the cation, neutral molecule, monoanion, and dianion are at 448, 456, 460 and 485 (double maxima), and 502 nm, respectively. In Figure 2, log $(\epsilon - \epsilon_i)/(\epsilon_j - \epsilon)$ is plotted against pH. The straight lines were drawn with slopes of 1 to correspond to the sets of experimental points. The values of ϵ_i and ϵ_j, which correspond to each of the several forms of the dye, were taken from the absorption spectra but have been slightly corrected by an iterative process for the presence of small amounts of other forms.[2b] The corresponding values of pK_3', pK_2, and pK_1 are, respectively, 4.95, 3.50, and 0.47. These values are based on the assumption that the activity coefficients of the reactants are each equal to 1. The correction for K_1 should be relatively small, but the correct constants corresponding to K_2 and K_3' must be smaller than those listed.

Our absorption data for fluorescein are in good agreement with those published by Lindquist.[2b] Accordingly, we have omitted our absorption spectra and have accepted his values for the equilibrium constants (see Table II).

Aqueous solutions of fluorescein, at pH 1.0, 3.3, and 5.5, conform to Beer's law in the concentration range 10^{-6} to 10^{-5} *m*.[2b] We obtained similar results for dichlorofluorescein at pH 0.0, 4.6, and 12.0 and between 5×10^{-7} and 5×10^{-6} *m* at a pH of 2.0. Presumably dimerization in those solutions is of negligible importance. However, in the pH range 1 to 3 the solubility of dichlorofluorescein is less than 10^{-5} *m*.

In strongly acid solutions, the absorption maximum is shifted to shorter wavelengths by increasing concentrations of $HClO_4$ or H_2SO_4, but not of HNO_3 (see Table I).

Table I: Shift of Absorption Maxima in Acid Solutions

[Acid], *m*	λ_{max}, nm, fluorescein	λ_{max}, nm, dichlorofluorescein
$HClO_4$		
0.50	436	448
1.00	436	448
1.70	436	
2.15		449
2.50	435	
3.00	434	446
4.00	434	
5.40		445
7.40	431	443
11.7		441
H_2SO_4		
10.0 *m*	433	444
HNO_3		
7.0 *m*	436	

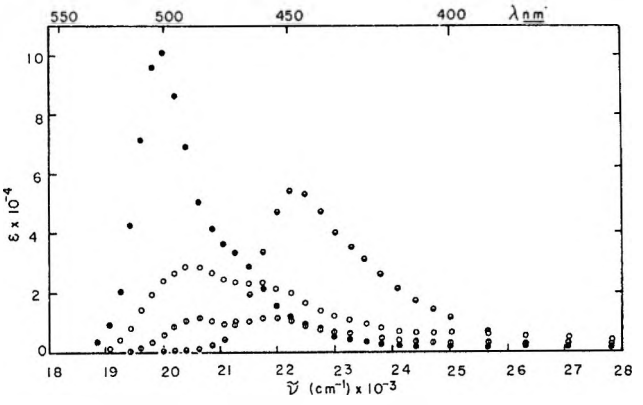

Figure 1. Absorption spectra of dichlorofluorescein: ●, pH 12.0; ○, pH 3.89; ◑, pH 2.05; ◒, pH −0.33.

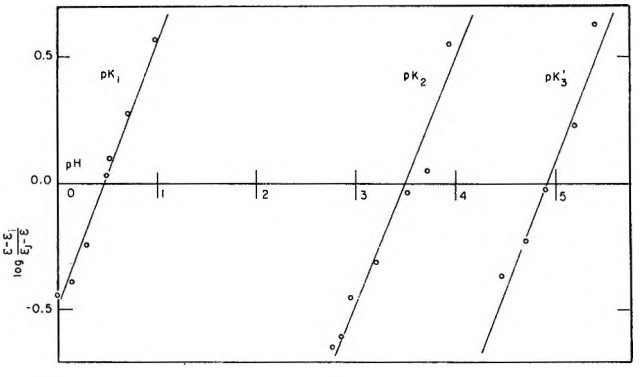

Figure 2. Graphical determination of the pK_i for dichlorofluorescein.

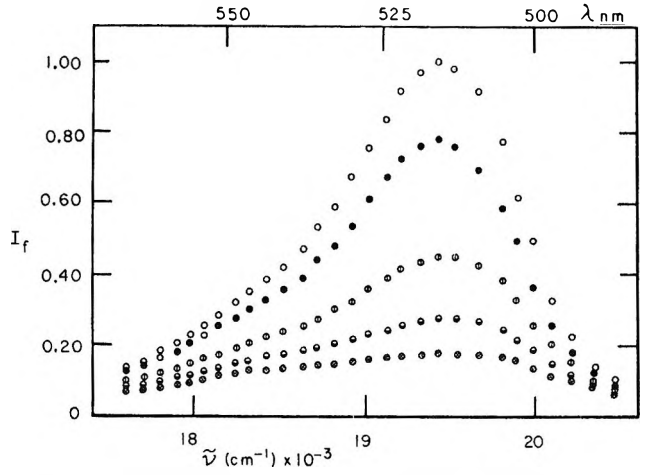

Figure 3. Emission spectra of fluorescein in basic and weakly acidic solutions. I_f, normalized to maximum for pH 11.7: O, pH 11.7; ●, pH 7.40; ⊕, pH 6.70; ◒, pH 6.0; ⊗, pH 2.75.

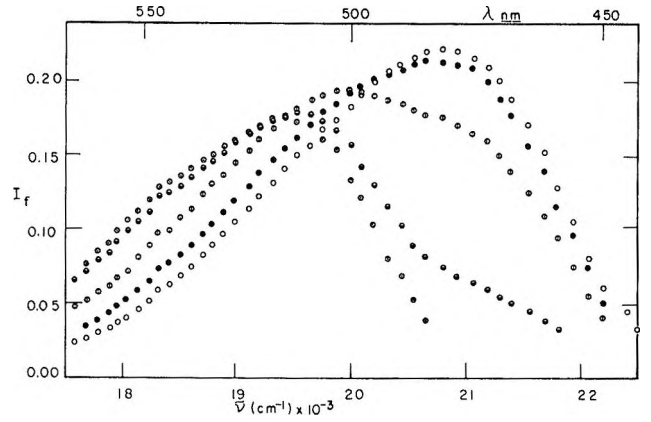

Figure 4. Emission spectra of fluorescein in acidic solutions. I_f normalized to maximum for pH 11.7, see Figure 3: O, [HClO$_4$] 7.4 *m*; ●, [HClO$_4$] 3.0 *m*; ⊕, [HClO$_4$] 1.7 *m*; ◒, [HClO$_4$] 0.5 *m*; ⊗, pH 2.80.

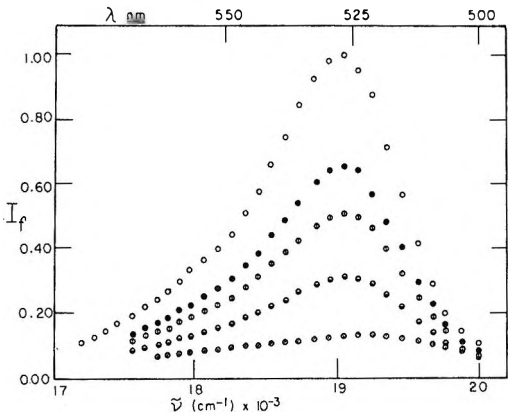

Figure 5. Emission spectra of dichlorofluorescein in basic and weakly acidic solutions. I_f normalized to maximum for pH 12.0: O, pH 12.0; ●, pH 5.45; ⊕, pH 5.19; ◒, pH 4.69; ⊗, [HClO$_4$] 0.50 *m*.

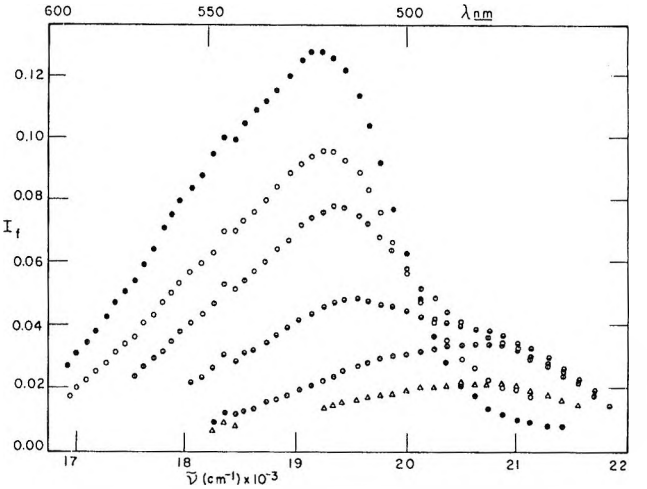

Figure 6. Emission spectra of dichlorofluorescein in acidic solutions. I_f normalized to maximum for pH 12.0, see Figure 5: O, 1.09 *m*; ●, 3.24 *m*; ⊕, 4.34 *m*; ◒, 5.4 *m*; ⊗, 7.55 *m*; △, 11.7 *m* (*zm* ≡ [HClO$_4$]).

Florescence as a Function of pH. The normalized (see the section of Experimental Methods) values of the intensities of fluorescence, I_f, vary with wavelength and pH but are independent of intensity of exciting light and concentration of the dye. The fluorometer readings, upon which the I_f values are based, were not corrected for variation with wavelength of the sensitivity of the photomultiplier or of the transmissivity of the optical system. In Figures 3–6, values of I_f, for various typical acidic and basic solutions, are plotted against $\tilde{\nu}$ (cm^{-1}). Rozwadowski[4] published qualitatively similar data for fluorescein.

The values of I_f for fluorescein in acidic solutions exhibit an isobestic point near 508 nm (Figure 4). However, the data show a greater scatter about the isobestic point than is consistent with the estimated uncertainty ($\lesssim$2%) of the measurements. This scatter appears to be the result of weak quenching of fluorescence and a concurrent shift of the maximum of fluorescence occurring in concentrated HClO$_4$. Similar quenching, etc., were produced by H_2SO_4 and by the addition of NaClO$_4$ to 1.0 *m* HClO$_4$. The scatter can be reduced to the expected range if the data are corrected, assuming that the wavelength shifts for absorption and emission are identical and that the Stern–Vollmer constant is about 0.025 m^{-1}. For dichlorofluorescein, similar corrections can be made but appear to be even more arbitrary.

The several curves of Figures 3 and 4 can be represented by the sum of the intensities of fluorescence of each species, β_i, weighted by their relative concentrations

$$I_f = \sum_i C_i\beta_i / \sum_i C_i$$

The β_i are the values which I_f would have if the excited

(4) M. Rozwadowski, *Acta Physiol. Pol.*, **20**, 1005 (1961).

dye were all in its ith acid–base form. Inspection of the data for fluorescein in the pH range from 1 to 3 showed that β_N cannot be greater than β_A; either $\beta_N \cong 0$ or $\beta_N \cong \beta_A$. Postulating that $\beta_N = 0$ (for all wavelengths), values of β_C, β_A, and β_D of fluorescein and β_A and β_D of dichlorofluorescein have been estimated and are plotted in Figure 6. The values, particularly of β_D and β_C, are not seriously affected by the assumption that $\beta_N = 0$. However, corrections for quenching, etc., would increase the values of β_C perhaps by as much as 7%.

The quantum yields of fluorescence can be estimated from the areas under the β_i curves, using

$$\varphi_i = \varphi_D \sum_{\bar{\nu}} \beta_i \Delta\bar{\nu} / \sum_{\bar{\nu}} \beta_D \Delta\bar{\nu}$$

We have taken the absolute values of φ_D for fluorescein[5] and dichlorofluorescein[6] as 0.93 and 0.88, respectively. The corresponding values of φ_A and φ_C (fluorescein) and of φ_A (dichlorofluorescein) are 0.26, 0.39, and 0.17, respectively. The values for fluorescein are not directly comparable to those reported by Rozwadowski,[4] since his experimental conditions were different and he used $\varphi_D = 1.00$. Also it should be remembered that our values of I_f were not corrected for the variation of photomultiplier sensitivity with wavelength and that this introduces a corresponding uncertainty in the values of β and φ.

Comparison of the effect of pH on the absorption and emission spectra demonstrates that the protolytic equilibria are different in the ground and excited states. It is possible to evaluate $K_3'^*$ by plotting log $(\beta_D - I_f)/(I_f - \beta_A)$ against pH, as is shown in Figure 8. The straight lines drawn with a slope of unity indicate that $pK_3'^*$ for excited fluorescein and dichlorofluorescein are 6.93 and 5.24, respectively. In obtaining these values, it was assumed that equilibrium between the di- and monoanions was attained in their excited states, but nothing was assumed about the behavior or properties of the neutral and cationic forms.

If it is assumed that the several species attain protolytic equilibria during the lifetimes of their excited states and that relative concentrations of the isomeric forms of the neutral dyes do not depend on pH, the following equation can be derived by a straightforward steady-state analysis.

$$I_f = \frac{\beta_C[H^+]^3 + \beta_N K_1^*[H^+]^2 + \beta_A K_1^* K_2^*[H^+] + \beta_D K_1^* K_2^* K_3'^*}{[H^+]^3 + K_1^*[H^+]^2 + K_1^* K_2^*[H^+] + K_1^* K_2^* K_3'^*}$$

For acid concentrations greater than 10^{-3} m, terms containing $K_1^* K_2^* K_3'^*$ may be neglected and the equation put into the following simplified form

$$(I_f - \beta_C)[H^+]^2 + (I_f - \beta_N)K_1^*[H^+] + (I_f - \beta_A)K_1^* K_2^* = \rho$$

where ρ is the residual and K_1^*, K_2^* and the β_i are adjustable constants. An attempt was made to evaluate K_1^* and K_2^* with aid of a computer program for a stepwise, multiple regression analysis[7] using values of β_A and β_C from Figure 7 and setting β_N equal either to 0 or

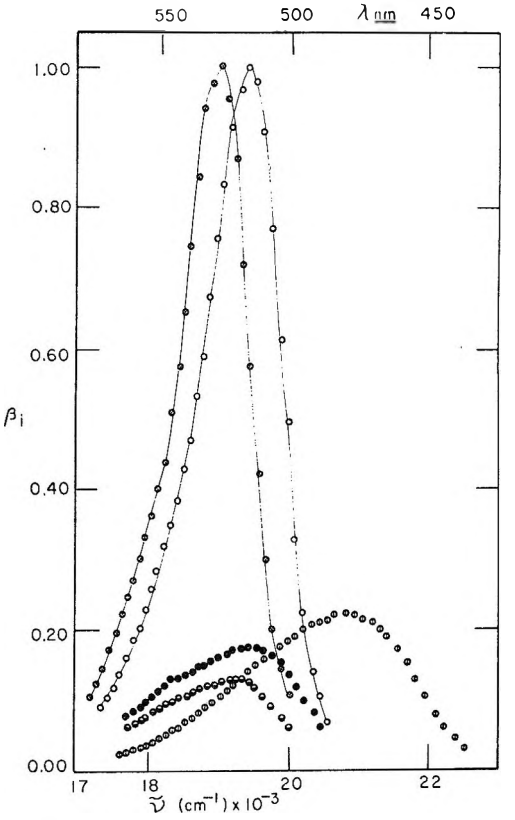

Figure 7. Emission spectra of several acidic forms of fluorescein and dichlorofluorescein: ⊗, β_D; ◒, β_A, dichlorofluorescein; ○, β_D; ●, β_A; ⊙, β_C, fluorescein.

to β_A. Although values ($K_1^* = 0.18$ and $K_2^* = 9.0$) obtained in this way (for fluorescein) are compatible with the experimental data, it is doubtful if they have physical significance. Probably, the isomerization reactions are slow, relative to the decay of fluorescence, and are acid–base catalyzed. Furthermore, the values of K_1^* and K_2^*, obtained in this way, depart widely from predictions based upon Förster's cycle.[8,9] If $\beta_N = 0$, the excited neutral form must have a very short life and cannot reach protolytic equilibrium. The values of K_1^* and K_2^* given by the computer analysis are strongly correlated, which introduces an additional uncertainty.

(5) P. Seybold, M. Goutermon, and J. Collis, *Photochem. Photobiol.*, 9, 229 (1969).

(6) L. Forster and D. Dudley, *J. Phys. Chem.*, 66, 838 (1962).

(7) IBM System 360, Scientific Subroutine Package 360-CM-03X, Version III, Manual H20-020503, 1968.

(8) A. Weller, *Progr. React. Kinet.*, 1, 189 (1961).

(9) E. Vander Donckt, *ibid.*, 9, 273 (1969).

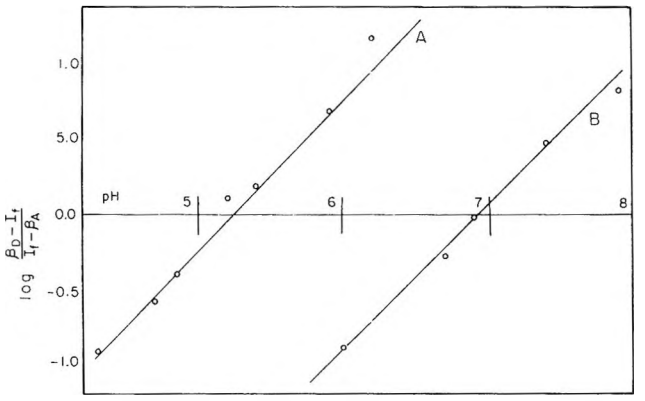

Figure 8. Graphical determination of $K_3'^*$: A, dichlorofluorescein; B, fluorescein.

Discussion

The pK_i for fluorescein and dichlorofluorescein are listed in Table II. The ground-state fluorescein values are quoted from Lindquist.[2b] The others are from Figures 2 and 8.

Table II: Values of pK_i

	pK_1	pK_2	pK_3'	$pK_3'^*$	$pK_3' - pK'^*$	$0.625\ \Delta\bar{\nu}/T$[a]
Fluorescein	2.2	4.4	6.7	6.9	−0.2	0.1
Dichlorofluorescein	0.5	3.5	5.0	5.2	−0.2	0.3

[a] See ref 8.

Consistent with Förster's cycle,[8,9] excitation has only a small effect on pK_3'. In computing $\Delta\bar{\nu}$, we have neglected the absorption maximum at 2.20×10^4 cm^{-1} (Figure 1 and Figure 7, ref 2) and the emission maximum at 1.83×10^4 cm^{-1} (Figures 4 and 6). These secondary maxima which occur at the same frequencies for fluorescein and dichlorofluorescein may be due to the presence of small amounts of persistent impurities. This view is supported by the fact that the fluorescein samples used in the present study and by Lindquist[2] and Rozwadowski[4] were purified in the same way.[3]

Substitution of chlorine atoms in the 2′ and 7′ positions renders the ground-state species and the excited monoanion stronger acids. The difference, 1.7, is the same for pK_1, pK_3', and $pK_3'^*$. For pK_2, it is 0.9.

The present data support Rozwadowski's[4] opinion (based on Zanker and Peter's[2b] evidence) that neutral fluorescein is practically nonfluorescent. This is in contradiction to the view of Stoughton and Rollefson[10] and of Umberger and La Mer[11] that the neutral rather than the monoionic form is fluorescent. Their opinion was based on the observation that the Stern–Vollmer constant, for the quenching of fluorescein by I^-, shows no significant dependence on ionic strength. A possible interpretation of this apparent contradiction is that small changes in fluorescence intensity due to salt effects on the quenching constant are approximately canceled by corresponding effects on the K_i and K_i^*.

Lumry and Georghiou[12] measured the mean lifetime of fluorescence of fluorescein in solutions containing, severally, 7.0 *m* $HClO_4$, 0.20 *m* $HClO_4$, and a buffer having a pH of 2.73. Their results in general agree with those published by Rozwadowski.[4] Their measurements, which were made with a modified Bennet-type apparatus,[13] showed no significant departure from simple exponential decay. This latter result indicates that, at each of these acidities, there is only a single fluorescent species present.

Acknowledgments. The authors wish to thank L. Lindquist for reading the section on the ground-state equilibria, D. Coffey for advice and assistance in setting up the computer analysis, and R. Lumry and Georghiou for making the fluorescence lifetime measurements. We are also grateful for financial assistance from the Research Corporation and from the National Science Foundation Undergraduate Research Participation Program.

(10) R. Stoughton and G. Rollefson, *J. Amer. Chem. Soc.*, **61**, 2634 (1939).

(11) J. Umberger and V. La Mer, *ibid.*, **67**, 1099 (1945).

(12) R. Lumry and S. Georghiou, unpublished work, 1969.

(13) W. Ware, "Creation and Detection of the Excited State," A. Lamola, Ed., Marcel Decker. New York, N. Y., 1970.

Reduction of Cerium(IV) by Hydrogen Peroxide. Dependence of Reaction Rate on Hammett's Acidity Function[1,2]

by H. A. Mahlman, R. W. Matthews,[3a] and T. J. Sworski*[3b]

Chemistry Division, Oak Ridge National Laboratory, Oak Ridge, Tennessee 37830 *(Received June 12, 1970)*

Publication costs assisted by the U. S. Atomic Energy Commission

The rate of cerium(IV) reduction by hydrogen peroxide adheres well to $d[Ce^{IV}]/dt = -2k_{obsd}[Ce^{IV}]^2[H_2O_2]/[Ce^{III}]$. A marked decrease in k_{obsd} with increase either in sulfuric acid concentration from 2.0 to 8.0 M or in ammonium bisulfate concentration from 1.0 to 5.0 M is consistent with an equilibrium between HO_2 and $H_2O_2^+$. A marked increase in k_{obsd} with further increase in sulfuric acid concentration from 8.0 to 13.0 M is consistent with an equilibrium between H_2O_2 and $H_3O_2^+$. The dependence of k_{obsd} on sulfuric acid concentration is expressed quantitatively as a function of Hammett's acidity function H_0.

Introduction

Reduction of cerium(IV) by hydrogen peroxide in aqueous solutions has been postulated[4,5] to proceed through two consecutive one electron transfer reactions. Sigler and Masters[6] obtained kinetic evidence

$$Ce^{IV} + H_2O_2 \xrightarrow{k_1} Ce^{III} + H^+ + HO_2 \qquad (1)$$

$$Ce^{IV} + HO_2 \xrightarrow{k_2} Ce^{III} + H^+ + O_2 \qquad (2)$$

for the HO_2 radical as an intermediate in their study of isotopic exchange between cerium(IV) and radioactive cerium(III) in 0.4 M sulfuric acid solutions induced by hydrogen peroxide. They postulated the reverse of reaction 1

$$Ce^{III} + H^+ + HO_2 \xrightarrow{k_{-1}} Ce^{IV} + H_2O_2$$

and determined $k_{-1}[H^+]/k_2 = 0.129 \pm 0.013$ at 0°. Direct evidence for the HO_2 radical as an intermediate was obtained[7,8] by electron spin resonance spectroscopy.

Reduction of cerium(IV) by hydrogen peroxide is fast, the reaction reportedly[5] being complete within a few seconds even at micromolar reagent concentrations. Therefore, dynamic-flow methods[9] were used by Czapski, Bielski, and Sutin[10] to study the kinetics of this reaction. They confirmed the reaction mechanism of Sigler and Masters and determined $k_1 = (1.0 \pm 0.1) \times 10^6\ M^{-1}\ sec^{-1}$ and $k_1k_2/(k_{-1}[H^+]) = (1.28 \pm 0.1) \times 10^7\ M^{-1}\ sec^{-1}$ in 0.4 M sulfuric acid at 25°.

In a preliminary communication[11] on our study of cerium(III) oxidation in 4.0 M sulfuric acid induced by ^{60}Co γ radiation, we reported the rate of cerium(IV) reduction by hydrogen peroxide to be much slower in 4.0 M sulfuric acid with $k_1k_2/(k_{-1}[H^+]) = 2.15 \times 10^5\ M^{-1}\ sec^{-1}$. In this paper, we report a kinetic study of the reduction of cerium(IV) by hydrogen peroxide both in sulfuric acid solutions from 2.0 to 13.0 M and in ammonium bisulfate solutions from 1.0 to 5.0 M.

Experimental Section

Materials. Water from a Barnstead still was further purified by successive distillations from an acid dichromate solution, from an alkaline permanganate solution, and from an all-silica system to be stored in silica vessels. Solutions were prepared using reagent grade chemicals: G. Frederick Smith ceric ammonium sulfate and cerous sulfate, Baker and Adamson ammonium bisulfate, E. I. du Pont de Nemours and Co. sulfuric acid, and J. T. Baker Chemical Co. hydrogen peroxide. The cerous sulfate was further purified by a procedure which we previously reported.[12]

Analytical Procedure. Cerium(IV) concentrations in all solutions were determined by absorbance measurements with a Cary Model 15 recording spectrophotometer. For sulfuric acid solutions, the molar extinction coefficients reported by Boyle[13] were used. For ammonium bisulfate solutions, the following molar ex-

(1) Research sponsored by the U. S. Atomic Energy Commission under contract with Union Carbide Corp.

(2) Presented at the 157th National Meeting of the American Chemical Society, Minneapolis, Minn., Apr 14–18, 1969.

(3) (a) Guest Scientist from the Australian Atomic Energy Research Establishment, Sydney, Australia. (b) To whom correspondence should be addressed.

(4) S. Baer and G. Stein, *J. Chem. Soc.*, 3176 (1953).

(5) J. H. Baxendale, Special Publication No. 1, The Chemical Society, London, 1954, p 40.

(6) P. B. Sigler and B. J. Masters, *J. Amer. Chem. Soc.*, **79**, 6353 (1957).

(7) E. Saito and B. H. J. Bielski, *ibid.*, **83**, 4467 (1961).

(8) B. H. J. Bielski and E. Saito, *J. Phys. Chem.*, **66**, 2266 (1962).

(9) H. Harridge and F. J. W. Roughton, *Proc. Roy. Soc., Ser. A*, **104**, 376 (1923).

(10) G. Czapski, B. H. J. Bielski, and N. Sutin, *J. Phys. Chem.*, **67**, 201 (1963).

(11) R. W. Matthews, H. A. Mahlman, and T. J. Sworski, *ibid.*, **72**, 3704 (1968).

(12) R. W. Matthews, H. A. Mahlman, and T. J. Sworski, *ibid.*, **74**, 2475 (1970).

(13) J. W. Boyle, *Radiat. Res.*, **17**, 427 (1962).

tinction coefficients were determined for cerium(IV) at 320 nm: 6498 for 1.0 *M* NH_4HSO_4, 6996 for 3.0 *M* NH_4HSO_4, and 7472 for 5.0 *M* NH_4HSO_4. Cerium(III) concentrations in cerium(III) and cerium(IV) stock solutions were determined by oxidation of cerium(III) by argentic oxide[14] followed by spectrophotometric analyses for cerium(IV).

Experimental Procedure. The experimental procedure was similar to that which we previously used to study the kinetics of cerium(IV) reduction by nitrous acid in sulfuric acid solutions.[15] All kinetic studies were made with air-saturated solutions in a 2-cm cylindrical spectrophotometer cell at ambient room temperature of about 25°. The synchronous drive feature of the spectrophotometer was used to record the solution absorbance as a function of time. A negligibly small volume of stock hydrogen peroxide solution was injected by a micropipet into the cerium(IV)–cerium(III) solutions in a 2-cm cell, and the chart drive was simultaneously activated. The cell was then capped, shaken vigorously with a small air space present, and placed into the sample cavity of the spectrophotometer; the decreasing absorption due to cerium(IV) was recorded as a function of time.

Results

We assume that the stoichiometry for the reduction of cerium(IV) by hydrogen peroxide is well established. Two cerium(IV) ions are reduced by each molecule of hydrogen peroxide.[4] All experiments were conducted with initial concentrations of hydrogen peroxide that were insufficient to reduce all of the cerium(IV). The reaction kinetics could then be studied by monitoring only the cerium(IV) concentration. Hydrogen peroxide concentrations were not determined, but inferred.

Typical experimental data that demonstrate the feasibility for a kinetic study using classical spectrophotometric techniques are shown in Figure 1. First, the initial solution absorbance was recorded. After hydrogen peroxide was added, about 7 sec was consumed in capping, shaking, and placing the 2-cm cell in the spectrophotometer before the solution absorbance could be recorded as a function of time. The dotted line in Figure 1 indicates the amount of reaction that occurred during this 7-sec period. The solid line from 7 to 163 sec is the recorded solution absorbance that shows the decrease in cerium(IV) concentration with time. Many hours later, when the reaction is sensibly complete, the final solution absorbance is recorded.

The reaction mechanism of Sigler and Masters requires that the rate of reaction adhere to eq I. We con-

$$\frac{d[Ce^{IV}]}{dt} = -2k_1[Ce^{IV}][H_2O_2] \Big/ \left(1 + \frac{k_{-1}[H^+][Ce^{III}]}{k_2[Ce^{IV}]}\right) \quad (I)$$

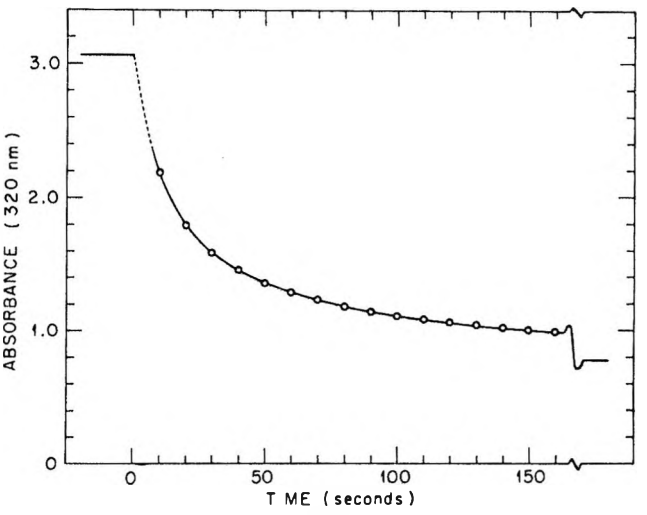

Figure 1. Reduction of cerium(IV) by hydrogen peroxide in 5.0 *M* ammonium bisulfate solutions. Solid curve is cerium(IV) absorbance in a 2.0-cm cell; initial $[Ce^{IV}] = 19.7 \times 10^{-5}$ *M*; initial $[Ce^{III}] = 52.35 \times 10^{-5}$ *M*; $a_{obsd} = 5.43 \times 10^{-5}$ *M*; $a_{calcd} = 5.20 \times 10^{-5}$ *M*; O, data selected at 10-sec intervals for computer analysis.

firm the approximation[10] that $k_{-1}[H^+][Ce^{III}]$ is much greater than $k_2[Ce^{IV}]$ since all of our data adhere well to eq II. Since $[Ce^{IV}]$, $[H_2O_2]$, and $[Ce^{III}]$ all change with

$$\frac{d[Ce^{IV}]}{dt} = -\frac{2k_{obsd}[Ce^{IV}]^2[H_2O_2]}{[Ce^{III}]} \quad (II)$$

time, we must obtain relations between them in order to integrate eq II.

Let a denote the concentration of cerium(IV) when reaction is complete, x denote $[Ce^{IV}] - a$, and c denote the sum of the initial concentrations of cerium(IV) and cerium(III). Then $[Ce^{IV}] = a + x$, $[H_2O_2] = 0.5x$ due to stoichiometry, $[Ce^{III}] = c - a - x$, and the rate of reaction is given by eq III. Integration

$$\frac{dx}{dt} = -\frac{k_{obsd}x(a + x)^2}{(c - a - x)} \quad (III)$$

yields eq IV in which C_I is the constant of integration.

$$\frac{a}{a + x} - \left(1 - \frac{a}{c}\right)\ln\left(\frac{c + x}{x}\right) = -\frac{a^2k_{obsd}t}{c} + C_I \quad (IV)$$

Figure 2 shows the applicability of eq IV, specifically for the experimental data also shown in Figure 1.

A computer program SLOPULSE, previously used[15] in a kinetic study of cerium(IV) reduction by nitrous acid, was adapted for use in this study. The experimental data were fit to eq IV by the method of least squares using our laboratory's IBM 360/75 computer.

(14) J. J. Lingane and D. J. Davis, *Anal. Chim. Acta*, 15, 201 (1956).

(15) T. J. Sworski, R. W. Matthews, and H. A. Mahlman, Advances in Chemistry Series, No. 81, American Chemical Society, Washington, D. C., 1968, p 164.

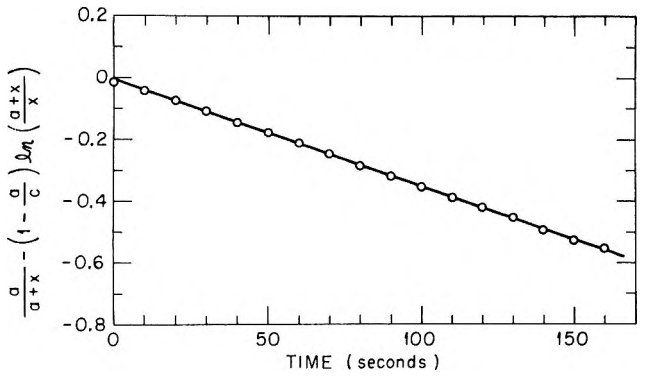

Figure 2. Test for applicability of eq IV: O, ordinate values for selected data shown in Figure 1.

At first, the observed values for a were used. Later, the computer program was modified to determine that value for a which would give the best fit of the data to eq IV. The results from the use of this modified computer program are listed in Table I for sulfuric acid solutions and in Table II for ammonium bisulfate solutions.

Table I: Reduction of Cerium(IV) by Hydrogen Peroxide in Sulfuric Acid Solutions

$[H_2SO_4]$, M	$[Ce^{III}]$ $M \times 10^4$	k_{obsd}, M^{-1} sec^{-1} $\times 10^{-4}$
2.0	324	123 ± 2 (5)[a]
2.0	162	129 ± 6 (2)
3.0	388	43.4 ± 1.6 (4)
3.0	194	43.3 ± 1.3 (4)
4.0	339	22.5 ± 0.9 (4)
4.0	169.7	22.2 ± 0.9 (4)
4.0	42.4	21.2 ± 0.1 (2)
6.0	324	5.62 ± 0.04 (2)
6.0	162	4.70 ± 0.21 (4)
8.0	162	2.83 ± 0.35 (6)
8.0	32.4	2.52 ± 0.16 (4)
8.0	9.7	3.20 ± 0.09 (2)
10.0	162	4.50 ± 0.02 (3)
10.0	32.4	4.21 ± 0.06 (2)
12.0	162	27.0 ± 1.3 (4)
12.0	97.2	50.4 ± 8.2 (4)
12.0	32.4	49.9 ± 2.8 (2)
13.0	648	441 ± 133 (4)
13.0	486	461 ± 42 (4)
13.0	324	394 ± 134 (7)

[a] Number of experiments indicated within parentheses.

Comparison of observed (a_{obsd}) and calculated (a_{calcd}) values of a proved to be instructive. For 1.0 M ammonium bisulfate solutions and 2.0–4.0 M sulfuric acid solutions, a_{calcd} was randomly either slightly larger or slightly smaller than a_{obsd}. For 3.0 and 5.0 M ammonium bisulfate solutions and 6.0 to 10.0 M sulfuric acid solutions, a_{calcd} was generally smaller than a_{obsd}. For 12.0 and 13.0 M sulfuric acid solutions, a_{calcd} was always larger than a_{obsd}.

Table II: Reduction of Cerium(IV) by Hydrogen Peroxide in Ammonium Bisulfate Solutions

$[NH_4HSO_4]$, M	$[Ce^{III}]$,[a] $M \times 10^5$	k_{obsd} M^{-1} sec^{-1} $\times 10^{-3}$
1.0	648	766 ± 4 (2)[b]
1.0	324	621 ± 9 (2)
3.0	324	17.6 ± 0.3 (2)
3.0	162	15.4 ± 0.4 (2)
5.0	104	1.19 ± 0.09 (4)
5.0	52.0	1.21 ± 0.06 (4)
5.0	26.0	1.22 ± 0.09 (4)
5.0	13.0	1.19 ± 0.10 (3)
5.0	6.5	1.33 ± 0.12 (2)
5.0	0	1.21 ± 0.01 (2)

[a] Additional cerium(III) (0.35×10^{-5} M) present in 5.0 M ammonium bisulfate solutions due to presence of cerium(III) in cerium(IV) stock solution. [b] Number of experiments indicated within parentheses.

The lower values of a_{calcd} for 6.0 to 10.0 M sulfuric acid solutions were dramatically called to our attention. Results from seven experiments had to be withdrawn from inclusion in Table I because no best fit of the data to eq IV was indicated for any positive value of a_{calcd}. The solutions for these seven experiments must have contained excess hydrogen peroxide. The lower values of a_{calcd} probably result from recording of a_{obsd} before reactions were truly complete.

The higher values for a_{calcd} in 12.0 and 13.0 M sulfuric acid solutions suggested an interfering reaction. This may be the formation of peroxymonosulfuric acid from hydrogen peroxide, recently investigated[16,17] in 5.0–12.0 M sulfuric acid solutions. To test this possibility, we conducted some experiments in which cerium(IV) was added to sulfuric acid solutions at varying delay times after addition of hydrogen peroxide. The results for 8.0 and 10.0 M sulfuric acid solutions are listed in Table III.

Table III: Effect of Delay Time for Cerium(IV) Addition after Hydrogen Peroxide Addition

$[H_2SO_4]$, M	$[Ce^{III}]$, M	Delay time, min	$a_{calcd} - a_{obsd}$, $M \times 10^5$	k_{obsd} M^{-1} sec^{-1} $\times 10^{-4}$
8.0	0.013	0	1.9	3.97
8.0	0.013	5	2.6	3.94
8.0	0.013	10	2.4	4.19
8.0	0.013	120	3.1	3.79
10.0	0.052	0	3.7	9.33
10.0	0.052	5	8.9	10.3
10.0	0.052	10	8.9	9.21
10.0	0.052	120	16.0	9.12
10.0	0.052	1080	15.5	9.08
10.0	0.052	1080	25.0	9.58

(16) J. M. Monger and O. Redlich, *J. Phys. Chem.*, **60**, 797 (1956).
(17) O. Redlich and W. E. Gargrave, *ibid.*, **72**, 3045 (1968).

The effect of delay times for cerium(IV) addition was examined qualitatively for hydrogen peroxide solutions in 13.0 *M* sulfuric acid containing no cerium(III) initially. An initially fast reduction of cerium(IV) was followed by slow reduction. The fraction of cerium(IV) reduction by the slow reaction increased with increase in delay time. The rate of this slow reaction was not markedly affected by the presence of 0.052 *M* cerium(III). Since reaction of cerium(IV) with peroxymonosulfuric acid is inhibited[18] by high concentrations of cerium(III), the slow reaction results from slow hydrolysis of peroxymonosulfuric acid to yield hydrogen peroxide as reported by Boyle.[13]

For the experiments summarized in Tables I and II, the cerium(IV) solutions were prepared the previous day to allow reduction of cerium(IV) by the impurities in sulfuric acid to go to completion. In 8.0 *M* sulfuric acid solutions, the amount of cerium(IV) reduced by impurities in one day amounted to about 3×10^{-6} *M*. We attribute the small values of $a_{calcd} - a_{obsd}$ listed in Table III for zero delay times to reduction of cerium(IV) by impurities.

The very large values of $a_{calcd} - a_{obsd}$ for 10.0 *M* sulfuric acid solutions with long delay times, listed in Table III, are attributed to formation of peroxymonosulfuric acid from hydrogen peroxide prior to addition to cerium(IV). Despite the presence of peroxymonosulfuric acid, use of the modified computer program yielded values for k_{obsd} which are essentially independent of delay time. Therefore, the positive values of $a_{calcd} - a_{obsd}$ observed for 12.0 and 13.0 *M* sulfuric acid solutions do not invalidate the values for k_{obsd} listed in Table I but only indicate a cause for the increase in experimental error that is pronounced for 13.0 *M* sulfuric acid solutions.

Discussion

The lowest value for k_{obsd} was observed for 5.0 *M* ammonium bisulfate solutions. Then, as indicated in Table II, the rate of cerium(IV) reduction is so slow that it is unnecessary to purposefully add cerium(III) initially to be able to monitor the reaction. Our objective for the experiments with no cerium(III) added initially was to determine both k_1 and $k_2/(k_{-1}[H^+])$ through the use of eq V which results from the integration of eq I. However, the result was only to further establish the validity of eq II and IV.

$$\frac{a}{a+x} - \left[1 - \frac{a}{c}\left(1 - \frac{k_2}{k_{-1}[H^+]}\right) \times \ln\left(\frac{a+x}{x}\right) = -\frac{a^2 k_1 k_2 t}{c k_{-1}[H^+]} + C_I \quad \text{(V)}$$

Comparison of eq IV and V reveals the reason for the validity of eq IV in 5.0 *M* ammonium bisulfate solutions with no cerium(III) added initially. $k_2/(k_{-1}[H^+])$ must be much less than 1 in marked contrast with the value of 12.8 determined[10] in 0.4 *M* sulfuric acid solutions. Therefore, the marked decrease in k_{obsd} with increase either in ammonium bisulfate concentration from 1.0 to 5.0 *M* or in sulfuric acid concentration from 0.4 to 8.0 *M* can be attributed to a marked decrease in $k_2/(k_{-1}[H^+])$.

Protonation of HO_2. The dependence of k_{obsd} on sulfuric acid concentration from 0.4 to 8.0 *M* can be quantitatively explained by assuming a sensible equilibrium between HO_2 and $H_2O_2^+$ with $K_{H_2O_2^+} = h_0[HO_2]/[H_2O_2^+]$. The function h_0 is related to Hammett's acidity function H_0 by the relationship $H_0 = -\log h_0$.[19] The experimental data are consistent with the following reaction mechanism.

$$Ce^{IV} + H_2O_2 \underset{k_{-3}}{\overset{k_3}{\rightleftharpoons}} Ce^{III} + H_2O_2^+ \quad (3)$$

$$H_2O_2^+ \rightleftharpoons H^+ + HO_2 \quad (4)$$

$$Ce^{IV} + HO_2 \xrightarrow{k_5} Ce^{III} + HO_2^+ \quad (5)$$

$$HO_2^+ \longrightarrow H^+ + O_2 \quad (6)$$

$$Ce^{IV} + H_2O_2^+ \longrightarrow Ce^{III} + H_2O_2^{2+} \quad (7)$$

$$H_2O_2^{2+} \longrightarrow H^+ + HO_2^+ \quad (8)$$

$K_{HO_2^+}$ and $K_{H_2O_2^{2+}}$ are assumed to be so large that reactions 5–8 are sensibly irreversible. The rates of reaction of HO_2 and $H_2O_2^+$ with cerium(III) and cerium(IV) are assumed to be negligibly small compared with the rates of protonation of HO_2 and dissociation of $H_2O_2^+$ so that virtual equilibrium exists between HO_2 and $H_2O_2^+$. The rates of reduction of cerium(IV) by HO_2 and $H_2O_2^+$ are assumed to be negligibly small compared with the rate of oxidation of cerium(III) by $H_2O_2^+$. The rate of cerium(IV) reduction is then given by eq II with

$$k_{obsd} = \frac{k_3 k_7}{k_{-3}}\left(1 + \frac{k_5 K_{H_2O_2^+}}{k_7 h_0}\right) \quad \text{(VI)}$$

There should be a linear correlation between log k_{obsd} and Hammett's acidity function H_0 when $H_2O_2^+$ is essentially completely dissociated. Figure 3 does indicate just such a correlation at low sulfuric acid concentrations. Log $k_{obsd} - H_0$ approaches a limiting constant value with decreasing sulfuric acid concentration. H_0 values were obtained by interpolation from the data of Ryabova, Medvetskaya, and Vinnik.[20]

The experimental data for sulfuric acid solutions from 2.0 to 8.0 *M* were fit to eq VI by the method of least squares using the computer program of Lietzke[21] and assuming that all determinations had a constant

(18) M. H. Mariano, *Anal. Chem.*, **40**, 1662 (1968).

(19) L. P. Hammett, "Physical Organic Chemistry," McGraw-Hill, New York, N. Y., 1940, Chapter 9.

(20) R. S. Ryabova, I. M. Medvetskaya, and M. I. Vinnik, *Russ. J. Phys. Chem.*, **40**, 182 (1964).

(21) M. H. Lietzke, ORNL-3259, Mar 21, 1962.

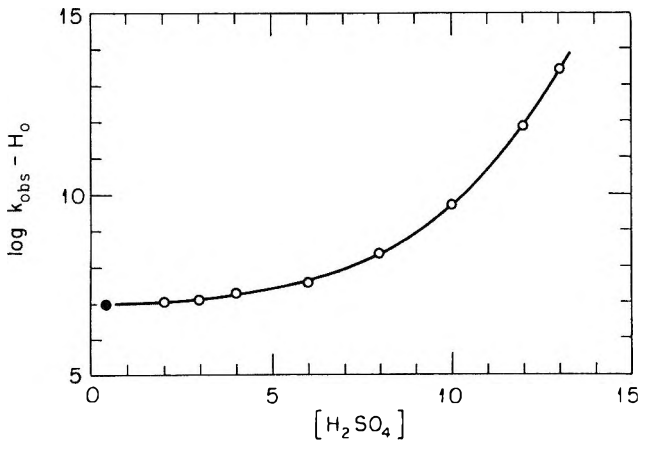

Figure 3. Test for correlation between log k_{obsd} and Hammett's acidity function H_0: O, data of this paper; ●, data of Czapski, Bielski, and Sutin.[10]

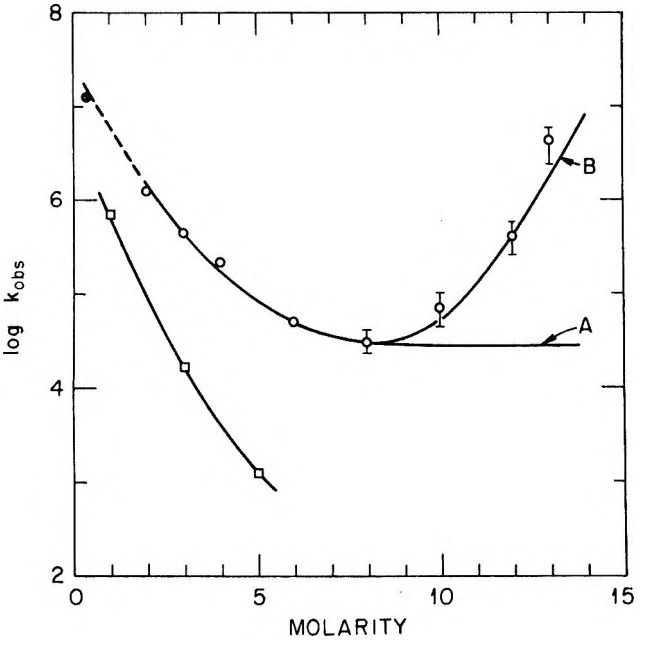

Figure 4. Dependence of k_{obsd} on ammonium bisulfate and sulfuric acid concentrations: □, ammonium bisulfate solutions; O, sulfuric acid solutions, data of this paper; ●, sulfuric acid solutions, data of Czapski, Bielski, and Sutin;[10] A, computed curve using eq VI; B, computed curve using eq VII.

percentage error. The data adhere well to eq VI as indicated by the computed curve A in Figure 4 with $k_3k_7/k_{-3} = (2.8 \pm 0.2) \times 10^4\ M^{-1}\ \text{sec}^{-1}$ and $k_5K_{H_2O_2^+}/k_7 = (4.4 \pm 0.3) \times 10^2\ M$. The dashed line in Figure 4 that extends curve A to 0.4 M sulfuric acid shows that our results are in excellent agreement with those of Czapski, Bielski, and Sutin.[10]

The original evidence[22] for the existence of $H_2O_2^+$ has been refuted.[23] However, new evidence has been obtained by Pucheault, Ferradini, and Buu[24] from a study of iron(II) oxidation in perchloric and sulfuric acid solutions induced by ^{60}Co γ radiation. They attributed the influence of pH on the dependence of $G(Fe^{III})$ on iron(II) and iron(III) concentrations to oxidation of iron(II) by $H_2O_2^+$ and reduction of iron(III) by HO_2. The apparent validity of eq VI for sulfuric acid solutions from 0.4 to 8.0 M is considered further evidence for the existence of $H_2O_2^+$.

Pucheault, Ferradini, and Buu[24] assumed that HO_2 and $H_2O_2^+$ were not in equilibrium owing to reactions of HO_2 and $H_2O_2^+$ with iron(II) and iron(III). A similar approach for the reduction of cerium(IV) by hydrogen peroxide would predict a complex dependence of k_{obsd} on cerium(III) and cerium(IV) concentrations. The independence of k_{obsd} on both cerium(III) and cerium(IV) concentrations as originally reported by Czapski, Bielski, and Sutin[10] is justification for our assumption of virtual equilibrium between HO_2 and $H_2O_2^+$.

Protonation of H_2O_2. As shown in Table I and Figure 4, k_{obsd} has a minimum value at a sulfuric acid concentration near 8.0 M and then increases with further increase in sulfuric acid concentration. There may be a correlation between this increase in k_{obsd} and the reported increase in rate of peroxymonosulfuric acid formation from hydrogen peroxide for the same concentration range. Although Redlich and Gargrave[17] support the original proposal[16] that peroxymonosulfuric acid formation results from reaction of hydrogen peroxide with undissociated sulfuric acid molecules, they do admit a possible linear correlation for 9.0–12.5 M sulfuric acid solutions between the rate of peroxymonosulfuric acid formation and Hammett's acidity function H_0. Such a correlation suggests the existence of $H_3O_2^+$.

The increase in k_{obsd} with increase in sulfuric acid concentration from 8.0 to 13.0 M can be quantitatively explained by assuming a sensible equilibrium between H_2O_2 and $H_3O_2^+$ with $K_{H_3O_2^+} = h_0[H_2O_2]/[H_3O_2^+]$. The experimental data are consistent with inclusion of reactions 9–11 in our proposed reaction mechanism.

$$H_3O_2^+ \rightleftharpoons H^+ + H_2O_2 \qquad (9)$$

$$Ce^{IV} + H_3O_2^+ \xrightarrow{k_{10}} Ce^{III} + H_3O_2^{2+} \qquad (10)$$

$$H_3O_2^{2+} \longrightarrow H^+ + H_2O_2^+ \qquad (11)$$

$K_{H_3O_2^{2+}}$ is assumed to be so large that reactions 10 and 11 are sensibly irreversible. The rates of reaction of cerium(IV) with H_2O_2 and $H_3O_2^+$ are assumed to be negligibly small compared with the rates of protonation of H_2O_2 and dissociation of $H_3O_2^+$ so that virtual equilibrium exists between H_2O_2 and $H_3O_2^+$. The depen-

(22) B. H. J. Bielski and A. O. Allen, "Proceedings of the 2nd Tihany Symposium on Radiation Chemistry," Akademiai Kiado, Budapest, 1967, p 81.

(23) B. H. J. Bielski and H. A. Schwarz, *J. Phys. Chem.*, 72, 3836 (1968).

(24) J. Pucheault, C. Ferradini, and A. Buu, *Int. J. Radiat. Phys. Chem.*, 1, 209 (1969).

dence of k_{obsd} on sulfuric acid concentration is consistent with $K_{H_3O_2^+}$ being much greater than h_0, k_{obsd} being well approximated by eq VII.

$$k_{obsd} = \frac{k_3k_7}{k_{-3}}\left(1 + \frac{k_5K_{H_2O_2^+}}{k_7h_0}\right)\left(1 + \frac{k_{10}h_0}{k_3K_{H_3O_2^+}}\right) \quad \text{(VII)}$$

The experimental data for sulfuric acid solutions from 2.0 to 13.0 M were fit to eq VII by the method of least squares. The data adhere well to eq VII as indicated by the computed curve B in Figure 4 with $k_3k_7/k_{-3} = (2.6 \pm 0.3) \times 10^4\ M^{-1}\ sec^{-1}$, $k_5K_{H_2O_2^+}/k_7 = (4.8 \pm 0.6) \times 10^2\ M$, and $k_3K_{H_3O_2^+}/k_{10} = (1.1 \pm 0.2) \times 10^5\ M$. These values for k_3k_7/k_{-3} and $k_5K_{H_2O_2^+}/k_7$ agree within standard errors with those obtained with the use of eq VI. The apparent validity of eq VII for sulfuric acid concentrations from 8.0 to 13.0 M is presented here as kinetic evidence for the existence of $H_3O_2^+$.

The quantitative correlation between k_{obsd} and Hammett's acidity function H_0 for sulfuric acid solutions is good evidence for the importance of equilibria involving hydrogen ions. Our proposed reaction mechanism is admittedly not a unique one, however, but only favored for the reasons cited. As previously pointed out for the acid dependence in oxidations of hydrogen peroxide, many alternative mechanisms can be shown to yield the same acid dependence.[5]

Ammonium Bisulfate Solutions. Values for Hammett's acidity function H_0 have not been determined for ammonium bisulfate solutions. This precludes any quantitative test of our reaction mechanism for the dependence of k_{obsd} on ammonium bisulfate concentration. The dependence of k_{obsd} on ammonium bisulfate concentration cannot be given by eq VI or VII with the constants determined for sulfuric acid solutions, however, since k_{obsd} for 3.0 and 5.0 M ammonium bisulfate solutions is less than the value determined for k_3k_7/k_{-3}.

Corresponding State Relations for the Newtonian Viscosity of Concentrated Polymer Solutions. Temperature Dependence

by Robert Simha* and F. S. Chan

Division of Macromolecular Science, Case Western Reserve University, Cleveland, Ohio 44106 *(Received July 30, 1970)*

Publication costs borne completely by The Journal of Physical Chemistry

Previous studies have demonstrated the validity of a corresponding states principle in respect to molecular weight under isothermal conditions. This restriction is now removed by investigating the Newtonian viscosities of polystyrene solutions in 1-chlorodecane. The molecular weights are varied from 10^4 to 1.7×10^6, the temperatures from 6.6° (θ) to 90°, and the upper limit of concentration is about $4/[\eta]$. The results lead to temperature superposition with limitations mainly affecting the lowest fraction. That is, a characteristic concentration factor can be defined as a function of a reduced molecular weight and a reduced temperature which depend solely on the choice of a reference molecular weight M_0 and a reference temperature T_0. The proposition is examined that a reduced temperature $\tilde{T} = T/T_c(M_0)$ can be defined in terms of $T_c(M_0)$, the thermodynamic critical solution temperature of the reference polymer. Only an indirect estimate of $T_c(M_0)$ is given, which is based on thermodynamic and intrinsic viscosity data for the polystyrene–cyclohexane system in the critical region. With this current limitation, the above proposition is found to be valid. The positive temperature coefficients of the intrinsic viscosities present the appearance observed in other solvents and suggested by others as an indication of a conformational "transition" around 50°. With increasing concentration a change in the sign of the temperature dependence occurs, with an intermediate region of vanishing temperature coefficients. The conditions for the occurrence of such in terms of molecular weight, temperature, and concentration are discussed semiquantitatively by means of analytical representations of the results.

I. Introduction

Several hydrodynamic and thermodynamic factors determine the concentration and molecular weight dependence of the viscosity of coiling molecules, which place considerable obstacles in the development of quantitative theory, even in relatively dilute solutions. With this in mind we have explored, in a series of investigations,[1-3] the possibility of obtaining generalized functional representations, or in other words, superposition schemes. Under isothermal or nearly isothermal conditions, reduced variables $\tilde{\eta} = \eta_{sp}/(c[\eta])$ and $\tilde{c} = c/\gamma(M)$ could be defined which result in a single master curve for a given polymer series–solvent combination. Here $\gamma(M)$ represents a characteristic concentration factor, which varies inversely with a fractional power of the molecular weight. These results, originally obtained for moderate concentrations $c[\eta] \lesssim 4$, were subsequently shown to apply also to concentrated solutions, in a region extending beyond the so-called entanglement concentration.[3] However, deviations from the superposition scheme are noticeable in a range of lower molecular weights which appears to depend on the type of polymer.[4]

A series of predictions follow immediately from the validity of the superposition principle. For example, we obtain in dilute solution a dependence of the Huggins parameter k_1 on M in good solvents,[1] and a relationship between the molecular weight and concentration dependence of the viscosity which involves the thermodynamic characteristics of the solution, even at elevated concentrations.[3]

For the polystyrene–cyclohexane system in the neighborhood of the θ temperature, the reducing concentration γ can at least approximately be identified with the critical thermodynamic concentration.[2] In concentrated solutions the entanglement concentration can be shown to play the role of a reducing factor.[3] It follows that this concentration should vary with an inverse fractional power of M which, however, depends again on the solvent.

As said before, these results apply under isothermal conditions and the question arises whether superposition is valid in respect to temperature. That is, can a reduced temperature $\tilde{T}$ be obtained such that $\gamma = \gamma(M,\tilde{T})$? Our earlier experiments[1,2] suggest that γ will be a slowly varying function of T. Moreover, it could be established that the critical solution temperature represents a corresponding temperature for the intrinsic visocity.[5]

The purpose of this paper is to explore temperature superposition by measuring the viscosity of moderately concentrated solutions over a range of about 80° and for molecular weights varying by a factor of more than

(1) L. Utracki and R. Simha, *J. Polym. Sci. A*, **1**, 1089 (1963).
(2) L. Utracki and R. Simha, *J. Phys. Chem.*, **67**, 1052 (1963).
(3) R. Simha and L. Utracki, *J. Polym. Sci., Part A-2*, **5**, 853 (1967).
(4) L. Utracki, R. Simha, and N. Eliezer, *Polymer*, **10**, 43 (1969).
(5) L. Utracki and R. Simha, *J. Phys. Chem.*, **67**, 1056 (1963).

Table I: Characteristics of Polystyrene Fractions in 1-Chlorodecane at Four Temperatures and Cyclohexane at 34.4°

$M_w \times 10^{-4}$	M_w/M_n	$[\eta]$ (cyclohexane), dl g^{-1}	$M_v^a \times 10^{-4}$	5.6° $[\eta]$ dl g^{-1}	5.6° k_1	30° $[\eta]$ dl g^{-1}	30° k_1	60° $[\eta]$ dl g^{-1}	60° k_1	90° $[\eta]$ dl g^{-1}	90° k_1	T_θ^b (cyclohexane), °K	T_θ^c (1-chlorodecane), °K	$[\eta]_{T_\theta}^c$ dl g^{-1}
1	1.09	0.088	1.1	0.091	0.98	0.090	0.69	0.085	0.64	0.084	0.57	286.3	258.5	0.094
13	1.05	0.282	12	0.270	0.73	0.293	0.54	0.310	0.53	0.330	0.43	297.1	269.3	0.259
24	1.08	0.376	21	0.364	0.63	0.403	0.50	0.430	0.44	0.446	0.44	298.9	271.1	0.357
67	1.05	0.667	66	0.607	0.70	0.717	0.54	0.791	0.51	0.835	0.51	301.1	273.3	0.628
170	1.06	1.044	162	0.892	0.93	1.136	0.58	1.520	0.50	1.660	0.44	302.6	274.8	0.853

[a] Calculated from $[\eta]_{\text{cyclohexane}} = 8.2 \times 10^{-4} M_v^{0.5}$. [b] Calculated from $\log (T_\theta - T_c) = 2.491 - 0.290 \log M_w$; see text. [c] See text for explanation.

10^2. Aside from the principal question at hand, the quantitative results on the temperature coefficients are of interest because of the wide variations in the variables M and T and the coverage of the range from infinite dilution to well beyond the overlap of the molecular coils.

II. Experimental Section

Polymer. Five narrow molecular weight distribution polystyrenes were used. Their weight and number average molecular weights are given in the first two columns of Table I. Fractions 2 and 3 are identical with fractions 4 and 6 used previously.[2] The other three fractions were obtained from Pressure Chemical Co., Pittsburgh, Pa., and used without further purification. As a further check of their molecular weight, intrinsic viscosities were measured in cyclohexane at 34.4° (θ temperature). Values of $[\eta]$ are given in the same table together with the viscosity molecular weights M_v, calculated from the equation[6] $[\eta] = 8.2 \times 10^{-4} M_v^{0.5}$.

Solvent. 1-Chlorodecane was chosen because of its low volatility (bp = 108° at 17 mm) and known θ-temperature (6.6°).[7] It was the highest grade obtained from Aldrich Chemical Co., Inc., Milwaukee, Wis., with a refractive index (n^{20}D) of 1.4362.

Density. Densities of polystyrene solutions in 1-chlorodecane were measured in a 10-ml pycnometer at different temperatures and concentrations for a Dow polystyrene sample PS-2 ($M_w:M_n$ = 45,000:13,000). By assuming solution densities to be independent of polymer molecular weight at a given weight percentage concentration, density values at all concentrations were obtained by linear interpolation. Neglect of quadratic terms should not result in errors exceeding 0.6% for the highest concentration (40%) reached in this work.[8]

Viscosity. The polymer sample was left in a vacuum desiccator overnight and solutions were made up by weight at least 24 hr prior to measurement. The highest molecular weight fraction took 4–5 days for complete dissolution. In order to normalize the concentration scale for different molecular weights, we have imposed an upper limit of $4/[\eta]$ for all fractions. This corresponds to about 4 times the concentration at which the average polymer coils begin to overlap and amounts to about 40% and 5% by weight, respectively, for the lowest and highest molecular weight. To cover such a wide range, at least three internal dilution Ubbelohde viscometers with overlapping regions were used for each molecular weight fraction at each temperature. A total of eight viscometers were employed interchangeably. The calibrations were obtained by means of sucrose solutions at 20° and the pertinent viscometer characteristics are exhibited in Table II.

(6) W. R. Krigbaum and P. J. Flory, *J. Polym. Sci.*, 11, 37 (1953).
(7) T. A. Orofino and A. Ciferri, *J. Phys. Chem.*, 68, 3136 (1964).
(8) Th. G. Scholte, *J. Polymer. Sci., Part A-2*, 8, 841 (1970).

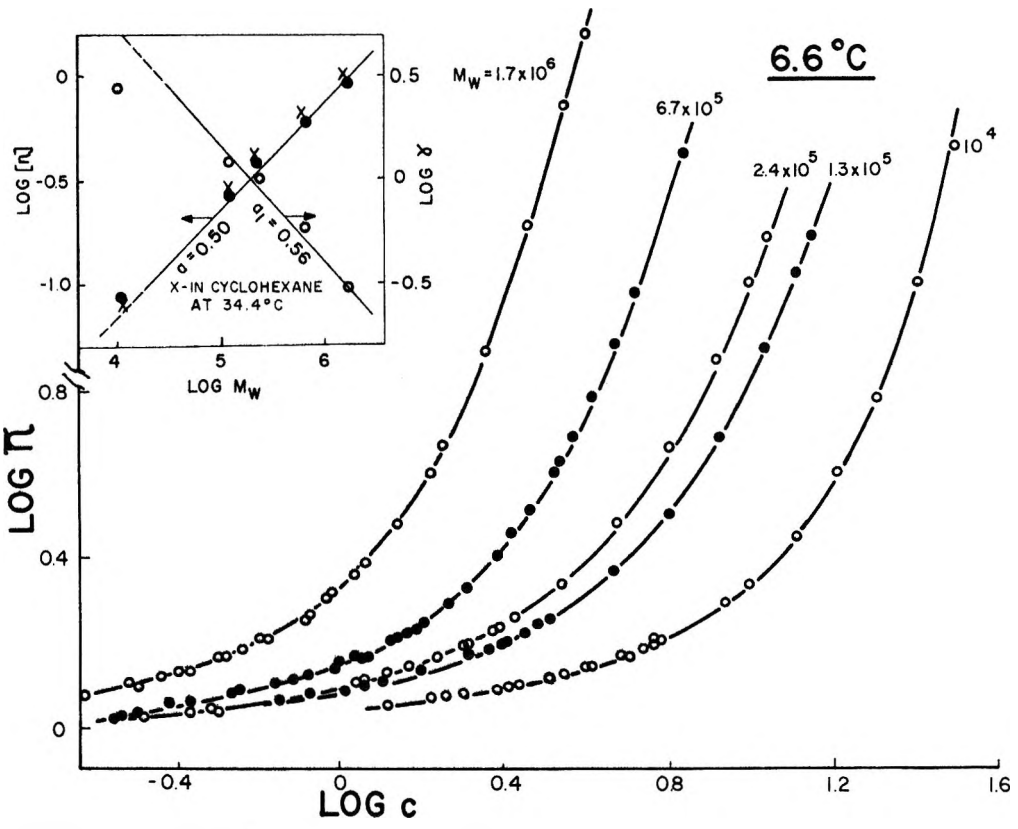

Figure 1. Reduced viscosity quantity ($\bar{\eta} = \eta_{sp}/(c[\eta])$ as a function of concentration (in g dl^{-1}) at 6.6°. Insert, intrinsic viscosity $[\eta]$ and characteristic concentration factor γ as a function of M_w for 1-chlorodecane and $[\eta]$ for cyclohexane at 34.4°.

Table II: Viscometer Constants and Dimensions

Viscometers	Viscometer constants, $cm^2\ sec^{-2}$	Capillary		Bulb volume, ml
		Diameter, mm	Length, cm	
1	0.383	0.442	8.9	3.11
2	0.352	0.446	9.0	3.68
3	1.474	0.354	12.5	0.29
4	1.610	0.370	12.4	0.33
5	2.874	0.432	12.2	0.33
6	3.087	0.434	12.4	0.32
7	8.767	0.582	12.4	0.35
8	9.176	0.584	12.3	0.34

The kinetic energy correction for these viscometers was minimized by using flow times above 150 sec. This represents a maximum error of less than 0.2% in the absolute viscosity. The maximum generalized rate of shear was calculated to be 0.07 in the worst case as compared to a value of 0.1 below which the viscosity of polystyrene solutions was found to be independent of shear.[9]

Measurements were made at temperatures of 6.6, 30, 60, and 90° in constant temperature baths controlled to ±0.05°. Starting from the highest concentration, dilutions were made by weight with a Friedman–LaMer weighing buret after each measurement of flow time, until the 150-sec limit was reached. A new polystyrene solution with a slightly higher concentration than the last was made up and placed in another viscometer with a lower viscometer constant. The same measuring procedure was repeated until the lowest concention was reached. Flow times were corrected for density differences.

III. Results and Discussion

Isothermal Conditions. The definition of the dimensionless reduced viscosity $\bar{\eta} = \eta_{sp}/(c[\eta])$ requires that the intrinsic viscosity of each fraction be known. Values of $[\eta]$ and the Huggins parameter k_1 at the four temperatures of measurement are given in Table I. They were obtained from finite concentration data using the extrapolation procedure of Maron and Reznik[10] in which the uncertainties of other methods could be minimized. In the inserts of Figures 1–4 are shown the Mark–Houwink plots of $[\eta]$ *vs.* M. Deviations from the general linear relationship are observed for the lowest molecular weight fraction ($M_w = 10^4$) at all four temperatures. Determinations of $[\eta]$ in cyclohexane at 34.4° (see Figure 1 and Table I) indicate that the deviation cannot be accounted for by errors in the molecular weight of this fraction. In the polystyrene-

(9) T. Kotaka, H. Suzuki, and H. Imagaki, *J. Chem. Phys.*, 45, 2770 (1966).

(10) S. H. Maron and R. B. Reznik, *J. Polym. Sci., Part A-2*, 7, 309 (1969).

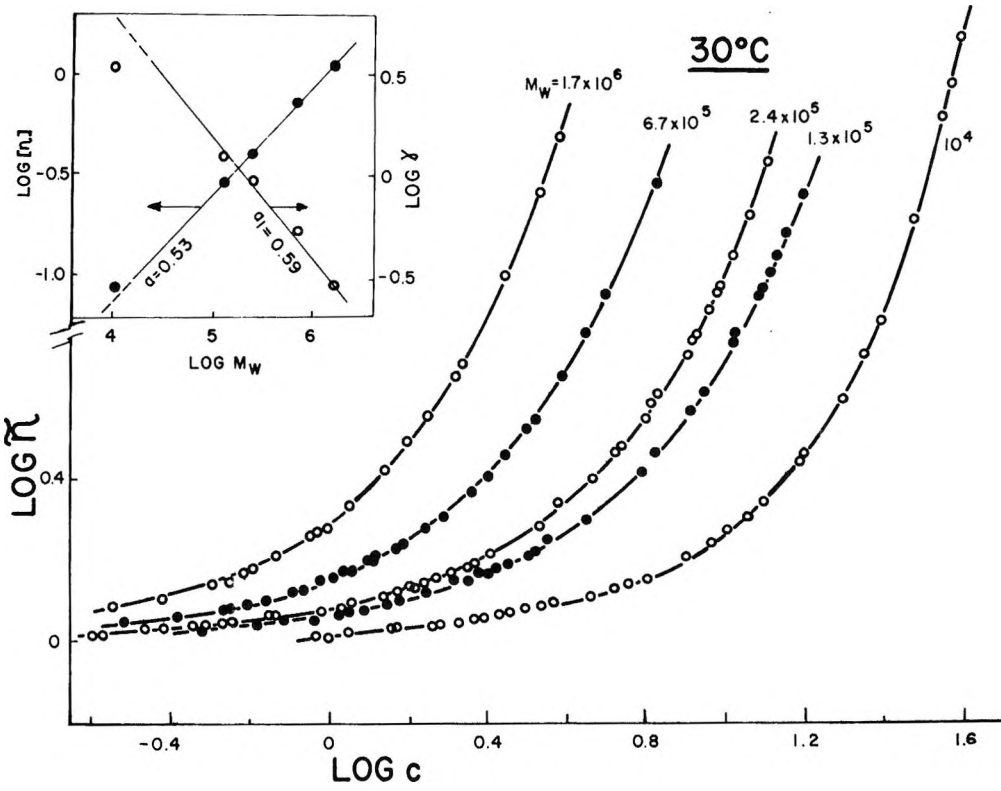

Figure 2. Reduced viscosity quantity $\bar{\eta} = \eta_{sp}/(c[\eta])$ as a function of concentration (in g dl^{-1}) at 30°. Insert, intrinsic viscosity $[\eta]$ and characteristic concentration factor γ as a function of M_w for 1-chlorodecane.

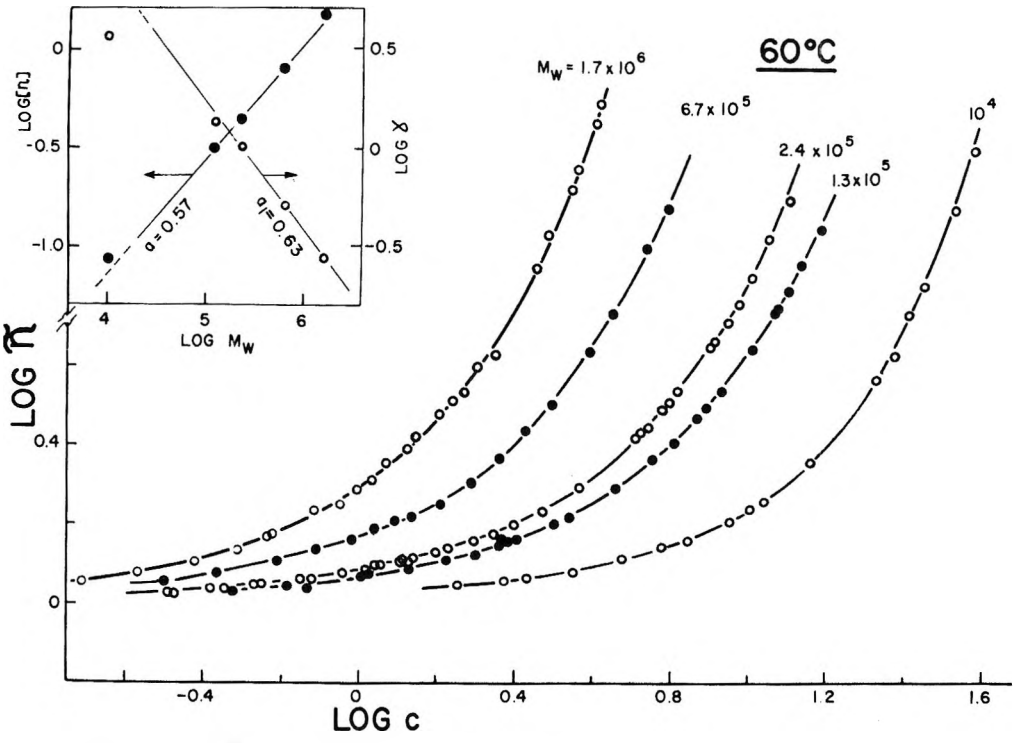

Figure 3. Reduced viscosity quantity $\bar{\eta} = \eta_{sp}/(c[\eta])$ as a function of concentration (in g dl^{-1}) at 30°. Insert, intrinsic viscosity $[\eta]$ and characteristic concentration factor γ as a function of M_w for 1-chlorodecane.

1-chlorodecane system, the breakdown of the Mark–Houwink relation at low molecular weights is more pronounced. Other peculiar behavior of this lowest molecular weight fraction will be demonstrated later. Over 80° the coefficient a increases from 0.5 at the θ temperature to only 0.6 at 90°, indicating the relative

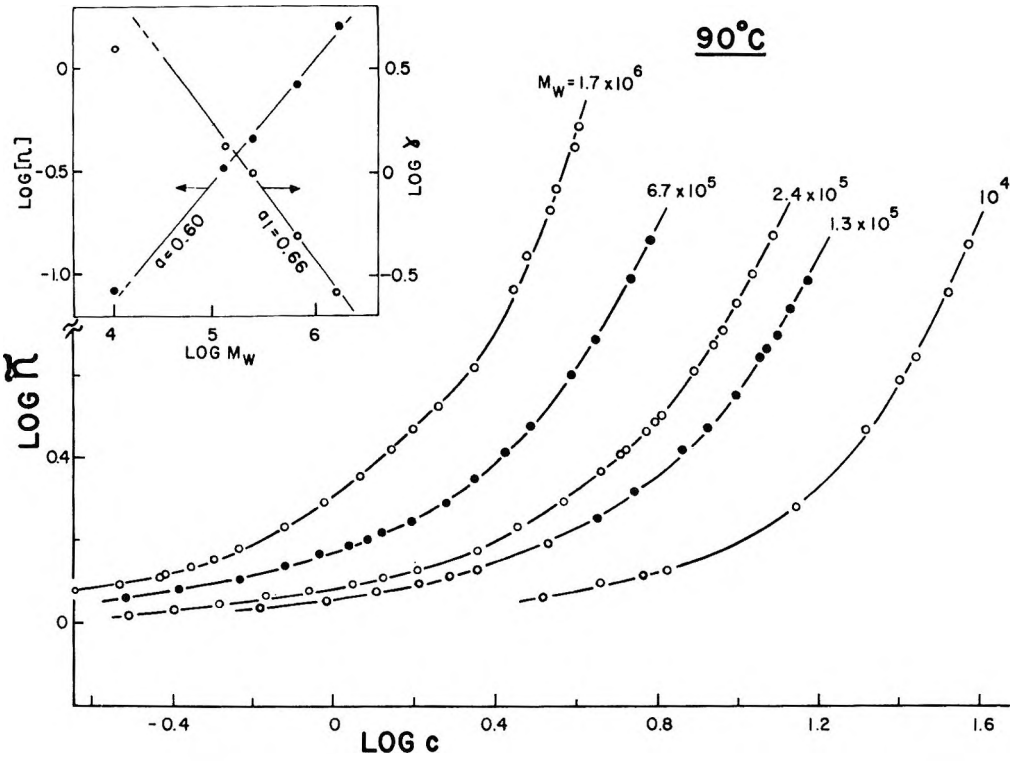

Figure 4. Reduced viscosity quantity $\bar{\eta} = \eta_{sp}/(c[\eta])$ as a function of concentration (in g dl^{-1}) at 90°. Insert, intrinsic viscosity $[\eta]$ and characteristic concentration factor γ as a function of M_w for 1-chlorodecane.

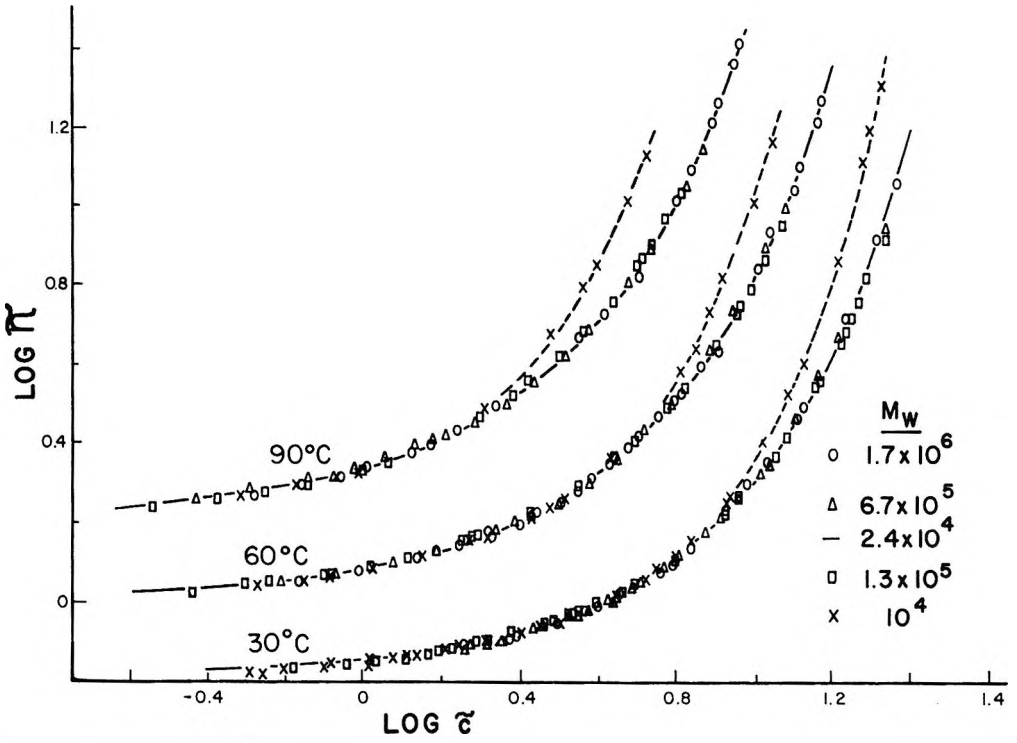

Figure 5. Reduced viscosity quantity $\bar{\eta}$ as a function of reduced concentration $\bar{c} = c/\gamma$ at three temperatures. Ordinates for the data at 30 and 90° are shifted by 0.2 unit downward and upward, respectively.

poorness of the solvent even at the highest temperature.

The experimental data are represented in Figures 1–4 as double logarithmic plots of $\bar{\eta}$ *vs.* c for the five polystyrene fractions at four temperatures. As in the previous work,[1,3] the characteristic concentration factor γ for each fraction at each temperature was determined by selecting the middle fraction, $M_w = 2.4 \times 10^5$, as the

reference substance and shifting each curve horizontally along the abscissa toward the reference curve until the best superposition was obtained. From the magnitude and direction of the shift, the value of log γ was obtained. In general, there is no ambiguity in producing superposition over the whole range of concentrations investigated here. However, in cases where superposition over the whole range was not possible, (lowest molecular weight fraction throughout and the two highest molecular weights at 6.6°), emphasis was placed on superposing the experimental points at lower concentrations. The resulting γ values are exhibited as a function of M in the inserts of Figures 1–4. With the exception of the lowest fraction, the linear relationship observed is in conformity with the equation obtained earlier,[1-3] *viz.*, $\gamma = AM^{-a_1}$ or $\gamma = (M/M_0)^{-a_1}$ where M_0 is the reference molecular weight. The similiarities between the behavior of $[\eta]$ and γ are worth noting. For the lowest fraction, both deviate from the power relation. Both coefficients a and a_1 increase with temperature and the goodness of the solvent. In our system, a_1 exceeds a by a nearly constant magnitude of 0.06 at all temperatures, whereas previously we have observed $a_1 \lesssim a$ in toluene and cyclohexane, respectively.[1] From the superposition principle and the expressions for γ and $[\eta]$ there follows $k_1 \propto M^{a_1-a}$. Thus in our system k_1 should increase with increasing M, except for the lower end of our molecular weight range, where a and a_1 vary with M (see the inserts in Figures 1–4). This result tests rather severely the accuracy of both superposition procedure and experimentation. The data exhibited in Table I cannot be taken as a confirmation of the predicted increase. The numerical values and behavior of the product $k_1[\eta]$ are considered in the last section and Table IV.

With γ determined for each fraction at the specified temperature, the same data can be replotted in terms of the reduced variables $\tilde{\eta}$ and $\tilde{c}$ as shown in Figures 5 and 6 at the temperatures indicated. Data for the reference molecular weight ($M_w = 2.4 \times 10^5$) are represented by the solid line, and various symbols differentiate results for the other fractions. With the exception of the lowest fraction in Figure 5, the closeness of these points to the reference curve to form a single master curve at each temperature demonstrates once more the validity of the superposition principle under isothermal conditions.

The breakdown of superposition at elevated concentrations for the lowest molecular weight fraction together with its deviant behavior in respect to $[\eta]$ and γ deserve further attention. Judging from similar results in other polymer solvent systems, it appears that there exists a limiting molecular weight below which superposition applies over a very limited concentration range only. Chain stiffness as the limiting factor and a correlation between the conformational parameter and this minimum molecular weight have been suggested.[4] A

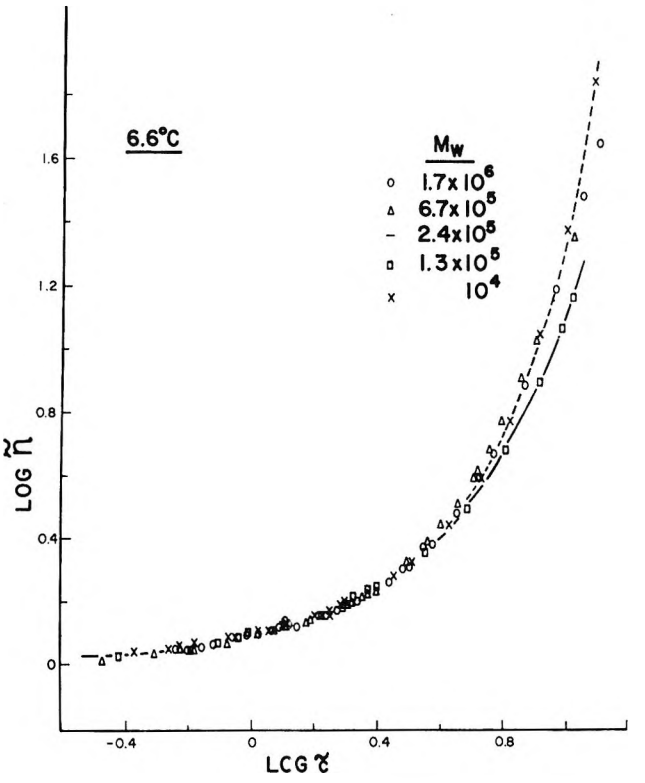

Figure 6. Reduced viscosity quantity $\tilde{\eta}$ as a function of reduced concentration $\tilde{c}$ at 6.6°.

positive deviation at elevated concentrations for the two highest molecular weights is also observed in the θ solvent, see Figure 6. One might speculate that this effect is related to the proximity of the critical temperatures for these two fractions to the θ point (about 5–6°, as estimated below).

The basic problem of deriving from theory functional relationships between viscosity, molecular weight, and concentration still remains, of course, but it can now at least be reduced to obtaining $\tilde{\eta}$ as a function of $\tilde{c}$, a matter beyond the scope of our corresponding states considerations. It may be convenient, however, to have analytical representations of our reduced master curves, Figure 5 and 6. For toluene and cyclohexane solutions of polystyrene, we have previously provided such equations[1] which are most simply expressed as semilogarithmic relationships between $\tilde{\eta}$ and $\tilde{c}$. For θ and near-θ conditions, this results in a linear function, the so-called Martin equation, in accord with earlier observations.[11] Better and poorer solvents yield negative and positive deviations, respectively, with increasing $\tilde{c}$.[3] It would be too much to say that the curves below the θ temperature are approaching the theoretical curve for suspensions of compact, hard spheres,[12] but they tend in that direction (see Figure 1 of ref 3). Such results suggest a close

(11) S. G. Weissberg, R. Simha, and S. Rothman, *J. Res. Nat. Bur. Stand.*, **47**, 298 (1950).

(12) R. Simha, *J. Appl. Phys.*, **23**, 1020 (1952); R. Simha and T. Somcynsky, *J. Colloid Sci.*, **20**, 278 (1965).

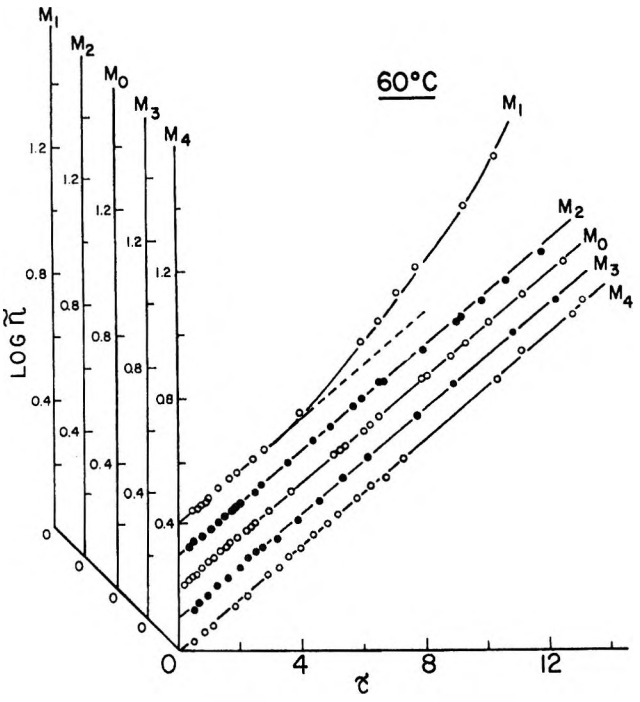

Figure 7. Semilogarithmic plots of $\tilde{\eta}$ *vs.* $\tilde{c}$ for the five fractions of Table I at 60° ($M_1 < M_2 < M_0 < M_3 < M_4$).

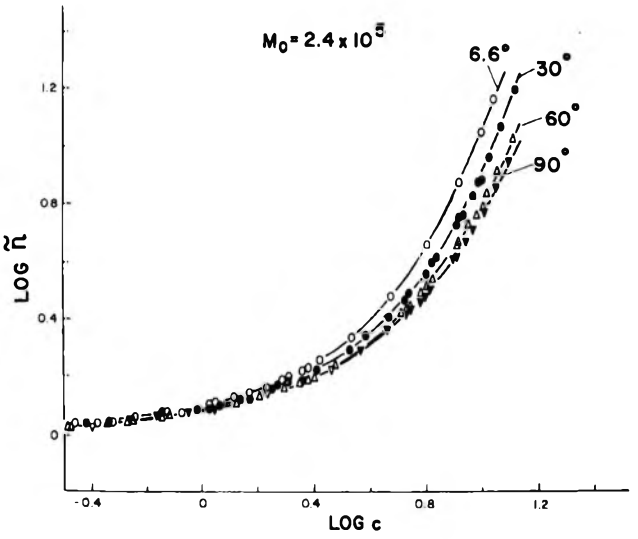

Figure 8. Reduced viscosity quantity $\tilde{\eta}$ as a function of concentration (in g dl^{-1}) for the reference molecular weight fraction ($M_w = 2.4 \times 10^5$) at four temperatures.

examination of the viscosity over the limited concentration range available in the neighborhood of the critical solution temperature.

Figure 7 shows a semilogarithmic plot at 60°. The lines for the five molecular weights have been separated for reasons of visibility, but all points fall on a single straight line, except for the lowest molecular weight in the upper range of concentrations. This deviation persists at all temperatures and is related to the fact that suspensions of rods show a more rapid increase of viscosity then spherical particles. It does not imply, of course, that polystyrene of degree of polymerization 100 assumes a rod-like conformation. The picture for 90° is the same with a decrease in slope. At 30° we observe a positive deviation from Martin's equation for the highest molecular weight and $\tilde{c} > 6$. The trend becomes more pronounced and extends to lower molecular weights and lower $\tilde{c}$ values at 6.6°. This result is in qualitative accord with the earlier observations for poor solvents discussed above[1,3] and corresponds to the departures from superposition at 6.6°, noted in Figure 6.

The equation of the straight line in Figure 7 is

$$\tilde{\eta} = \exp[K(T)\tilde{c}] \qquad (1)$$

where $K(T)$ is a decreasing function of temperature solely, which varies in our range from 0.230 to 0.182.

Equation 1 and its limitations can be discussed here only in the context of the present concentration range. Similar deviations as those noted here at the lower temperatures can, however, be expected to occur at higher concentrations and in better solvents. This can be true irrespective of the validity of the superposition scheme, which has been shown to extend considerably beyond the current c values for a variety of polymer–solvent systems.[3]

Temperature Superposition. With the exceptions noted, superposition of different molecular weights at constant temperature has been accomplished, as in the systems studied earlier. Therefore the question of corresponding temperatures can be resolved by examining the temperature dependence of $\tilde{\eta}$ as a function of $\tilde{c} \equiv c$ for a given reference molecular weight M_0 solely. Figure 8 exhibits double logarithmic plots for $M_0 = 2.4 \times 10^5$ at four temperatures. In spite of the considerable variation in temperature, the differences are relatively small. This is consistent with the relatively weak variation of a and a_1 with temperature.

The natural procedure now is to select a reference isotherm corresponding to a reference temperature T_0 and to attempt shifts along the log c axis. The result, shown in Figure 9 with $T_0 = 60°$, represents indeed a universal curve and the picture is thus complete in respect to both a molecular weight and temperature correspondence principle. To improve the accuracy in what follows, it will be useful to use each of the individual temperatures as a reference and compute the respective factors $\gamma(M_0, T)$ for the other three temperatures with $\gamma(M_0, T_0) \equiv 1$, by definition. The results appear in the fifth column of Table III, with $T_0 = 60°$.

Our observations can be epitomized as follows. There exists a reduced viscosity quantity $\tilde{\eta} = \eta_{sp}/(c[\eta])$ which is a unique function of the reduced concentration variable

$$\tilde{c} = c/\gamma(M,T) \qquad (2)$$

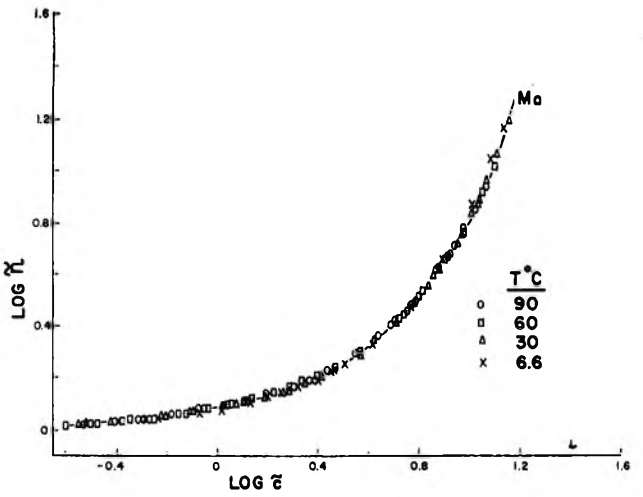

Figure 9. Reduced viscosity quantity $\tilde{\eta}$ as a function of reduced concentration $\tilde{c}$ for the reference molecular weight fraction at different temperatures, with 60° as the reference temperature.

Table III: Comparison of Experimental and Calculated Values of a_1 and $\gamma(M_0,T)$, Eq 6 and 5′, with $M_0 = 2.4 \times 10^5$

Temp, °C	$\tilde{T}$	a_1 Exptl	a_1 Calcd	$\gamma(M_0,T)$ Exptl	$\gamma(M_0,T)$ Calcd
6.6	1.0314	0.564	0.563	0.804	0.820
30	1.1177	0.595	0.592	0.892	0.936
60	1.2283	0.630	0.628	1.000	1.000
90	1.3390	0.660	0.665	1.047	1.040

for different molecular weights and at different temperatures. Moreover

$$\gamma(M) = (M_0/M)^{a_1} = \tilde{M}^{-a_1} \qquad (3)$$

for constant T. The generalization of eq 3 for variable T is

$$\gamma(M,T) = \gamma(M_0,T) \times (M_0/M)^{a_1(T)} \qquad (4)$$

where $\gamma(M_0,T)$ is the temperature-dependent concentration factor for the reference molecular weight M_0 and $\gamma(M_0,T_0) \equiv 1$. The result summarized in Figure 9 implies the existence of a reduced temperature $\tilde{T}$ and of functions $\gamma(M_0,\tilde{T})$ and $a_1(\tilde{T})$. In order to obtain explicit expressions for these functions one could continue by introducing an arbitrary reducing temperature T^* with $\tilde{T} \equiv T/T^*$. However, a different approach is suggested by two observations on the polystyrene–cyclohexane system[5] mentioned in the Introduction. These are the role of the critical composition as the characteristic concentration factor γ and the apparent role played by the critical solution temperature T_c as a corresponding temperature in respect to the intrinsic viscosity. The second result is displayed in Figure 10, which shows $[\eta]$ at $T = T_c$ to be related to M by a Mark–Houwink expression, although T_c varies between approximately 8 and 29°. The dashed line with approximately identical slope represents the critical volume fraction of solute.

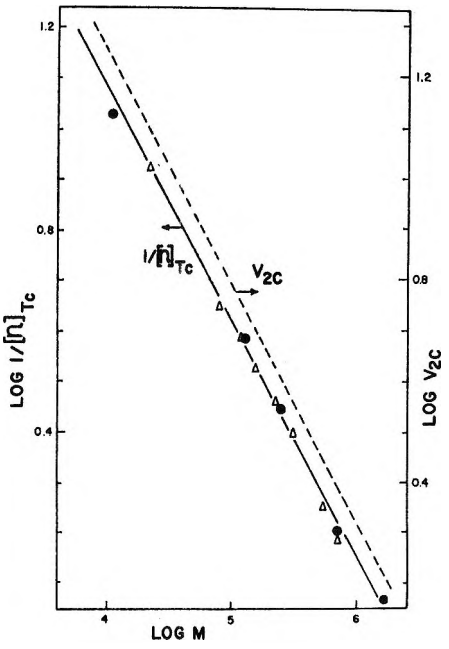

Figure 10. Intrinsic viscosity at the critical temperature $[\eta]_{Tc}$ and critical volume V_{2c} (broken line) as a function of molecular weight for polystyrene in cyclohexane (triangles) and estimates for 1-chlorodecane (circles). For explanation see text.

We wish to explore the proposition that the critical solution temperature represents a reducing temperature at finite concentrations as well. No firm conclusions can be reached, since the appropriate thermodynamic studies for our system are lacking. We shall instead estimate T_c in an indirect manner by assuming, without real theoretical justification, that the difference $T_\theta - T_c$ for polystyrene is independent of the solvent, and testing the result by means of intrinsic viscosities. For cyclohexane, Maron and Nakajima[13] offer the following empirical equation

$$\log (T_\theta - T_c) = 2.491 - 0.290 \times \log M$$

It is in fair accord with experimental results of Debye, *et al.*,[14] the maximum deviation being 4°. On substituting $T_\theta = 6.6°$ and extrapolating $[\eta]$ maximally over 21° and minimally over 5° to the T_c's so computed, the numerical values listed in the last two columns of Table I result. The intrinsic viscosities $[\eta]_{Tc}$ are shown in Figure 10. The close correspondence with the cyclohexane data is encouraging both in respect to the estimate of T_c and its role as a corresponding temperature for the intrinsic viscosity. Detailed studies at corresponding but conveniently higher temperatures are indicated.

(13) S. H. Maron and N. Nakajima, *J. Polym. Sci.*, **54**, 587 (1961).
(14) P. Debye, H. Coll, and D. Woermann, *J. Chem. Phys.*, **33**, 1746 (1960).

Table IV: Comparison of Experimental and Calculated Values of $\gamma(M,T)$, Eq 7, and $k_1[\eta]$, Eq 10 for Different Fractions at Various Temperatures

	Temp, °C															
	6.6°				30°				60°				90°			
	$\gamma(M,T)$		$10 \times k_1[\eta]$		$\gamma(M,T)$		$10 \times k_1[\eta]$		$\gamma(M,T)$		$10 \times k_1[\eta]$		$\gamma(M,T)$		$10 \times k_1[\eta]$	
$M_w \times 10^{-4}$	a	b	a	b	a	b	a	b	a	b	a	b	a	b	a	b
1	2.29	4.53	0.89	0.42	3.09	5.65	0.62	0.34	3.63	6.73	0.54	0.28	4.17	7.84	0.48	0.24
13	0.99	1.12	1.97	1.70	1.15	1.30	1.58	1.47	1.29	1.41	1.64	1.36	1.41	1.50	1.42	1.29
24	0.80	0.78	2.29	2.44	0.89	0.89	2.02	2.14	1.00	0.95	1.89	2.02	1.05	0.98	1.96	1.96
67	0.47	0.44	4.25	4.37	0.47	0.48	3.87	4.02	0.50	0.50	4.03	3.80	0.51	0.49	4.26	3.92
170	0.24	0.26	8.30	7.31	0.26	0.28	6.59	6.82	0.28	0.28	7.60	6.84	0.28	0.27	7.30	7.14

[a] Experimental. [b] Calculated.

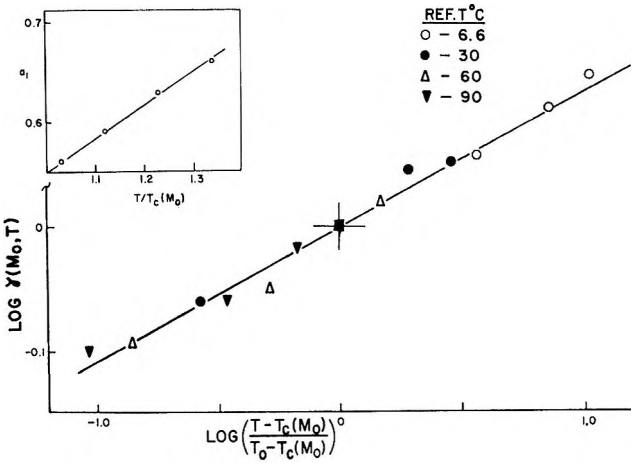

Figure 11. Characteristic concentration factor for the reference molecular weight $M_0(M_w = 2.4 \times 10^5)$, $\gamma(M_0,T)$ as a function of temperature, using reference temperatures of 6.6° (○), 30° (●), 60° (△) and 90° (▼). Insert: coefficient a_1 as a function of the reduced temperature $\tilde{T} = T/T_c(M_0)$.

Turning now to eq 4, $\gamma(M_0,T)$ will clearly be a weak function of T or, as we shall assume, of the difference $T - T_c(M_0)$, between T and the critical temperature of the reference polymer. A power relationship is frequently invoked in such situations and we write tentatively

$$\gamma(M_0,T) = [(T - T_c(M_0))/(T_0 - T_c(M_0))]^x \quad (5)$$

A plot of log $\gamma(M_0,T)$ is shown in Figure 11. If eq 5 is to hold, x should not depend on the choice of a reference temperature. Hence four alternative T_0's are utilized for a better estimate of x. Equation 5, with $x = 0.1$, is in fair accord with the experimental results and may be written in terms of the reduced temperature $\tilde{T} = T/T_c(M_0)$ as

$$\gamma(M_0,\tilde{T}) = [(\tilde{T} - 1)/(\tilde{T}_0 - 1)]^{0.1} \quad (5')$$

Equation 5′ is restricted to $\tilde{T} > 1$, when $\tilde{T}_0 > 1$. The range could be extended in principle by selecting a low molecular weight as the reference, provided of course, the superposition principle is still obeyed. An alternative to eq 5′ could be

$$[\gamma(M_0,T) - \gamma(M_0,T_c)]/$$
$$[1 - \gamma(M_0, T_c)] = (\tilde{T} - 1)/(\tilde{T}_0 - 1)$$

Here $\gamma(M_0,T_c)$ would effectively be an empirical parameter, to be determined from data at $T > T_c(M_0)$.

The insert of Figure 11 shows that a_1 is a linear function of temperature, *viz.*

$$a_1 = 0.219 + \tilde{T}/3 \quad (6)$$

Equations 4′, 5′, and 6 yield the final result

$$\gamma(\tilde{T},\tilde{M}) = [(\tilde{T} - 1)/(\tilde{T}_0 - 1)]^{0.1}/(\tilde{M})^{0.219+\tilde{T}/3} \quad (7)$$

with $\tilde{M} = M/M_0$; $\tilde{T} = T/T_c(M_0)$; $\tilde{T}_0 = T_0/T_c(M_0)$, where the subscript 0 refers to the reference polymer.

As a further check on the adequacy of eq 7 we compare in Tables III and IV observed and computed values of $\gamma(M_0,T)$, a_1 and $\gamma(M,T)$, for $T_0 = 60°$ and $M_0 = 2.4 \times 10^5$. Reasonable agreement is noted, with the largest discrepancies occurring for the lowest molecular weight, as was to be anticipated in view of the findings in Figures 1–4.

Within the deviations noted and the range of our variables, in particular concentration, eq 7 and 1, together with the intrinsic viscosity, provide a complete description of the polystyrene–1-chlorodecane system. Numerically improved representations could, of course, be developed from our data by appropriate modifications of these relations.

Temperature Coefficients. Intrinsic viscosities either increase or decrease with increasing temperature, depending on the nature of the polymer–solvent interaction. The former is the case for the four highest molecular weights, as is seen in Table I and the bottom curve in Figure 12. This behavior, most pronounced for the highest molecular weight and the lower temperatures, is characteristic of a poor solvent, where an expansion of the molecular coils, that is, the long-range interaction effect, predominates. For the lowest fraction, $M = 10^4$ on the other hand, a slight decrease is noted. We recall in this connection observations for the polystyrene–cyclohexane system[5] at and below the θ temperature, which indicate a but slightly positive temperature coefficient below a number average molecular weight of 10^4.

The decrease of the temperature coefficient with increasing temperature, see Figure 12 and Table V, is suggestive of the transition in the neighborhood of 50°, proposed by others[15] and attributed to conformational changes in the chain.

Table V: Experimental Temperature Coefficients ($M_w = 2.4 \times 10^5$), Computed (Eq 9) Crossover Concentrations c^* and Molecular Weight Limits M^*

T, °C	(d ln $[\eta]$/dT)	c^*, g dl^{-1}	M^*
6.6	0.0050	1.7	3.3×10^9
30	0.0025	3.7	3.1×10^6
60	0.0016	4.9	8.9×10^5
90	0.0013	5.9	5.8×10^5

The temperature coefficients at finite concentrations may be estimated as a function of temperature, molecular weight, and concentration by means of eq 1 and 7. We have

$$\ln (\eta_{sp}/c) = 0.191c[(\tilde{T}_0 - 1)/(\tilde{T} - 1)]^{0.1} \times (M/M_0)^{a_1(T)} + \ln [\eta] \quad (8)$$

where the factor $K(T)$ in eq 1 is set equal to 0.191, the value at the reference temperature $T_0 = 60°$, and a_1-

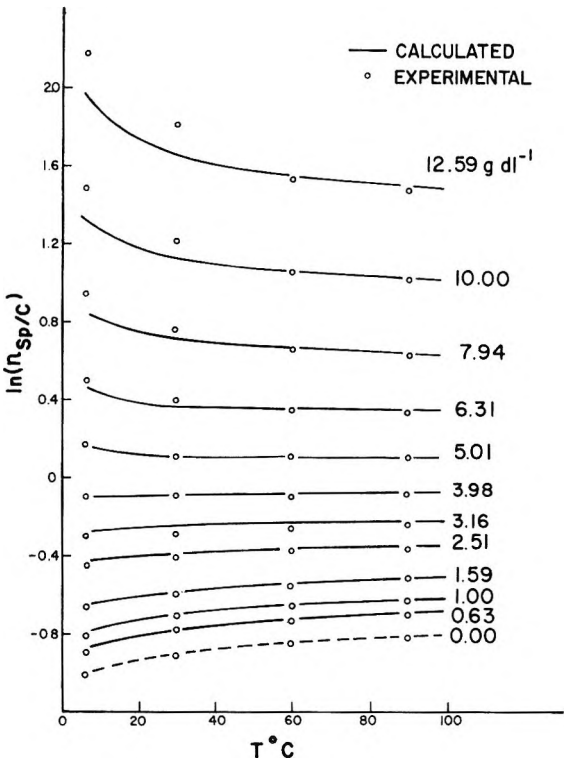

Figure 12. Semilogarithmic plots of η_{sp}/c *vs.* T at different concentrations for $M_w = 2.4 \times 10^5$.

(T) is given by eq 6. Because of the limitations already noted, we show as an illustration the application of eq 8 to the reference molecular weight $M_0 = 2.4 \times 10^5$. The result appears in Figure 12 for a series of concentrations between 0 and 12.6 g dl^{-1}, with the experimental data indicated by circles. The most striking although not unexpected feature of this figure is the changeover from a positive to a negative temperature coefficient which is indicative of the passage between two concentration regions. At sufficiently low concentrations the intramolecularly determined conformational changes still predominate. With increasing concentration aggregation effects set in and conformational changes are increasingly determined by intermolecular effects. A temperature increase in an initially poor solvent reduces the extent of aggregation and the improvement in solvent power favors coil contraction. Both factors tend to reduce the viscosity. From Figure 12 one would estimate the crossover region to be around 4 g dl^{-1}, corresponding from Table I to a value of the product $[\eta]c$ of about 1.5 between 6.6 and 30°. One might anticipate a shift of this transition zone to lower concentrations with increasing molecular weight. Since it cannot be accurately located by an inspection of the experimental data, we are unable to confirm such a dependence. However, as seen in Figure 12, eq 8 correctly reproduces the shape of the experimental

(15) For example, W. R. Krigbaum, F. Mark, J. G. Pritchard, and W. L. Hunter, *Makromol. Chem.*, 65, 101 (1963).

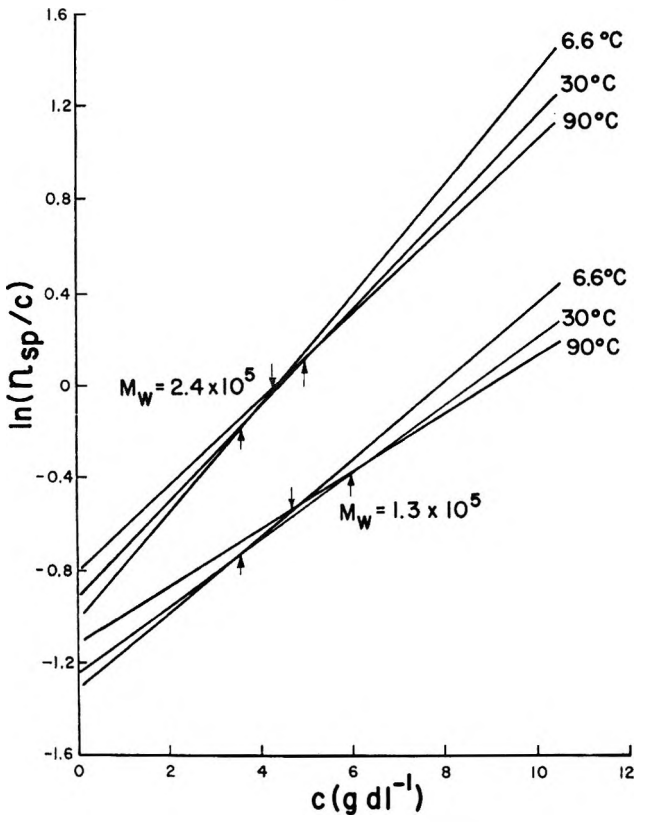

Figure 13. Semilogarithmic plots of η_{sp}/c *vs.* c at different temperatures for $M_w = 2.4 \times 10^5$ and 1.3×10^5, eq 8. Arrows indicate crossover concentrations.

curves and may be used to estimate the crossover concentrations. Figure 13 shows the linear plots corresponding to eq 8 for two molecular weights. The intersection between the 6.6 and 30° lines is slightly shifted to the right for the lower molecular weight. Moreover, different crossovers are possible at different temperatures. One expects the intrinsic viscosity to decrease at sufficiently elevated temperatures, if short-range interactions favor more highly coiled conformations. A minimum for the function of $\ln(\eta_{sp}/c)$ *vs.* T observed in our temperature range for the highest molecular weight at the maximum concentration available may indicate a rearrangement, such as a formation of new aggregates. The temperature coefficients for the lowest fraction are negative throughout.

In view of the semiquantitative success of eq 8 it is instructive to examine the expression for the temperature coefficient. From eq 1, 6, and 8 there follows

$$(\partial \ln(\eta_{sp}/c)/\partial T)_c = \mathrm{d}\ln[\eta]/\mathrm{d}T + \ln\tilde{\eta}\{\ln\tilde{M}/[3T_c(M_0)] - (1/10)/[T - T_c(M_0)]\} \quad (9)$$

Since the derivative on the right-hand side is positive for the four highest molecular weights, a necessary condition for the existence of a crossover concentration is a negative value of the brace. This condition imposes limitations on the permissible ranges of molecular weight and temperature favoring a crossover. At a given T, M should not exceed a maximum M^* with

$$\ln\tilde{M}^* = (3/10)/[T/T_c(M_0) - 1]$$

The last column of Table V contains M^* corresponding to our four temperatures, and two of these are within the present range of molecular weights.

Alternatively, the above equation provides limits on the temperature for a prescribed molecular weight $\tilde{M}$. When $M < M_0$, all temperatures above a lower limit are possible. For $M = 1.3 \times 10^5$, this limit is $0.51 \times T_c(M_0)$, well within the present temperature range. When $M > M_0$, the range between $T_c(M_0)$ and an upper limit is permissible, which amounts to $1.15 \times T_c(M_0)$ and $1.29 \times T_c(M_0)$ for the highest and next molecular weight, respectively. Since $T_c(M_0) \simeq 271°K$ (see Table I), there still remains a sufficiently wide temperature band.

When the necessary conditions just discussed are satisfied, one can compute by means of eq 9 and 1 a concentration c^* (M,T) at which the positive temperature coefficient of $[\eta]$ is just balanced by the second and negative term. Numerical values for c^* can be in error due to inaccuracies in the determination of $\mathrm{d}[\eta]/\mathrm{d}T$ and in the analytical expression. They are listed in Table V for the reference molecular weight and the four temperatures. A comparison with Figure 12 shows that the computed results are quite reasonable except at 6.6° where $c^* = 1.7$ g dl^{-1} appears to be too small. It would be possible also to locate numerically the extrema in Figure 12, but in view of the shape of the curves this does not appear to be worthwhile.

Finally from eq 8 and 6 there follows the expression for the Huggins parameter k_1 as a function of M and T, *viz.*

$$k_1[\eta] = 0.191[(\tilde{T}_0 - 1)/(\tilde{T} - 1)]^{0.1} \times (M/M_0)^{0.229+\tilde{T}/3} \quad (10)$$

The isothermal dependence of $k_1[\eta]$ on M is given by the second factor on the right-hand side. The temperature coefficient at constant M is positive or negative, depending on whether the reduced molecular weight is larger or smaller than $\tilde{M}^*$, defined above. Computed and experimental values are compared in Table IV. Disregarding the lowest fraction, reasonable agreement will be noted, the maximum deviation being 14%.

IV. Conclusions

The analysis of several polymer–solvent systems has established the generality of the $\tilde{\eta} - \tilde{c}$ superposition scheme at constant temperature. Moreover, it has suggested, where this information was available, a connection with the thermodynamic critical state of the solution. The present work demonstrates temperature superposition over a temperature range which is wide on an absolute scale, but only moderate in terms of changes in the polymer–solvent interaction. It also

shows or at least suggests the role of the critical solution temperature. As for the generality of these new results, it would be desirable to expand the current range of temperature and one can expect that the actual equations, *e.g.*, eq 1 and 6, are of limited validity. However, there is no reason to presume a restriction of the basic correspondence principle to the particular polymer–solvent system studied here.

In many instances it is not convenient, if not actually impossible, to establish the thermodynamic critical coordinates. Provided a good solvent over a sufficiently wide range of temperatures is available, the function $\gamma(M,T)$ can be expressed in terms of an arbitrarily chosen M_0 and T_0. If, by varying M_0, the parameters of this function change in an expected manner, an estimate of $T_c(M_0)$ may then be obtained from the temperature coefficients of viscosity.

Finally, we recall the persistent deviations of the lowest molecular weight at elevated concentrations from our superposition scheme, based on higher molecular weights, and analogous departures in respect to $[\eta]$ and γ. These results suggest separate studies of low molecular weight series with $M < 10^5$ as a function of concentration and temperature.

Kinetics of Proton-Transfer Reactions of Polyacrylic and Polymethacrylic Acids with an Indicator

by Shmuel Weiss,*[1] Hartmut Diebler,

Max-Planck-Institut für Physikalische Chemie, Göttingen, West Germany

and Isaac Michaeli

Weizmann Institute of Science, Rehovot, and the University of the Negev, Beer-Sheva, Israel *(Received July 2, 1970)*

Publication costs borne completely by The Journal of Physical Chemistry

The kinetics of proton transfer between polyacrylic acid and the pH indicator phenol red and between polymethacrylic acid and phenol red have been studied by the temperature-jump relaxation technique in the pH range 6–8.5. In every case only a single and well defined relaxation time was observed. The rate constant for direct proton transfer from the polyacid to the indicator was found to be $(2 \pm 1) \times 10^7\ M^{-1}\ \text{sec}^{-1}$ (acid concentration expressed in terms of monomeric units) for both systems, essentially independent of pH in the pH range studied. No evidence was found from these kinetic studies and additional ones at pH 5–6 for conformational transitions of the polyacids. Possible effects of the macromolecular nature of the polyacids on the proton-transfer kinetics are discussed.

Introduction

A great deal of information is now available concerning the kinetics of proton transfer reactions in aqueous solutions.[2a,b] This information, however, has been obtained from experiments with low molecular weight materials. The purpose of the present investigation was therefore to obtain some information about proton-transfer reactions involving polyelectrolyte reactants.

When passing from low molecular weight to polyelectrolyte systems one might expect to find new patterns of behavior in the kinetics of proton transfer, due to the macromolecular nature of the polyelectrolyte. More specifically, in the case of polyelectrolytes the question arises whether all the acidic sites are equally available to proton exchange; evidently conditions can be envisaged in which some of the acidic groups may be more exposed while some others are "buried" within the coiled polymeric matrix. Also, the affinity of a given acceptor group for a proton will depend on whether the neighboring groups are in the ionized or in the protonated form. Under such circumstances a whole series of proton transfer processes may be expected. Moreover, the binding of protons to a polyanion usually brings about conformational transitions in the macromolecule. Such transitions are known to affect the acidic strength of the molecule[3] and thus will lead to a

(1) On leave from Nuclear Research Centre, Negev, Israel Atomic Energy Commission.

(2) (a) M. Eigen, *Angew. Chem., Int. Ed. Engl.*, **3**, 1 (1964); (b) M. Eigen, W. Kruse, G. Maass, and L. De Maeyer, *Progr. React. Kinet.* **2**, (1964).

(3) J. C. Leyte and M. Mandel, *J. Polymer Sci. Part A*, **2**, 1879 (1964); I. Michaeli, *J. Polymer Sci. Part C*, **16**, 4169 (1968).

distribution of reaction rate constants for proton transfer; they also could give rise to the observation of additional time constants, typical of the conformational transitions themselves.

The present investigation deals with the study of the relaxation processes in a system containing a polyacid and a low molecular weight pH indicator over the pH range 6–8.5. Two weak polyacids were chosen, polyacrylic acid (PAA), and polymethacrylic acid (PMA). The two are known to differ in the run of their potentiometric titration curves: unlike PAA, PMA has an "anomalous" titration curve which has been attributed to a cooperative conformational transition.[3] (However, see also ref 4.) Because of its suitable dissociation constant (pK = 7.7 at 20°) phenol red was used as indicator. The indicator is negatively charged (−1 and −2) both in its acidic and basic forms.

Experimental Section

PAA was obtained by polymerization of the distilled monomer in aqueous solution in the presence of H_2O_2 (3%).[5] The system was kept for 4 hr at 90°. The polymer was subsequently precipitated in H_2SO_4 and redissolved in water. A low degree of fractionation was obtained by fractional reprecipitation with H_2SO_4. The fractions thus obtained were dialyzed and dried by lyophilization.

PMA was prepared from the monomer by polymerization with azobisisobutyronitrile initiator in aqueous solution at 60°. The polymer was dialyzed and freeze dried. The degree of polymerization of both PAA and PMA was estimated from light scattering to be of the order of 1000.

The kinetic studies were carried out using a commercially available T-jump apparatus with spectrophotometric detection.[6] Polyacid concentrations were 0.2×10^{-3} M to 5×10^{-3} M (in monomeric units); all solutions contained 0.1 N Na_2SO_4[7] (to provide sufficient electrical conductivity) and 4×10^{-5} M phenol red. The solutions were thermostated at 15.0 (±0.2)° prior to a temperature jump of 5.0°. The chemical relaxation was followed spectrophotometrically at 560 mμ, close to the absorption maximum of the basic indicator species. Time constants were evaluated as the mean of 4 or 5 individual measurements; the average deviation was within 10% of the mean.

Results and Discussion

As outlined in the Introduction, the acidic and basic sites of the polycarboxylic acids are expected not to be equivalent with regard to their acidities or basicities, due to differing local environments. Proton transfer between indicator and polyacid sites of different reactivities may then lead to a series of relaxation times, which may appear as a discrete set or as a close distribution, depending on the distribution of the acidic and basic groups and on their interactions. However, carboxylic groups of different reactivities are certainly capable of interconversion. Such interconversion processes may be brought about by local changes in conformation and/or by proton exchange between different polyacid molecules or between different parts of the same molecule (perhaps *via* a system of hydrogen bonds along the chain).[8] If the rate of interconversion is high as compared to the rate of reaction with the indicator, the differences in reactivity will average out and the polyacid will behave as if all the protonated (or dissociated) carboxylic groups were equivalent. In this case proton transfer will evidently give rise to a single relaxation time, whereas the interconversion process will not be detected by the applied technique.

From studies of equilibrium properties it has been shown that, at least in the case of PMA, the behavior of the polyacid can be formally interpreted in terms of the existence of two conformations.[3] Under our experimental conditions these two conformations differ in acidic strength by close to two pK units. The existence of two such distinct forms would suggest that at least two time constants appear in the relaxation spectrum (one of which being due to the change in conformation) unless the rate of the conformational transition is high as compared to the rate of proton transfer. Another possibility, not ruled out by the equilibrium studies and favored by a recent report,[9] is that the polyacid really exists as a mixture of a multiplicity of structures (except at very low and at very high degrees of ionization). In this case a distribution of relaxation times would be expected unless, again, the structural changes are too fast.

Experimentally it was found that over the pH range studied both systems are characterized by a single and well defined relaxation process. Its time constant varied between 20 and 250 μsec, depending on polyacid concentration and pH. A summary of the observed time constants is given in Table I.

The dependence of the relaxation time on polyacid concentration at constant pH is evidence against its being related to conformational transitions. To further check this point, the investigations were extended to pH values at which the ratio of the two conformations of PMA should be close to 1.[3] Using chlorophenol red and bromocresol green as indicators, the pH could be decreased to 5.1 (degree of dissociation of PMA α = 0.19[3]) (as a check similar experiments were performed

(4) A. R. Matheson and J. V. McLaren, *J. Polymer Sci. Part A*, **3** 2555 (1965).

(5) Z. Alexandrowicz, *J. Polymer Sci.*, **40**, 91 (1959).

(6) Messanlagen Studiengesellschaft m.b.H., Göttingen, W. Germany.

(7) The same medium had been used by Michaeli (ref 3 and unpublished data) in his equilibrium studies.

(8) See A. Silberberg, J. Eliassaf, and A. Katchalsky, *J. Polymer Sci.*, **23**, 259 (1957).

(9) J. L. Koenig, A. C. Angood, J. Semen, and J. B. Lando, *J. Amer. Chem. Soc.*, **91**, 7250 (1969).

Table I: Dependence of the Reciprocal Relaxation Time $\times 10^{-3}$ (sec^{-1}) on Polyacid Concentration and pH

	PAA					PMA					
pH	0.2×10^{-3} M	0.5×10^{-3} M	1×10^{-3} M	2×10^{-3} M	5×10^{-3} M	pH	0.2×10^{-3} M	0.5×10^{-3} M	1×10^{-3} M	2×10^{-3} M	5×10^{-3} M
6.20	24	31	36			6.23	43	33	45		
6.70	13.3	14.9	17.9	22		6.58	17.6	17.8	24	27	
7.10		(7.8)[a]	9.7	13.2	18.5	6.85		11.5	16.9	19.2	29
7.50			(6.1)[a]	8.7	12.0	7.30		(6.3)[a]	9.5	12.7	21
7.90		(4.5)[a]	(5.3)[a]	6.8	11.3	7.73		(5.1)[a]	(7.4)[a]	11.0	17.5
8.30			(5.2)[a]	6.7	11.4	8.10			(8.0)[a]	11.2	17.9
						8.48			(9.8)[a]	11.8	15.2

[a] Values given in parentheses correspond to instances where polymer concentrations were so low that the condition $C_{In^{2-}}, C_{HIn^-} \ll C_{HPA}$ was not completely satisfied. However, these experimental $1/\tau$ values are so close to those predicted by eq 2 as to suggest that even in these cases the approximation by which eq 2 was derived from eq 1 was not a very drastic one. These values were not used for the evaluation of rate constants.

with PAA down to pH 5.5). In all these experiments again only a single well defined relaxation time was observed.

To test for the occurrence of a conformational transition which is too fast to be measured by the T-jump technique, some sound absorption studies were performed in the megacycle range (2–30 Mc/sec) over a wide range of pH values (3.0–7.0) and polyacid concentrations (up to 0.25 *M*). No evidence was found for a pronounced chemical reaction in PMA or PAA whether in the presence of 0.1 *N* Na_2SO_4 or without salt. This result does not exclude, however, the possibility of rapid transitions between a series of conformational states which will be present in systems undergoing progressive (noncooperative) structural rearrangements. A rapid equilibration between two well defined conformations can also not be ruled out in case such a transition is accompanied by a rather small volume change (ΔV).

The observation of one relaxation time only in all the T-jump experiments points to the fact that the carboxylic groups of the polyacids are *kinetically* equivalent under the conditions of this study. It is therefore concluded that interconversion and structural transitions are rapid processes as compared to the reaction with the indicator.

In dealing with the protolytic reactions in a system consisting of two acids and their conjugate bases in aqueous solution, a fairly complicated reaction scheme has to be considered to account for all possible reaction pathways[1]

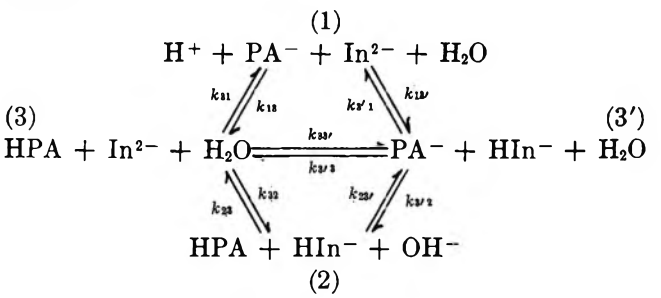

(HIn^- denotes the protonated (acidic) form of the indicator and HPA any given protonated carboxylic group of the polyacid).

A reaction scheme of this type is characterized by three relaxation times.[1] Under the experimental conditions of this study, however, the concentrations of H^+ and OH^- were always small compared to those of HPA, PA^-, HIn^-, and In^{2-}. Therefore, the intermediate states 1 and 2 can be considered to be in a steady state and only one time constant describing the overall reaction $3 \rightleftharpoons 3'$ is to be expected. But even then equilibration between 3 and 3′ may proceed in part *via* state 1 (particularly at pH <7) and/or *via* state 2 (particularly at pH >7). The reciprocal relaxation time for this process is given by

$$\frac{1}{\tau} = \left(k_{33'} + \frac{k_{31}k_{13'}}{k_{13}C_{PA^-} + k_{13'}C_{In^{2-}}} + \frac{k_{32}k_{23'}}{k_{23'}C_{HPA} + k_{23}C_{HIn^-}}\right)(C_{HPA} + C_{In^{2-}}) + \left(k_{3'3} + \frac{k_{3'1}k_{13}}{k_{13}C_{PA^-} + k_{13'}C_{In^{2-}}} + \frac{k_{3'2}k_{23}}{k_{23'}C_{HPA} + k_{23}C_{HIn^-}}\right)(C_{PA^-} + C_{HIn^-}) \quad (1)$$

When the indicator concentrations are sufficiently low, so that $C_{In^{2-}}, C_{HIn^-} \ll C_{PA^-}, C_{HPA}$, the terms in $C_{In^{2-}}$ and C_{In^-} can be neglected (at least to a good approximation: the rate constants k_{13}, $k_{13'}$, k_{23}, $k_{23'}$ are all for diffusion-controlled protolytic reactions) and eq 1 can then be simplified and rearranged to

$$\frac{1}{\tau} = k_{33'}\left(1 + \frac{K_{HIn}}{C_{H^+}}\right)(1 - \alpha)C + k_{13'}\left(1 + \frac{K_{HIn}}{C_{H^+}}\right)C_{H^+} + k_{23}\left(1 + \frac{C_{H^+}}{K_{HIn}}\right)C_{OH^-} \quad (2)$$

where C is the total polyacid concentration (in terms of monomeric units), α is its degree of dissociation, and

Table II

PAA				PMA			
pH	α[a]	$k_{33'}$,[b] M^{-1} sec^{-1}	$k_{3'3}$,[b] M^{-1} sec^{-1}	pH	α[a]	$k_{33'}$,[b] M^{-1} sec^{-1}	$k_{3'3}$,[b] M^{-1} sec^{-1}
6.20	0.69	4.6×10^7	0.5×10^6	6.23	0.61	1.2×10^7	0.2×10^6
6.70	0.81	2.5×10^7	0.5×10^6	6.58	0.71	1.9×10^7	0.5×10^6
7.10	0.88	1.5×10^7	0.4×10^6	6.85	0.78	1.6×10^7	0.5×10^6
7.50	0.94	1.2×10^7	0.4×10^6	7.30	0.89	1.9×10^7	0.7×10^6
7.90	~0.97	~2.4×10^7	0.9×10^6	7.73	0.94	1.9×10^7	1.1×10^6
8.30	~0.99	~5×10^7	1.8×10^6	8.10	~0.97	~2.7×10^7	1.7×10^6
				8.48	~0.99	~2.5×10^7	1.2×10^6

[a] From ref 3 and I. Michaeli, unpublished results. The values for high pH have been extrapolated. [b] Experimental uncertainty ±30% between about pH 6.50 and pH 8.00. Outside these limits precision deteriorates rapidly. Evaluation of $k_{33'}$ depends on $1 - \alpha$, which is rather uncertain at high pH; evaluation of $k_{3'3}$ depends on α.

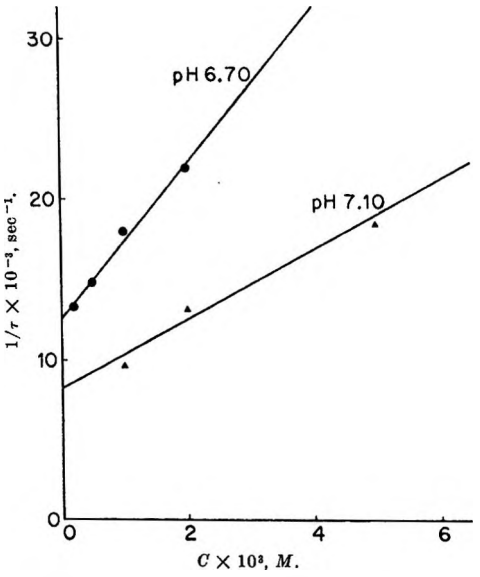

Figure 1. Dependence of $1/\tau$ on PAA concentration at constant pH.

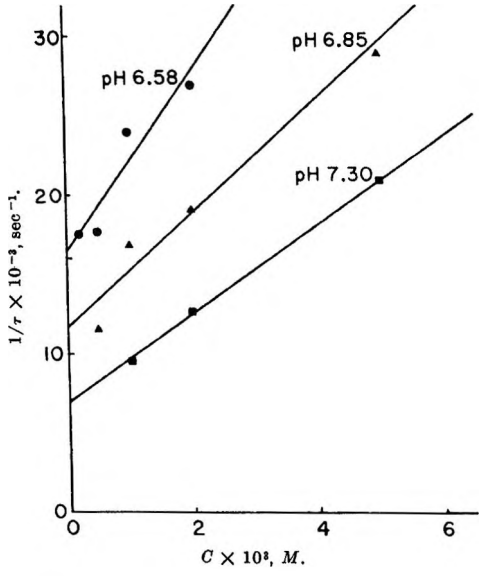

Figure 2. Dependence of $1/\tau$ on PMA concentration at constant pH.

$K_{\mathrm{HIn}} = k_{3'1}/k_{13'}$ is the dissociation constant of the indicator (2×10^{-8} M for phenol red[10]).

The rate constant for proton transfer from the polyacid to the indicator, $k_{33'}$, is thus obtainable from the slope of plots of $1/\tau$ *vs.* C at constant pH. The variation of the intercept with pH allows the determination of $k_{13'}$ and k_{23} as well. With the equilibrium condition $k_{3'3} = k_{33'}(1 - \alpha)/\alpha \times (K_{\mathrm{HIn}}/C_{\mathrm{H}^+})$ values are obtained also for the rate constant $k_{3'3}$ of the reverse reaction. At high pH values, where α is close to 1, the uncertainty in $(1 - \alpha)$ prevents a reliable determination of $k_{33'}$ from eq 2; the rate constant for the reverse reaction, however, can still be evaluated with sufficient accuracy since the first term of eq 2 can be written also as $k_{3'3}(1 + C_{\mathrm{H}^+}/K_{\mathrm{HIn}})\alpha C$.

Examples for the dependence of $1/\tau$ on total polyacid concentration C at constant pH are shown in Figure 1 (for PAA) and in Figure 2 (for PMA). The values obtained for the rate constants $k_{33'}$ and $k_{3'3}$ are presented in Table II. Between about pH 6.5 and pH 8.0 the values have an uncertainty of approximately ±30%; outside these limits precision deteriorates rapidly.[11]

The evaluation of the intercepts yielded the following results.

$$\mathrm{H}^+ + \mathrm{In}^{2-} \xrightarrow{k_{13'}} \mathrm{HIn}^-$$

$$k_{13'} = 3(\pm 1) \times 10^{10}\ \mathrm{mol}^{-1}\ \mathrm{sec}^{-1}$$

$$\mathrm{OH}^- + \mathrm{HIn}^- \xrightarrow{k_{23}} \mathrm{In}^{2-} \qquad k_{23} \simeq 3 \times 10^9\ \mathrm{mol}^{-1}\ \mathrm{sec}^{-1}$$

(10) H. Diebler, M. Eigen, and G. Hammes, *Z. Naturforsch.*, **15b**, 554 (1960); M. Eigen and G. Hammes, *J. Amer. Chem. Soc.*, **82**, 5951 (1960); **83**, 2786 (1961).

(11) Equation 2 for $1/\tau$ contains three terms which represent contributions from the direct proton exchange, acidic path, and basic path (in that order). At low pH it is necessary to use low polyacid concentrations so that relaxation times do not become too short. The relative importance of the first term in eq 2 is thus lowered and so is the precision to which $k_{33'}$ can be determined. Also, at low pH, the pH dependence of the relaxation times is strong, leading to considerable scatter since it is difficult to maintain high pH constantly in these unbuffered solutions. At high pH the main difficulty is the uncertainty in $1 - \alpha$ which depends on extrapolated values for α.

These rate constants are typical for diffusion-controlled reactions of H^+ and OH^-. The value for $k_{13'}$ is in good agreement with one obtained in an earlier determination.[10] k_{23} has been evaluated from the data for the PMA system; its determination may be less reliable than that of $k_{13'}$, due to the condition $k_{23'} C_{HPA} \gg k_{23} C_{HIn^-}$ not being sufficiently fulfilled.

Both PAA and PMA are stronger proton donors than the acidic indicator species, the apparent pK values ($= -\log C_{H^+} \cdot \alpha/1 - \alpha$) of the former varying approximately between 5.8 and 6.4 in the pH range studied, whereas $pK_{HIn} = 7.7$. Because of these differences in pK it would be expected[1] that $k_{33'} \simeq 2 \times 10^7$ mol^{-1} sec^{-1} represents the rate constant for a diffusion-controlled proton-transfer process. It should be borne in mind, however, that hydrogen bonding between the carboxylic groups of the polyacids may lead to a rate constant for proton transfer somewhat below the diffusion-controlled limit[12] (the same may apply to $k_{23'}$, the rate constant for the reaction of HPA with OH^-). For the analogous reactions of the monomeric acids $ATPH^{3-}$ and $ADPH^{2-}$ with phenol red, diffusion-controlled rate constants of 7×10^8 mol^{-1} sec^{-1} have been reported.[10] These values are not fit for direct comparison, however, since there is no theory available yet to predict rate constants for diffusion-controlled reactions in which the reactive sites of a polyelectrolyte chain represent one of the reactants.[13]

The values for $k_{33'}$ do not show a significant dependence on C_{H^+} in the pH range within which a reliable determination can be accomplished. The slight increase in the rate constant for the reverse reaction, $k_{3'3}$, with increasing pH therefore mainly reflects the variations of the apparent pK values of the polyacids. Apparently the variations in charge and conformation of the macromolecules between $\alpha \simeq 0.65$ and $\alpha \simeq 0.99$ are not so severe as to have an appreciable effect on $k_{33'}$. More pronounced effects may show up at small values of α, but proton transfer will be difficult to study under these conditions by the present technique.

Acknowledgment. The authors wish to express their appreciation to Dr. L. De Maeyer for helpful discussions and to Dr. F. Eggers for help with the sound absorption experiments.

(12) Reference 2, Table IV.

(13) If the concentration of the polyacids is expressed in terms of *polymeric* species, the rate constant for proton transfer from the polyacid to the indicator has a value of about 1×10^{10} M^{-1} sec^{-1} at $\alpha \simeq 0.6$. For particles of spherical symmetry (which is not fulfilled here) and with negligible electrostatic interaction, a diffusion-controlled rate constant of 1×10^{10} M^{-1} sec^{-1} corresponds to a distance of reaction of $\sim$30 Å^2 (taking 0.5×10^{-5} cm^2 sec^{-1} as the sum of the two diffusion coefficients). Obviously use of concentrations expressed in terms of polymeric species does not affect the validity of the derivation of eq 2 since indicator species concentrations still remain small relative to polymer concentration in terms of equivalents per unit volume.

A Kinetic Investigation of the Amylose–Iodine Reaction[1]

by John C. Thompson[2] and Eugene Hamori*

Department of Chemistry, University of Delaware, Newark, Delaware 19711 *(Received July 17, 1970)*

Publication costs assisted by the Petroleum Research Fund

The fast reaction between amylose, iodine, and iodide ions was studied in aqueous solution by a rapid mixing technique. The observed changes in absorbance at 6283 Å could be converted to changes in free and bound iodine concentrations using a calibration procedure based on simultaneous potentiometric and spectrophotometric titrations. The initial rates observed followed the rate law, $-d[I_2]/dt = k[P][I_2]^{4-c}[I^-]^{3-c}[I_3]^c$. Due to the equilibrium between iodine, iodide, and triiodide ions the value of exponent c could be established only to the extent that, $0 \leq c \leq 3$. According to the mechanism proposed for the explanation of the kinetic results, the rate-determining step in the initial phase of the complexation is the slow formation of stable nuclei (apparently I_{11}^{3-}) inside the amylose helices. The observed molecular-weight dependence of initial rates, the reactions involved in equilibrium, and some other characteristic properties of the amylose iodine system are discussed in terms of this mechanism.

Introduction

The reaction in aqueous solution between starch and iodine which leads to the formation of a characteristic blue complex has been extensively studied following its discovery in 1814.[3] It has been established that the product is a unique iodine polymer which is formed inside the tubular cavities of the helically coiled amylose macromolecules present in starch.[4-8] Due probably to the very fast reactions involved, the mechanism of the formation of the complex has not been investigated in the past. It is known however, that the reaction is fully reversible and that in equilibrium a significant concentration of free iodine is present in the system.[9]

We have undertaken a series of reaction rate studies using some of the instrumental methods which recently have become available for the investigation of fast chemical reactions.[10] The primary goal of our experiments has been the precise characterization of the reaction rates involved in the formation of the amylose–iodine complex. We were interested in establishing a rate law and in formulating a mechanism which would explain both the observed rates and the dynamic equilibrium which exists in the system following the completion of the reaction. It was also our objective to provide additional information by our new experimental approach to the still unsettled problem concerning the exact chemical composition of the complex.

To facilitate the interpretation of the kinetic results in the study of this complex reaction, we have carefully chosen our experimental conditions to provide a minimum number of changing parameters during the time course of the studied reactions. (We used dilute solutions, fractionated amylose samples, low iodine/amylose and iodine/iodide ratios etc.) Special precautions were taken also to avoid the slow precipitation which might occur in the solutions of pure amylose and those of the amylose–iodine complex.

Experimental Section

Materials. Potato amylose was purchased from Calbiochem, Los Angeles, Calif. Dimethyl sulfoxide (DMSO) used for viscosity studies was purified by drying Fisher Certified DMSO over CaO, filtering through a sintered glass filter, and vacuum distilling. All DMSO solutions were stored in desiccators containing $CaCl_2$. The viscosity standard (No. S-3-65-1b) was purchased from the Cannon Instrument Company (State College, Pa.). The aqueous solutions were prepared with doubly distilled, degassed water.

Solutions. Stock solutions of 1.00 *M* citric acid, 1.00 *M* K_2HPO_4, 0.150 *M* KI, and 0.150 *M* KCl were stored in a refrigerator. Combined aliquots of these solutions were diluted to give the desired concentrations no more than 2 days before the experiments. The $Na_2S_2O_3$ stock solution used was standardized with KIO_3 and KI in a closed system. Its concentration (0.1005 *M*) was constant over a 2-year period. Stock iodine solutions were prepared by stirring powdered

(1) Supported by a Research Grant (3074-A 4,5) from the Petroleum Research Fund of the American Chemical Society and by a Research Grant (GM-15112) from the National Institute of General Medical Sciences of the National Institutes of Health, U. S. Public Health Service.

(2) National Institutes of Health Pre-Doctoral Fellow of the National Institute of General Medical Sciences, 1968–1970.

(3) Colin and H. Gauthier de Claubry, *Ann. Chim. (Paris)*, **90**, 87 (1814).

(4) C. S. Hanes, *New Phytol.*, **36**, 189 (1937).

(5) K. Freudenberg, E. Schaaf, G. Dumpert, and T. Ploetz, *Naturwissenschaften*, **27**, 850 (1939).

(6) R. E. Rundle and D. French, *J. Amer. Chem. Soc.*, **65**, 1707 (1943).

(7) R. E. Rundle and F. C. Edwards, *ibid.*, **65**, 2200 (1943).

(8) F. Cramer, *Chem. Ber.*, **84**, 855 (1951).

(9) F. L. Bates, D. French, and R. E. Rundle, *J. Amer. Chem. Soc.*, **65**, 142 (1943).

(10) E. M. Eyring and B. C. Bennion, *Ann. Rev. Phys. Chem.*, **19**, 129 (1968).

iodine (Fisher, Certified) into solutions of the required KI and KCl concentrations. After filtration, these solutions were kept in the refrigerator in glass-stoppered bottles. Their concentrations (approximately 1 mM) were determined by thiosulfate titrations on each day they were used. These titrations were performed under the same conditions as the standardization of $Na_2S_2O_3$. The amylose samples were dissolved in purified DMSO by stirring for about 7 days in tightly sealed vials on a magnetic stirring plate. During and after the solubilization the vials were kept in a closed compartment containing $CaCl_2$ to prevent absorption of water by DMSO. All measurements reported here were carried out at pH 2.92 ± 0.02 in a citric acid (0.0289 M)–K_2HPO_4 (0.0111 M) buffer. This pH was used to avoid a slow reaction between DMSO and iodine occurring at higher pH values. The ionic strength was kept constant, when the KI concentration was changed, by making equal but opposite changes in the concentration of KCl. The sum of the concentrations of the two salts was always kept at 3.00 mM. In all kinetic experiments the iodine/iodide and iodine/amylose ratios were kept low. (Less than 10% of the iodine binding capacity of the dissolved amylose was used.)

Fractionation of Amylose. The fractionation was carried out according to the method of Geddes, *et al.*,[11] in a DMSO–acetone solvent system. Amylose (30 g) was dissolved in 6 l. of DMSO by stirring for several days in a 20-l. carboy in a cold room. Acetone was added in small increments, and the precipitate was separated by continuous-flow centrifugation after each addition using a Sorvall Model RC 2 centrifuge at 15,000 rpm and 0°. Constant stirring was maintained in the carboy containing precipitated amylose not only during the addition of acetone, but also during the continuous-flow centrifugation. During the whole fractionation 16 l. of acetone was added. Each amylose fraction was washed twice with absolute ethanol and dried for 2 days at 60° in a vacuum oven.

Molecular Weight Determinations. Weighted portions of the amylose fractions were dissolved in purified DMSO. The efflux times of the solvent (t_0) and the amylose solutions (t) were measured in a semimicro dilution viscometer (Cannon-Ubbelohde, size 100). During the measurements the openings of the viscometer were kept in a dry nitrogen atmosphere to prevent absorption of atmospheric moisture by the solutions. A Neslab constant temperature bath (Model T9) was used to maintain the temperature at 25.00 ± 0.02°. The viscometer was calibrated by obtaining efflux times for pure water and for the viscosity standard. The end-effect correction (A) was found to be 1.245×10^{-4} dyn cm g^{-1} and the kinetic energy correction (B) 1.63×10^{-2} erg sec^2 g^{-1}. Relative viscosities were calculated from the relationship: $\eta_r = (t - B/At)/(t_0 - B/At_0)$, and they were not corrected for changes in density with amylose concentration, since this factor was found to be negligible in comparison to experimental error. For each amylose fraction $(1/c)\cdot \ln \eta_r$ and $(\eta_r - 1)/c$, were plotted against the concentration of amylose, c (in g ml^{-1}). The intrinsic viscosity $[\eta]$ was obtained from the common intercept of the resulting straight lines on the ordinate. The molecular weights were calculated from the Mark–Houwink equation; $[\eta] = KM^a$. The constants K and a have been determined for amylose in DMSO at 25° by Everett and Foster[12] and independently by Cowie.[13] Since the two sets of reported values are different, we have calculated a least-squares line for the log $[\eta]$ *vs.* log M plot of the combined sets of original data. In Table I are listed the K and a values previously reported by the authors above, and also those calculated by us from the combined sets of data.

Table I: Mark–Houwink Constants for Amylose in DMSO at 25°

Ref	K, dl g^{-1} × 10^5	a
Everett, Foster[a]	30.6	0.64
Cowie[b]	1.25	0.87
Combined set of data	1.89	0.84

[a] See ref 12. [b] See ref 13.

Construction of Calibration Curves. The general method of obtaining calibration curves which are needed for the conversion of transmission values (measured during the kinetic experiments) to amylose-bound iodine concentrations has been reported.[14] The procedure involves spectrophotometric and potentiometric titrations of amylose with iodine. From these titration curves, and from a curve of emf *vs.* $[I_2]$ obtained in the absence of amylose, a calibration plot of A_{6283} *vs.* $[I_2]_{bound}$ can be constructed. A recent modification of this method[15] has made it possible to carry out the spectrophotometric and potentiometric titrations simultaneously. In this new procedure a temperature-controlled cell of 5.08-cm path length equipped with a buret and pressure-equalizing arm was used in conjunction with a Cary 14 recording spectrophotometer and a Beckman Expandomatic pH meter. The electrodes used in the emf measurements were shiny platinum and saturated calomel. The experiments were performed in a closed system at 25.00 ± 0.05° with

(11) R. Geddes, C. T. Greenwood, A. W. MacGreggor, A. R. Procter, and J. Thomson, *Makromol. Chem.*, **79**, 189 (1964).

(12) W. W. Everett and J. F. Foster, *J. Amer. Chem. Soc.*, **81**, 3459, 3464 (1959).

(13) J. M. G. Cowie, *Makromol. Chem.*, **42**, 230 (1961).

(14) J. C. Thompson and E. Hamori, *Biopolymers*, **8**, 689 (1969).

(15) J. C. Thompson, Ph.D. Dissertation, University of Delaware, 1970.

constant stirring. In each run 150 ml of solution was titrated with standardized 1 mM iodine. The titrant and titrate were of the same KI and KCl concentrations. A total of 0.9 ml of the iodine solution was added in seven increments and readings of emf and A_{6283} were taken at 2 min after each addition. This time period was found to be long enough to allow a thorough mixing and a reliable electrode response and was short enough so that the titration could be completed before any significant aggregation of the complex or loss of iodine to the air space could occur.

Kinetic Measurements. The rate of the reaction between amylose and iodine was measured by monitoring the development of the blue color of the complex in a Durrum–Gibson stopped-flow apparatus (Durrum Instrument Co.). Instead of a monochromator, an interference filter of 6283-Å transmission peak was used (Baird-Atomic Inc.) with a half-point bandwidth of 6.5 Å. A 60-W tungsten iodide lamp (General Electric, No. 1960) was the light source. The temperature of the solutions inside the instrument was kept at 25.00 ± 0.05° with a Neslab constant-temperature bath (Model T9). A Tektronix storage oscilloscope (Type 549) was used to display and record the transmission changes occurring after the rapid mixing of the reactants. Due to the transmission of small amounts of light outside the peak range of the interference filter, a curve relating stopped-flow transmission to Cary-14 absorbance at 6283 Å was required for a comparison of data between these instruments. This curve was obtained by making measurements with both instruments on a series of blue solutions of brom cresol green indicator buffered at pH 7.0. Points obtained using amylose–iodine complex were found to be on this same transmission (stopped-flow) *vs.* absorbance (Cary 14) curve.

Amylose solutions were prepared[14] by diluting aliquots of a stock solution of amylose in DMSO with the buffer containing KI and KCl. The final DMSO concentration, after stopped-flow mixing with iodine solutions, was 0.75%. (All percentages in this paper refer to g of solute/100 ml of solution.) To evaluate the possible effect of DMSO on the results, the following experiments were performed. An amylose sample was dissolved in 1 M KOH (this method was not used for the rest of the work reported here to avoid the possibility of polymer degradation) and was diluted, neutralized, and buffered. Stopped-flow experiments were carried out with this solution, and the kinetic behavior was found to be the same as that of systems containing 0.75% DMSO. Also, no significant differences were found between the spectra of amylose–iodine solutions prepared with and without DMSO. To avoid the effects of a possible slow aggregation (retrogradation) freshly prepared amylose solutions were always used. The results showed no variations, however, when the solutions were stored for 3–4 hr.

Temperature-jump relaxation measurements were made with a temperature-jump apparatus (Enfield Specialty Co., Model DH1-A) which utilized the same light source, interference filter, and oscilloscope as the stopped-flow instrument described above. The temperature of the solution in the cell was maintained at 25.00 ± 0.08° with a Haake constant-temperature circulator (Model F). The temperature-jump cell had a 0.4-cm light path and 2.8 ml capacity. The volume between the two platinum electrodes in the cell was 0.75 ml. Further details of the measuring technique and the apparatus used have been published previously.[16,17] Temperature jumps were carried out in 0.1 M KCl and 0.00375% amylose (fraction 2) solutions at various concentrations of I_2 and KI.

Results

Molecular Weights. Listed in Table II are the molecular weight data for the amylose fractions obtained. The sample collected after the first addition of acetone (fraction 1) was not utilized, since it was somewhat discolored from impurities. Also, this fraction was expected to contain all the amylopectin contamination of the original sample.

Table II: List of Intrinsic Viscosities, Molecular Weights, and Rate Constants for the Amylose Fractions Studied

Fraction no.	$[\eta]$, ml g^{-1}	$M_v \times 10^5$, daltons	DP[a] × 10^2	kK^c, M^{-1} sec^{-1} × 10^2
2	209	10.2	63.0	3.06
3	171	8.00	49.4	3.03
4	123	5.41	33.4	2.75
5	94.3	3.94	24.3	2.04
6	85.5	3.50	21.6	1.71
7	61.7	2.36	14.6	1.41
8	35.9	1.25	7.7	0.40
9	21.0	0.66	4.1	0.37

[a] DP = degree of polymerization.

Calibration Curves. During the spectrophotometric–potentiometric titrations, the first few additions of iodine were accompanied by practically instantaneous attainments of equilibrium absorbance and emf values. Above iodine concentrations of 2.2 μM, however, a minor (*i.e.*, about 5% of total) slow reaction was observed in addition to the major fast one. This slow process was also characterized by a decrease in the free iodine concentration (indicated by a decrease in emf) and increases in A_{6283}. In order to complete the titrations in a reasonable period of time, all emf and A_{6283} readings were made 2 min after iodine additions. Therefore, in titrating beyond an iodine concentration

(16) M. Eigen and L. de Maeyer, *Tech. Org. Chem.*, **8**, 966 (1963).
(17) G. C. Krescheck, E. Hamori, G. Davenport, and H. A. Scheraga, *J. Amer. Chem. Soc.*, **88**, 247 (1966).

of 2.2 μM, each data point was obtained prior to the completion of this slow reaction. Since these calibration curves were to be used for the assignment of free iodine concentration values to the fast absorbance changes observed in the stopped-flow instrument, the question arises whether the slow reaction seen during the titrations will not interfere with the results. It can be easily seen that if this minor reaction leads to the same product as the fast reaction, it is correct to use the calibration curves obtained in the described manner for the kinetic evaluation of the fast reaction. Two observations indicate that the fast and slow reactions indeed lead to the same product. (1) The effect of changing the length of waiting periods during the emf, A_{6283} readings was simply to shift the calculated A_{6283}, $[I_2]_b$ points up to a new position which was still on the same calibration curve. (2) The spectrum recorded 10 min after the mixing of amylose and iodine appears to be the same as that recorded 1 min after mixing. Although the absorbance is slightly greater after 10 min, the λ_{max} values and the shapes of the curves are identical.

Several calibration curves were obtained on different polymer fractions using various iodine–ion concentrations. They were all linear and appeared to pass through the origin. An example is shown in Figure 1 for the following experimental conditions: 25°, pH 2.92 and 3.00 mM (KI + KCl) with 1.50 mM KI. A value of 3.75×10^4 M^{-1} cm^{-1} was calculated for the extinction coefficient (ϵ_{6283}) of bound iodine from the slope of the line of Figure 1. This value was found to be independent of the molecular weight of the amylose in the range from 1.02×10^6 to 2.39×10^5 daltons. Below the latter value decreases in the extinction coefficient were observed (fractions 8 and 9 yielded ϵ_{6283} values of 3.51×10^4 and 3.19×10^4 M^{-1} cm^{-1}, respectively). Changing the amylose concentration had no effect on the value of the extinction coefficient. Using fraction number 2, ϵ_{6283} was determined at four KI concentrations (Table III). Below 0.75 mM KI concentrations experimental difficulties were encountered during the potentiometric–spectrophotometric titrations (the emf readings were unreproduceable). Solutions containing 3.00 mM KI yielded a somewhat lower value of the extinction coefficient, indicating that the composition of the complex at this (and possibly higher) KI concentrations is different from that formed at lower concentrations. Due to these problems at high and low KI concentrations all kinetic experiments in this study were carried out in the limited 0.75–1.50 mM KI range.

The data of these titrations were also used to construct bound *vs.* total iodine concentrations plots (Figures 2 and 3). It can be seen from these that increases in the molecular weight of amylose and the concentration of KI lead to increases in the ratios of bound to total iodine concentrations in the range studied.

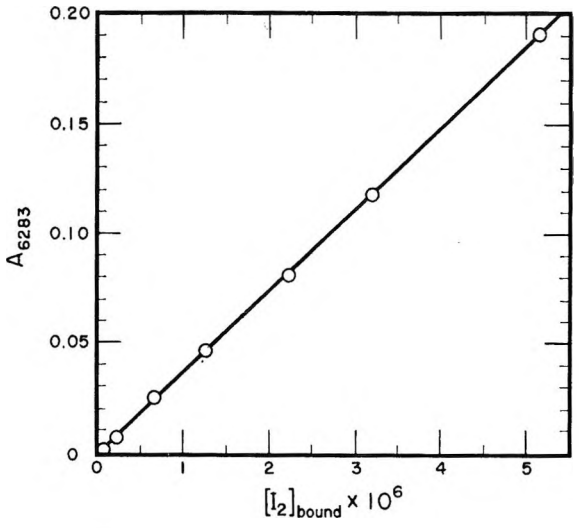

Figure 1. Calibration curve of absorbance *vs.* bound iodine concentration for amylose (fraction 2) in 1.50 mM KI. (See text for experimental conditions.)

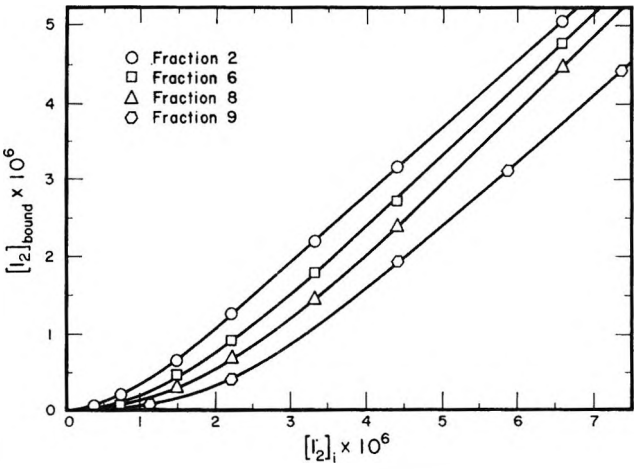

Figure 2. Plots of bound *vs.* total iodine concentration for 0.0018% solutions of different amylose fractions in 1.50 mM KI.

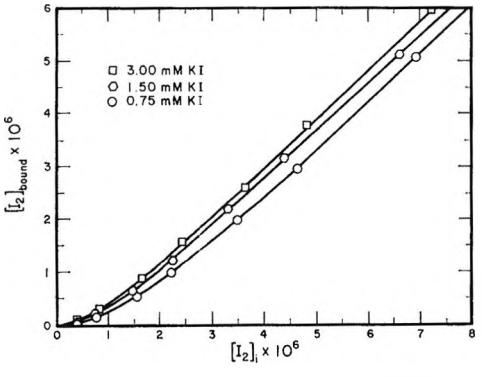

Figure 3. Plots of bound *vs.* total iodine concentration for 0.0018% amylose (fraction 2) at different KI concentrations.

Kinetic Experiments. During the initial course of the complexation, the following rate law is expected to hold[14]

$$R \equiv -\frac{d[I_2]}{dt} = k[P]^a[I^-]^b[I_3^-]^c[I_2]^d \qquad (1)$$

where P designates the iodine binding sites of amylose. This equation can be integrated to yield

$$t_{1/4} = \frac{[(3/4)^{1-n} - 1](1 + K[I^-])^{n-1}}{kK^c[P]^a[I^-]^m(n-1)}[I_2]_t^{1-n} \qquad (2)$$

where K is the equilibrium constant for the very rapid[18] reaction $I_2 + I^- \rightleftarrows I_3^-$, $t_{1/4}$ is the quarter-life of the reaction, $[I_2]_t = [I_2]_0 + [I_3^-]_0 = [I_2]_0(1 + K[I^-])$ the total initial concentration of iodine, $n = d + c$ and $m = b + c$. Since all quantities in the above fraction are constant, n can be determined from the slope of a log $t_{1/4}$ *vs.* log $[I_2]_t$ plot. We reported previously[14] that $n = 4$, for 1.50 mM KI with fraction 2 amylose, and this finding has not been altered by the reevaluation of our previous data using the new and more accurate calibration curves. In similar studies with fraction 2, using 0.75 mM KI, and with fraction 8, using 1.50 mM KI, the same value was found for n.

Table III: ϵ_{6233} Values Obtained at Different KI Concentrations

[KI] × 10³	ϵ_{6233}
0.75	3.75
1.13	3.75
1.50	3.75
3.00	3.47

It follows from eq 2 that for constant $[I^-]$ and $[I_2]_t$, a logarithmic plot of $t_{1/4}$ *vs.* amylose concentration will be linear with a slope of $-a$, assuming that [P] is proportional to amylose concentration. Such a plot of data is shown in Figure 4, the slope indicating that $a \cong 1$. Thus it appears that the initial reaction is first order in amylose.

In order to determine the value of $m = b + c$ (the combined order of the reaction with respect to I^- and I_3^-) $t_{1/4}$ values were measured at 0.00375% amylose (fraction 2) and 2.73 μM $[I_2]_t$, using different concentrations of KI. It follows from eq 2 that

$$Z \equiv \log t_{1/4} - (n-1)\log(1 + K[KI^-]) = \log K' - m \log [I^-] \qquad (3)$$

where

$$K' = [(3/4)^{1-n} - 1][I_2]_t^{1-n}[kK^c[P]^a(n-1)]^{-1}$$

Using[19] $K = 715\ M^{-1}$, $n = 4$, and experimental $t_{1/4}$ and $[I^-]$ values, Z was plotted against log $[I^-]$. The slope indicated a value of 3.1 ± 0.3 for m (Figure 5).

The dependence of reaction rate on molecular weight was investigated at 1.50 mM KI. Since the iodine binding capacity is known to decrease with decreasing molecular weight,[20] it was necessary to determine the concentration of iodine binding sites, [P], for each of these experiments. These values were calculated from ϵ_{6283} and from values of A_{6283} for iodine-saturated amylose similarly to a procedure published in the literature.[20] For 0.00375% amylose [P] was found to be 28 ± 1 μM and constant over a molecular weight range from $1.25 \times 10^5 - 1.02 \times 10^6$ daltons. Fraction 9 (6.5×10^4 daltons) however, yielded a value of 24 ± 1 μM. Using eq 2, the quantity kK^c was determined for each molecular weight fraction from known values of [P], a, K, n, m, $[I^-]$, and $[I_2]_t$ and from measured $t_{1/4}$ values (see Table II). Note, that since we could not establish c, the order of the initial reaction with respect to I_3^-, the closest we can get to the value of the rate constant (k) in eq 1 is kK^c, a quantity proportional to k.

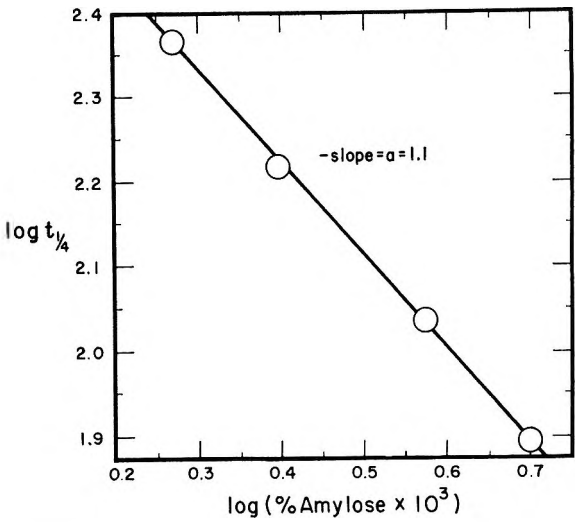

Figure 4. Logarithmic plot of $t_{1/4}$ (in msec) *vs.* concentration of amylose (fraction 2) at 1.50 mM KI and 2.36 μM $[I_2]_t$.

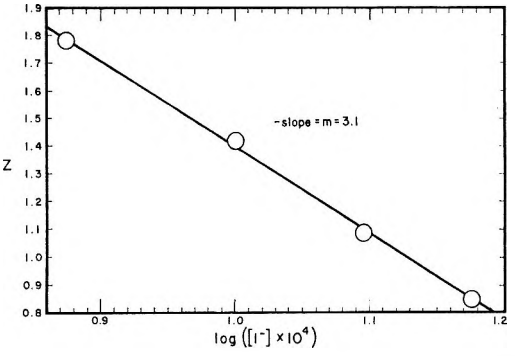

Figure 5. Plot of Z *vs.* (log $[I^-] \times 10^4$) at constant amylose and iodine concentrations. (See text for concentration data and for the definition of Z.)

(18) O. E. Myers, *J. Chem. Phys.*, **28**, 1027 (1958).

(19) A. D. Awtrey and R. E. Connick, *J. Amer. Chem. Soc.*, **73**, 1842 (1951).

(20) J. Szejtli, M. Richter, and S. Augustat, *Biopolymers*, **6**, 27 (1968).

Experiments were carried out in order to determine whether the spectrum of the complex changes over the time course of the reaction. A solution of amylose (0.0075%) and iodine at the standard pH and salt concentrations was mixed in the stopped-flow instrument and the transmission changes were recorded at seven different wavelengths between 500 and 750 mμ. From these curves the absorption spectrum of the complex could be constructed for various times during the reaction. The spectra showed no experimentally observable changes in the region of maximum absorption (630 ± 20 mμ) over the entire course of the reaction, indicating that the complexes formed during the different time stages of the reaction have basically the same composition. This observation appears to justify the use of calibration curves obtained under near-equilibrium conditions for the purpose of converting rapidly changing stopped-flow transmission values to concentrations of bound iodine.

"Concentration-jump" experiments were carried out in the stopped-flow apparatus in the following manner. Equilibrated solutions of the amylose–iodine complex were mixed with solutions containing (in addition to the standard buffer and KI concentrations) sufficient amounts of iodine to raise the concentration of iodine above the original (equilibrium) concentration. The rates and iodine order observed were the same in these experiments as those seen when iodine and fresh amylose solutions were mixed. Significantly, we could not detect an initial fast component in the reaction, which would have indicated rapid complexation from existing nuclei.

Temperature-jump experiments, carried out under conditions described in the Experimental Section, indicated a very fast reaction which was complete before 15 μsec. The overall negative change in A_{6283} for this relaxation was found to decrease with increasing total iodine concentration. Thus below 3 μM total iodine the signal/noise ratio was too low for obtaining useful data. Due to the limitations of the instrument, neither the use of this minimum practical iodine concentration nor that of low (0.15 mM) KI concentration led to quantitatively measurable relaxation times.

Spectral Studies. The spectrum of the amylose–iodine complex was recorded at different $[I_2]_t$ values using 0.00375% amylose (fraction 2) in 1.50 mM KI. The use of a 5.08-cm path length cell and the expanded absorbance scale in the spectrophotometer made absorbance measurements possible at very low iodine concentrations. No significant changes in λ_{max} (615 ± 5 mμ) were found over the range of iodine concentration 6–1 μM. However, λ_{max} was found to be 600 ± 10 mμ at 0.15 μM and 580 ± 15 mμ at 0.07 μM $[I_2]_t$. The large errors indicated here result from the broadness of the absorption maxima and the very low absorbances involved.

Discussion

The observation that the absorption spectrum of the amylose–iodine system does not change during the reaction suggests that the composition of the complex species formed is the same both at the beginning and at the end of the reaction. It appears, therefore, that the complexation proceeds by a relatively slow formation of nuclei which instantaneously grow into long polyiodine chains by a rapid propagation process. That would mean, of course, that during the reaction an increase in the concentration of the complete polyiodine chains is observed, rather than a growth of chains.

Direct evidence that the propagation (growth) of complex chains is much faster than their nucleation rate comes from our temperature-jump measurements. In these experiments we observed a relaxation process which was faster than about 15 μsec. (The reaction recorded was the dissociation of the complex, as expected from the known decrease of iodine binding at higher temperatures.[21]) Since in these relaxation experiments one observes the readjustment of the equilibrium between free iodine and the complex due to a sudden temperature rise,[16] the fast process seen is an indication that the rates involved in the limited growth and breakdown of the complex near equilibrium are much faster than the initial formation of the complex, which is in the millisecond range.

In such a mechanism the lengths of helical regions available for complexation would be expected to have an effect on the initial rate of the reaction (longer iodine polymers formed in long helical regions would lead to faster rates). Indeed, our observations indicate increasing initial rates with increasing molecular weights (Table II). Since the distribution of helical regions in the amylose molecules is not known, the average length of polyiodine chains of the complex cannot be estimated. It is interesting to observe, however (Table II), that the initial rates increase steadily until a DP of about 5000 is reached, and after that limit they level off. This indicates that even very long helical regions which are expected to be present only in amylose molecules of high molecular weight are participating in the reaction, and apparently they are being filled by the forming polyiodine chains. Szejtli and coworkers[22] concluded from their photometric and amperometric titrations studies, that in amylose solutions the average length of helical regions increases only slightly after the polymer reaches a DP of about 120. The above interpretation of our kinetic results does not agree with this conclusion and suggests that under our experimental conditions the average length of helices increases up to an amylose DP of approximately 5000.

(21) J. Holló and J. Szejtli in J. A. Radley, Ed., "Starch and Its Derivatives," 4th ed, Chapman and Hall Limited, London, 1968, p 203.

(22) J. Szejtli, M. Richter, and S. Augustat, *Biopolymers*, 5, 5 (1967).

In the concentration-jump experiments carried out in the stopped-flow apparatus, the rates observed were the same as those of the slow initial reaction. Under the conditions of these experiments, if the complexed helices were not filled with polyiodine, a dominating fast reaction associated with the propagation of the polyiodine chain would be expected, such as observed in the temperature-jump experiments. Our interpretation of the concentration-jump results is, that in the equilibrated amylose–iodine system the complexed helical regions are essentially filled with iodine, and when extra iodine is added the new complex is formed in the *empty* helical regions by the slower (nucleation-controlled) reaction. If the temperature-jump and concentration-jump experiments were comparable relaxation measurements, one would expect to see both the slow and fast processes in both experiments. However, in the former experiment very small concentration changes, caused by a minute perturbation are recorded, while in the latter measurement, the effect of a comparatively large perturbation (concentration increase) is observed. Furthermore, due to a certain amount of uncertainty about the initial transmission of the solution in the stopped-flow instrument, the presence of a fast reaction, which is only a small fraction of the total reaction observed, is compatible with our results.

It was reported previously[23] that both λ_{max} and ϵ_{max} of the complex decrease drastically if the DP of the amylose used is less than about 30–40. We have observed a similar change in the absorption characteristics of the complex under different conditions. We used a high molecular weight amylose fraction (DP 6300), but measured the spectrum of the complex at very low iodine concentrations. The above shifts occurred around $[I_2]_i = 0.1\ \mu M$, indicating that perhaps below this concentration region the polyiodine chains are shorter and presumably do not fill the complexed helical segments of the amylose. (Due to experimental difficulties we were unable to carry out kinetic measurements under these low $[I_2]_i$ conditions.)

The further and quantitative interpretation of our kinetic data requires the assumption of a detailed mechanism for the complexation reaction between amylose and iodine. Due to the complexity of the reaction, the mechanism we have chosen and will discuss below is a speculative one by necessity. Since we can only corroborate and not prove this mechanism by our kinetic observations, it should be considered mainly as a representation of our current thinking about this very unusual reaction. The essence of our mechanism is the formulation of a stable polyiodine tetramer inside the amylose helix which can serve as a polymerization nucleus for the rapid growth of an individual polyiodine chain. We propose that the initial rate of the complexation is controlled by the slow rate of formation of these nuclei and suggest that a relationship exists between the observed kinetic order of the nucleation and the composition of the nuclei.

If we designate the amylose binding sites by P, free iodine or triiodide by B, monomers, dimers and trimers of iodine or triiodide bound to the amylose by B_1, B_2, and B_3, respectively, and higher polymers of iodine or triiodide bound to amylose by C_4, C_5, ... C_z, the mechanism we have considered for the interpretation of our kinetic results can be represented as follows

$$\begin{aligned}
&P + B \underset{k_1}{\overset{k_f}{\rightleftharpoons}} B_1 \\
&B_1 + B \underset{k_2}{\overset{k_f}{\rightleftharpoons}} B_2 \\
&B_2 + B \underset{k_3}{\overset{k_f}{\rightleftharpoons}} B_3 \\
&B_3 + B \underset{k_r}{\overset{k_f}{\rightleftharpoons}} C_4 \\
&C_4 + B \underset{k_r}{\overset{k_f}{\rightleftharpoons}} C_5 \\
&\text{----------} \\
&C_{z-1} + B \underset{k_r}{\overset{k_f}{\rightleftharpoons}} C_z
\end{aligned} \qquad (4)$$

$$k_1, k_2, k_3 \gg k_r, k_f[B]$$

The constraint on the rate constants is equivalent to the assumption that monomers, dimers, and trimers are very weakly bound in the amylose helix, but tetramers and higher polyiodines are strongly bound and relatively stable. If it is assumed that during the reaction the first three equilibria are established much faster than the rate of formation of C_4 from B_3, then the concentration of B_3 can be expressed as

$$[B_3] = \frac{k_f^3}{k_1 k_2 k_3}[P][B]^3 \qquad (5)$$

When B_3 reacts to form C_4 a rapid propagation sequence ensues leading to C_z, provided that $k_f[B]$ is sufficiently large and that the reaction is in its initial phase (*i.e.*, the dissociation of polymers higher than tetramers is negligible). Thus in this mechanism the availability of B_3 (which is very low due to the tendency of bound monomers, dimers, and trimers to dissociate rather than react further) would control the reaction rate. Assuming further that after a brief induction period all the intermediates will be in a steady-state concentration, the rate of reaction can be expressed by

$$R \equiv -\frac{d[B]}{dt} = z\frac{d[C_z]}{dt} = zk_f[B_3][B] \qquad (6)$$

Substitution of eq 5 into eq 6 yields

$$R = \frac{zk_f^4}{k_1 k_2 k_3}[P][B]^4 \qquad (7)$$

(23) J. M. Bailey and W. J. Whelan, *J. Biol. Chem.*, **236**, 969 (1961).

According to our experimental data the order of the initial reaction with respect to P is 1 ($a \cong 1$) and the combined order with respect to I_2 and I_3^- is four ($n = d + c = 4$). Since in the above mechanism B represents both I_2 and I_3^- the observed orders are in full agreement with those derived from the mechanism. To check independently the result given in eq 7 we constructed an electronic analog of the reaction mechanism using an analog computer (EAI 231-R).[15] The number of steps (z) used was 7, but changing the program to 6 or to 5 steps did not effect the conclusions. By evaluating the concentration *vs.* time curves drawn by the computer we found that with the constraints stipulated in eq 4, the initial phase of the reaction is first order in P and fourth order with respect to B in agreement with our steady-state derivation and with the kinetic results.

It is worthwhile to speculate about the chemical nature of C_4 in eq 4. At first sight this mechanism appears to suggest that the C_4 nucleus is formed from 4 I_2 and/or I_3^- reacting species. The following complication must be considered, however. Our results indicate that in eq 1 which characterizes the initial phase of the complexation, $m = b + c = 3$ and $n = d + c = 4$. Lacking a third relationship among these quantities we cannot assign respective values to b, c and d. Thus the stable polyiodine nucleus (C_4) of our mechanism, in reality, could form from any of the following combinations of components: $4I_2+3I^-$, $3I_2+2I^-+I_3^-$, $2I_2+I^-+2I_3$, or $I_2+3I_3^-$. All four of these possibilities would lead to the observed order of initial rates. Notice however, that in all cases, (if each component remains bound) the nucleus would have 11 iodine atoms, 3 negative charges ($m = 3$) and 4 I_2 and/or I_3^- species ($n = 4$). In an early investigation, Gilbert and Marriott[24] proposed that at low iodine and iodide concentrations the complex is composed of I_8^{2-} units. The 11-atom nucleus considered here (I_{11}^{3-}) differs from this I_8^{2-} unit by one triiodide molecule. Recently, Cronan and Schneider[25,26] have confirmed the conclusion of Gilbert and Marriott[24] that the ratio of $[I^-]$ to $[I]_2$ bound in the helix at equilibrium is about 0.7 in the iodide range studied here. An interesting similarity exists between this ratio and the value of 0.75 characterizing our I_{11}^{3-} nucleus.

We do not wish to justify the arbitrary assumption concerning the stability of a polyiodine tetramer on grounds other than that this property of the mechanism leads to the experimentally observed reaction rates; it is interesting to consider, however, the following comparison. The minimum amylose chain length required for the formation of the blue complex is about 30–40 glucose units.[23] If one assumes that about 5 of these units at each end of the amylose polymer will be loose and will not be part of the helical structure, then using distances derived from X-ray studies on the solid complex,[6] the length of this minimal helical cavity is calculated to be between 27 and 40 Å. The iodine atom repeat distance of 3.06 Å, determined by X-ray studies for the blue α-dextrin–iodine complex[8] predicts 31 Å as the end-to-end distance for an 11-atom polyiodine chain. Assuming a similarity between the amylose and the α-dextrin complexes of iodine, it appears that the stable polyiodine nucleus suggested by our kinetic observations is about the same size as the minimum length of polyiodine chain in the blue complex. This correspondence of sizes appears to support the salient feature of our proposed reaction mechanism.

According to eq 4, the growth of the complex abruptly terminates after the addition of the zth B unit. This chain length, of course, must be considered as an average of a variety of polyiodine chain lengths occurring in the amylose–iodine complex. (A more realistic but also mathematically more cumbersome version of the mechanism, which is hardly justifiable under the circumstances, could take into account the distribution of polyiodine chain lengths). The reason for the abrupt termination of the growing chains follows from the concept discussed above; that is, when the complexing helical cavity becomes filled with polyiodine the propagation of the chain stops. According to our temperature-jump studies, a fast depolymerization and repolymerization process takes place in the system when the complex is in equilibrium. We believe that these reactions occur at the ends of chains and cause a statistical variation of completed polyiodine chain lengths in time (*i.e.*, the end of polyiodine chain will rapidly oscillate to and from the end of the helical cavity). The extent of the variation of chain lengths must be small since in our concentration-jump studies we could not detect a sizable fast reaction which would be expected if large "prenucleated" helical regions would be available in the equilibrated complex.

According to our concept of the amylose–iodine system, the following reactions occur in the solution of the complex in equilibrium: (1) slow nucleation and polymerization of *new* polyiodine chains in the empty helical regions of amylose, (2) rapid *partial* depolymerization and (3) repolymerization of polyiodine chains at the ends of chains, and (4) complete depolymerization of polyiodine chains in complexed regions. Reactions 2 and 3 compensate in equilibrium and maintain an average polyiodine chain length in the solution of the complex. Since reaction 4 is also slow (it is the statistically rare version of partial depolymerization) the constant number of complexed regions is maintained in the system by a balance between reactions 1 and 4.

The decrease of equilibrium iodine concentration with increasing amylose molecular weight, reported by Bates

(24) G. A. Gilbert and J. V. R. Marriott, *Trans. Faraday Soc.*, **44**, 84 (1948).

(25) F. W. Schneider, C. L. Cronan, and S. K. Podder, *J. Phys. Chem.*, **72**, 4563 (1968).

(26) C. L. Cronan and F. W. Schneider, *ibid.*, **73**, 3990 (1969).

and coworkers[9] in an early investigation of the amylose–iodine reaction, is in full agreement with this suggested balance between reactions 1 and 4. According to the concept discussed above, the shorter polyiodine chains in the shorter helical regions of the low molecular weight amylose would be more susceptible to this complete depolymerization (reaction 4) than the long complex chains of a high molecular weight amylose. Thus higher equilibrium iodine concentrations would be expected for the former case and lower ones for the latter. The above considerations may also explain why the salt-induced precipitation of the complex from amylose solutions of heterogeneous molecular weight is selective for high molecular weight amylose.[27,28] In such a solution all amylose fractions must be in equilibrium with a common free iodine concentration; therefore, the high molecular weight fractions will bind much more iodine than the low molecular weight fractions and will become more susceptible to precipitation by the salt than the low molecular weight amylose fractions which are "solubilized" by their uncomplexed regions.

Due to the mathematical complexity of the problem in the absence of an initial state assumption it is difficult to compare the *entire* observed time course of the reaction (*e.g.*, Figure 1 in ref 14) to the concentration *vs.* time curves predicted from the mechanism. At the present time we are using the analog computer mentioned above to solve this problem and our initial data are very encouraging. We hope that a complete discussion of the results will be a part of our next communication on this subject.

Acknowledgment. The authors wish to thank Mr. John W. Chang for the assistance in the analog computer study and Mr. Alex Vivod for the expert help offered in several instrumentation problems.

(27) R. E. Rundle, J. F. Foster, and R. R. Baldwin, *J. Amer. Chem. Soc.*, **66**, 2116 (1944).

(28) K. Ohashi, *J. Agr. Chem. Soc. Jap.*, **33**, 576 (1959).

NOTES

The Partial Molal Volumes of Tetraphenylarsonium Tetraphenylboron in Water at Infinite Dilution. Ionic Partial Molal Volumes

by Frank J. Millero

Contribution No. 1295 from The University of Miami, Rosenstiel School of Marine and Atmospheric Sciences, Miami, Florida 33149

(Received August 7, 1970)

Publication costs assisted by the Institute of Marine Sciences

The partial molal volumes, $\bar{V}_2$, of electrolytes have proved to be very useful in elucidating ion–ion and ion–solvent interactions.[1-3] The partial molal volumes of electrolytes at infinite dilution, $\bar{V}^\circ_2$, where ion–ion interactions vanish, are particularly appropriate to study ion–solvent interactions since volume properties are easy to visualize (geometrically) and relatively easy to determine (experimentally). The difficulty of using $\bar{V}^\circ_2$ data (as well as other thermodynamic data) to study ion–solvent interactions on an absolute basis stems from the problem of assigning $\bar{V}^\circ$'s to individual ions. The division of the $\bar{V}^\circ$'s of electrolytes into their ionic components, $\bar{V}^\circ$ (ion), can normally be made only by nonthermodynamic methods. Lack of adequate theories or knowledge of such fundamental parameters as ionic radii[1,3,4] increase the difficulties of assigning absolute ionic properties. Once the $\bar{V}^\circ$ of one ion is estimated (usually the proton), the $\bar{V}^\circ$'s of other ions are fixed due to the additivity principle.

Millero[1,3] and Panckhurst[4] have recently reviewed the various methods used to estimate ionic $\bar{V}^\circ$'s. As pointed out elsewhere[1,3] to compare the estimates of ionic $\bar{V}^\circ$'s obtained by these various methods on a common basis, it is necessary to use the most reliable $\bar{V}^\circ$ data. For example, Panckhurst[4] has criticized most of the methods used by various workers to estimate the $\bar{V}^\circ(H^+)$. He selects $\bar{V}^\circ(H^+) = 1.5$ cc/mol at 25° in water as the "best" estimate; however, when one uses more reliable $\bar{V}^\circ$ data one obtains $\bar{V}^\circ(H^+) = -0.1$ cc/mol as the "best" estimate (*i.e.*, using similar techniques).[3] Thus, although some of the criticisms made by Panckhurst[4] are valid, most of the methods yield results of $\bar{V}^\circ(H^+)$ between 0 and −5.0 cc/mol at 25° in water. As discussed elsewhere,[3] Panckhurst's criticism[4] of Zana and Yeager's[5] ionic potential mea-

(1) F. J. Millero, *Chem. Rev.*, in press.

(2) F. J. Millero in "A Treatise on Skin," Vol. I, H. R. Elden, Ed., Interscience, New York, N. Y., 1971, Chapter 11.

(3) F. J. Millero in "Structure and Transport Processes in Water and Aqueous Solutions," R. A. Horne, Ed., Interscience, New York, N. Y., 1971, Chapter 15.

(4) M. H. Panckhurst, *Rev. Pure Appl. Chem.*, **19**, 45 (1969).

surements (which yield $\bar{V}^\circ(H^+) = -5.4$ cc/mol) also appear to be invalid. Due to the internal consistency of the $\bar{V}^\circ$ (ions) obtained by Zana and Yeager[5] and the agreement of the estimates for $\bar{V}^\circ(H^+)$ obtained by other workers,[3] we feel that $\bar{V}^\circ(H^+)$ should be *ca.* -5.0 cc/mol at 25°.

The purpose of this note is to examine the use of the $\bar{V}^\circ$ of the large electrolyte tetraphenylarsonium tetraphenylboron (Ph_4AsBPh_4) in estimating ionic partial molal volumes. Since Ph_4AsBPh_4 contains a very large cation and anion of nearly the same size, we hoped to determine ionic partial molal volumes by the methods used by other workers to calculate ionic heats of transfer[6] and ionic changes in partial molal free energies.[7]

The $\bar{V}^\circ$'s of aqueous Ph_4AsBPh_4 solutions at 0, 25, and 50° were calculated from the $\bar{V}^\circ$'s of $NaBPh_4$,[8] Ph_4AsCl,[9] and NaCl[10,11] using the additivity principle. The $\bar{V}^\circ$'s of these electrolytes (as well as HCl[3]) are tabulated in Table I.

Table I: The Partial Molal Volumes at Infinite Dilution, $\bar{V}_2^\circ$, of $NaBPh_4$, Ph_4AsCl, NaCl, and Ph_4AsBPh_4 in Water at 0, 25, and 50° (cc/mol)

Temp, °C	$NaBPh_4$[a]	Ph_4AsCl[b]	NaCl[c]	HCl[d]	Ph_4AsBPh_4
0	267.16	307.57	12.90	16.45	561.83
25	276.41	318.48	16.62	17.83	578.27
50	283.63	327.94	17.71	18.00	593.86

[a] Results taken from ref 8. [b] Results taken from ref 9. [c] Results taken from ref 9 and 10. [d] Results taken from ref 3.

The simplest method of using the $\bar{V}^\circ$ of Ph_4AsBPh_4 to estimate ionic $\bar{V}^\circ$'s would be to assume $\bar{V}^\circ(Ph_4As^+) = \bar{V}^\circ(BPh_4^-)$. This method yields $\bar{V}^\circ(H^+) = -11.5$ cc/mol at 25°. This value is more negative by ~6.0 cc/mol than the estimates made by other methods.[1,3] This is not surprising since one would expect the $\bar{V}^\circ(Ph_4As^+)$ to be larger than the $\bar{V}^\circ(BPh_4^-)$ since the covalent radius of >As< is 1.18 Å compared to 0.88 Å for >B<.[12]

The first method to be used to estimate the $\bar{V}^\circ$'s of ions from the $\bar{V}^\circ(Ph_4AsBPh_4)$ is based on the technique first used by Bernal and Fowler.[13] This method assumes that the ratio of the $\bar{V}^\circ$'s of the ions Ph_4As^+ and BPh_4^- is equal to the ratio of the cubes of the radii of Ph_4As^+ and BPh_4^-

$$\bar{V}^\circ(Ph_4As^+)/\bar{V}^\circ(BPh_4^-) = r(Ph_4As^+)^3/r(BPh_4^-)^3 \quad (1)$$

The biggest problem associated with using this method is the difficulties involved in estimating the radii of the large ions Ph_4As^+ and BPh_4^-.

Owing to the problems[7] involved in estimating the radii of these large ions from covalent radii, we have estimated the Stokes radii of these ions from conductance data, $r_s = 91.5/\lambda^\pm$. Using $\lambda^\circ(NaBPh_4) = 69.94$,[14] $\lambda^\circ(Ph_4AsCl) = 95.80$,[15] $\lambda^\circ(Na^+) = 50.12$,[16] and $\lambda^\circ(Cl^-) = 76.33$,[16] we obtain $\lambda^\circ(Ph_4As^+) = 19.47$ and $\lambda^\circ(BPh_4^-) = 19.82$. From these λ°'s we obtain $r_s(Ph_4As^+) = 4.70$ Å and $r_s(BPh_4^-) = 4.62$ Å. These radii yield $\bar{V}^\circ(H^+) = -3.0$, -4.1, and -5.4, respectively, at 0, 25, and 50° (using eq 1). This method is quite sensitive to the radii used; for example, the quoted[14,15] maximum uncertainty of ±0.1 in the λ°'s yields an error of ±0.02 Å in the Stokes radii or ±1.8 cc/mol in $\bar{V}^\circ(H^+)$.

The second method to be used to estimate the $\bar{V}^\circ(H^+)$ from the $\bar{V}^\circ(Ph_4AsBPh_4)$, which hopefully eliminates the errors involved in estimating the radii of the ions Ph_4As^+ and BPh_4^-, is based on the equation

$$\bar{V}^\circ(Ph_4As^+) - \bar{V}^\circ(BPh_4^-) = \bar{V}^\circ(-\overset{|}{\underset{|}{As}}-) - \bar{V}^\circ(-\overset{|}{\underset{|}{B}}-) \quad (2)$$

where $\bar{V}^\circ(>As<) = 2.52r(>As<)^3$ and $\bar{V}^\circ(>B<) = 2.52r(>B<)^3$ are the tetrahedral covalent volumes of the ions >As< and >B<. Using $r(>As<) = 1.18$ Å[12] and $r(>B<) = 0.88$ Å,[12] we obtain $\bar{V}^\circ(H^+) = -3.6$, -4.9, and -6.4 cc/mol, respectively, at 0, 25, and 50°. This method is not as sensitive to errors selected for the radii of >As< and >B< (*e.g.*, an error of ±0.02 Å in r yields an error of ±0.3 cc/mol in $\bar{V}^\circ(H^+)$).

The third method to be used to estimate the $\bar{V}^\circ(H^+)$ from the $\bar{V}^\circ(Ph_4AsBPh_4)$ is based on the van der Waals volumes, V_w, of the ions Ph_4As^+ and BPh_4^-. King[17] has recently shown that the $\bar{V}^\circ$'s of large ions have nearly the same packing fraction $f = \bar{V}$ (ion)$/V_w$ (ion). By assuming that the large ions Ph_4As^+ and BPh_4^- have the same packing fraction we obtain

$$\bar{V}^\circ(Ph_4As^+)/\bar{V}^\circ(BPh_4^-) = V_w(Ph_4As^+)/V_w(BPh_4^-) \quad (3)$$

Using the van der Waal radii $r_w(C) = 1.70$ Å,[18] $r_w(B)$

(5) R. Zana and E. Yeager, *J. Phys. Chem.*, **70**, 954 (1966); **71**, 521, 4241 (1967).
(6) C. V. Krishnan and H. L. Friedman, *ibid.*, **74**, 2356 (1970).
(7) E. Grunwald, G. Baughman, and G. Kohnstam, *J. Amer. Chem. Soc.*, **82**, 5801 (1960).
(8) F. J. Millero, *J. Chem. Eng. Data*, **15**, 562 (1970).
(9) F. J. Millero, *ibid.*, in press.
(10) F. J. Millero, *J. Phys. Chem.*, **74**, 356 (1970).
(11) L. A. Dunn, *Trans. Faraday Soc.*, **64**, 2951 (1968).
(12) L. Pauling, "The Nature of the Chemical Bond," 3rd ed, Cornell University Press, Ithaca, N. Y., 1960, p 246.
(13) J. D. Bernal and R. H. Fowler, *J. Chem. Phys.*, **1**, 515 (1933).
(14) J. F. Skinner and R. M. Fuoss, *J. Phys. Chem.*, **68**, 1882 (1964).
(15) G. Kalfoglou and L. H. Bowen, *ibid.*, **73**, 2728 (1969).
(16) H. S. Harned and B. B. Owen, "The Physical Chemistry of Electrolytic Solutions," ACS Monograph No. 137, Reinhold, New York, N. Y., 1958.
(17) E. J. King, *J. Phys. Chem.*, **73**, 1220 (1969); *ibid.*, **74**, 4590 (1970).
(18) A. Bondi, *ibid.*, **68**, 441 (1964).

= 1.70 Å,[18] r_w(As) = 1.85 Å,[18] and bond lengths l(C–As) = 1.90 Å,[19] l(C–C) = 1.54 Å,[20] and l(C–B) = 1.56 Å[20] and the V_w's tabulated by Bondi,[18] we obtain $V_w(Ph_4As^+)$ = 193.2 cc/mol and $V_w(BPh_4^-)$ = 186.9 cc/mol. These V_w's yield $\bar{V}°(H^+)$ = −5.4, −6.6, and −7.9 cc/mol, respectively, at 0, 25, and 50°. Errors in the r_w for B and As have little effect on the $\bar{V}°(H^+)$ calculated by this method (*e.g.*, if r_w(B) = 1.65[18] and r_w(As) = 1.94[18] are are used, $V_w(BPh_4^-)$ = 187.0 and V_w (Ph_4As^+) = 193.5 are found or $\bar{V}°(H^+)$ = −6.5 cc/mol at 25°). Errors in the bond lengths l(C–B) and l(C–As), however, can cause a considerable error in $\bar{V}°(H^+)$ (*e.g.*, if l(C–As) = 1.98 Å[20] is used $V_w(Ph_4As^+)$ = 1.96.4 or $\bar{V}°(H^+)$ = −3.3, −4.4, and −5.7 cc/mol, respectively, at 0, 25, and 50°). Considering the uncertainty of the van der Waals radii of B and the length of the C–B bond these estimates agree fairly well with the other estimates made using the $\bar{V}°(Ph_4AsBPh_4)$. The average values (given in Table II) of $\bar{V}°(H^+)$ = −4.0, −5.0, and −6.6 cc/mol, respectively, at 0, 25, and 50° (av dev ±0.9 cc/mol) agree very well with the estimates made by other workers[1,3] and support the contention[1,3] that $\bar{V}°(H^+)$ is *ca.* −5.0 cc/mol at 25° in water. Since the electrolyte Ph_4AsBPh_4 is soluble in many organic solvents, the methods developed in this note may prove useful in estimating $\bar{V}°(H^+)$ in a wide range of solvent systems.

Table II: Estimates of the Partial Molal Volumes of the Proton in Water at 0, 25, and 50° (cc/mol)

Temp, °C	Method (1)[a] $\bar{V}°(H^+)$	Method (2)[b] $\bar{V}°(H^+)$	Method (3)[c] $\bar{V}°(H^+)$	Average $\bar{V}°(H^+)$
0.0	−3.0	−3.6	−5.5 (−3.3)	−3.9
25.0	−4.1	−4.9	−6.7 (−4.4)	−5.0
50.0	−5.4	−6.4	−8.1 (−5.7)	−6.4

[a] $\bar{V}°(Ph_4As^+)/\bar{V}°(BPh_4^-) = r_s(Ph_4As^+)^3 r_s(BPh_4^-)^3 = (4.70)^3/(4.62)^3$. [b] $\bar{V}°(Ph_4As^+) - \bar{V}°(BPh_4^-) = 2.52\,r(\text{–As–})^3 - 2.52r(\text{–B–})^3 = 2.52(1.81)^3 - 2.52(0.88)^3$. [c] $\bar{V}°(Ph_4As^+)/\bar{V}°(BPh_4^-) = V_w(Ph_4As^+)/V_w(BPh_4^-) = 193.2/186.9$ (=196.4/186.9 for values given in parentheses).

Acknowledgment. The author wishes to thank Dr. E. J. King for making his manuscript available prior to publication and for assisting in the calculations of the van der Waals volumes of Ph_4As^+ and BPh_4^-. This work was supported by the Office of Naval Research (NONR 4008-02) and the National Science Foundation (GA-17386).

(19) G. J. Palenik, *Acta Cryst.*, **23**, 85 (1967); J. G. Scane, *ibid.*, **20**, 471 (1966).

(20) "International Tables for X-Ray Crystallography," Vol. III, The Kynoch Press, Birmingham, England, 1962, p 275.

Complex Formation in Aluminum Iodide–Diethyl Ether Solutions

by Paul J. Ogren,* James P. Cannon, and C. F. Smith, Jr.

Department of Chemistry, Maryville College, Maryville, Tennessee 37801 *(Received August 24, 1970)*

Publication costs assisted by Maryville College

Solid complexes of the aluminum halides $AlCl_3$, $AlBr_3$, and AlI_3 with various ethers have been known for a number of years.[1] Complexes such as $AlCl_3 \cdot OEt_2$ and $AlBr_3 \cdot OEt_2$ are readily isolated by evaporation of excess solvent from diethyl ether solutions of the halides near room temperature.[2,3] The importance of etherate complexes in solution has been established by both chemical and physical evidence in many cases.[4–6] Nevertheless, recent interpretations of ^{27}Al nmr spectra have favored Al_2X_6 as the primary initial solute in diethyl ether and either Al_2X_6 or $AlX_3 \cdot OC_4H_8$ in tetrahydrofuran.[7,8] Changes in the ^{27}Al nmr spectra of $AlCl_3$ and $AlBr_3$ in diethyl ether over a period of a few weeks were thought to indicate slow etherate formation in the most recent work.

The studies reported here deal with the AlI_3–diethyl ether system, which has been less thoroughly investigated than the corresponding bromide and chloride systems. The results indicate that the major solute present in our observations is $AlI_3 \cdot OEt_2$. This is in line with the bulk of the previous evidence on the nature of such solutions but casts considerable doubt on the identifications which have been made on the basis of ^{27}Al nmr studies. With pure AlI_3 and diethyl ether, solutions are stable at room temperature for at least several hours, although a small amount of I_2 impurity catalyzes a slow decomposition of the ether.

Experimental Section

Preparations of aluminum iodide and its solutions were carried out *in vacuo* to avoid moisture and air contamination. Solvents were degassed and dried over P_2O_5. Following the reaction of I_2 with an excess of granular Al, white crystalline AlI_3 was isolated by dis-

(1) N. N. Greenwood and K. Wade in "Friedel-Crafts and Related Reactions," Vol. 1, G. A. Olah, Ed., Wiley-Interscience, New York, N. Y., 1963, Chapter 7, pp 572, 577, 580.

(2) (a) J. W. Walker and A. Spencer, *J. Chem. Soc.*, **85**, 1106 (1904); (b) G. B. Frankforter and E. A. Daniels, *J. Amer. Chem. Soc.*, **37**, 2560 (1915).

(3) W. A. Plotnikow, *Z. Anorg. Allg. Chem.*, **56**, 53 (1908).

(4) Reference 1, G. A. Olah, Chapter 4, pp 249–252.

(5) R. E. Van Dyke and H. E. Crawford, *J. Amer. Chem. Soc.*, **72**, 2829 (1950).

(6) D. G. Walker, *J. Phys. Chem.*, **65**, 1367 (1961).

(7) D. E. O'Reilly, *J. Chem. Phys.*, **32**, 1007 (1960).

(8) H. Haraguchi and S. Fujiwara, *J. Phys. Chem.*, **73**, 3467 (1969).

tillation in an apparatus which allowed solutions to be prepared without removing the products from the apparatus. Solution aliquots could then be removed for gas chromatographic analysis or sealed off in nmr tubes. Nmr spectra were determined within the first hour following sample preparation.

Ether analysis for the solid AlI_3–ether complex was performed by measuring the mass gained by a known amount of AlI_3 dissolved in ether and then dried by evaporation *in vacuo*. Iodine analysis was carried out using the Volhard technique. Aluminum analysis was performed using a standard EDTA technique.[9]

Results and Discussion

Isolation of Crystalline $AlI_3 \cdot OEt_2$. This complex was first reported by Domanizki.[10] In the present work, 1 to 3-g samples of AlI_3 were dissolved in ether near room temperature. The excess solvent was then pumped from the colorless solution over a period of 10 min to 3 hr. The best products were completely white; most samples had a faint yellow tinge which became stronger when exposed to traces of air (mp 54–57° in open capillary, hydroscopic).

Anal. Calcd for $AlI_3 \cdot OEt_2$: Al, 5.60; I, 79.0; $C_4H_{10}O$, 15.36. Found: Al, 5.49; I, 78.9; $C_4H_{10}O$, 15.46 (10 min evacuation) 15.26 (3 hr evacuation).

Chemical Evidence for $AlI_3 \cdot OEt_2$ in Ether Solution. We have studied reaction 1 near 25° in ethyl bromide and methyl iodide solvents using gas chromatographic techniques and have found that the reaction is complete by the time of our first measurements (*ca.* 5 min).

$$AlI_3 + 3CH_3CH_2Br \xrightarrow{EtBr,\ MeI} AlBr_3 + 3CH_3CH_2I \quad (1)$$

Similar observations have been made on related systems by Brown and Wallace.[11] In contrast to the rapid reaction in alkyl halide solutions, the addition of ethyl bromide to a solution of AlI_3 in diethyl ether produced no measurable formation of ethyl iodide in 12 hr at room temperature. This was also true for solutions produced by addition of ethyl bromide to solid $AlI_3 \cdot OEt_2$.

The rapid halogen exchange of ethyl bromide with AlI_3 in alkyl halide solutions is consistent with a normal reaction of an ethyl carbonium ion or near-ion with an Al–I bond in solution, catalyzed by formation of the $AlI_3 \cdot RX$ complex typical of Friedel–Crafts reactions. As with several other Friedel–Crafts systems,[4] the absence of reaction in ether indicates that all of the AlI_3 forms a strong etherate complex, resistant to exchange reactions involving displacement by ethyl bromide. Complex formation is probably very rapid and is certainly complete within 10 min, the time between formation of the ether solution and the addition of the bromide.

Proton Nmr Spectra of $AlI_3 \cdot OEt_2$ in CCl_4 and Ether. It is to be expected that the nmr resonances of complexed ether protons would be shifted downfield relative to the solvent protons as a result of the electron-withdrawing Lewis acid.[12] To study this, nmr spectra were obtained for the solutions made up as indicated in Table I. Comparison of the methylene and methyl proton absorptions from $AlI_3 \cdot OEt_2$ dissolved in CCl_4 with the well-known absorption positions for diethyl ether clearly reveals the expected downfield shift. To minimize the number of components, no TMS reference was added to three of the ether solutions; instead, the center line of the solvent methyl quartet was used as a reference lock. Since there was a slight dependence of the relative positions of δ_{CH_3} and δ_{CH_2} on the lock used, values reported in each column are consistently based on only one lock system.

Table I: Chemical Shifts of Ether Protons in Solutions Containing AlI_3

Solution composition	δ_{CH_3}[a]	δ_{CH_2}[a]	$\delta_{CH_3} - \delta_{CH_2}$[b]
7 mol % diethyl ether in CCl_4	1.14	3.36	
Diethyl ether			2.27
1 mol % $AlI_3 \cdot OEt_2$[c] in ether			2.28
14 mol % $AlI_3 \cdot OEt_2$[c] in ether			2.39
6 mol % $AlI_3 \cdot OEt_2$ in CCl_4	1.63	4.64	3.03

[a] TMS reference lock. [b] Reference lock on central CH_3 line. [c] Calculated from mass of AlI_3 dissolved in ether.

Only one group of methylene protons was observed for the AlI_3–ether solutions, even at high sensitivity. For the last four solutions it can be seen that the changes in the positions of the methylene protons relative to the methyl protons ($\delta_{CH_3} - \delta_{CH_2}$) are nearly proportional to the $(AlI_3 \cdot OEt_2)/(\text{total ether})$ ratios calculated for the solutions. The results strongly suggest that $AlI_3 \cdot OEt_2$ is the primary species present in diethyl ether at these concentrations and that the solvent ether molecules undergo rapid exchange with the complexed molecules.

In the similar chloride and bromide systems involving dimethyl ether, evidence has been obtained for solution complexes of the type $AlX_3 \cdot (OMe_2)_2$ and $(AlX_3)_2 \cdot OMe_2$ as well as the 1:1 complexes.[5,6] The magnitudes of the nmr shifts given in Table I are readily understood as-

(9) H. Flaschka and H. Abdine, *Z. Anal. Chem.*, **152**, 77 (1956).

(10) N. Domanizki, *J. Russ. Ges. (Chem.)*, **46**, 1079 (1914); *Chem. Zentralbl.*, 982 (1915).

(11) H. C. Brown and W. J. Wallace, *J. Amer. Chem. Soc.*, **75**, 6279 (1953).

(12) D. E. McLaughlin, M. Tamres, and S. Searles, Jr., *ibid.*, **82**, 5621 (1960).

suming the presence of $AlI_3 \cdot OEt_2$ and rapid exchange. Although other complexes cannot be completely ruled out on this basis, their importance would require further rationalizations of the nmr data. A small amount of $AlI_3 \cdot (OEt_2)_2$ might be an important intermediate in the rapid ether exchange.

This work shows that complexed aluminum iodide is the important initial solute species in diethyl ether. The similar observations for $AlBr_3$ and $AlCl_3$[4-6] indicate that etherate complexes are formed in solution near room temperature in all these cases. Assignment of ^{27}Al nmr spectra in such systems to Al_2X_6 has been based primarily on line width considerations.[7,8] Reassignment of these spectra to $AlX_3 \cdot OEt_2$ is required in the case of aluminum iodide and may well be warranted for other ether–halide systems not examined in the present work.

The stability of $AlI_3 \cdot OEt_2$ solutions depends on several factors. Samples prepared in the present work were water-white and apparently stable for at least 12 hr *in vacuo* at room temperature. Both solutions and solid slowly decompose in air, first turning yellow, then brown. The presence of I_2 impurity catalyzes a slow ether cleavage in this system, leading to an observed ethyl iodide product.[13] Rapid thermal cleavages leading to mixed aluminum halide–alkoxides have been reported for several systems at elevated temperatures[14] and could be assisted by the heat released during complex formation if mixtures were not cooled. Some of these processes may account for the slow changes at room temperature observed by ^{27}Al nmr in some of these systems.

Acknowledgment. We wish to thank Research Corporation for support of this work through the Cotrell grant program. We also wish to acknowledge both the work of Dan Quarles, Maryville College, on some of the initial phases of this study, and the generous assistance of Mr. William Peed of the University of Tennessee at Knoxville in obtaining the nmr data.

(13) P. J. Ogren and J. P. Cannon, in progress.

(14) See reference 1, Vol. 4, Chapter 47.

Chemical HF Lasers from NF_3–H_2 and NF_3–C_2H_6 Systems

by M. C. Lin

Chemical Spectroscopy Section, Naval Research Laboratory, Washington, D. C. 20390 *(Received August 25, 1970)*

Publication costs assisted by the Naval Research Laboratory

Chemical HF lasers based on the elementary reaction

$$F + H_2 \longrightarrow HF^{\dagger} + H \quad (\Delta H_1^{\circ} = -32 \text{ kcal/mol}) \quad (1)$$

have recently been produced from the flash photolysis or pulsed electrical discharge of various fluorine-containing compounds in the presence of H_2.[1-5] Laser action initiated at high temperatures by shock waves has also been reported;[6] and, most recently, continuous-wave (cw) emission resulted from a very rapid mixing of F atoms produced either from the dissociation of SF_6 with a high-current density arc[7] or from the dissociation of F_2 initiated by an rf discharge or by the reaction of NO.[8]

In this note, we report the results of a chemical HF laser obtained from a repetitive pulsed electrical discharge of the mixtures of $NF_3 + H_2$ or $NF_3 + C_2H_6$. Six vibrational–rotational transitions from $\Delta v = 2 \rightarrow 1$ were observed in the former system and a total of ten lines, with six from $2 \rightarrow 1$ and four from $1 \rightarrow 0$ transitions, were identified in the latter. At the inception of this work, it was learned that the flash photolysis of $NF_3 + H_2$ mixtures did not lead to laser action, whereas initiation by a high-energy electron beam of 1.2 MeV led to a single line oscillation at P_{21}.[3,9]

The experimental setup was similar to the one described previously.[10] The reaction tube consisted of an 80 cm long, 12-mm i.d. Pyrex tube maintained at room temperature. The emission was analyzed with a 50-cm Model 305-SMP grating monochromator and detected with a Ge–Au cell operating at 77°K. Electrical pulses were produced by switching two 0.01-μF capacitors connected in parallel through a spark gap. The maximum repetition rate was 2.5 pulses/sec. The peak voltage employed was ~25 kV and the pulse width at half maximum was ~2 μsec.

I. NF_3–H_2 System. The results obtained from the NF_3–H_2 system are given in Table I. The observed frequencies are listed together with the calculated values[11] for comparison. As mentioned before, oscillation in this system took place exclusively on $2 \rightarrow 1$ transitions, which always prevailed in the chemical laser

(1) J. H. Parker and G. C. Pimentel, *J. Chem. Phys.*, **48**, 5273 (1968), and their previous work cited therein.

(2) R. W. F. Gross, N. Cohen, and T. A. Jacobs, *ibid.*, **48**, 3821 (1968).

(3) N. G. Basov, L. V. Kulakov, E. P. Markin, A. I. Nikitin, and A. N. Oraevskii, *JETP Letters*, **9**, 375 (1969).

(4) P. Gensel, K. L. Kompa, and J. Wanner, *Chem. Phys. Lett*, **5**, 179 (1970).

(5) T. F. Deutsch, *Appl. Phys. Lett.* **10**, 234 (1967).

(6) R. W. F. Gross, R. R. Giedt, and T. A. Jacobs, *J. Chem. Phys.*, **51**, 1250 (1969); J. R. Airey and S. F. McKay, *Appl. Phys. Lett.*, **15**, 401 (1969).

(7) D. J. Spencer, H. Mirels, and T. A. Jacobs, *ibid.*, **16**, 384 (1970); M. A. Kwok, R. R. Giedt, and R. W. F. Gross, *ibid.*, **16**, 386 (1970).

(8) T. A. Cool. T. J. Folk, and R. R. Stevens, *ibid.*, **15**, 318 (1969); T. A. Cool and R. R. Stevens, *J. Chem. Phys.*, **51**, 5175 (1969).

(9) D. W. Gregg, *et al.*, private communication through Professor S. H. Bauer.

(10) M. C. Lin and S. H. Bauer, *Chem. Phys. Lett.*, **7**, 223 (1970); M. C. Lin, *ibid.*, **7**, 209 (1970).

(11) P. A. Kittle and D. W. Placzek, Technical Report S-139, Rohm and Haas Company, Redstone Research Laboratories, 1967.

Table I: Observed HF Chemical Laser Lines from the NF_3–H_2 System

Transition	Frequency, cm^{-1} Obsd[a]	Frequency, cm^{-1} Calcd[b]	Relative intensity (I_{max})
$\Delta v = 2 \rightarrow 1$			
$P(4)$	3622.0	3622.6	1.5
$P(5)$	3576.8	3577.5	4.5
$P(6)$	3530.3	3531.2	7.0
$P(7)$	3482.7	3483.7	7.0
$P(8)$	3435.0	3435.0	5.0
$P(9)$	3384.8	3385.3	1.5

[a] Slit width used was 0.25 mm. [b] Calculated by Kittle and Placzek.[11]

emission produced from reaction 1. The absence of transitions with $v > 3$ probably indicates that reaction 2

$$H + NF_3 \longrightarrow HF^{\dagger} + NF_2 \qquad (\Delta H_2^{\circ} = -77 \text{ kcal/mol}) \quad (2)$$

does not produce HF with partial population inversion. A similar abstraction reaction, $H + UF_6 \rightarrow HF + UF_5$ ($\Delta H^{\circ} \approx -46$ kcal/mol), was also believed to be unimportant,[1] although $H + IF_5 \rightarrow HF + IF_4$ ($\Delta H^{\circ} \approx -70$ kcal/mol) was shown to be operative in laser emission.[4]

Under the present conditions, the optimum pressure of NF_3 was found to be $P_{NF_3} \simeq 0.3 \pm 0.1$ Torr. The pulse repetition rate depended rather strongly on the partial pressure of NF_3; however, it varied only slightly with H_2 or He pressure. The effects of H_2 and He on the total emission intensity are shown in Figure 1. It is seen to be extremely sensitive to He, which, however, has an opposite effect on the emission from the NF_3–C_2H_6 system, as will be discussed later. With $P_{NF_3} = 0.20$ Torr, the threshold pressure of H_2 is about 1.1 Torr and the optimum output occurs at $P_{H_2} \simeq 1.6$ Torr, in the absence of He. The decrease in output at higher H_2 pressure, *i.e.*, $P_{H_2} > 1.6$ Torr, can be readily accounted for by the deactivation of a vibrationally excited HF by H_2 *via* the V–V transfer process

$$HF(v) + H_2(0) \longrightarrow HF(v-1) + H_2(1) \qquad (\Delta E \approx 380 \text{ cm}^{-1}) \quad (3)$$

Reaction 3 is expected to take place with a faster rate for lower v values. This might account, at least partly, for the absence of $1 \rightarrow 0$ transition in the NF_3–H_2 system under our present conditions. This argument is further supported by the fact that addition of H_2 tends to eliminate the $1 \rightarrow 0$ transitions of HF produced in a transverse electrical pulsed discharge of freons.[12]

II. NF_3–C_2H_6 System. The reaction of F atoms with various hydrocarbons has been investigated by Parker and Pimentel.[1] In their work, no significant

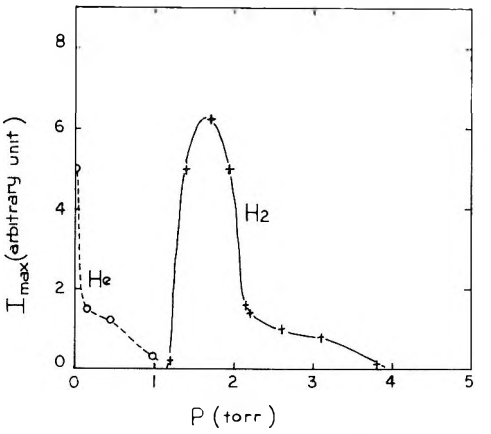

Figure 1. The effects of H_2 and He on the total HF laser intensity: ○, $P_{NF_3} = 0.20$ Torr, $P_{H_2} = 2.10$ Torr; +, $P_{NF_3} = 0.20$ Torr; $P_{He} = 0$.

difference was observed between the reaction of F with H_2, CH_4, C_2H_6, and C_3H_8. In this study, ethane was selected because of its immediate availability. The results obtained from this system are listed in Table II.

Table II: Observed HF Chemical Laser Lines from the NF_3–C_2H_6 System

Transition	Frequency, cm^{-1} Obsd[a]	Frequency, cm^{-1} Calcd[b]
$\Delta v = 2 \rightarrow 1$		
$P(4)$–$P(9)$	See Table I	
$\Delta v = 1 \rightarrow 0$		
$P(7)$	3643.9	3644.3
$P(8)$	3593.8	3593.8
$P(9)$	3542.1	3542.3
$P(10)$	3489.5	3489.6

[a] The intensities of the $1 \rightarrow 0$ transitions were about 3 times as strong as those of the $2 \rightarrow 1$ transitions. [b] Calculated by Kittle and Placzek.[11]

A total of ten lines were identified, six $2 \rightarrow 1$ and four $1 \rightarrow 0$ transitions. Each line in the latter transitions was found to be about 3 times as strong as the former. The significant difference between H_2 and a hydrocarbon molecule has not been previously reported. It may be attributed to a molecular dynamical effect that can be best studied by a low-pressure chemiluminescence or molecular beam experiment. The reaction of atomic fluorine with C_2H_6

$$F + C_2H_6 \longrightarrow HF^{\dagger} + C_2H_5 \qquad (\Delta H_4^{\circ} = -38 \text{ kcal/mol}) \quad (4)$$

is 6 kcal/mol more exothermic than reaction 1. The ethyl radical produced above can undergo the following reactions.

(12) M. C. Lin and W. H. Green, *J. Chem. Phys.*, **53**, 3383 (1970).

$$C_2H_5 + NF_3 \longrightarrow C_2H_5F + NF_2 \quad (\Delta H_5^\circ = -48 \text{ kcal/mol}) \quad (5)$$

$$C_2H_5 + NF_2 \longrightarrow C_2H_5NF_2^\dagger \longrightarrow 2HF^\dagger + CH_3CN \quad (\Delta H_6^\circ = -148 \text{ kcal/mol}) \quad (6)$$

$$C_2H_5 + F \longrightarrow C_2H_5F^\dagger \longrightarrow HF^\dagger + C_2H_4 \quad (\Delta H_7^\circ = -97 \text{ kcal/mol}) \quad (7)$$

Reaction 5 cannot produce HF, since its exothermicity is lower than the energy barrier of HF elimination from C_2H_5F. Nevertheless, it may be a very efficient path for removing the C_2H_5 radical formed from reaction 4. Reactions 6 and 7 have the potential of providing vibrationally excited HF; however, their importance in comparison with reaction 4 cannot be determined in the present work. Further study, using N_2F_4 as a fluorine source in a flash tube, is underway.

The pressure effects of C_2H_6 and He are plotted in Figure 2. He markedly enhances the total emission intensity, in contrast to its negative effect on the NF_3–H_2 system. It is interesting to note that the introduction of a small amount of He eliminated completely the

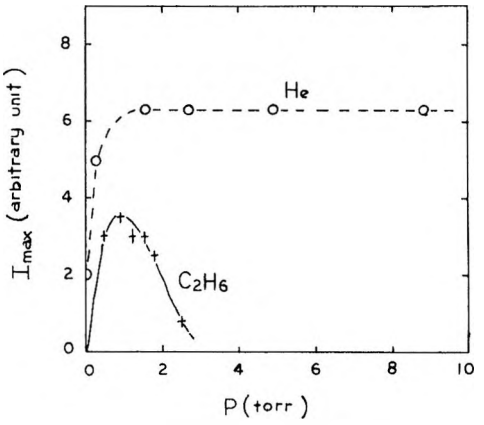

Figure 2. The effect of C_2H_6 and He on the total HF laser intensity: ○, P_{NF_3} = 0.20 Torr, $P_{C_2H_6}$ = 2.00 Torr; +, P_{NF_3} = 0.20 Torr, P_{He} = 0.

1 → 0 transitions, although the overall laser output was increased by a factor of 3 as shown in Figure 2. No transitions additional to those six P_{21} lines listed in Table II were observed when He was added. It is to be noted that, in an electrical discharge system, inert gases cannot only transfer the vibrational and rotational energies from the lasing molecules but also change the characteristics of discharge. Accordingly, it is more difficult to interpret the observed effects. In a flash-photolytic study of the UF_6–H_2 system, Kompa, *et al.*,[13] have investigated the effects of some gases (SF_6, C_2F_6, and He), which were found, mainly, to moderate the temperature rise and reduce the number of transitions observed.

The presence of the strong 1 → 0 transitions in the NF_3–C_2H_6 system offers a promising future application: the direct excitation of HF molecules from the ground state for vibrational energy transfer studies, especially in view of the fact that a very simple method of producing a short high-power chemical laser pulse is available.[12]

Acknowledgment. This work was sponsored by the Advanced Research Projects Agency, ARPA Order No. 660, and by ONR under contracts RO-001-01 and RR-002-09-41; it is gratefully acknowledged. The author also thanks Drs. S. H. Bauer and G. Wolga for the use of their equipment.

(13) K. L. Kompa, J. H. Parker, and G. C. Pimentel, *J. Chem. Phys.*, 49, 4257 (1968).

New Absorption Bands in Solutions of Alkali Metals in Amines

by G. Gabor and K. Bar-Eli*

Institute of Chemistry, Tel-Aviv University, Tel-Aviv, Israel
(Received April 6, 1970)

Publication costs borne completely by The Journal of Physical Chemistry

Optical absorption spectra of solutions of potassium in mixtures of methyl- and ethylamines have been studied extensively.[1-3]

It was shown that they have essentially two absorption bands: in the visible region (V band), λ_{max} 890 nm, and in the near-ir region (ir band), λ_{max} 1400–1600 nm. These results are obtained provided one is careful to work in quartz vessels to avoid sodium contamination, which causes the appearance of absorption at 680 nm.[4]

The ratio ir/V increases with the methylamine fraction of the mixture. On cooling a relatively dilute solution (OD_V (+20°) < 1.5), one observes two effects. (a) One effect is a blue shift of the V peak maxima of $\simeq -10$ cm^{-1}/deg.[2,5,6] As seen in Figure 1, this shift depends on the molar ratio of the solvents, being −8.3, −10, and −11.9 cm^{-1}/deg for X_{me} = 0.0, 0.509, and 1.0, respectively. [X_{me} and X_{et} denote molar fractions of methylamine and ethylamine, respectively, in a mixture of these solvents.] These results are in complete

(1) H. Blades and J. W. Hodgins, *Can. J. Chem.*, 33, 411 (1955).

(2) M. Ottolenhi, K. Bar-Eli, and H. Linschitz, *J. Chem. Phys.*, 43, 206 (1965).

(3) J. L. Dye and R. R. Dewald, *J. Phys. Chem.*, 68, 135 (1964).

(4) I. Hurley, T. R. Tuttle, Jr., and S. Golden, *J. Chem. Phys.*, 48, 2818 (1968).

(5) M. Ottolenghi, K. Bar-Eli, H. Linschitz, and T. R. Tuttle, Jr., *ibid.*, 40, 3729 (1964).

(6) S. Matalon, S. Golden, and M. Ottlenghi, *J. Phys. Chem.*, 73, 3098 (1969).

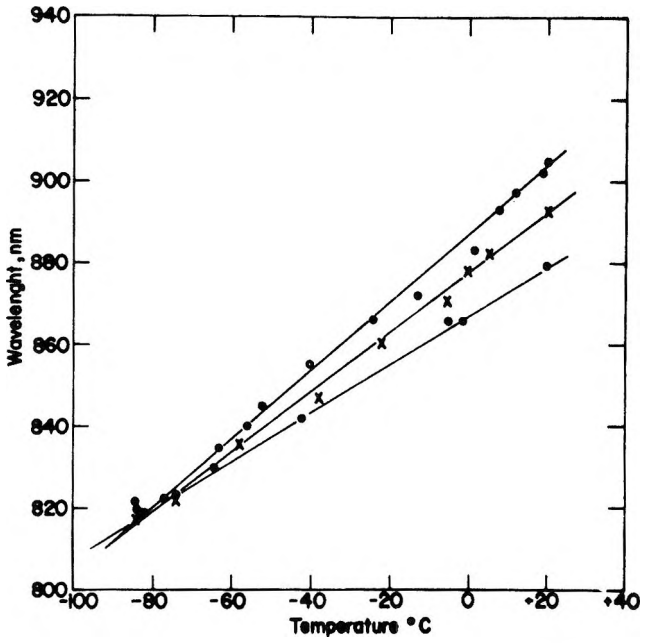

Figure 1. λ_{max} at different temperatures in dilute solutions of potassium in ethylamine–methylamine mixtures: O, X_{me} = 1.0; ×, X_{me} = 0.509; ●, X_{me} = 0.0.

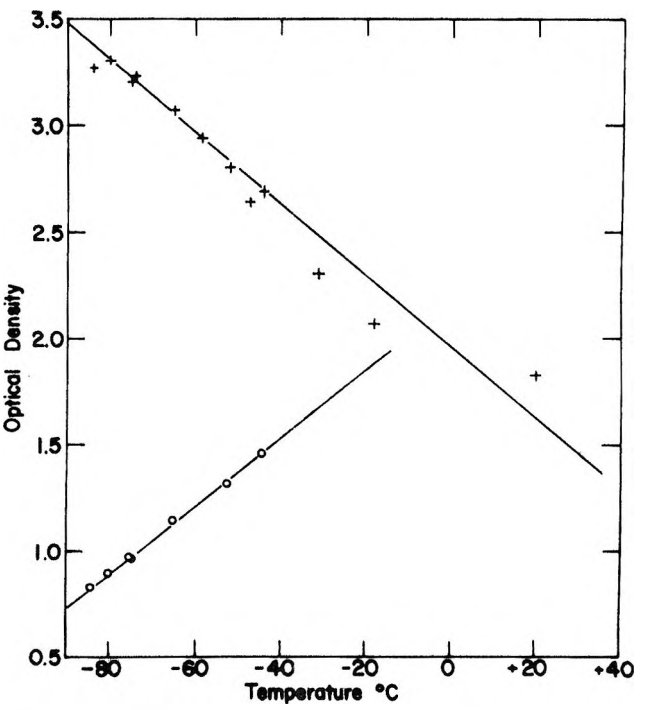

Figure 2. OD at λ_{max} of the V band (+) and of the ir band (O) of a dilute solution of potassium in methylamine.

agreement with the results of Matalon, *et al.*,[6] where the blue shift of the V band was measured in solutions of sodium in ethylamine–ammonia mixtures. (b) The other effect is an increase of the V band and a simultaneous decrease of the ir band. However, on cooling a more concentrated solution (OD_V (+20°) $\simeq$ 3.5), we observe an entirely different behavior of the spectrum. The V band is split, and as a result two new bands appear with maxima at 770 ± 5 and 870 ± 5 nm. At the same time the maximum absorption of the V band decreases slightly, in contrast to the more dilute solution, having the same composition of solvents, as described above (Figure 2). On adding potassium chloride to the solution, we notice the same phenomena; however, the splitting occurs at higher temperature (room temperature as compared to −50°) or lower concentration (OD_V (+20°) $\approx$ 2.0).

The three bands decay thermally at completely different rates, *e.g.*, the V band decays at room temperature at least an order of magnitude slower than the two new bands. (This is probably the reason that these bands were not observed previously.) We conclude, therefore, that the three bands are associated with three different species.

All the bands are red shifted with temperature increase, the 770-nm peak to 795 nm and the 870-nm peak to 950 nm on warming from −80 to +20°. Thus the V band is located between the newly observed bands in the entire temperature range investigated (+20 to −80°).

In pure ethylamine solutions, no splitting was observed because one cannot reach the necessary concentration of potassium (maximum absorbancy achieved $\simeq$1.0). In pure methylamine, no splitting was observed in a 1-cm cell; only broadening of the band was noticed, probably because the potassium concentration is too low. However, when a 0.1-cm cell was used at the same optical density, *i.e.*, at concentration ten times higher, the same splitting was observed as shown in Figure 3, even at room temperature. The splitting, however, occurred in mixtures having as low as 0.02 molar fraction of ethylamine. Solutions of rubidium also show this phenomenon. Dilute solutions in ethylamine show the V band at 940 nm at room temperature. This band is blue shifted on cooling; it appears at 855 nm at −80°. In methylamine at room temperature, the peak is shifted to larger wavelengths, similar to what is seen in Figure 1 in the case of potassium. When the solutions are more concentrated, and this can be easily achieved in rubidium even in pure ethylamine, the peak is split: one peak at 785 nm and the other at 935 nm at −53° (Figure 4). On cooling the short wavelength peak increases while the longer wavelength peak decreases similarly to potassium solutions (Figure 3).

Considering the concentration and the temperature dependence, as well as the effect of the addition of potassium positive ion (M^+) on the splitting, the assignment of at least one of the new bands obtained to a dimeric species is reasonable. Dimer (or aggregate) formation on cooling is a well-known phenomenon in solutions of dyes,[7-9] and their existence was postulated

(7) F. Leterrier and P. Douzou, *Photochem. Photobiol.*, **8**, 369 (1968).
(8) G. Gabor, Y. F. Frei, and E. Fisher, *J. Phys. Chem.*, **72**, 3266 (1968).

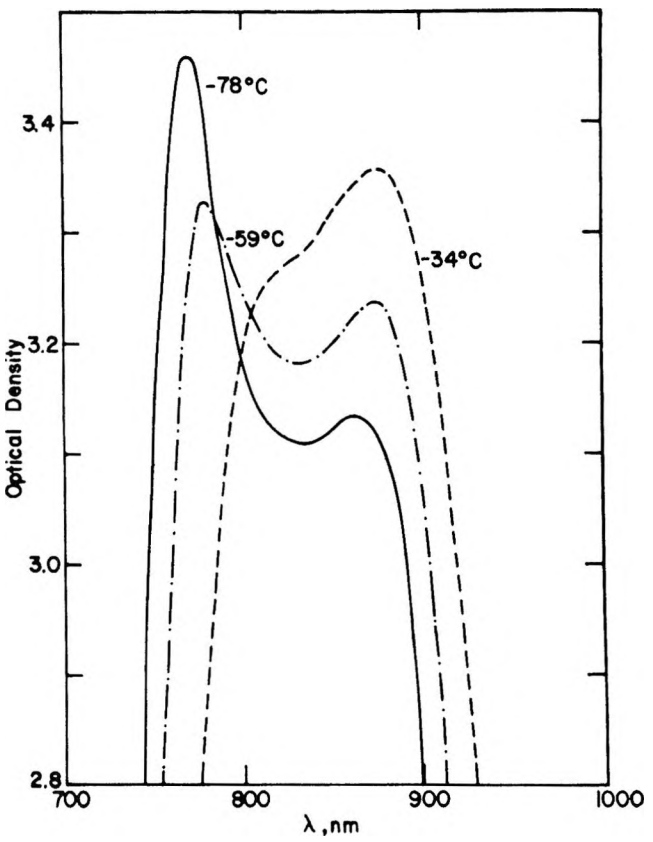

Figure 3. Splitting of the V band at different temperatures in a concentrated solution of potassium in ethylamine–methylamine mixture; X_{me}, 0.365.

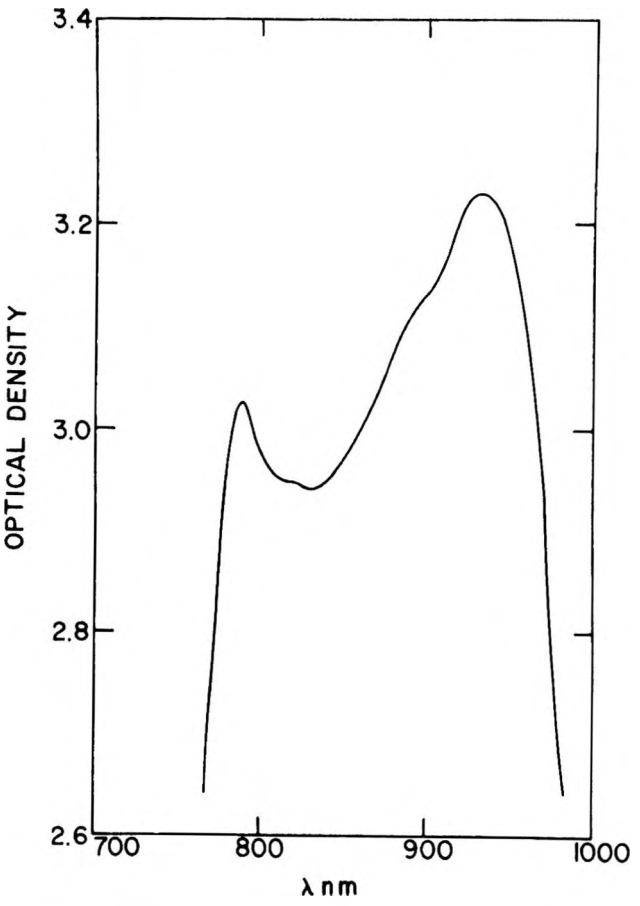

Figure 4. Spectrum of the split V band in solution of rubidium in pure ethylamine at −53°.

in most models of alkali metal–amine solutions.[10] Another conclusion is drawn from the fact that very small quantities of ethylamine (X_{et} = 0.02) are needed to produce splitting on cooling. This implies that production of these new species may be facilitated by preferential solvation[11] by ethylamine as compared to methylamine. A similar interpretation involving preferential solvation was given by Dalton, *et al.*,[12] for the dependence of the hfs of the esr spectra on the solvent composition in potassium–ethylamine–ammonia solutions. Since ethylamine has a lower dielectric constant than methylamine,[13] it is reasonable to assume that the species which are preferentially solvated by it are not charged. Therefore, both species represented by the newly found peaks, namely the 770 and 870 nm for potassium and 785 and 935 nm for rubidium, are probably not charged.

The V band was recently assigned to M^- in solution of sodium in ethylamine–ammonia mixtures.[6] The assignment is based on the theory of Stein, *et al.*,[14] for the temperature dependence of negative ion bands in solutions; the assignment is confirmed by the temperature dependence of the peak (λ_{max}) of the V band of potassium solutions described above. Similar results were obtained in other alkali metal–amine solutions and will be described more fully elsewhere.[15] Analysis of the kinetic data, obtained by laser photolysis[16] of sodium in ethylenediamine and propylenediamine solutions, yields further confirmation to this assignment. The ir band is usually associated with absorption of the solvated electron.[1-3]

We suggest, therefore, that the newly discovered bands at 770 and 870 nm for potassium and 785 and 935 nm for rubidium should be assigned to the dimer M_2 and the monomer M, respectively, for the following reasons. (a) Both fulfill the condition of being noncharged species. (b) Addition of the cation (M^+) facilitates

(9) E. Rabinowitch and L. F. Epstein, *J. Amer. Chem. Soc.*, **63**, 69 (1941).

(10) (a) E. Becker, R. H. Lindquist, and B. J. Adler, *J. Chem. Phys.*, **25**, 971 (1956); (b) S. Golden, C. Guttman, and T. R. Tuttle, Jr., *ibid.*, **44**, 3791 (1966); (c) E. Arnold and A. Patterson, Jr., *ibid.*, **41**, 3089, 3098 (1964).

(11) S. Arai and M. C. Sauer, Jr., *ibid.*, **44**, 2297 (1966).

(12) L. R. Dalton, J. D. Rynbrandt, E. M. Hansen, and J. L. Dye, *ibid.*, **44**, 3969 (1966).

(13) "Table of Dielectric Constants of Pure Liquids," National Bureau of Standards Circular 514, U. S. Government Printing Office, Washington, D. C., 1951.

(14) G. Stein and A. Treinin, *Trans. Faraday Soc.*, **55**, 1086, 1091 (1959).

(15) K. Bar-Eli and G. Gabor, to be published.

(16) D. Huppert and K. Bar-Eli, *J. Phys. Chem.*, **74**, 3285 (1970).

splitting (production of the new bands) *via* reactions $M^+ + e \rightleftarrows M$, $M + M \rightleftarrows M_2$, and $M^+ + M^- \rightleftarrows M_2$, thus causing the observed decrease of the ir band. (c) Cooling increases relatively the short wavelength peak, and therefore it is reasonable to associate it with the dimeric form.

These assignments contradict the expectation that M should absorb at somewhat higher energy than M^- and M_2 at lower energy than M as observed in the gas phase.[17,18]

With the above assignments and the fact that the positive ions are always present in excess, we can estimate, from the data of Figure 2, the free energy of the reaction $M^-(V) \rightleftarrows M^+ + 2e$ (ir) to be 2.8 kcal/mol. In a similar manner, we estimate from the data of Figure 3 the free energy of the reaction $2M(870) \rightleftarrows M_2(770)$ to be 1–2 kcal/mol. These estimates are for potassium. Values for rubidium will be given elsewhere.

Experimental Section

All spectroscopic measurements were carried out by a Cary 14 spectrophotometer in 1- and 0.1-cm cells. The cells were located in a quartz dewar flask, equipped with optical windows. The dewar was cooled by dry nitrogen as described earlier.[2] The reference compartment contained pure solvent (in an appropriate cell). As the cell in the reference compartment was not cooled, the base line was taken in the whole temperature range +20 to −80°, in which the experiments were then performed and in case the solvent absorbed the spectra were corrected accordingly. As the new peaks were observed at high absorbancies the accuracy, resolution, and reproducibility of the Cary 14 were checked as follows. (1) All spectra were run in the 0.0–1.0 OD region of the instrument. Appropriate neutral density filters (NDF) were used in the reference compartment. All NDF were calibrated. (2) A recording of NDF's of total OD = 3.3 (against 2.8 as reference; *i.e.*, the actual OD measured was 0.5) yielded a straight line confirming that the optical density does not change with wavelength. (3) The spectrum of a dilute solution (OD $\simeq$ 0.9) of potassium in a mixture of ethylamine and methylamine was recorded at room temperature. A single peak with a λ_{max} at 895 nm was observed. On addition of NDF of OD = 2.8 to the solution and to the reference cell the shape of the absorption band was reproduced although the total OD measured was 3.7. (4) Measurement of potassium permanganate is reproduced under these conditions. (5) Neocyanine-[1,1′-diethyl-11-(4-quinolyl ethiodide)-4,4′-dicarbocyanine iodide] has an absorption band in the same region as our potassium–amine solutions. A dilute solution of neocyanine in methanol has a peak at 770 nm and a shoulder at 710 nm independent of the absorbancy of the solution, *i.e.*, at OD $\simeq$ 0.35 in a 1-cm cell and at OD $\simeq$ 3.5 in a 10-cm cell. (6) To ascertain temperature measurements all spectra were recorded after the cell had been kept at least 10 min at a certain temperature. After another 10 min the spectra were rerun. No changes were observed. (7) After observing the splitting, *i.e.*, the new bands at 770 and 870 nm at −85°, at which temperature the 770-nm peak is dominant, the solution was heated to −50° at which temperature the absorbancy at 870 nm increases while the 770-nm peak decreases; the solution was repeatedly cooled and heated. The 770 $\rightleftarrows$ 870 interconversion is completely reversible; *i.e.*, the relative absorbancies of these peaks depend solely in the measured temperature. (8) To prevent photochemical production of any species absorbing in the 700–1000-nm region from the decay products that absorb below 450 nm a Corning filter No. 3385 was used cut off at 460 nm. In the absence of this filter the V band is produced by the strong light of the ir lamp.[19] (9) To prove that no photochemical reactions occur in these concentrated solutions the spectrum of a solution at −85° was reproduced after 15-min illumination (by the ir lamp), as well as after 15-min darkness.

Acknowledgment. It is a pleasure to acknowledge the technical assistance of Mr. Y. Lavie.

(17) G. Herzberg, "Atomic Spectra and Atomic Structure," Dover Publications, New York, N. Y., 1944, p 72.

(18) G. Herzberg, "Molecular Spectra and Molecular Structure I. Spectra of Diatomic Molecules," Van Nostrand, Princeton, N. J., 1950, p 544.

(19) M. Ottolenghi and H. Linschitz, "Solvated Electron," E. S. Hart, Ed., Advances in Chemistry Series, No. 50, American Chemical Society, Washington, D. C., 1965.

COMMUNICATIONS TO THE EDITOR

The Identity of the Free Radical in Solutions of $\Delta^{10,10'}$-Bianthrone[1]

Publication costs assisted by the Union Carbide Corporation

Sir: Kortüm and Koch[2] have shown that the thermochromism and paramagnetism of solutions of bianthrone (I) are independent phenomena and that no esr

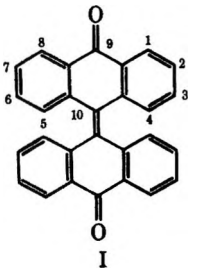

I

is observed for the green form of I in the absence of light. Recently, Agranat, *et al.*,[3] published the results of their esr investigations of the thermochromism of I and concluded that the esr was due to a phenoxy radical produced by an irreversible photochemical reaction. We had also measured the esr of I in a variety of solvents and had independently arrived at the same conclusions. We were led to propose the phenoxy radical (II) for the paramagnetic species.

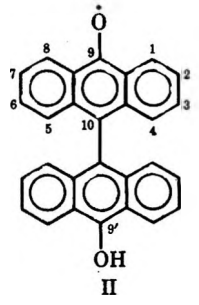

II

The coupling constants for II determined in biphenyl solvent at 90° were as follows: 2H, 3.38 ± 0.01 G; 2H, 3.04 ± 0.01 G; 2H, 1.03 ± 0.01 G; 2H, 0.80 ± 0.01 G. These values differ slightly from those reported by Agranat, *et al.*[3,4] The g value of II was determined to be 2.00338 ± 0.00002 at 90°.

We have also observed well resolved esr spectra for the 2,2′-dimethyl and 2,2′-dibromo derivatives of I. The results confirm that the 2 position is a site of high spin density. No comparable esr was seen for the 4,4′-dimethylbianthrone which is not thermochromic.

We have now obtained direct evidence for the identity of II by preparing a structurally related aryloxy radical from the oxidation of bianthryl (III). After treatment with O_2 at 275°, a solution of III in *o*-terphenyl turned

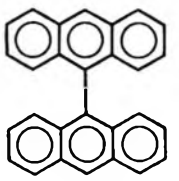

III

pale yellow and showed an esr signal consisting of approximately 100 lines 0.12 G wide. The spectrum was reduced to the following coupling constants: 2H, 3.42 ± 0.01 G; 2H, 3.06 ± 0.01 G; 2H, 1.03 ± 0.01 G; 2H, 0.82 ± 0.01 G; 1H, 0.19 ± 0.01 G. The g value for the radical was 2.00338 ± 0.00002.

Since the oxidation of anthracene has been shown to lead to the anthryloxy radical,[5] we can assign the structure IV to the radical resulting from the oxidation of

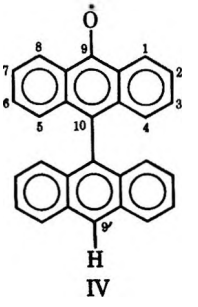

IV

III. The aryloxy radical (IV) forms by the substitution of oxygen at the most reactive ring position of III.

The similarity of coupling constants and g values for the two radicals II and IV is remarkable. The only difference between the spectra of these two radicals is the presence of an additional single small proton splitting in the spectrum of IV. This splitting is tentatively assigned to the proton at the active 9′ position of IV and arises from the slight conjugation between the two anthryl ring systems. The proton of the OH group at the 9′ position in II produces no observable splitting.

(1) Supported in part by the U. S. Army Research Office, Durham.

(2) G. Kortüm and K. W. Koch, *Chem. Ber.*, **100**, 1515 (1967).

(3) I. Agranat, M. Rabinovitz, G. R. Luckhurst, and J. N. Ockwell, *J. Chem. Soc. B*, 294 (1970).

(4) Slightly different coupling constants were obtained for solutions of (I) in α-methylnaphthalene. These were determined from an average of 14 measurements by T. Richerzhagen and G. Vincow, relative to the tetracene cation [J. S. Hyde, *J. Chem. Phys.*, **43**, 1806 (1965)] as: 2H, 3.36 ± 0.01 G; 2H, 3.01 ± 0.02 G; 2H, 1.00 ± 0.01 G; 2H, 0.76 ± 0.01 G.

(5) T. Yoshida, Y. Veno, and S. Wakabayashi, *Kogyo Kagaku Zasshi*, **72**, 338 (1969).

By computer simulation it was shown that an additional single proton splitting of 0.15 G or greater would have been observable in the spectrum of II.

In summary, we conclude that the paramagnetic species detected in solutions of $\Delta^{10,10'}$-bianthrone is the 10,10′-bi-9-anthranoxy radical II. This radical is an expected intermediate in the photochemical conversion of bianthrone to bianthranol, helianthrone, and meso-naphthobianthrone,[6] or alternatively, could form through an oxidation–reduction reaction between bianthrone and bianthranol.

Acknowledgments. We wish to thank Dr. Thomas Harris, who performed some of the initial experiments in this study, and Mrs. S. B. Wallon for the synthesis of 9,9′-bianthryl.

(6) H. Brockmann and R. Mühlmann, *Chem. Ber.*, **82**, 348 (1949).
(7) Alfred P. Sloan Research Fellow.

UNION CARBIDE CORPORATION
CARBON PRODUCTS DIVISION
CLEVELAND, OHIO 44101
L. S. SINGER*
I. C. LEWIS

DEPARTMENT OF CHEMISTRY
UNIVERSITY OF WASHINGTON
SEATTLE, WASHINGTON 98105
T. RICHERZHAGEN
G. VINCOW[7]

RECEIVED SEPTEMBER 14, 1970

Ion Pairing in 2:2 Electrolytes

Publication costs borne completely by The Journal of Physical Chemistry

Sir: In a recent paper Masterton and Brierly[1] reported conductivity measurements on dilute aqueous solutions of $[Co(NH_3)_5NO_2]SO_4$. The results were analyzed using the semiempirical conductivity and activity coefficient equations of Shedlovsky and Davies, respectively, and gave the parameter values Λ^∞ = 144.9 cm^2 ohm^{-1} equiv^{-1}, K_A = 400 l. mol^{-1}. Although the authors do not claim the highest precision for their results, they are obviously of good quality, and seemed to us to be worthy of further analysis using a more recent conductivity equation. There is considerable current interest in ion association of 2:2 salts in aqueous solution,[2] and we[3] have recently made an extensive reanalysis of conductometric data for dilute aqueous solutions of simple 2:2 sulfates using the following set of equations.

$$\Lambda/\Lambda_i = \alpha \tag{1}$$

$$\Lambda_i = \Lambda^\infty - S(\alpha c)^{1/2} + E\,\alpha c \ln(\alpha c) + J_1(\alpha c) - J_2(\alpha c)^{3/2} \tag{2}$$

$$K_A = (1 - \alpha)/\alpha^2 c y^2 \tag{3}$$

$$-\log y = 8A(\alpha c)^{1/2}/[1 + 2Bd(\alpha c)^{1/2}] \tag{4}$$

The symbols have the meaning: Λ, equivalent conductivity; c, concentration; α, degree of dissociation; K_A, association constant; y, mean ionic activity coefficient of free ions; d, closest distance of approach of *free* ions, or association distance. A, B, S, and E are familiar electrolyte theory parameters[3] which do not depend on the choice of d. On the other hand, J_1 and J_2 are functions of d. The physical meaning which we attach to the parameter d differs from that of Fuoss and coworkers;[4] we merely remark here that our interpretation[3] gives an excellent fit of results for 2:2 sulfates in water and removes the need for postulating significant degrees of association for sodium and potassium chlorides in dilute aqueous solutions.[4b] Some uncertainty still remains concerning the relationship between the J parameters and d; to facilitate comparison with results in our earlier paper, we have used equations derived by Fernández-Prini[5] from the Fuoss–Hsia[6] treatment, but do not wish at this stage to imply a final choice between the conductivity equations of Pitts[7] and of Fuoss, *et al.*[6] The Fernández-Prini expressions for J_1 and J_2 are[5]

$$J_1 = \sigma_1 \Lambda^\infty + \sigma_2;\quad J_2 = \sigma_3 \Lambda^\infty + \sigma_4$$

with

$$\sigma_1 = [(\kappa db)^2/24(\alpha c)]\{1.8147 + 2\ln[\kappa d/(\alpha c)^{1/2}] + (2/b^3)(2b^2 + 2b - 1)\}$$

$$\sigma_2 = B_1B_2 + B_2[\kappa d/(\alpha c)^{1/2}] - B_2[(\kappa db)/16(\alpha c)^{1/2}] \times \{1.5337 + (4/3b) + 2\ln[\kappa d/(\alpha c)^{1/2}]\}$$

$$\sigma_3 = [b^2(\kappa d)^3/24(\alpha c)^{3/2}][0.6094 + (4.4748/b) + (3.8284/b^2)]$$

$$\sigma_4 = [B_1(\kappa db)^2/24\alpha c][(2/b^3)(2b^2 + 2b - 1) - 1.9384] + B_1B_2[\kappa d/(\alpha c)^{1/2}] + [B_2(\kappa d)^2/\alpha c] - [B_2b(\kappa d)^2/16\alpha c][1.5405 + (2.2761/b)] - [B^2{}_2\kappa db/16\Lambda^\infty(\alpha c)^{1/2}][(4/3b) - 2.2194]$$

where $b = 4e^2/dD\kappa T$ and B_1 and B_2 are, respectively, the electrophoretic and relaxation coefficients of the limiting law.

For any selected pair of values of Λ^∞ and d, an estimate of the association constant K_A is obtained for

(1) W. L. Masterton and T. Brierly, *J. Phys. Chem.*, **74**, 139 (1970).
(2) (a) R. A. Matheson, *ibid.*, **72**, 3330 (1968); (b) *ibid.*, **73**, 4425 (1969); (c) P. Hemmes and S. Petrucci, *ibid.*, **73**, 4426 (1969).
(3) E. M. Hanna, A. D. Pethybridge, and J. E. Prue, *Electrochim. Acta*, in press.
(4) (a) K.-L. Hsia and R. M. Fuoss, *J. Amer. Chem. Soc.*, **90**, 3055 (1968); (b) Y.-C. Chiu and R. M. Fuoss, *J. Phys. Chem.*, **72**, 4123 (1968).
(5) R. Fernández-Prini, *Trans. Faraday Soc.*, **65**, 3311 (1969).
(6) R. M. Fuoss and K.-L. Hsia, *Proc. Nat. Acad. Sci. U.S.*, **57**, 1550 (1967); **58**, 1818 (1968).
(7) (a) E. Pitts, *Proc. Roy. Soc. A.*, **217**, 43 (1953); (b) E. Pitts, B. F. Tabor, and J. Daly, *Trans. Faraday Soc.*, **65**, 849 (1969).

each experimental point from eq 1 through 4. The average value of K_A is then used with the same Λ^∞ and d values to calculate Λ(calcd) for each point and the standard deviation for the whole set of data. The value of Λ^∞ is then altered until the standard deviation between the observed and calculated values of the conductivity is a minimum. A fresh value of d is then selected and the procedure repeated. This approach not only finds the set of parameters which gives the best fit of the experimental results but also examines the latitude available in varying the parameters while obtaining an acceptable fit of the data.

The general pattern of the outcome of our analysis closely follows that found for the 2:2 sulfates. From the 28 conductivity values reported by Masterton and Brierly[1] the best fit set of parameters is $\Lambda^\infty = 144.7_9$ cm^2 ohm^{-1} equiv^{-1}, $K_A = 368$ l. mol^{-1}, and $d = 12.5$ Å, with a standard deviation between observed and calculated Λ values of $\sigma = 0.14_2$ cm^2 ohm^{-1} equiv^{-1}. Almost identical parameter values are obtained by Justice's method.[8] If points with a standard deviation exceeding 0.1% are rejected, the 18 points that remain give $\Lambda^\infty = 144.7_6$, $K_A = 367$, $d = 12.5$ Å, with $\sigma = 0.06_0$. The association constant is substantially less than the value of 400 l. mol^{-1} reported by the original workers.[1] As we expect from earlier experience,[3] values of σ only slightly greater than the value of 0.06_0 can be obtained with other suitable combinations of the three adjustable parameters, *e.g.*, $\Lambda^\infty = 144.7_1$, $K_A = 320$, $d = 7.2$, $\sigma = 0.06_5$, but once the value of one parameter (usually d) is selected, the fit is very sensitive to the values of the other two parameters, and in particular K_A. It is a matter of choice, and of the degree of faith in the experimental data, how far one regards the lowest σ value as locating a unique value of K_A, but we emphasize that such an association constant cited without specifying also the other parameters involved, and in particular d, is *meaningless*. The same situation pertains in other cases[3,2a] and also when ion pairs are invoked to fit osmotic coefficient data for 2:2 electrolytes.[9] Indeed, if the Bjerrum type of treatment is correct and sufficiently accurate to be useful, the predicted values for physicochemical properties, but not the association constant, should be virtually independent of d over some nonzero range.[9c]

The difference between the association constants corresponding to two different values of d represents a difference in the allocation of ions between free and associated classes. If the values of K_A given above for $d = 12.5$ Å and $d = 7.2$ Å, respectively, are inserted in the Bjerrum equation[9,10]

$$K_A = \int_a^d 4\pi L r^2 \exp(4e^2/drkT)\, dr \qquad (5)$$

they should ideally give identical a values. The values are in fact 3.48 and 3.38 Å, respectively. A value of 3.4 Å is about 0.4 Å less than the average value for the simple 2:2 sulfates,[9] which have association constants[3] roughly half that of $[Co(NH_3)_5NO_2]SO_4$. The value $a = 3.4$ Å is about 2 Å less than a rough estimate from crystallographic radii suggests, and ion association is certainly considerably more pronounced than corresponds to the Bjerrum model. It is another example of enhanced association between pairs of large ions with a well dispersed charge; causative factors are probably weak hydration of the ions reinforced by dispersion forces.[1,9]

A few years ago, Atkinson and coworkers[11] concluded from an analysis in which the Fuoss–Onsager conductivity equation was applied to results for a series of 2:2 benzene disulfonates that these salts could be treated as essentially completely dissociated. This conclusion is not confirmed by an analysis using our set of equations. For the nine salts Atkinson, *et al.*, studied, we obtain association constants within the range 40–80 l. mol^{-1} with $d = 11.0 \pm 1.5$ Å. These association constants are approximately one third of the values for simple sulfates,[3] but nevertheless significant.

Acknowledgment. E. M. H. thanks the University of Basrah for a leave of absence and the Calouste Gulbenkian foundation for a Scholarship.

(8) J. C. Justice, *Electrochim. Acta*, in press.

(9) (a) J. E. Prue, "Ionic Equilibria," Pergamon Press, London, 1966, Chapters 6 and 10; (b) J. E. Prue in "Chemical Physics of Ionic Solutions," B. E. Conway and R. G. Barradas, Ed., Wiley New York, N. Y., 1966, p 163; (c) E. A. Guggenheim and R. H. Stokes, "Equilibrium Properties of Aqueous Solutions of Single Strong Electrolytes," Pergamon Press, London, 1969, p 61.

(10) J. E. Prue, *J. Chem. Educ.*, **46**, 12 (1969).

(11) G. Atkinson and S. Petrucci, *J. Phys. Chem.*, **67**, 1880 (1963), and earlier references therein.

DEPARTMENT OF CHEMISTRY
THE UNIVERSITY
READING, U. K.

E. M. HANNA
A. D. PETHYBRIDGE
J. E. PRUE*

RECEIVED JUNE 19, 1970

Radiation-Induced Chain Isomerization of *cis*-1,2-Diphenylpropene in Cyclohexane

Publication costs assisted by the Air Force Office of Scientific Research

Sir: The 1,2-diphenylpropenes, although little studied as isomerization solutes in the γ irradiation of organic liquids,[1] appear to exhibit reaction properties which make them preferable to the extensively investigated stilbenes[2-4] in such systems. Although this desirable

(1) R. A. Caldwell, D. G. Whitten, and G. S. Hammond, *J. Amer. Chem. Soc.*, **88**, 2659 (1966).

(2) E. Fischer, H. Lehman, and G. Stein, *J. Chem. Phys.*, **45**, 3905 (1966).

behavior is confirmed under usual conditions of excitation scavenging experiments, we wish to report a limitation on our earlier statement of strategic advantage of the system. Photochemical isomerization of diphenylpropene appears to proceed largely through the triplet of the olefin.[5] The γ irradiation of diphenylpropene in benzene[1] gave a $G_{c\rightarrow t}/G_{t\rightarrow c}$ ratio equal to $\phi_{c\rightarrow t}/\phi_{t\rightarrow c}$ and invariant with concentration under the conditions used. This is in contrast to the reported behavior of stilbene[3] where this G ratio increased with concentration in benzene and cyclohexane. This behavior was attributed to a contribution to the isomerization of the cis isomer by a chain mechanism at higher concentration. Such a chain isomerization was subsequently demonstrated,[6] although more recent experiments[4] have failed to reproduce the high G values reported.

This communication is concerned with the isomerization behavior of *cis*-1,2-diphenylpropene in cyclohexane under those conditions where *cis*-stilbene exhibited the greatest extent of chain isomerization, namely high concentration and low radiation dose. A recent study by Hentz and coworkers[7] indicates that under their experimental conditions no abnormal behavior was exhibited by *cis*-1,2-diphenylpropene in either benzene or cyclohexane. We find that in cyclohexane the initial G values for cis → trans isomerization are high enough to clearly demand a chain mechanism. However, the effect is quickly attenuated and becomes negligible at doses commonly used in γ irradiation experiments. The extent of this chain isomerization was not very reproducible from one set of irradiations to another. Although G values as high as *ca.* 370 were measured in one instance, Table I gives the dose dependence of $G_{c\rightarrow t}$ for a set of samples with more typical yields. Each value is the average of two identical samples and all were irradiated as a single set. The deviation of the duplicate samples was on the order of 10%, about twice that expected from analytical reproducibility.

Table I: Dose Dependence of *cis*-1,2-Diphenylpropene Isomerization

Dose, eV ml^{-1} × 10^{-19}	$G_{c\rightarrow t}$	$\Delta G_{c\rightarrow t}$	% Chain
0.12	127		~100
0.23	59		~100
0.35	37		~100
0.86	17		~100
2.60	7.8	2.4	69
9.50	3.8	2.3	39
25.68	2.6	2.1	19

It was observed that at low doses the actual yield of *trans*-1,2-diphenylpropene remained essentially invariant within a given irradiation set and increased slowly at higher doses. This indicates that the chain isomerization is effectively inhibited by some material produced by irradiation.[8] Using the average value of the yields obtained at doses $<10^{19}$ eV ml^{-1} as the initial chain isomerization, the amount of nonchain isomerization was calculated as the difference between the actual isomerization at a given dose and this initial isomerization. The G value based on this difference, designated $\Delta G_{c\rightarrow t}$ in Table I, is essentially constant at ~2.3. The per cent of isomerization which is due to chain reaction is then found from the ratio of initial to actual isomerization. (For doses $< 10^{-19}$ eV ml^{-1} this will be close enough to 100% to leave the contribution from the nonchain process completely hidden by normal experimental error.) Such behavior was observed for independently irradiated sets of solutions. Although the initial isomerization yields were generally different for different sets, reflecting the large variations observed in $G_{c\rightarrow t}$ at low doses, the values of $\Delta G_{c\rightarrow t}$ were the same within experimental error.

Table II: Scavenger Effects on $G_{c\rightarrow t}$

(a) 0.045 *M* 1,2-Diphenylpropene; 2.0×10^{20} eV ml^{-1}

Quencher	Concn, *M*	$G_{c\rightarrow t}$
...		0.90
CCl_4	0.24	0.48
CH_3OH	0.12	0.55

(b) 0.50 *M* 1,2-Diphenylpropene; 3.5×10^{18} eV ml^{-1}

...		37
CCl_4	0.10	35
CH_3OH	0.06	19

The nature of the chain mechanism for isomerization of *cis*-1,2-diphenylpropene was investigated using cation and electron scavengers under two sets of conditions: (a) at 0.045 *M* and 2.0×10^{20} eV ml^{-1} and (b)

(3) R. R. Hentz, D. B. Peterson, S. B. Srivastava, H. F. Barzynski, and M. Burton, *J. Phys. Chem.*, **70**, 2362 (1966).

(4) R. R. Hentz and H. P. Lehman, *ibid.*, **73**, 4283 (1969).

(5) G. S. Hammond, J. Saltiel, A. A. Lamola, N. J. Turro, J. S. Bradshaw, D. O. Cowan, R. S. Counsell, V. Vogt, and C. Dalton, *J. Amer. Chem. Soc.*, **86**, 3197 (1964).

(6) R. R. Hentz, K. Shima, and M. Burton, *J. Phys. Chem.*, **71**, 461 (1967).

(7) R. R. Hentz and H. G. Altmiller, *ibid.*, **74**, 2646 (1970).

(8) We realize that the same observation would be made if this amount of *trans*-1,2-diphenylpropene were initially present as an impurity in the cis isomer which was purified by preparative gas chromatography, followed by sublimation. Correction was made for the small amount (~0.01%) of isomeric impurity actually detected. Although a slow isomerization of *cis*-1,2-diphenylpropene was observed in 0.5 *M* degassed solutions, this contributed negligibly to the observed trans product under the preparation conditions used. As has been pointed out by a referee, the result could also be attributed to the presence of a small amount of an initiator in the original samples. Destruction of this material might lead to rapid fall-off of the anomalous effect. A super reactive electron scavenger might fill the bill, although we have difficulty in thinking of a suitable candidate that would be a likely contaminant.

at 0.50 M and 3.5×10^{-8} eV ml^{-1}. Under condition a the chain isomerization is small as evidenced by $G_{c\rightarrow t} \approx \phi_{t\rightarrow c}$ while under condition b it is predominant. Table II shows that both methanol, used as a cation scavenger, and CCl_4, an electron scavenger, diminish the isomerization under the high dose condition a. Under condition b, although methanol still quenches isomerization, CCl_4 enhances it. This situation is not the same as that of Hentz, *et al.*,[4] who found that some electron scavengers enhanced $G_{c\rightarrow t}$ for stilbene in cyclohexane. This was attributed to initiation of chain isomerization by a free radical mechanism. In the present case the *same* scavenger has qualitatively different effects depending on irradiation conditions. The most plausible explanation for this is that the chain process is effected through 1,2-diphenylpropene cations, not anions as has been suggested for *cis*-stilbene.[3] The cations may be formed directly by interaction with Compton electrons, by charge transfer from solvent cations, or by both mechanisms. The quenching effect of scavengers at low concentration and high dose is consistent with the previously suggested mechanism[4] in which isomerization takes place from olefin triplets formed by charge neutralization. $G_{t\rightarrow c}$, which does not exhibit the dose effect that $G_{c\rightarrow t}$ does, is also decreased by both cation and electron scavengers, in accordance with this mechanism.

Acknowledgment. This work was supported by the Directorate of Chemical Sciences, Air Force Office of Scientific Research, Contract No. F44620-70 C-0025. We are grateful to the Jet Propulsion Laboratory of the National Aeronautics and Space Administration for use of a ^{60}Co source and to Dr. D. Lawson who made the facility available.

(9) Holder of National Research Council of Canada Predoctoral Fellowship, 1966–1969.

CONTRIBUTION NO. 4099
THE GATES AND CRELLIN LABORATORIES OF CHEMISTRY
CALIFORNIA INSTITUTE OF TECHNOLOGY
PASADENA, CALIFORNIA 91109

THOMAS L. PENNER[9]
GEORGE S. HAMMOND

RECEIVED JULY 22, 1970

Inorganic Chemistry is the one...

that publishes both experimental and theoretical fundamental studies in *all phases of inorganic chemistry.*

These studies include synthesis and properties of new compounds, quantitative studies regarding structure, and thermodynamics and kinetics of inorganic reactions. Articles may range from the borders of organic chemistry to the borders of theoretical physics . . . giving you a broad expanse of authoritative information.

Besides the 35 or more papers presented in each monthly issue, you'll also profit from the shorter *Notes* and the *Correspondence* sections, that provide an informal medium of exchange for scientific views and ideas.

Inorganic Chemistry is the one . . . to order right now for your own professional interests. Simply complete and return the form below.

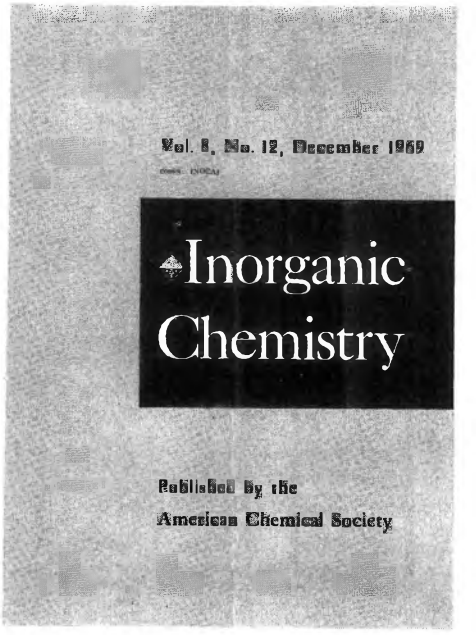

American Chemical Society / 1155 Sixteenth Street, N.W., Washington, D.C. 20036

Please enter my subscription to **Inorganic Chemistry** at the rates checked below:

ACS Members: ☐ U.S. $18 ☐ Canada, PUAS $21 ☐ Other Nations $21.50
Nonmembers: ☐ U.S. $36 ☐ Canada, PUAS $39 ☐ Other Nations $39.50

☐ Bill me ☐ Bill employer ☐ Payment enclosed (Payable to American Chemical Society)

Name _____ Title _____

Employer _____

Address: ☐ Home ☐ Business _____

City _____ State/Country _____ Zip _____

Nature of employer's business? ☐ Manufacturing or processing ☐ Academic ☐ Government ☐ Other _____
(Please indicate)

Note: Subscriptions at ACS Member Rates are for personal use only.

☐ I am an ACS member ☐ I am not an ACS member

Payment must be made in U.S. currency, by international money order, UNESCO coupons, U.S. bank draft; or order through your book dealer.